The University Of Sheffield.

Faculty of Engineering

Department of Civil and Structural Engineering

DEVELOPMENT OF A DUCTILE CONNECTION TO IMPROVE STRUCTURAL ROBUSTNESS IN FIRE

By

Yu Liu

A thesis submitted in partial fulfilment of the requirements

for the degree of Doctor of Philosophy

August 2021

ACKNOWLEDGEMENTS

I would like to express my most sincere thanks to my supervisors, Dr. Shan-Shan Huang and Professor Ian Burgess, for their patient guidance, warm support and encouragement during my PhD study. Their rich experience, profound knowledge, rigorous academic attitude, and down-to-earth work style left a deep impression on me. I am very proud to be a member of the Structural Fire Engineering Research Group at the University of Sheffield, and I will cherish this experience forever. I would also like to thank the China Scholarship Council for its financial support.

My deepest gratitude goes to my parents, my father Xiao-Min Liu and my mother Xin-Jun Qian. Thank them for their firm support for my PhD study in the UK. Without your support and dedication, I would not be able to successfully complete my PhD study, especially in the difficult period when the COVID-19 broke out around the world. Your support will always be my strongest backing. I always believe that success is in my stride, because I have parents like you by my side.

DECLARATION

I declare that this thesis is the result of my own work except where specific reference has been made to the work of others. No portion of it has been submitted for another degree qualification, diploma to any other university or institution.

Yu Liu

(Signature of candidate)

15th August 2021

ABSTRACT

Connection failures which occurred in the Cardington full-scale fire tests and in the collapse of the World Trade Centre indicate that connections are the most vulnerable parts of the structure in fire. Failure of connections can lead to a series of consequences, including the detachment of a connected beam from an adjacent column, the collapse of floors, the spread of fire into other compartments, the buckling of the column, and even the final progressive collapse of the entire building. Therefore, connections play a key role in maintaining structural integrity and stability under exposure to fire. However, conventional connection types lack the ductility to accommodate either the thermal expansion of beams during initial heating by a fire, or the tensile deformation generated by the catenary action of beams at high temperatures.

In order to prevent connection failures and improve structural robustness in fire, a novel connection with high ductility has been proposed in this research project. This novel ductile connection consists of two identical parts, each of which takes the form of a fin-plate, a face-plate and a semi-cylindrical section between these two parts. The latter can provide additional deformability by allowing the fin-plate to move towards and away from the face-plate. Equations have been proposed to quantify the ductility demand of both bare-steel and composite beams under fire conditions, which can be used as an indicator to determine the radius of the semi-cylindrical section of the ductile connection.

The analytical models of the semi-cylindrical section and the face-plate parts have been developed based on simple plastic theory. Experiments and Abaqus simulations have been carried out at both ambient and elevated temperatures to validate the analytical models of the semi-cylindrical section. An initial component-based ductile connection model has been proposed. Analytical models of the FPSC (face-plate-semi-cylindrical) component have been built, in which the face-plate part and the semi-cylindrical section are considered to deform as a whole. A second component-based model has been proposed based on the analytical models of the FPSC component. The two component-based models have been compared and validated against both experiments and Abaqus simulations. Compared with the first model, results from the second component-based model are more consistent with Abaqus simulation results. The component-based model of the composite ductile connection has been established by adding a reinforcement component to the bare-steel connection model, which can consider the pull-out of reinforcing bars the anchorage from the weld points in the mesh.

The component-based models of the ductile connection have been converted into connection elements following the principles of finite element method, and incorporated into the software Vulcan. Single beam models and 2-D bare-steel and composite sub-frame models with ductile connections have been created using both Vulcan and Abaqus to check the performance of the ductile connection elements. The 2-D bare-steel sub-frame models have also been used to compare the performance of the ductile connection with that of other connection types. Comparative results show that, the axial force generated in the beam with ductile connections is significantly reduced compared with those of the beams with other types of connections, indicating that the proposed ductile connection can provide excellent ductility to accommodate the axial deformation of beams in fire. Parametric studies have been carried out on several key parameters, including the connection thickness, inner radius of the semi-cylindrical section, connection temperature, vertical bolt spacings and connection material. The progressive collapse

of a three-storey three-bay plane frame with ductile connections has been modelled using the static-dynamic solver in Vulcan.

Parametric studies have also been conducted to test the effects of connection thickness, inner radius of the semi-cylindrical section, and the number of longitudinal reinforcing bars within the effective width of slab, on the performance of the composite ductile connection using the 2-D composite sub-frame models. In order to consider the influence of out-of-plane structure on the composite connection behaviour, 3-D composite frame models have been built to compare the performance of the ductile connection with other connection types within composite structures. Finally, the effects of shear stud spacings and unconnected length between slab and beam at the beam end on the performance of the composite ductile connection have also been investigated.

PUBLICATIONS

Journal papers:

1. LIU, Y., HUANG, S.-S. & BURGESS, I. (2019). "Investigation of a steel connection to accommodate ductility demand of beams in fire" *Journal of Constructional Steel Research*, 157, 182-197.
2. LIU, Y., HUANG, S.-S. & BURGESS, I. (2020). "Component-based modelling of a novel ductile steel connection" *Engineering Structures*, 208, 110320.
3. LIU, Y., HUANG, S.-S. & BURGESS, I. (2020). "Performance of a novel ductile connection in steel-framed structures under fire conditions" *Journal of Constructional Steel Research*, 169, 106034.
4. LIU, Y., HUANG, S.-S. & BURGESS, I. (2021). "Fire performance of axially ductile connections in composite construction" *Fire Safety Journal*, 121, 103311.
5. LIU, Y., HUANG, S.-S. & BURGESS, I. (2021). "Ductile Connection to Improve the Fire Performance of Bare-steel and Composite Frames" *Journal of Structural Fire Engineering*.
6. LIU, Y., HUANG, S.-S. & BURGESS, I. (2022). "Three-Dimensional Modelling of Composite Frames with Ductile Connections in Fire" *Structures*, 36, 665-677.

Conference papers:

1. LIU, Y., HUANG, S.-S. & BURGESS, I. Ductile connections to improve structural robustness in fire. Proceedings of the 6th Applications of Structural Fire Engineering Conference (ASFE'19), 2019 Singapore. Nanyang University of Technology
2. LIU, Y., HUANG, S.-S. & BURGESS, I. Investigation of the performance of a novel ductile connection within bare-steel and composite frames in fire. Proceedings of the 11th International Conference on Structures in Fire (SiF2020), 2020 Australia, Queensland. The University of Queensland, 662-672.
3. LIU, Y., HUANG, S.-S. & BURGESS, I. Performance of ductile connections in 3-D composite frames under fire conditions. Proceedings of the 7th Applications of Structural Fire Engineering (ASFE'21), 2021 Ljubljana. University of Ljubljana, 43-48.
4. LIU, Y., HUANG, S.-S. & BURGESS, I. A numerical study on the structural performance of a ductile connection under fire conditions. Proceedings of the 9th European Conference on Steel and Composite Structures, 2021 UK, Sheffield. The University of Sheffield

CONTENTS

LIST OF FIGURES

LIST OF TABLES

1.

INTRODUCTION

1.1. Background

Fire accidents occur frequently all over the world every year, causing huge losses to people's lives and properties. The tragic fire accident in the 24-storey Grenfell Tower block of flats in North Kensington, London caused huge casualties, including 72 deaths and more than 70 injuries, which brought great shock to the British society (MacLeod, 2018). This was the most serious building fire in the UK since the Piper Alpha disaster in 1988, and was also the worst residential fire in the UK since World War II. This disaster also prompted a review of building regulations and fire safety in the UK, Scotland, and Australia. The high temperatures caused by fire lead to the degradation of building materials. Taking steel as an example, the advantages of steel, including high strength to weight ratio, fast erection speed, high robustness and ductility, make steel one of the most popular building materials in the world. However, steel is a highly temperature-dependent material. The yield strength and elastic modulus of steel start to decrease dramatically at 400°C, and the residual strength of steel after being heated at 800°C is only 11% of the ambient temperature strength. In addition, steel has a high thermal conductivity, which leads to a rapid rise in its temperature. The thermal expansion of steel members can also generate compressive forces on adjacent structural elements. Compared with steel, concrete has a much lower thermal conductivity, and can therefore act as its own insulation, generally resulting in a slow temperature rise. However, concrete can experience heat-induced explosive spalling when it is exposed to high and rapidly-increasing temperatures, which can lead to a significant reduction of the cross-section and direct exposure of reinforcement to fire, resulting in a significant reduction of the load-bearing capacity of a structural member.

Connections play a key role in maintaining the integrity of a structure, by connecting all other structural elements together. Traditionally it is assumed that connections have adequate fire resistance, since they can be much cooler than the structural members to which they are connected in a fire. Connection failures occurred in the collapse of the World Trade Centre (McAllister and Corley, 2002) and in the Cardington full-scale fire tests (Newman et al., 2000), indicating that connections are potentially the most vulnerable parts of a structure exposed to fire, and connection failures may trigger the progressive collapse of the entire building (Gann et al., 2008). Typical

connection failures include buckling of the beam lower flange during heating, nut thread stripping at the end-plate for end-plate connection, fracture at the heel of a web-cleat and double shear of bolts at the beam web for web-cleat connections, and block shear failure of the beam web for fin-plate connections. Connection failures can occur during cooling. Figure 1-1 shows some examples of connection failures for flexible end-plate connections and fin-plate connections, observed in the cooling stage of the Cardington fire tests (Burgess et al., 2012). The failure of connections may lead to a sequence of consequences. For example, if beams separate from their connected columns, the consequences can be collapse of the local floors, the spread of fire to other compartments, the increase of slenderness ratio of the separated columns, leading to their possible buckling, and even the final collapse of the whole structure.

(a) Flexible end-plate connection failure (b) Fin-plate connection failure

Figure 1-1. Two typical connection failures (Newman et al., 2000)

The behaviour of connections under fire conditions is quite different from that at ambient temperature. During a fire accident, the internal forces experienced by connections can be approximately divided into four stages. The first stage is at ambient temperature. At this time, connections are mainly subject to vertical shear forces, accompanied by some moments, depending on the types of the connection. During the initial heating of the fire, the restrained thermal expansion of the connected beam will generate additional compressive force on the connection and the attached column will therefore be pushed out, as shown in Figure 1-2 (a), which can be regarded as the second stage. As the temperature rises to a high level, the weakening of its material dominates the behaviour of the connected beam, and the beam enters the catenary action stage, resulting in tensile force being applied to the connection, as shown in Figure 1-2 (b).

The final stage is during the cooling of the fire, in which the thermal contraction of the connected beam will superpose large tensile force on the connection.

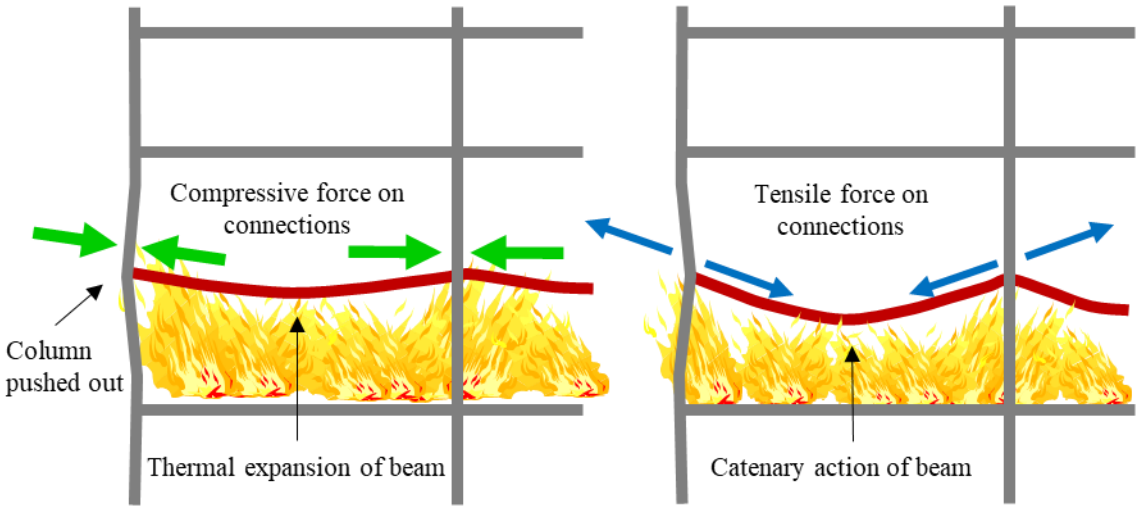

(a) At low temperatures (b) At high temperatures

Figure 1-2. Force variation of connections in fire

Current commonly-used connection types lack axial ductility to accommodate the thermal expansion of connected beams at low temperatures, their net shortening caused by catenary action at high temperatures, or their thermal contraction during the cooling stage of the fire. Therefore, this research aims to propose a novel connection with high axial ductility to accommodate the axial deformation generated by the connected beam under fire conditions, so as to prevent the brittle failure of the connection and improve the robustness of the structure in fire.

Numerical simulation is the main method adopted in this research to investigate the fire performance of the novel ductile connection. However, using a detailed finite element method to simulate the ductile connection involves a large number of elements and usually requires a dynamic solver, due to the complex contacts between bolts and bolt holes. This hinders the modelling of the real connection behaviour in an overall frame analysis to consider the effects of the connection on the structural performance. Compared with continuous FE modelling, using a high-temperature component-based method to simulate connection behaviour within a structural frame modelling FE software is a more feasible and efficient way to carry out large frame analysis including connections in fire. It was therefore decided to develop component-based connection elements of the ductile connection and to incorporate these elements into Vulcan to facilitate

global frame analysis.

1.2. Scope of research

The scope of this research is to develop a novel ductile connection and investigate its fire performance within bare-steel and composite structures. There are four main research objectives, listed below:

I. To engineer a novel connection with high ductility to prevent the brittle failure of connections and to enhance structural robustness in fire.
II. To develop component-based connection elements of the ductile connection for structural fire engineering frame analysis of both bare-steel and concrete-steel composite structures.
III. To understand the fire performance of the ductile connection within both 2-D and 3-D bare-steel and composite frames.
IV. To develop practical design guidance for the ductile connection.

1.3. Thesis outline

The thesis consists of eight chapters. Each chapter begins with an introductory section and ends with a concluding section that outlines the key findings and conclusions.

Chapter 2 - Literature Review

This chapter presents background information related to connection behaviour in fire. The basic knowledge is briefly reviewed, including material properties at high temperatures, different fire time-temperature curves, the definition and classification of joints, and three principal numerical methods to simulate connection behaviour. Among these, component-based modelling is the main numerical simulation method adopted in this research and is, therefore, introduced in detail. In addition, relevant numerical and experimental research work on the behaviour of bare-steel and composite connections in fire is also reviewed.

Chapter 3 - Proposal of the Novel Ductile Connection

This chapter presents the design and initial investigation of the novel ductile connection. Equations are derived to quantify the ductility demands of bare-steel beams under fire conditions, which can be used as important criteria for the design of the ductile connection. The tensile and compressive analytical models of the semi-cylindrical section of the ductile connection are

developed based on simple plastic theory, and validated against experiments and Abaqus simulations at both ambient and elevated temperatures. The rotational behaviour of the whole connection is modelled using a set of identical connection strips as parallel components according to the concepts of the component-based method. Simple case studies are carried out to test the performance of the ductile connection.

Chapter 4 - Component-based Modelling of the Ductile Connection

This chapter introduces an improved design version of the ductile connection, and presents a comparison between the performance of the improved version and that of the original version. The analytical models of the face-plate component of the ductile connection, and the face-plate/semi-cylindrical component (FPSC), in which the semi-cylindrical section and the face-plate component are considered to deform as a whole, based on simple plastic theory, are developed. Combined with some research work conducted by researchers from the Structural Fire Engineering Research Group at the University of Sheffield, two component-based models of the ductile connection are proposed. The loading and unloading behaviour are incorporated into individual components, and the results of the two component-based models are compared and validated against both experiments and Abaqus simulations. Two simple example applications are modelled using the proposed component-based element, to illustrate how different spring rows affect the connection deformation process.

Chapter 5 - Performance of the Ductile Connection in Steel-framed Structures

This chapter describes the incorporation of the component-based model of the ductile connection into the software Vulcan. An analytical model of bolt pull-out failure is added to the component-based model, since it is a major failure mode of the ductile connection. The tangent stiffness matrix derived by Block (2006) is used to convert the component-based model of the ductile connection into a connection element following the principles of the finite element method. A single beam with ductile connections at both ends is modelled using both Vulcan and Abaqus to check whether the connection element has been correctly incorporated into Vulcan. The analytical model of a web-cleat connection developed by Yu (2009d) is implemented within Vulcan in the same way as the ductile connection element. Sub-frame models are created using Vulcan to compare the performance of the ductile connection with that of other connection types, including idealised rigid and pinned connections, and the commonly-used end-plate and web-cleat

connections. Parametric studies are carried out to optimize the performance of the ductile connection under the tensile axial forces generated by the eventual catenary action of unprotected beams at high temperatures. The progressive collapse of a three-storey, three-bay plane frame with ductile connections is modelled using the static-dynamic solver of Vulcan.

Chapter 6 - Fire Performance of the Ductile Connection in Composite Construction

This chapter investigates the performance of the ductile connections in composite structures. Equations are derived to represent the axial ductility demands of composite beams in fire. By adding a reinforcement component to the bare-steel ductile connection model, the component-based model of the composite ductile connection is established and incorporated into Vulcan, and this is then validated against detailed Abaqus simulations. Parametric studies using Vulcan are carried out to study the effect of three parameters on the performance of the composite ductile connection. The influence of the spacing of shear studs on the connection performance is also investigated.

Chapter 7 - Three-Dimensional Modelling of Composite Frames with Ductile Connections

This chapter presents 3-D modelling of composite frames with ductile connections in fire. The 3-D composite frames with different connection types, including the ductile connection, idealised rigid and pinned connections, and conventional end-plate and web-cleat connections, are modelled using Vulcan. The influence of unconnected length between slab and beam on the connection performance is also investigated.

Chapter 8 - Conclusions and Recommendations for Future Work

This chapter summarises the main conclusions, and puts forward recommendations for future work.

2.

LITERATURE REVIEW

2.1. Chapter introduction

This chapter briefly reviews the fundamental knowledge and research work related to connection behaviour in fire. Material properties of steel and concrete, and different fire time-temperature curves are introduced first. Definition and classification of joints is then reviewed. Three principal numerical methods to simulate the connection behaviour at elevated temperatures are introduced in detail. Finally, relevant numerical and experimental research work on fire performance of bare-steel and composite connections are reviewed.

2.2. Structures under fire conditions

2.2.1. Material properties of steel at elevated temperatures

To analyse the behaviour of structures in fire, the priority is to understand the performance of materials at high temperatures. It is well known that steel is a temperature-dependent material, and its strength, stiffness, thermal expansion coefficient, specific heat and thermal conductivity are all affected by temperature. For heating rates between 2 and 50 K/min, the high-temperature stress-strain relationship of carbon steel can be calculated using the Equations (2-1) - (2-9) given in the Eurocode 3 (CEN, 2005b), and the stress-strain curves of S275 steel at different temperatures are shown in Figure 2-1. This figure shows that steel begins to lose strength from 400°C at a steady rate up to around 800°C. After that, the strength of the steel decreases at a lower rate up to about 1200°C, beyond which it has effectively zero strength.

When $\varepsilon \le \varepsilon_{p,\theta}$ $\quad \sigma = \varepsilon E_{a,\theta}$ (2-1)

When $\varepsilon_{p,\theta} < \varepsilon < \varepsilon_{y,\theta}$ $\quad \sigma = f_{p,\theta} - c + (b/a)\left[a^2 - \left(\varepsilon_{y,\theta} - \varepsilon\right)^2\right]^{0.5}$ (2-2)

When $\varepsilon_{y,\theta} \le \varepsilon \le \varepsilon_{t,\theta}$ $\quad \sigma = f_{y,\theta}$ (2-3)

When $\varepsilon_{t,\theta} < \varepsilon < \varepsilon_{u,\theta}$ $\quad \sigma = f_{y,\theta}\left[1 - \left(\varepsilon - \varepsilon_{t,\theta}\right)/\left(\varepsilon_{u,\theta} - \varepsilon_{t,\theta}\right)\right]$ (2-4)

When $\varepsilon_{t,\theta} < \varepsilon < \varepsilon_{u,\theta}$ $\quad \sigma = 0.0$ (2-5)

$\varepsilon_{p,\theta} = f_{p,\theta} / E_{a,\theta}$ $\quad \varepsilon_{y,\theta} = 0.02$ $\quad \varepsilon_{t,\theta} = 0.15$ $\quad \varepsilon_{u,\theta} = 0.20$ (2-6)

$a^2 = \left(\varepsilon_{y,\theta} - \varepsilon_{p,\theta}\right)\left(\varepsilon_{y,\theta} - \varepsilon_{p,\theta} + c / E_{a,\theta}\right)$ (2-7)

$$b^2 = c\left(\varepsilon_{y,\theta} - \varepsilon_{p,\theta}\right)E_{a,\theta} + c^2 \tag{2-8}$$

$$c = \frac{\left(f_{y,\theta} - f_{p,\theta}\right)^2}{\left(\varepsilon_{y,\theta} - \varepsilon_{p,\theta}\right)E_{a,\theta} - 2\left(f_{y,\theta} - f_{p,\theta}\right)} \tag{2-9}$$

in which, $f_{y,\theta}$ and $f_{p,\theta}$ are the effective yield strength (stress at 2% strain) and proportional limit, respectively. $E_{a,\theta}$ is the slope of the linear elastic range. $\varepsilon_{p,\theta}$, $\varepsilon_{y,\theta}$ and $\varepsilon_{u,\theta}$ are the proportional limit strain, yield strain and ultimate strain, respectively. $\varepsilon_{t,\theta}$ is the limiting strain for yield strength. Eurocode 3 Part 1-2 gives the reduction factors for the effective yield strength, proportional limit, and the slope of the linear elastic range at elevated temperatures, as shown in Figure 2-2.

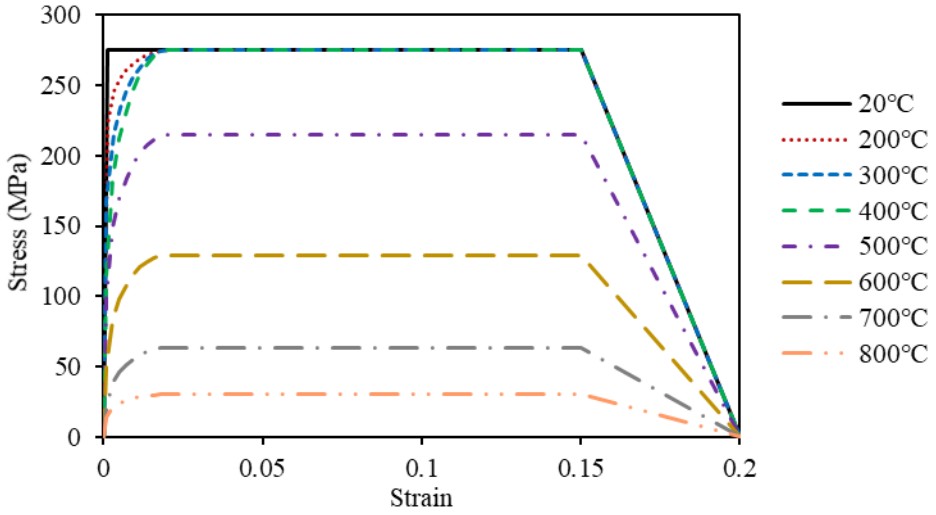

Figure 2-1. Stress-strain curves of S275 steel at different temperatures

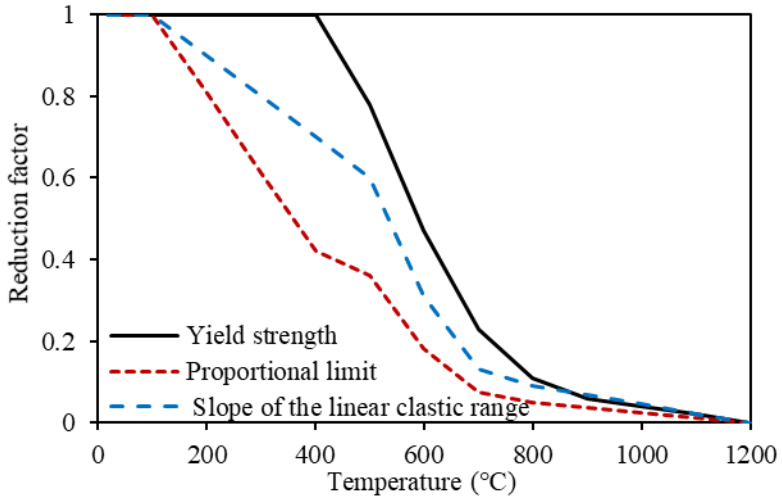

Figure 2-2. Reduction factors of carbon steel at elevated temperatures

The thermal properties of steel are also important parameters to analyse the behaviour of steel-framed structures in fire. For example, the thermal expansion of a steel beam will generate compressive axial displacement on the connections at its ends, which can potentially lead to the buckling of both beam and column if rigid connections are used. Eurocode 3 (CEN, 2005b) gives Equations (2-10) - (2-12) for calculating the thermal expansion of steel at different temperatures. It should be noted that the thermal expansion of steel increases with temperature until about 750°C, at which point the crystal structure of steel begins to change.

When $20℃ \le \theta_a < 750℃$ $\Delta l / l = 1.2\times10^{-5}\theta_a + 0.4\times10^{-8}\theta_a^2 - 2.416\times10^{-4}$ (2-10)

When $750℃ \le \theta_a < 860℃$ $\Delta l / l = 1.1\times10^{-2}$ (2-11)

When $860℃ \le \theta_a < 1200℃$ $\Delta l / l = 2.0\times10^{-5}\theta_a - 6.2\times10^{-3}$ (2-12)

in which l is the original length at ambient temperature, Δl is the temperature-induced elongation and θ_a is the steel temperature. The relative elongation of carbon steel with increase of temperature is shown in Figure 2-3 (a).

The amount of heat stored per unit mass of steel for a temperature rise of 1°C is defined as the specific heat. The rate of heat transfer over a unit cross-sectional area of a material at a unit temperature gradient is defined as the thermal conductivity. Compared with concrete, the thermal conductivity of steel is much higher, about 50 times that of concrete. Eurocode 3 (CEN, 2005b) provides Equations (2-13) - (2-16) (the unit of c_a is J / kgK) and (2-17) - (2-18) (the unit of λ_a is W / mK) to calculate the specific heat and thermal conductivity of steel, respectively. The sudden rise in specific heat at around 750°C is actually an indicator of the energy required by the crystal structure transformation. The variation of specific heat and thermal conductivity of carbon steel with temperature are shown in Figure 2-3 (b) and (c) respectively

When $20℃ \le \theta_a < 600℃$ $c_a = 425 + 7.73\times10^{-1}\theta_a - 1.69\times10^{-3}\theta_a^2 + 2.22\times10^{-6}\theta_a^3$ (2-13)

When $600℃ \le \theta_a < 735℃$ $c_a = 666 + 13002/(738 - \theta_a)$ (2-14)

When $735℃ \le \theta_a < 900℃$ $c_a = 545 + 17820/(\theta_a - 731)$ (2-15)

When $900℃ \le \theta_a < 1200℃$ $c_a = 650$ (2-16)

When $20℃ \le \theta_a < 800℃$ $\lambda_a = 54 - 3.33\times10^{-2}\theta_a$ (2-17)

When $800℃ \le \theta_a \le 1200℃$ $\lambda_a = 27.3$ (2-18)

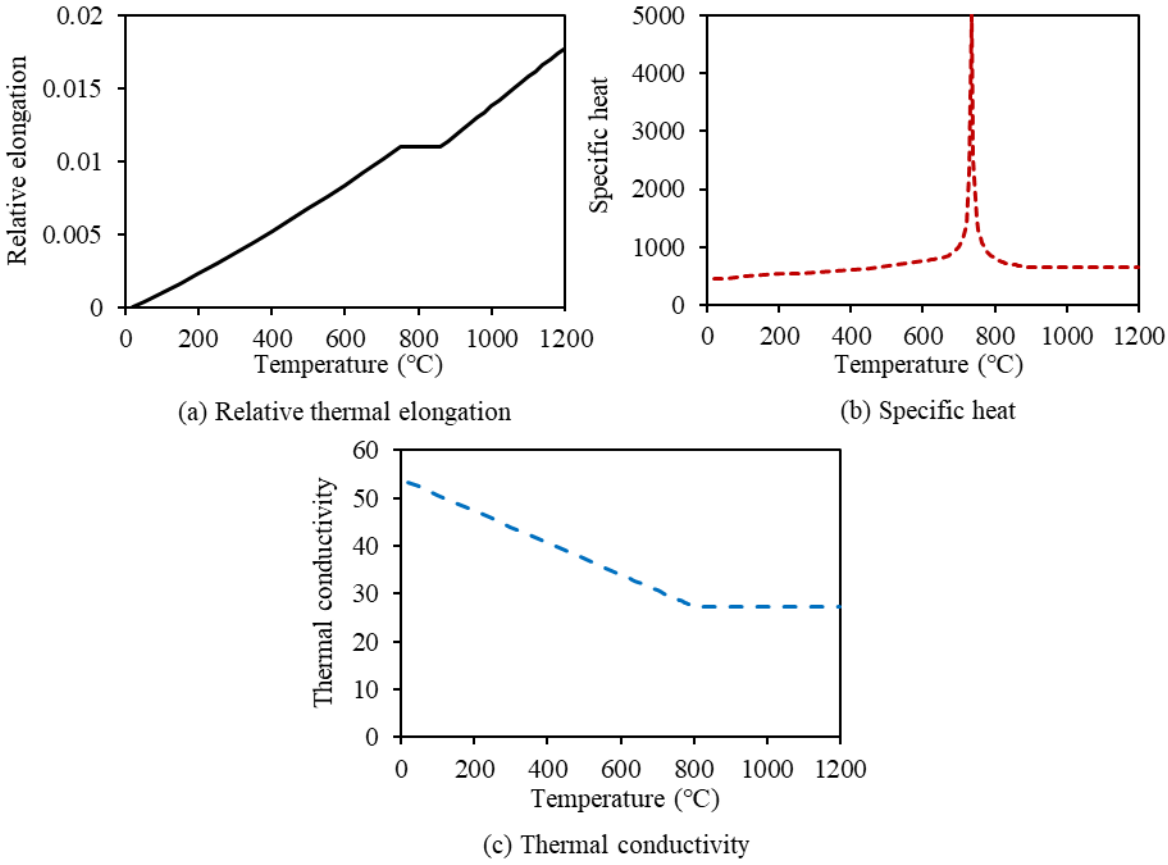

Figure 2-3. The change of thermal properties of carbon steel with temperature

2.2.2. Material properties of concrete at elevated temperatures

Steel-concrete composite structures have been widely used across the world in recent decades due to their higher structural efficiency and lower cost compared with bare-steel structures. The ductile connection proposed in this thesis can also be used in composite frames, and so it is necessary to review the performance of concrete under fire conditions. The high-temperature compressive stress-strain relationship of uniaxially stressed concrete given in Eurocode 2 (CEN, 2004a) is shown in Figure 2-4. The ascending part of the stress-strain curve can be calculated using Equation (2-19). The descending branch should be taken into consideration for numerical purposes, and linear or non-linear models can be used for this phase. It should be noted that the concrete material model presented here is applicable for heating rates between 2°K/min and 50°K/min, since the creep effect is not considered explicitly. The tensile strength of concrete is low and is usually neglected. In the case where the concrete tensile strength needs to be considered (e.g. in advanced calculation methods), Equations (2-20) - (2-22) given by Eurocode 2 can be

used.

When $\varepsilon \le \varepsilon_{c1,\theta}$ $\sigma(\theta) = 3\varepsilon f_{c,\theta} / \left[\varepsilon_{c1,\theta} \left(2 + \left(\varepsilon / \varepsilon_{c1,\theta} \right)^3 \right) \right]$ (2-19)

$f_{ck,t}(\theta) = k_{c,t}(\theta) f_{ck,t}$ (2-20)

When $20℃ \le \theta_a \le 100℃$ $k_{c,t}(\theta)$=1.0 (2-21)

When $100℃ < \theta_a \le 600℃$ $k_{c,t}(\theta)$=$1.0 - 1.0(\theta - 100)/500$ (2-22)

in which, $f_{c,\theta}$ is the high-temperature compressive strength of concrete, which can be calculated using the ambient-temperature compressive strength and reduction factors. Eurocode 2 (CEN, 2004a) specifies different reduction factors for normal weight concrete containing calcareous or siliceous aggregates.

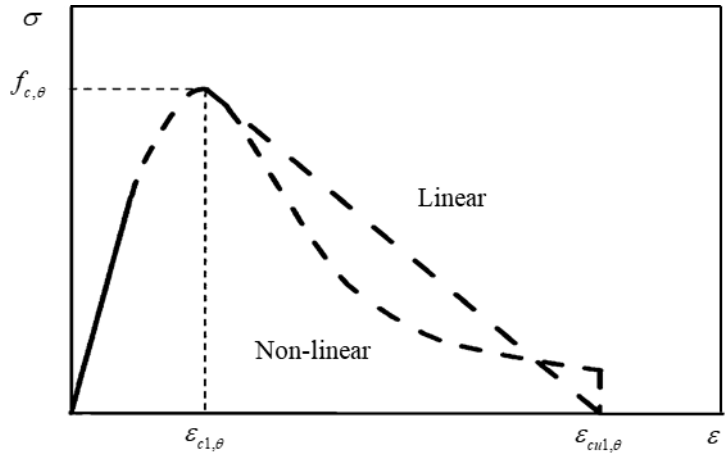

Figure 2-4. The compressive stress-strain relationship of concrete at elevated temperatures

As for the thermal properties of concrete, Eurocode 2 (CEN, 2004 a) provides Equations (2-23) - (2-26) to calculate the thermal elongation in different temperature ranges. The specific heat of dry concrete (moisture = 0%) at different temperatures can be obtained using Equations (2-27) - (2-30). The thermal conductivity of concrete can be determined between the maximum and minimum limits given in Equations (2-31) and (2-32).

For siliceous aggregates:

When $20℃ \le \theta \le 700℃$ $\varepsilon_c(\theta) = -1.8\times10^{-4} + 9\times10^{-6}\theta + 2.3\times10^{-11}\theta^3$ (2-23)

When $700℃ \le \theta \le 1200℃$ $\varepsilon_c(\theta) = 14\times10^{-3}$ (2-24)

For calcareous aggregates:

When $20℃ \le \theta \le 805℃$ $\varepsilon_c(\theta) = -1.2\times10^{-4} + 6\times10^{-6}\theta + 1.4\times10^{-11}\theta^3$ (2-25)

When $805℃ \le \theta \le 1200℃$ $\varepsilon_c(\theta) = 12 \times 10^{-3}$ (2-26)

When $20℃ \le \theta \le 100℃$ $c_p(\theta) = 900$ (J/kg K) (2-27)

When $100℃ < \theta \le 200℃$ $c_p(\theta) = 900 + (\theta - 100)$ (J/kg K) (2-28)

When $200℃ < \theta \le 400℃$ $c_p(\theta) = 1000 + (\theta - 200)/2$ (J/kg K) (2-29)

When $400℃ < \theta \le 1200℃$ $c_p(\theta) = 1100$ (J/kg K) (2-30)

When $20℃ \le \theta \le 1200℃$ $\lambda_c = 2 - 0.2451(\theta/100) + 0.0107(\theta/100)^2$ (W/m K) (2-31)

When $20℃ \le \theta \le 1200℃$ $\lambda_c = 1.36 - 0.136(\theta/100) + 0.0057(\theta/100)^2$ (W/m K) (2-32)

2.2.3. Design fires

In order to accurately simulate the behaviour of structures in fire, it is necessary to first understand the fire development process. The complete process of a natural compartment fire can be divided into two stages; pre-flashover and post-flashover. These two stages are separated by a 'flashover' point, at which all the contents in the compartment begin to burn, at which the atmosphere temperature has reached about 550℃ - 600℃. There are three methods of compartment fire simulation: single-zone model, in which the compartment is considered as uniformly heated; two-zone model, in which the compartment is divided into two layers of gases with different temperatures; and the more complex CFD (Computational Fluid Dynamics) model, which is based on a finite element method and is usually used to simulate smoke movement. Eurocode 1 (CEN, 2002) gives four different fire time-temperature curves for the single-zone model, as shown in Figure 2-5. Among them, the Standard curve, External curve and Hydrocarbon curve can be obtained using Equations (2-33), (2-34) and (2-35), respectively.

$$\Theta_g = 20 + 345\log_{10}(8t + 1) \quad (2\text{-}33)$$

$$\Theta_g = 660\left(1 - 0.687e^{-0.32t} - 0.313e^{-3.8t}\right) + 20 \quad (2\text{-}34)$$

$$\Theta_g = 1080\left(1 - 0.325e^{-0.167t} - 0.675e^{-2.5t}\right) + 20 \quad (2\text{-}35)$$

The parametric fire curve is more representative of a natural post-flashover fire as a single-zone model compared to the other three fire curves, and it considers the effects of fire load, ventilation characteristics (vertical vent height and vent area), compartment geometry and the thermal properties of walls, floor and ceiling. Eurocode 1 (CEN, 2002) provides Equations (2-36) - (2-39)

for the heating and cooling phases of the parametric fire curve. It should be noted that the parametric fire equations presented here are only applicable to compartments meeting the following criteria: 1) the floor area of the compartment should not be larger than 500m^2 in the generic Eurocode (the area is unrestricted in the UK National Annex); 2) there should be no openings in the compartment roof; and 3) the compartment height should not exceed 4m.

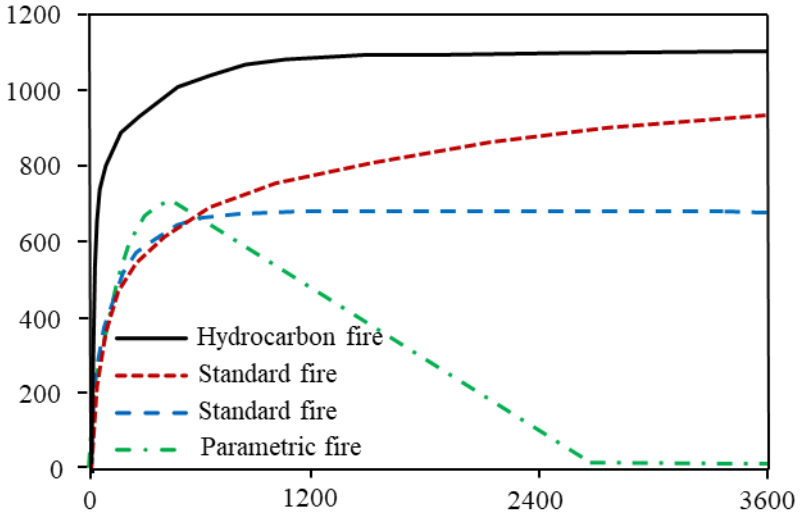

Figure 2-5. Fire curves

Heating phase:

$$\Theta_g = 20 + 1325\left(1 - 0.324e^{-0.2t^*} - 0.204e^{-1.7t^*} - 0.472e^{-19t^*}\right) \tag{2-36}$$

Cooling phase:

When $t^*_{max} \le 0.5$ $\Theta_g = \Theta_{max} - 625\left(t^* - t^*_{max} \cdot x\right)$ (2-37)

When $0.5 < t^*_{max} < 2$ $\Theta_g = \Theta_{max} - 250\left(3 - t^*_{max}\right)\left(t^* - t^*_{max} \cdot x\right)$ (2-38)

When $t^*_{max} \ge 2$ $\Theta_g = \Theta_{max} - 250\left(t^* - t^*_{max} \cdot x\right)$ (2-39)

in which Θ_g is the gas temperature in the fire compartment, t is time. $t^* = t \cdot \Gamma$ and the calculation of Γ is documented in detail in Eurocode, so it is not repeated here.

2.2.4. Structural fire engineering

Structural fire engineering involves calculating the possible fire conditions in different areas of a building, evaluating the impact of fire on structural members, and designing structural members to achieve sufficient fire resistance. In general, structural fire engineering includes three stages. The first stage is to predict the fire temperature development in a compartment. This can be

achieved by using the fire curves given in the Eurocode (CEN, 2002), including the standard fire or more complex parametric fires as mentioned in the previous section for regular compartments of appropriate area. For irregular or large compartments, the design fire needs to be simulated, using a single-zone, two-zone or CFD model. The second stage of structural fire engineering design is to predict the temperatures of individual structural members, which is usually affected by their location, size, and fire protection. The fire growth rates and the heat transfer relationships specified by the Eurocodes (CEN, 2002, 2005b) can be used in this stage to predict the member temperatures. The final stage is to analyse the response of the structural members and design them to have adequate fire resistance.

Conventionally, the "Yellow Book" (ASFP, 2004) prescribes insulation materials to keep the steel temperature below their critical temperatures. These may be specified as 550℃ (if the four sides of the steel member are exposed to fire) to 620℃ (if the concrete slab is on the top flange of the steel member), which is called the prescriptive fire protection approach. However, the disadvantage of prescriptive fire protection method is that it does not take into account the load level on structural members and is over conservative in most cases. Compared with the prescriptive fire protection method, the single member design methods given in BS5950 Part 8 (EN, 1990) and Eurocodes (CEN, 2004a, 2005b, 2005c) are more performance-based and less conservative in most cases, since they consider the fire limit state load level. These procedures are also included for passive protection materials in the “Yellow Book”. The single member design methods are based on furnace tests on isolated members, and do not consider structural continuity or the load-sharing between different structural members in real structures. The Cardington full-scale fire tests (Newman et al., 2000) show that the fire resistance of the test building was much higher than that predicted by either the prescriptive method or the single member design method. Taking this on board, the Steel Construction Institute published the BRE membrane action method in SCI P288 (Bailey et al., 2006). The BRE method considers the beam and slab as a whole, and accounts for the strength enhancement brought by the tensile membrane action and compensate for the reduction of beam bearing capacity. The conservative aspects of the BRE method include deflection limitations, ignoring the effects of beam catenary action, and ignoring the restraints from continuity to isolated slabs. However, the BRE method does not predict the connection forces, and connection failures may lead to the progressive collapse of the

entire building. In addition, the BRE method assumes that the supporting beams do not deflect and the edge beams remain composite, and ignores the column movement and possible column buckling, all of which are unconservative features of the BRE method. Advanced modelling is another approach to designing the structure to achieve the required fire resistance. In this method, representative areas of a structure are modelled using a structural finite element software. Therefore, the efficiency and reliability of the method is related to the selected finite element software. Modelling the representative areas of a structure under fire conditions using commercial finite element software (e.g., Abaqus and Ansys) is extremely time-consuming and computationally expensive. This is because it involves a huge number of elements and usually requires a dynamic explicit solver to overcome the convergence problems caused by large deformation and complex contact conditions. Vulcan is a specialist software designed for high-temperature global frame analysis considering geometric and material non-linearity. It was developed by the Structural Fire Engineering Research Group at the University of Sheffield for many years (Huang et al., 1999a, Huang et al., 1999b, Huang et al., 2000, Huang et al., 2002, Huang et al., 2009). Block (2006) and Dong (2016) incorporated the component-based end-plate connection elements into Vulcan, to enable it to consider the effects of connections in frame analysis. Sun et al. (2012a, 2012b) combined the static and dynamic solvers to develop a new solver and incorporated it into Vulcan, so that the advantages of these two solvers could be fully used to simulate the behaviour of structures in fire more effectively, from local failure to the final collapse of the entire structure. In the process of model calculation, the static solver is used until the local instability of the structure occurs, and then the dynamic solver is activated to track the motion of the structure until stability is regained. After that, the static solver is reactivated. With the component-based connection elements and the static-dynamic solver, Vulcan can efficiently simulate the complete behaviour of a structure under fire conditions, from local connection failures to the final collapse of the entire structure.

2.3. Definition and classification of joints

2.3.1. Definition of joints

To start with, it is necessary to distinguish the definition of joint from that of connection.

According to Eurocode 3 (CEN, 2005a), a 'connection' refers to the location at which two or more connected members meet, and it consists of components that transfer moments and internal forces between connected members. A 'joint' refers to the zone where two or more connected members meet, and it consists of all the relevant components required to transmit moments and internal forces between connected members. As shown in Figure 2-6, the joint includes a web panel in shear and a connection (if it is a single-sided joint), or a web panel in shear and two connections (if it is a double-sided joint).

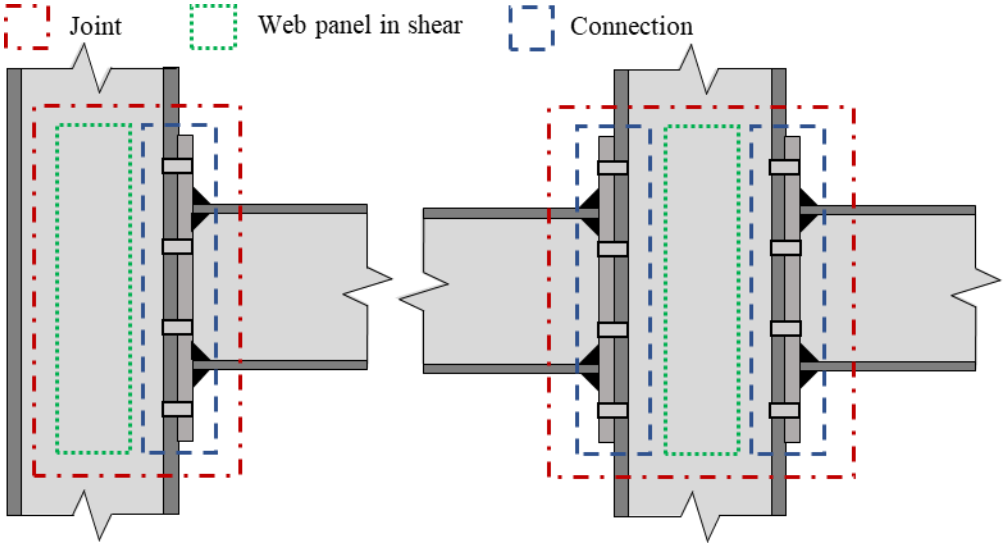

(a) Single-sided joint (b) Double-sided joint

Figure 2-6. Configuration of beam-to-column joints

2.3.2. Classification of joints

Joints can be classified as nominally pinned, semi-rigid or rigid, according to their rotational stiffness. A pinned joint should be able to transfer internal forces and bear certain rotations without developing significant moments. A rigid joint has infinite rotational stiffness, which can transfer all the moments between connected members without generating a change of rotation between the members. A joint which cannot meet the nominal-pinned or rigid joint criteria is classified as a semi-rigid joint. Eurocode 3 (CEN, 2005a) provides the classification boundaries for joints, as shown in Figure 2-7. In reality, no joint is ideally pinned or rigid, and all joints are semi-rigid. However, some joints are close enough to these two extremes and are classified as nominally-pinned or -rigid. For example, a fully welded joint can be simplified as nominally-rigid, and a web-cleat connections can be regarded as nominally-pinned.

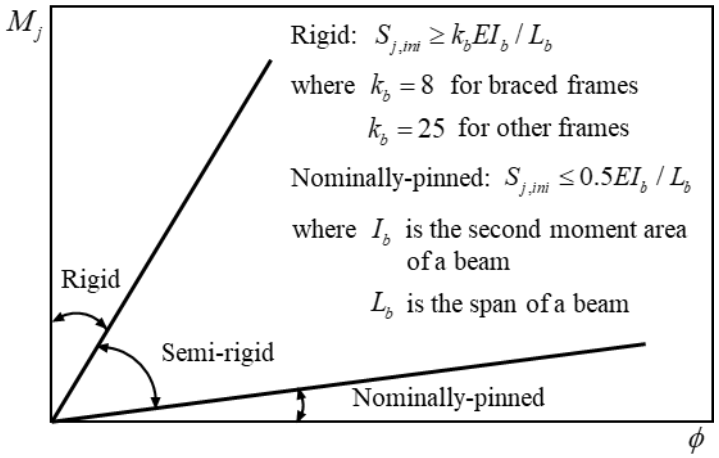

Figure 2-7. Classification of joints according to stiffness

Joints can also be classified as nominally-pinned, partial-strength or full-strength by comparing their strengths with the moment resistances of the connected members. A joint with design moment resistance equal to or larger than that of the connected members can be classified as a full-strength joint. A joint, of design resistance less than 25% of the required resistance of a full-strength joint, is regarded as nominally-pinned, provided that it still has sufficient rotation capacity. A joint between these two extremes is considered as a partial-strength joint.

Jaspart (2000) used the idea of member classes, and classified joints according to their rotation capacities. Joints with sufficient rotation capacity to allow the formation of plastic hinges in the connected members can be classified as Class 1 ductile joints. The other extreme is a Class 3 brittle joint, which should be only used in elastic design. A joint between these two boundaries is considered as a Class 2 semi-ductile joint.

When carrying out global analysis, the role of joints on the internal force transfer and overall structural behaviour should be considered in general. However, under some circumstances, the effect of joints is very small and can be neglected. There are three kinds of simplified joint model: simple, continuous, and semi-continuous. If it is assumed in design that the joint does not transfer bending moment, the simple joint model is adopted. If the influence of the joint on the structural performance is negligible, the continuous joint model should be adopted, otherwise, the semi-continuous joint model should be used. Table 2-1 summarizes how to select an appropriate joint model. This table shows that the selection of joint model depends on the joint classification and global analysis method.

Table 2-1. Selection of joint model (CEN, 2005a)

Global analysis method	Joint classification		
Elastic	Nominally pinned	Rigid	Semi-rigid
Rigid-plastic	Nominally pinned	Full-strength	Partial-strength
Elastic-plastic	Nominally pinned	Rigid and full-strength	Semi-rigid and partial-strength Semi-rigid and full-strength Rigid and partial-strength
Joint model	Simple	Continuous	Semi-continuous

2.4. Analysis methods of semi-rigid joints

Nethercot and Zandonini (1989) summarized early work on the modelling of the moment-rotation characteristics of semi-rigid joints. In general, several approaches can be used including simplified analytical models, curve-fit methods, detailed finite element modelling and the component-based method. In this section, the last three methods are introduced in detail.

2.4.1. Curve-fit method

The curve-fit method is usually used to fit data obtained from experiments, so as to incorporate test data into analytical models. Figure 2-8 illustrates typical mathematical expressions, ranging from linear, bi-linear, tri-linear, multi-linear to curvilinear.

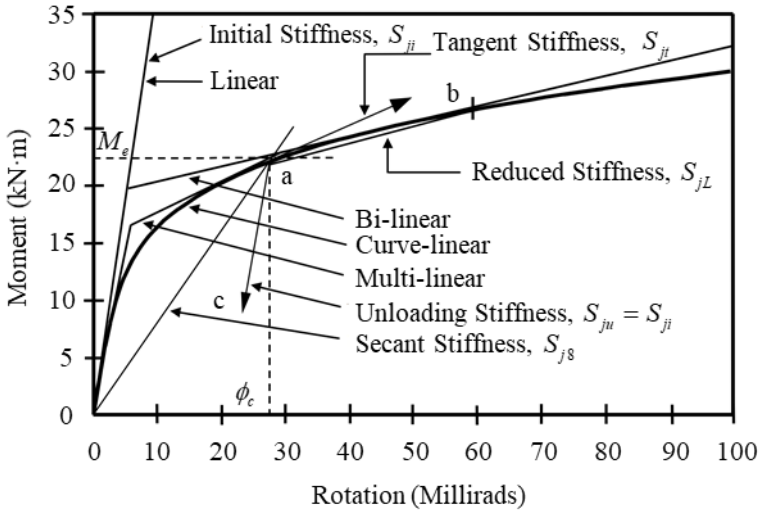

Figure 2-8. Typical mathematic expressions (Al-Jabri, 1999)

Baker (1934) and Rathburn (1936) were the first to use a mathematical expression to fit the initial slope of the connection moment-rotation curve by introducing a connection factor Z for a semi-rigid joint as shown in Equation (2-40) (Nethercot and Zandonini, 1989). Some early computer-based structural analyses (Jones et al., 1980) adopted this connection factor to investigate the

influence of semi-rigid end joints. However, this expression is too simple and conservative, and can only represent the elastic behaviour of the connection. In order to take into account high deformations, Romstad and Subramanian (1970) used a bi-linear expression for double-angle connections. This bi-linear expression is still insufficient to accurately predict connection performance, especially at high rotation levels. Moncarz and Gerstle (1981) adopted tri-linear forms in the development of an analysis program to consider the nonlinear behaviour of connections. Poggi and Zandonini (1985) used multi-linear expressions to represent joints in the analyses of single-storey portal frames. Sommer (1969) derived a polynomial expression for flexible end-plate connections using a least-square curve-fitting method, which can accurately predict the non-linear connection behaviour. However, because of the inherently oscillatory nature of polynomial expressions, negative connection stiffnesses can potentially be generated by using polynomial expressions (Sherbourne and Bahaari, 1997). To overcome this defect, Ang and Morris (1984) used and modified the Ramberg-Osgood (1943) function, which was originally derived to simulate the stress-strain relationships of metallic materials, to fit the moment-rotation curves of joints. This function always produces positive connection stiffness and can be used at both ambient and elevated temperatures. EI-Rimawi (1989, 1997) further extended this function to model connection behaviour in fire, as shown in Equation (2-41). The temperature-dependent parameters A, B and n in this equation represent the connection stiffness, connection capacity and shape of moment-rotation curve, respectively. This equation was later used by Leston-Jones (Leston-Jones et al., 1997, Leston-Jones, 1997) and Al-Jabri (1999) to model the moment-rotation-temperature behaviour of bare-steel and composite flush end-plate connections.

$$Z = \phi / M \tag{2-40}$$

$$\phi = \frac{M}{A} + 0.01\left(\frac{M}{B}\right)^n \tag{2-41}$$

in which ϕ and M respectively represent the rotation and moment of the connection.

The advantages of the curve-fit models are obvious. For example, they can predict the moment-rotation behaviour of connections with reasonable accuracy, and can easily be incorporated into the global frame analysis through a spring element at the beam end. However, the curve-fit models rely on experiments, and they can only be applied to connections that have been tested before. It is impossible to cover such a large range of connections of different types and sizes by

experiments. In addition, the forces that connections undergo under fire conditions are quite complex. The thermal expansion of beam will generate compressive axial force on connection, which is a key factor affecting connection performance, and is quite difficult to reproduce in experiments, except in full-scale tests. Therefore, the influence of beam thermal expansion on connection behaviour cannot be taken into consideration by the curve-fit methods.

2.4.2. Finite element modelling

As mentioned previously, the complex combinations of axial forces, shear forces and moments that connections undergo during a fire event cannot be reproduced in experiments on isolated members. Finite element modelling is a powerful and reliable technique to investigate connection behaviour under the effects of material degradation, thermal expansion and complex load combinations. In an FEA frame analysis that considers the connection behaviour, a large number of elements are needed to model the connections in detail, and the geometry, material properties, the contact details of the connections and the interactions between different structural members can be considered. The outputs can then reflect the deformation and the distributions of stress and strain within the connections.

Finite element modelling has already been widely used by researchers around the world. It was Liu (1996, 1998a, 1999) who made the first attempt to simulate joint behaviour at elevated temperatures using the FEM method. He developed a program called FEAST, which could take into account the non-linear material properties, non-uniform thermal expansion and large deformation of connections at high temperatures. Liu validated his program against various experiments (Lawson, 1990a, 1990b, Leston-Jones, 1997, Leston-Jones et al., 1997, Al-Jabri, 1999), and good agreement was found between the experimental and simulation results. Sarraj (Sarraj et al., 2007, Sarraj, 2007) built a series of Abaqus models considering geometric nonlinearity, material nonlinearity, large deformation and contact conditions to carry out parametric studies on the fire performance of beam-to-column fin-plate connections. Based on these parametric studies, Sarraj further proposed equations to describe the shearing behaviour of bolts, and the bearing behaviour at the bolt holes in the fin-plate and beam-web, which can be used to establish the component-based model of the fin-plate connection. To overcome

convergence problems induced by complex contacts within bolted steel connections, Yu (2008b) employed the dynamic-explicit solver in her Abaqus connection models, and validated the simulation results against experiments (Al-Jabri, 1999). Yu carried out parametric studies to investigate the effects of loading speed and mesh size on the simulation results, and concluded that by controlling the loading speed, such quasi-static problems could be simulated with a dynamic solver. Dai (2010) built Abaqus models to simulate fire tests on bare-steel beam-column assemblies with axial restraints (Dai et al., 2009). Five different connection types were adopted in the beam-column assemblies, including flexible end-plate connection, flush end-plate connection, extended end-plate connection, web-cleat connection, and fin-plate connection. Garlock and Selamet (2010) used Abaqus to model the single-plate shear connections, which are bolted to the secondary beam-web and welded to the girder (primary beam), to study the influence of slab, heating and cooling on the fire performance of steel plate connections. Gao et al. (2013) built Abaqus models of flush end-plate connections, which were verified against their experiments, to carry out parametric studies on the influence of the ratio between tension and shear on the connection behaviour under fire conditions. Qiang et al. (2014b) used Abaqus to simulate the fire behaviour of high-strength steel end-plate connections, and compared the moment-rotation characteristics, failure modes and yield-line patterns of the simulation results with their experimental results (Qiang et al., 2014a). Rahnavard and Thomas (2018) established three Abaqus connection models, including two bolted end-plate connections and one welded connection, to study the effect of fire on the connection performance, and validated their numerical results against the experiments conducted by Wald (2006) and Qiang (2015).

Finite element modelling can produce accurate simulation results considering a wide range of factors that affect connection performance. However, the establishment of finite element models usually takes a long time, and the computational costs required to complete a simulation are large. Therefore, finite element modelling is not suitable for practical structural fire engineering design, especially where global frame analysis is needed.

2.4.3. Component-based method

Compared with detailed finite element modelling, component-based modelling is a more practical

compromise between accuracy and computational costs. The component-based method divides the joint into several components, which can be represented by springs with known stiffness and strength. This method was initially proposed by Zoetemeijer (1990) to simulate the moment-rotation behaviour of steel connections at ambient temperature, and was later introduced into Eurocode 3 Part 1-1 (CEN, 2005a). Jaspart (2000) summarized the three fundamental steps of the component-based method; namely, the identification of active components, the specification of component characteristics and the final assembly of active components.

2.4.3.1. Identification of active components

The active components of a joint are the parts that may cause joint deformation or limit joint strength. Taking a joint with an end-plate connection as an example, its basic active components are shown in Figure 2-9.

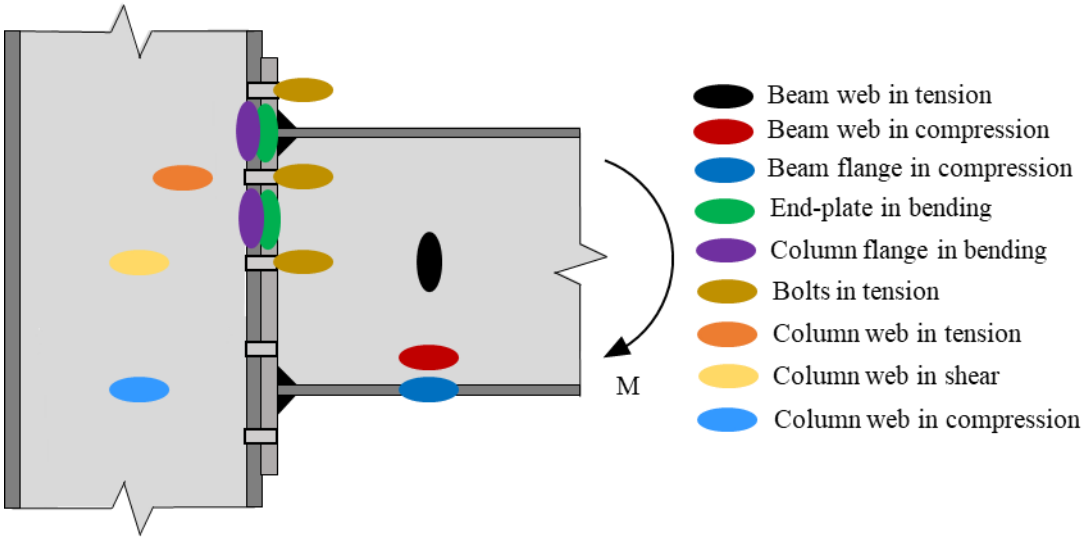

Figure 2-9. Active components of a joint with an end-plate connection

2.4.3.2. Specification of component characteristics

This is the most important step in component-based modelling, since the accuracy of the component-based model depends on the quality of the component characteristics. The component characteristics are usually represented by the force-displacement curves of the components, which can be bi-linear, tri-linear or curvilinear, and can be obtained through experiments, analytical models, or finite element modelling. In Eurocode 3, the characteristics of a component are

described by an elastic-perfectly-plastic curve, where the initial slope is the component's initial stiffness and the peak load is the design resistance of the component. This approach is appropriate for ambient-temperature analysis. However, under fire conditions, due to material degradation and the complex load combinations in the joints, the simple elastic-plastic curve is inadequate to describe the force-displacement curves of the components, and a more complex non-linear relationship is needed. This, in turn, requires the component-based model to be solved iteratively, which should not be a problem if the component-based model is incorporated into a non-linear finite element program.

2.4.3.3. Assembly of active components

The final step is to assemble all the components together and analyse the moment-rotation response of the joint. The joint with one end-plate connection shown in Figure 2-9 is again used here as an example. Figure 2-10 illustrates the component-based model of the joint, in which each component is represented by a horizontal spring. According to Eurocode 3, the moment resistance $M_{j,Rd}$ and the initial rotational stiffness S_j of the joint can be calculated using Equations (2-42) and (2-43), respectively.

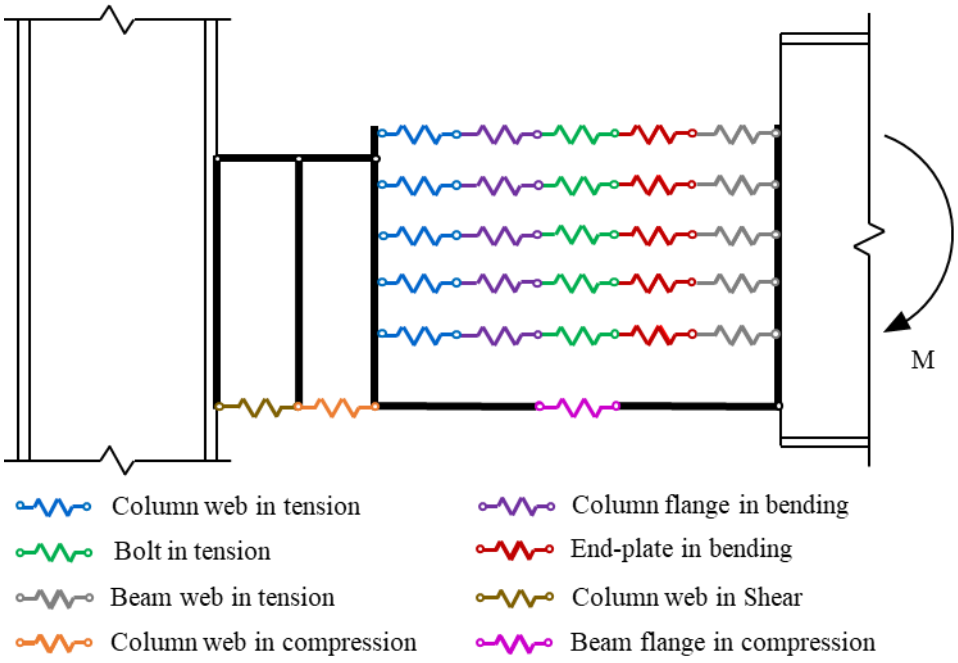

Figure 2-10. Component-based model of the joint with one end-plate connection

$$M_{j,Rd} = \sum_i h_i F_{ti,Rd} \tag{2-42}$$

$$S_j = Ez^2 / \left(\mu \sum_i \frac{1}{k_i} \right) \tag{2-43}$$

in which i is the number of bolt rows, h_i is the distance from the bolt row i to the centre of rotation, and $F_{ti,Rd}$ is the design tension resistance of the bolt row i. It should be noted that the design tensile resistance of the bolt row should be determined by the weakest component of the bolt row. In stiffness term, k_i is the stiffness of component i, z is the lever arm, and $\mu = S_{j,ini} / S_j$ is the stiffness ratio.

2.4.3.4. Research work on the component-based modelling by the Structural Fire Engineering Research group at the University of Sheffield

For many years, researchers from the Structural Fire Engineering Research group at the University of Sheffield have been applying the component-based method to the simulation of connection behaviour under fire conditions. Leston-Jones (1997) developed a high-temperate component-based model to simulate the rotational behaviour of flush end-plate connections, including components representing end-plate in bending, bolts in tension, column flange in bending and column web in compression. Continuing his work, Al-Jabri (1999) proposed component-based models for bare-steel and composite flexible end-plate connections, and validated his models against experiments. Block (2006) developed a component-based model for end-plate connections and incorporated this connection model into the software Vulcan. In Block's model, a simple analytical model developed by himself is used to predict the force-displacement curve of the column web in compression, and the analytical model for T-stubs proposed by Spyrou (2002) was adopted to represent the tension bolt rows of the end-plate connection. Sarraj (Sarraj, 2007, Sarraj et al., 2007) carried out a series of parametric studies, and derived equations to describe the characteristics of bolts in shear, fin-plate in bearing and beam web in bearing for fin-plate connections. Based on Sarraj's equations, Taib and Burgess (2013) proposed a component-based model for the fin-plate connection. Yu (2009a) established a T-stub model for end-plate connections considering large deformations and failure modes, and verified her model against

both experiments and finite element simulations. Yu (2009d) also developed a mechanical model to describe the behaviour of web cleats under tying forces. On the basis of this mechanical model, she further proposed a component-based model for web-cleat connections, which also includes other components, such as holes in bearing, bolts in tension, and bolts in double shear. Dong (2016) combined Yu's work with Block's, and proposed component-based models for end-plate connections and reverse-channel connections, which have all been incorporated into Vulcan. Hu (2009) developed a component-based model for flexible end-plate connections and validated his model against experimental results. In this study, the component-based method will be used to model the ductile connection, and some work conducted by the researchers from the Structural Fire Engineering Research group at the University of Sheffield will be directly applied to the component-based models of the ductile connection.

2.5. Connection behaviour under fire conditions

It is traditionally assumed that connections have sufficient fire resistance, since their temperatures in fire tend to be much lower than those of the structural elements to which they connected. However, the connection failures observed in many fire accidents and in large-scale frame fire tests indicate that connections are actually the weakest parts of the structure. It is, therefore, necessary to investigate the connection performance in fire.

2.5.1. Behaviour of bare-steel connections in fire

The numerical studies on the high-temperature behaviour of bare-steel connections have already been summarized in Section 2.4. Therefore, the work reviewed in this section focuses on high-temperature experiments on bare-steel connections.

Kruppa (1976) made the first attempt to conduct fire tests on connections, including fin-plates, angle cleats, flush end-plates, and extended end-plates. The purpose of these tests was to obtain the high-temperature performance of high-strength bolts, and the behaviour of the connections themselves was not given. Lawson (1990a, 1990b) carried out tests on eight cruciform joints exposed to the ISO 834 standard fire to study the global rotational behaviour of the joints. Leston-Jones (Leston-Jones, 1997, Leston-Jones et al., 1997) was the first to obtain the moment-rotation

curves of joints at different temperatures by conducting eleven tests on cruciform joints with flush end-plate connections. The experimental results confirmed that the stiffness and the strength of joints decreased with the increase of temperature, especially above 500°C. In a following project, Al-Jabri (Al-Jabri, 1999, Al-Jabri et al., 1999) continued Leston-Jones's work, conducting twenty high-temperature tests on flush and flexible end-plate joints. Al-Jabri further studied the effects of several parameters on joint behaviour, including connection type, member size and failure mechanism. It was during this project that Al-Jabri realized that, due to the lack of axial forces generated by the connected beam, the tests on isolated joints cannot reflect the actual behaviour of the joints within a structural frame under fire conditions.

Yu carried out a series of tests on web-cleat connections (Yu et al., 2008a, 2009c), fin-plate connections (Yu et al., 2009b), and flush end-plate connections (Yu et al., 2010) at both ambient and elevated temperatures. The experiments on web-cleat connections mainly studied the tying and rotational capacities of this kind of connection under different load combinations of tension and shear. It was found that the two main failure modes of the web-cleat connections, including fracture at the heel of the web-cleat and double shear of bolts at the beam web, are not particularly sensitive to the loading conditions, but are more related to the temperature. The tying capacity of web-cleat connections decreases rapidly with the increase of temperature, whereas their rotational capacity is much higher than that of other conventional connection types. The experimental results of 14 tests on fin-plate connections under tension and shear showed that temperature has a significant effect on the resistance of fin-plate connections, and bolt shear was the main failure mode in the tests of fin-plate connections. Using bolts with higher grade may change the failure mode of web-cleat connections into block shear failure of the beam web. According to Yu's experimental results on flush end-plate connections, flush end-plate connections exhibit much stiffer behaviour than web-cleat and fin-plate connections. The maximum resistance of the tested flush end-plate connections can be achieved when the connection is rotated by as little as 2°, and can be maintained until the connection is rotated by 7°. As with web-cleat and fin-plate connections, the failure mode of the flush end-plate connection is greatly affected by its temperature. With the increase of temperature, the failure mode of flush end-plate connections changed from failure of the end-plate to failure of bolts. During the same period, Hu (2008) conducted experiments on flexible end-plate connections, and found that the tying capacities of

the connections calculated on the basis of the Eurocode were overestimated compared with his test results. The experimental setup used by Yu and Hu is shown in Figure 2-11. Huang (2013) also conducted a series of tests on reverse-channel connections between a steel beam and a CFT column with this kind of test device. It was found that the main failure modes of reverse-channel connections include fracture of the reverse-channel web, punching failure and tensile fracture of bolts.

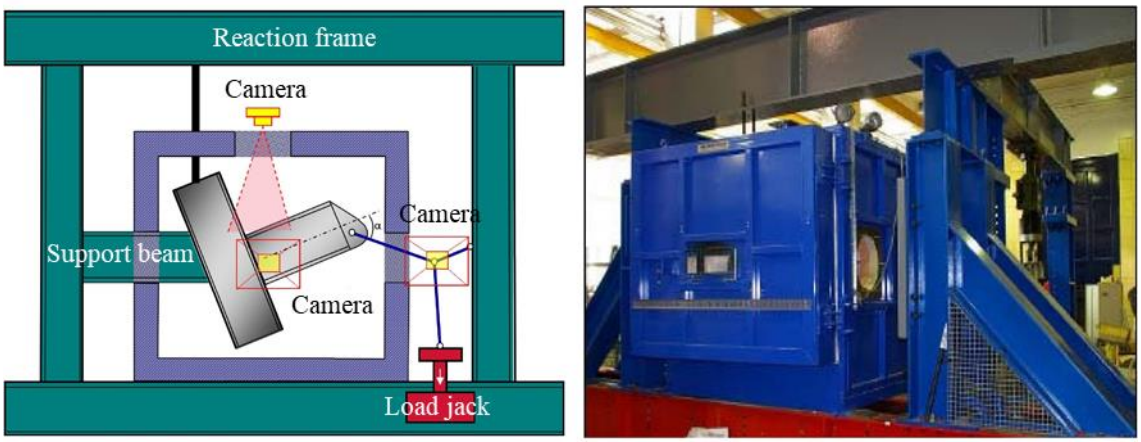

Figure 2-11. Experimental setup

In order to investigate the behaviour and ductility of connections with structural interaction under fire conditions, Wang conducted 10 high-temperature tests on restrained steel sub-frames with different connection types, including fin-plate, web-cleat, extended end-plate, flexible end-plate and flush end-plate connections. Two column sizes were used in the tests to apply different levels of axial restraint to the beam. The results showed that the ductility of the web-cleat connection is the best among the five kinds of connections, and this allowed the connected beam to develop catenary action without connection failure, while the ductility of the flexible end-plate connection was the worst. Wang (2011) concluded that if the catenary action of beams is considered in fire resistant design, the influence of connection type should be also taken into account.

The concept of the novel ductile connection was first proposed by Ian Burgess. Then, two MSc students at the University of Sheffield conducted simple tests on the model-scale specimens under the supervision of Ian Burgess. Briggs (2016) used 3D printing technique to produce 316L austenitic stainless-steel specimens, and selected four temperatures (including 350°C, 450°C, 550°C and 650°C) to carry out high-temperature compression tests. Kalawadwala (2018) used S275 steel to produce test specimens and conducted three tensile and three compression tests at ambient

temperature. In this research, the experiments done by Briggs and Kalawadwala are used to validate the analytical models of the ductile connection.

2.5.2. Behaviour of composite connections in fire

Due to the continuity of the concrete slab in composite floor, the behaviour of connections in composite structures is quite different from that of connections in bare-steel structures. The composite slab can act as insulation to the connection, reducing its temperature. In addition, it can restrain the thermal expansion of the steel beam, leading to the thermal bowing of the whole composite beam, which will also affect the connection behaviour. Leston-Jones (Leston-Jones et al., 1997, Leston-Jones, 1997) carried out three tests on composite flush end-plate connections with constant external loading and increasing temperature, and obtained the high-temperature moment rotation characteristics of the connections. Al-Jabri (1999) tested two composite flexible end-plate connections at elevated temperatures, and developed a component-based model for this kind of connection. Liu (1998b) further developed his finite element program FEAST to model the behaviour of composite connections in fire, considering the influence of non-linear temperature profile, and the interaction between bolts, shear studs and reinforcements. He validated the composite connection model against experiments done by Lennon and Jones (1995), and the numerical results were in good agreement with the experimental results. Li et al. (2012b) conducted three high-temperature tests to investigate the performance of composite flush end-plate joints in fire considering the influence of axial force. It was found that the failure of the composite joints without stiffeners was controlled by the buckling of the beam bottom flange near to the beam end, and that the axial force affected the rotational stiffnesses and moment capacities of the joints. They further built a three-dimensional Ansys model to simulate the behaviour of composite joints in fire considering the effects of axial force, which was verified with their experimental results, and developed a simplified component-based model to calculate the initial rotational stiffness and moment capacity of composite joints (Li et al., 2012a). Pucinotti et al. (2011) studied the performance of welded full-strength composite joints under seismically-induced fire, both numerically and experimentally.

2.6. Chapter conclusion

In this chapter, the basic knowledge and research work relevant to the performance of connections under fire conditions have been reviewed. The mechanical and thermal properties of steel and concrete at elevated temperatures have been introduced. Different fire time-temperature curves have been described. The definitions of joints and connections have been clarified to avoid confusion, and different classifications of joints according to their rotational stiffness, rotational capacity and strength have also been introduced. As the focus of this research is the numerical study of the performance of the ductile connection in fire, three commonly-used numerical methods have been introduced in detail, including curve-fitting, finite element analysis and the component-based method. Finally, experimental and numerical studies on the fire behaviour of bare-steel and composite connections have been reviewed.

The finite element method and the component-based method are the two principal methods adopted in this research to investigate the fire performance of the ductile connection. To accurately model connection behaviour in fire, the non-linear material properties at high temperatures should be taken into account. This can easily be achieved by inputting the high-temperature material stress-strain curves into the commercial finite element software when the connection is modelled using the FE method. If the degradation of material properties with increasing temperature is considered in a component-based model, then the component-based model should be solved iteratively. This should not be a problem if the component-based model is incorporated into a finite element program. Some research work conducted by the researchers from the Structural Fire Engineering Research group at the University of Sheffield will be directly applied to the component-based models of the ductile connection, which will be introduced in detail in the following chapters.

3.

PROPOSAL OF THE NOVEL DUCTILE CONNECTION

3.1. Chapter introduction

In maintaining structural integrity and preventing progressive collapse, connections play a very important role by acting as the critical components tying all other structural members together. As mentioned previously in the background, the internal forces experienced by connections in fire can broadly be classified into four stages. In the initial stage, at ambient temperature, the major force carried is vertical shear accompanied by some bending moment depending on the details of the connection, due to the design loading carried by the beams. After heating starts, a connection begins to experience additional compression normal to the column face due to the restrained thermal expansion of the connected beam at a stage when weakening of the beam's material is not very significant. Eventually, at very high temperature, when material weakening becomes more important than thermal expansion, the connected beam carries its load mainly by catenary action, and the connections become subject to tension. In cooling, from either of the two previous stages, the thermal contraction of the beam as it regains stiffness superposes tensile force on the connection.

However, conventional connection types lack the axial ductility to accommodate either the compressive or tensile axial forces mentioned above, and this could allow connection fractures to take place. This research aims to develop a novel ductile connection which allows the large tensile and compressive deformations imposed by the connected beam at elevated temperatures, so as to reduce the connection forces generated and prevent connection fracture in fire. This chapter illustrates the development and initial investigation of this new ductile connection. The analytical tensile and compressive model of the connection components has been developed on the basis of simple plastic theory, and the rotational model is achieved using an array of these components. The analytical model is compared against experiments and Abaqus finite element simulations at both ambient and elevated temperatures. Finally, simple case studies using a single beam model and a sub-frame model have been carried out to test the performance of the ductile connection.

3.2. Ductility demand and design of the novel ductile connection

Connections are restrained by adjacent structural members. As described previously, during the

initial stage of a fire accident a beam will apply axial compressive force to its connections due to restraint to its free thermal expansion. When the temperature increases further, and the beam has lost most of its bending resistance, tensile force will be applied to the connection due to the catenary action of the beam. The examples presented in Figure 3-1 illustrate this change in axial internal force acting on the connection. The difference between Figure 3-1 (a) and (b) is that the free thermal expansion of the beam in Figure 3-1 (b) is accommodated by ductile boundary conditions, so that both the compression and tension forces generated in (b) are much smaller than those in (a).

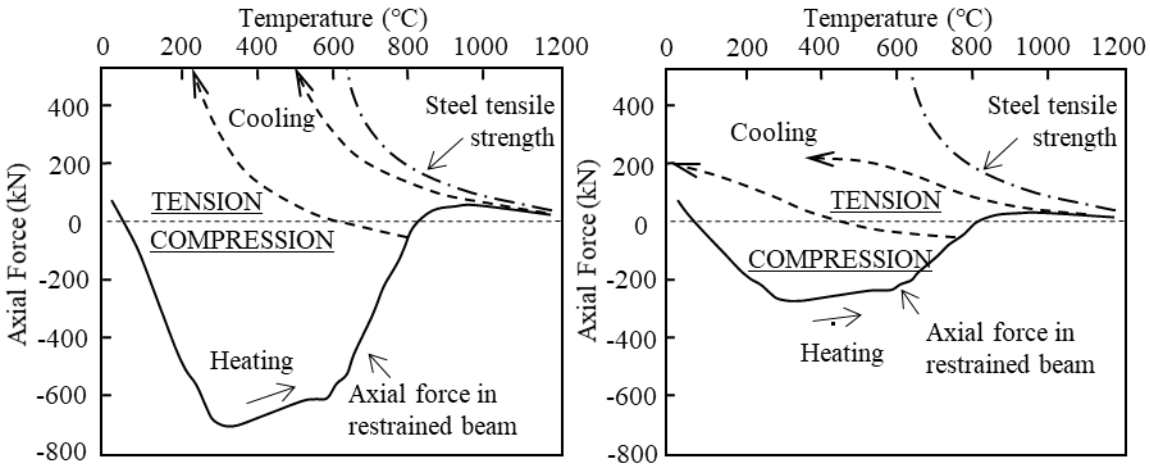

(a) with strong axial restraint (b) with axially ductile connections

Figure 3-1. Change of axial internal forces of a connection in fire conditions (Burgess et al., 2012)

It is clear that a structure requires connections with high ductility in order to retain its integrity and stability under exposure to fire. The design of a proposal for an appropriate ductile connection is therefore governed firstly by the degree of ductility required. In the early stage of a fire, usually while the beam temperature is below about 600°C, the connection should be able to accommodate the thermal expansion of the connected beam, together with the effects of beam-end rotation and effective shortening due to beam deflection. This reduces the force transmitted to the adjacent structure and prevents connection fracture in compression. As shown in Figure 3-2 (a), the bottom end of the connection should be able to withstand the horizontal movement:

$$\Delta_{low-temp} = \frac{1}{2}(\alpha l T + h\theta) - \frac{4}{3}\delta^2 / l \tag{3-1}$$

Where α is the thermal expansion coefficient of steel, T is the beam temperature, l is the length of the beam, h is the height of the beam section and δ is the mid-span deflection of the beam.

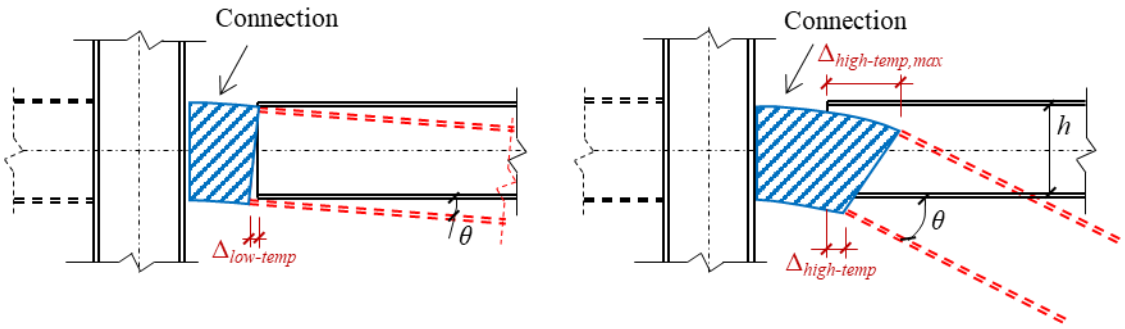

(a) Low-temperature movement (b) High-temperature movement

Figure 3-2. Beam-end movements in different temperature phases

In the high temperature range, when the beam acts essentially in catenary action, the top edge of the connection should be able to accommodate a movement $\Delta_{high-temp,\max}$ to prevent fracture at the top of the connection and to avoid hard contact between the beam bottom flange and column face, as shown in Figure 3-2 (b). Deformation $\Delta_{high-temp}$ and $\Delta_{high-temp,\max}$ can be calculated using Equations (3-2) and (3-3). Furthermore, the connection should be able to withstand the tensile force generated by the catenary action of the beam, which can be calculated according to Equation (3-4), in which w_f is the uniformly distributed line load intensity. The deformability provided in tension effectively reduces the tensile force in the connection, especially when the beam is subject to large deflection, and this in turn helps to prevent connection fracture.

$$\Delta_{high-temp} = \frac{4}{3}\delta_{\max}{}^2 / l - \frac{1}{2}(\alpha l T + h\theta) \tag{3-2}$$

$$\Delta_{high-temp,\max} = \frac{4}{3}\delta_{\max}{}^2 / l - \frac{1}{2}(\alpha l T - h\theta) \tag{3-3}$$

$$F = w_f l^2 / 8\delta_{\max} \tag{3-4}$$

To meet this prescribed ductility demand presented by the beam behaviour, taking into account ease of construction, the connection shown in Figure 3-3 is proposed. Advantages such as low cost and ease of installation currently make fin-plate and end-plate connections popular within the construction industry. The new connection consists of two identical parts, which can be considered as shaped web cleats. Each cleat includes; a fin-plate, bolted to the beam web; an end-plate, bolted to either the column web or flange, and; a semi-cylindrical section (which is either circular or elliptical in shape) between the fin-plate and end-plate. These deformed cleats can be

fabricated by bending a steel plate. An alternative fabrication method might be to weld two plates to a semi-tubular section, which is a costlier and more labour intensive, and therefore not preferred. The semi-cylindrical section is the key to providing the required push-pull ductility, allowing the fin-plate to move towards and away from the end-plate in order to accommodate the thermal expansion and catenary action of the connected beam, in surviving the different force conditions as the beam temperature rises. This is intended to enable the connection to resist large tensile and compressive deformations and to minimise the probability of brittle failure modes that may initiate progressive collapse.

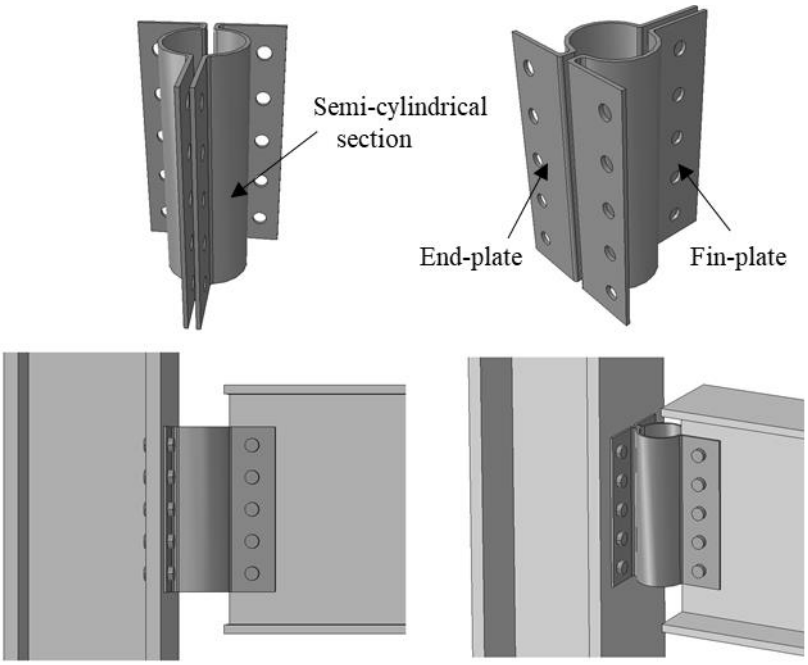

Figure 3-3. The proposed detail of the novel ductile connection

As mentioned above, the cylindrical section should be able to accommodate the deformation of the connected beam during fire within both the low-temperature and high-temperature ranges. The diameter of the cylindrical section is a critical design parameter, which has the greatest impact on the ductility of the whole connection, and should be selected according to the values of $\Delta_{low-temp}$, $\Delta_{high-temp,\max}$ and $\Delta_{high-temp}$. The example design demonstrated here is for a beam of length 7.5m, subject to a uniform line load at the Fire Limit State of 32.6 kN/m. The beam is designed to be UKB 533×210×109. The fin-plate and end-plate of the ductile connection have been designed to the Eurocode. The dimensions of the connection are shown in Figure 3-4, and M20 Grade 8.8 bolts in 22mm diameter bolt holes are adopted. The ductile cylindrical section of

the novel connection type will accommodate the large deflection of the connected beam at high temperature, which in turn significantly reduces the axial force in the connection. Therefore, the tensile forces in the welds and bolts will be modest. They will mainly take shear, which they are designed to Eurocode to take, and so they are not expected to be critical in this case. It is sized to satisfy Equations (3-1) - (3-3). When the temperature of the beam is 600°C, $\Delta_{low-temp}$ of the beam is 29mm. When its temperature reaches 800°C the catenary force is governed by the reduced tensile strength of the beam. Therefore, the maximum beam deflection $\delta_{\max}$, which is 548mm, can be calculated according to Equation (3-4), and is then substituted into Equations (3-2) and (3-3) to calculate the axial deformation of the beam. The movements $\Delta_{high-temp,\max}$ and $\Delta_{high-temp}$ of the beam at 800°C are 57mm and 22mm, respectively. Therefore, if the beam is designed to resist a temperature of 800°C, the connection should be able to accommodate at least 50mm axial deformation. If the inner radius of the cylindrical section is designed to be 50mm, this enables the cylindrical section to have enough deformability to accommodate the axial deformations of the beam in both directions. The connection must, of course, be adequate for ambient-temperature Ultimate Limit State conditions. This involves checking shear capacity of the cylindrical section using Equation (3-5), and verifying the resistance of the connection according to BS EN1993-1-8 (CEN, 2005a) at ambient temperature, under:

- bolt shear,
- bolt bearing,
- shear and bearing of the fin-plate,
- shear and bearing of the bolt group,
- shear of the end-plate.

$$V_{Rd} = A_v \frac{f_y}{\sqrt{3}\gamma_{M0}} \tag{3-5}$$

Where V_{Rd} and A_v are respectively the shear capacity and cross-sectional area of the cylindrical section.

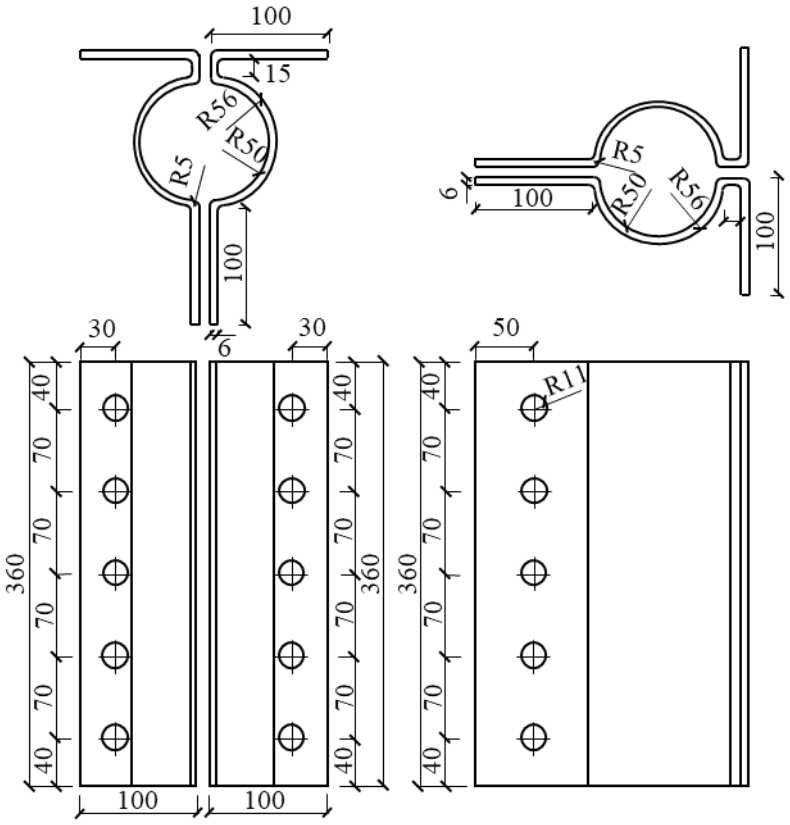

Figure 3-4. Dimensions of the connection for the case study

3.3. Development of simplified analytical models

Any horizontal slice through the connection is mainly subjected to tensile and compressive forces which cause the semi-cylindrical section to bend. Plastic hinges will form in the cross-section where the maximum internal bending moments occur. Therefore, simple plastic theory (Horne, 2014) is adopted to model the plastic behaviour of any slice through the cylindrical section. Material and geometric nonlinearities are considered. The effects of shear and axial forces on plastic moments are neglected, as they have very limited influence (Bhatt, 1999) on the formation and capacity of plastic hinges. According to the virtual work principle, the rate of work done by external loads should equal the rate of strain energy increase generated by the rotation of plastic hinges.

3.3.1. Calculation of the strain energy of a plastic hinge

A bi-linear stress-strain relationship is assumed at ambient temperature, changing to a tri-linear

constitutive law for high temperature analysis, as shown in Figure 3-5 (a).

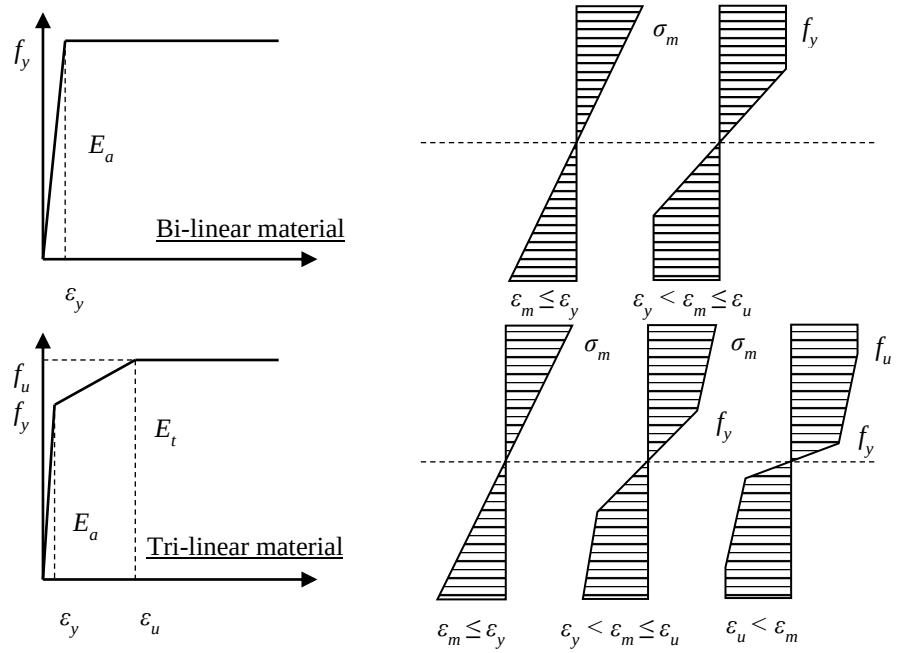

(a) Stress-strain relationships (b) Stress distributions within the bending cross-section

Figure 3-5 Material properties adopted

Yu's method (2009a) of calculating the strain energy of a plastic hinge is adopted. The derivation process is well documented, and so it is not described in detail here. The stress distributions across the bending cross-section of a plastic hinge under different conditions are shown in Figure 3-5 (b). The maximum strain is ε_m and the maximum stress within the cross-section is σ_m. The internal moment of the plastic hinge is calculated by integrating over the cross-section.

For the bi-linear stress-strain relationship:

When $\varepsilon_m \le \varepsilon_y$ $\quad M_p = \dfrac{B_{eff} t^2}{2}\left(\dfrac{E\varepsilon_m}{3}\right)$ *and* $\quad W_{PH} = B_{eff} t^2 \left(\dfrac{1}{12} E\theta^2\right)$ (3-6)

When $\varepsilon_m > \varepsilon_y$ $\quad M_p = \dfrac{B_{eff} t^2}{2}\left(\dfrac{E\varepsilon_y^3}{3\varepsilon_m^2} + \dfrac{f_y}{2}(1 - \dfrac{\varepsilon_y^2}{\varepsilon_m^2})\right)$ (3-7)

and $W_{PH} = B_{eff} t^2 \left(E\varepsilon_y^2 - 2 f_y \varepsilon_y + \dfrac{6 f_y \varepsilon_y^2 - 4E\varepsilon_y^3}{3\theta} + \dfrac{f_y \theta}{2}\right)$ (3-8)

For the tri-linear stress-strain relationship:

When $\varepsilon_m \le \varepsilon_y$, the equations are the same as for the bi-linear case.

When $\varepsilon_y < \varepsilon_m \le \varepsilon_u$ $M_p = \frac{B_{eff}t^2}{2}\left(\frac{E_t\varepsilon_m}{3} + \frac{(E-E_t)\varepsilon_y}{2} - \frac{(E-E_t)\varepsilon_y^3}{6\varepsilon_m^2}\right)$ (3-9)

and $W_{PH} = B_{eff}t^2\left\{\frac{E_t\theta^2}{12} + (E-E_t)\left(\frac{\theta\varepsilon_y}{2} + \frac{k^2\varepsilon_y^3}{6\theta} - \frac{k}{2}\varepsilon_y^2\right)\right\}$ (3-10)

When $\varepsilon_m > \varepsilon_u$ $M_p = \frac{B_{eff}t^2}{2}\left\{\frac{3\varepsilon_m^2 f_u + (E-E_t)(3\varepsilon_y\varepsilon_u^2 - \varepsilon_y^3) + 2E_t\varepsilon_u^3 - 3f_u\varepsilon_u^2}{6\varepsilon_m^2}\right\}$ (3-11)

and $W_{PH} = B_{eff}t^2\left\{\frac{E_t\varepsilon_u^2}{3} + (E-E_t)\left(\varepsilon_y\varepsilon_u - \varepsilon_y^2 + \frac{\varepsilon_y^3}{3\varepsilon_u}\right) + \Omega\left(\frac{k}{\varepsilon_u} - \frac{k^2}{\theta}\right) + \frac{f_u(\theta - k\varepsilon_u)}{2}\right\}$ (3-12)

in which $\Omega = (E-E_t)\left(\frac{\varepsilon_y\varepsilon_u^2}{2} - \frac{\varepsilon_y^3}{6}\right) + \frac{E_t\varepsilon_u^3}{3} - \frac{f_u\varepsilon_u^2}{2}$ (3-13)

where M_P is the plastic hinge moment capacity, W_{PH} is the strain energy, B_{eff} is the effective width of the cross-section and θ is the rotation angle of the hinge. If the length of the plastic hinge is assumed to be equal to the thickness t of the cross-section, the rotation angle can be calculated as:

$\theta = \int_0^t \frac{\varepsilon_m}{t/2} dx = 2\varepsilon_m$ (3-14)

3.3.2. Tensile analytical model

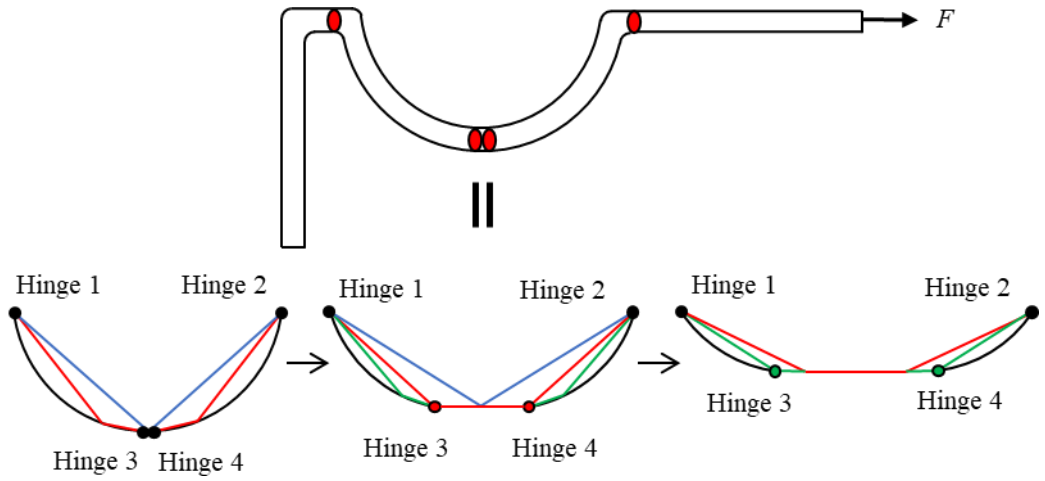

Figure 3-6. Location of plastic hinges in a deforming tensile mechanism

Since the proposed connection is symmetric, the analytical model is developed for half of the connection. Four plastic hinges, located at the two ends and the outer edge of the cylindrical

section, are assumed to form during the deformation of the connection, as shown in Figure 3-6. Several assumptions are made for the tensile geometric model. As shown in Figure 3-6, the positions of the two end plastic hinges (Hinges 1 and 2) remain unchanged throughout the deformation process. However, the two hinges (Hinges 3 and 4) at the outer edge of the cylindrical section will move towards the end hinges as the section is stretched. During this process, the curvatures of the parts of the cross-section between Hinges 1 and 3 and between Hinges 2 and 4 remain unchanged. Finally, Hinges 3 and 4 respectively meet Hinges 1 and 2 when the cylindrical section has been stretched flat. Since the strain energy equations have already been derived, the geometric relationship shown in Figure 3-7 (a) between the displacement of the moving hinges and the rotation angle of each plastic hinge is the key to solving the virtual work equation.

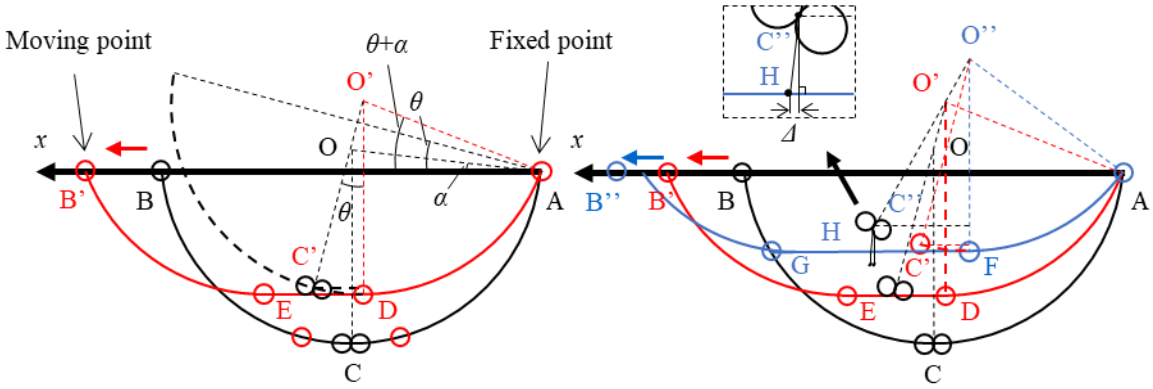

(a) Geometric relationship (b) Correction of displacement calculation

Figure 3-7 Geometric relationships in the tension model

The centre line of the semi-cylindrical cross-section is shown as OC in Figure 3-7. The black solid curve in the figure represents the original shape of the semi-cylindrical section. The red and blue solid lines represent the shapes of the cross-section at small and large deformations respectively. The angle of rotation about the plastic hinge of the arc centre relative to the x axis is α. It is assumed that the endpoint A of the arc is fixed, and the other end B moves along the x axis to deform the arc. It is obvious that the rotation angles of the four plastic hinges are always identical during the whole deformation process. When the plastic hinge at the fixed endpoint A rotates by a small angle θ (Figure 3-7 (a)), the black solid arc becomes the dashed arc. The new position of Hinge 4 should be the highest point on the dashed arc, which is the intersection point (D) of the vertical line (through the new centre point O') and the dashed arc. The new position of Hinge 3 should be at the mirrored position of Hinge 4 with respect to Point C'. Thus, the displacement of

the moving Point B is calculated as:

$$\Delta x = 2r\left[\sin\theta + \cos(\theta+\alpha) - \cos\alpha\right] \tag{3-15}$$

where r is the radius of the arc. Then, if there is a small rotation $d\theta$, the displacement increment of the moving point is:

$$dx = 2r\left[\cos\theta - \sin(\theta+\alpha)\right]d\theta \tag{3-16}$$

However, when the rotation angle of the plastic hinges is large, a displacement calculation error Δ occurs, shown as Figure 3-7 (b). Point C is the centre-point between Hinges 3 and 4 in the initial state and Point H is the centre-point between Hinges 3 and 4 in the large-rotation stage. According to the geometric model assumption, the x-coordinate of Point C'' should be equal to that of Point H. However, as illustrated in the magnified part of Figure 3-7 (b), this assumption is no longer true; there is a small horizontal distance Δ between Points C'' and H. The error Δ increases as the hinge rotates. Therefore, the originally calculated distance between Hinges 3 and 4 needs to be corrected. When the rotation angle θ is large, θ should be divided into n steps and the plastic hinge rotates by θ / n in each step. Accordingly, Equations (3-15) and (3-16) should be modified to:

$$\Delta x = 2r\left[n\sin\left(\theta/n\right) + \cos(\theta+\alpha) - \cos\alpha\right] \tag{3-17}$$

$$dx = 2r\left[\cos\left(\theta/n\right) - \sin(\theta+\alpha)\right] \tag{3-18}$$

According to the virtual work equation:

$$Fdx = \int_0^{\theta+d\theta} 4M_p d\theta - \int_0^{\theta} 4M_p d\theta \tag{3-19}$$

Substituting Equations (3-6) - (3-14) and (3-18) into (3-19), the relationship between the external force F and the rotation of plastic hinge θ can be obtained.

For the bi-linear stress-strain relationship:

When $\varepsilon_m \le \varepsilon_y$ $\quad F = \dfrac{Eht^2\theta}{6r\left[\cos(\theta/n) - \sin(\theta+\alpha)\right]}$ (3-20)

When $\varepsilon_m > \varepsilon_y$ $\quad F = \dfrac{ht^2\left[3\theta^2 f_y - \left(12 f_y \varepsilon_y^2 - 8E\varepsilon_y^3\right)\right]}{6\theta^2 r\left[\cos(\theta/n) - \sin(\theta+a)\right]}$ (3-21)

For the tri-linear stress-strain relationship:

When $\varepsilon_m \le \varepsilon_y$, the equation is the same as that in the case of the bi-linear material.

When $\varepsilon_y < \varepsilon_m \le \varepsilon_u$ $$F = \frac{ht^2\left[E_t\theta^3 + (E - E_t)(3\theta^2\varepsilon_y - 4\varepsilon_y^3)\right]}{6\theta^2 r\left[\cos(\theta/n) - \sin(\theta+\alpha)\right]} \quad (3\text{-}22)$$

When $\varepsilon_m > \varepsilon_u$ $$F = \frac{ht^2\left[3\theta^2 f_u + (E - E_t)(3\varepsilon_y\varepsilon_u^2 - \varepsilon_y^3) + 2E_t\varepsilon_u^3 - 3f_u\varepsilon_u^2\right]}{6\theta^2 r\left[\cos(\theta/n) - \sin(\theta+\alpha)\right]} \quad (3\text{-}23)$$

where h is the width of the connection and t is the thickness of the cross-section. A sensitivity analysis at ambient temperature is carried out to determine the appropriate value of n and the results are shown in Figure 3-8. Convergence is reached when n is larger than 10, and this value is therefore adopted.

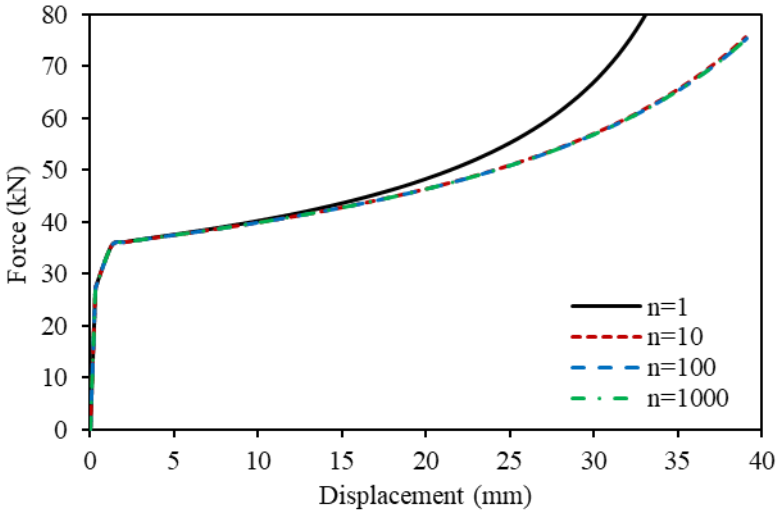

Figure 3-8. Influence of n value on tension curve

3.3.3. Compressive analytical model

The difference between the tensile and compressive models is that the positions of top two hinges (Hinges 3 and 4) remain unchanged in the compressive model. According to the geometric relationships shown in Figure 3-9, the calculation equation for displacement should be:

$$\Delta x = 2r[\cos\alpha - (\cos(\theta - \alpha) - \sin\theta)] \quad (3\text{-}24)$$

Then, if there is a small rotation $d\theta$, the displacement increment is:

$$dx = 2r\left[\sin(\theta - \alpha) + \cos\theta\right]d\theta \quad (3\text{-}25)$$

Substituting Equations (3-6) - (3-14) and (3-25) into (3-19), the relationship between external force F and the rotation angle θ of the plastic hinge can be obtained:

For the bi-linear stress-strain relationship:

When $\varepsilon_m \le \varepsilon_y$ $F = \dfrac{Eht^2\theta}{6r\left[\sin(\theta-\alpha)+\cos\theta\right]}$ (3-26)

When $\varepsilon_m > \varepsilon_y$ $F = \dfrac{ht^2\left[3\theta^2 f_y - \left(12 f_y\varepsilon_y^2 - 8E\varepsilon_y^3\right)\right]}{6\theta^2 r\left[\sin(\theta-\alpha)+\cos\theta\right]}$ (3-27)

For the tri-linear stress-strain relationship:

When $\varepsilon_m \le \varepsilon_y$, the equation is the same as that in the case of bi-linear material.

When $\varepsilon_y < \varepsilon_m \le \varepsilon_u$ $F = \dfrac{ht^2\left[E_t\theta^3 + (E-E_t)(3\theta^2\varepsilon_y - 4\varepsilon_y^3)\right]}{6\theta^2 r\left[\sin(\theta-\alpha)+\cos\theta\right]}$ (3-28)

When $\varepsilon_m > \varepsilon_u$ $F = \dfrac{ht^2\left[3\theta^2 f_u + (E-E_t)(3\varepsilon_y\varepsilon_u^2 - \varepsilon_y^3) + 2E_t\varepsilon_u^3 - 3f_u\varepsilon_u^2\right]}{6\theta^2 r\left[\sin(\theta-\alpha)+\cos\theta\right]}$ (3-29)

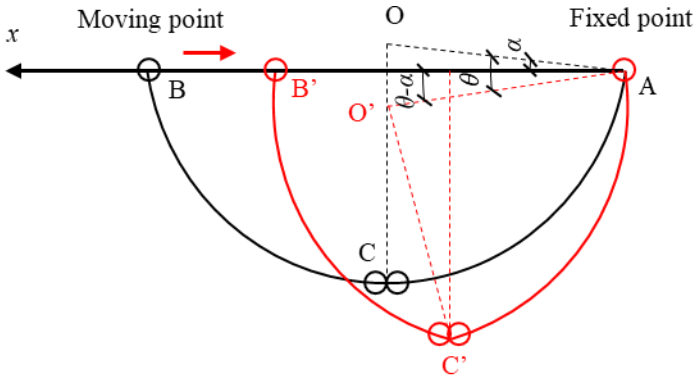

Figure 3-9. Geometric relationships of compression model

3.3.4. Push-pull behaviour of a connection

Applying Equations (3-20) - (3-23) and Equations (3-26) - (3-29) for a connection of depth 360mm and plate thickness 6mm with a semi-circular inner radius 50mm, fabricated in steel of grade S275, a continuous curve linking force and movement can be constructed, and this is shown in Figure 3-10. It can be seen that the tensile curve stiffens with displacement after its plastic mechanism has been created, while the compressive curve reduces its force with displacement, at least until it is fully compressed when the two edges contact one another.

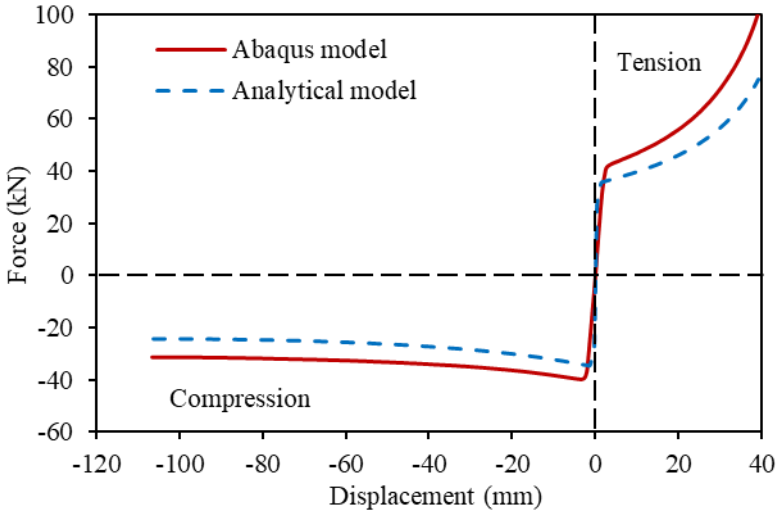

Figure 3-10. Full push-pull force-displacement curve for the example connection strip

3.3.5. Rotational model

The concept of the component-based method can be used here to model the rotational behaviour of the whole connection using a set of identical connection strips as parallel components. As can be seen in Figure 3-11, the whole connection is divided into a number of horizontal strips.

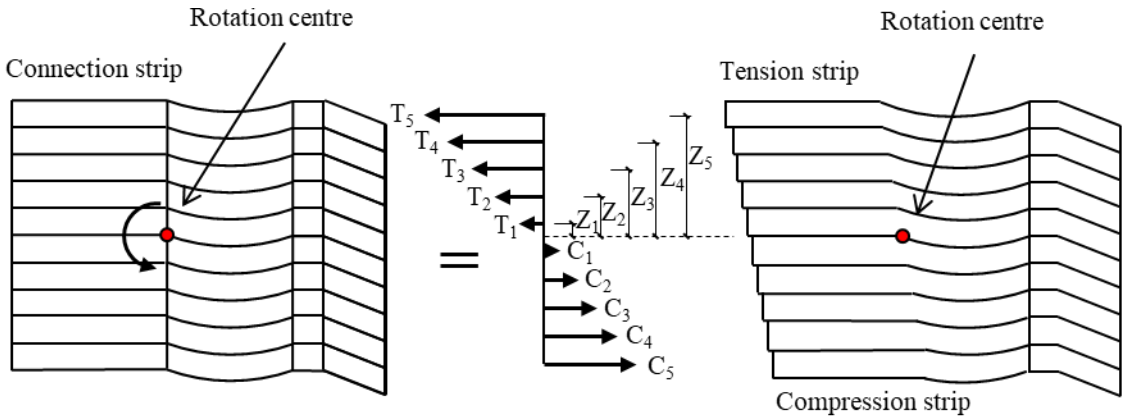

Figure 3-11. Rotational connection strip component-based model

When the connection is rotated about its centre point, these strips are either pushed or pulled. The normal force of each strip under tension or compression can be calculated using the tension or compression models described previously. Then the rotational moment of the whole connection can be obtained by calculating the moment of each strip's force about the centre of rotation:

$$M = \sum_{i=1}^{N/2} (T_i + C_i) Z_i \tag{3-30}$$

In this equation N is the total number of connection strips and Z_i is the distance between the

centre point of the i th connection strip and the centre of rotation of the entire connection. A sensitivity analysis was carried out at ambient temperature to find the appropriate strip number N, and the results are shown in Figure 3-12.

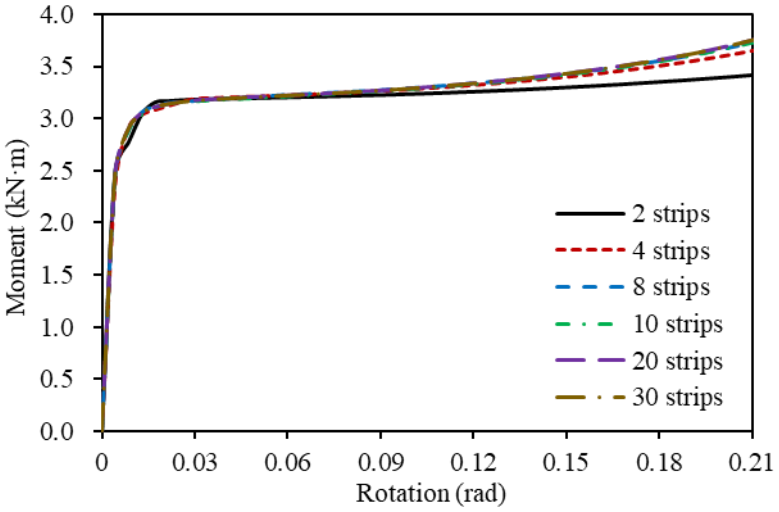

Figure 3-12. Influence of total number of strips on connection moment

It can be seen that the resulting curve of the analytical model with 8 connection strips is consistent enough, but the connection models at high temperatures have adopted 10 strips. However, it has been seen from Figure 3-10 that the tensile strength of the connection is higher than its compressive strength in the plastic stage. Under the same displacement, a tension connection strip will generate a larger force than the corresponding compression strip. Therefore, an external axial force, which may be the reaction at the centre of rotation, is required to equilibrate this model. A model to which a pure moment is applied will experience a shift of its centre of rotation in order to balance the total tension and compression forces; this will be accompanied by a horizontal movement of the centre of rotation.

3.4. Validation of analytical models against Abaqus simulations

In this section, the general-purpose finite element software Abaqus is used to validate the tensile, compressive, and rotational analytical models proposed, at both ambient and elevated temperatures. The shell element S4R is adopted in the Abaqus simulation, to save cost in computation compared with the use of solid elements.

3.4.1. Validation of tension and compression models at ambient temperature

The geometries of the tension and compression models are identical, and the details are those shown in Figure 3-4. The material used is S275 steel. As for the boundary conditions of the Abaqus model, the end-plate is fixed and the out-of-plane displacement of the fin-plate is constrained by being bolted to the beam web. A mesh sensitivity analysis indicated that an element size of 10mm x 10mm was adequate for the connection model, as shown in Figure 3-13.

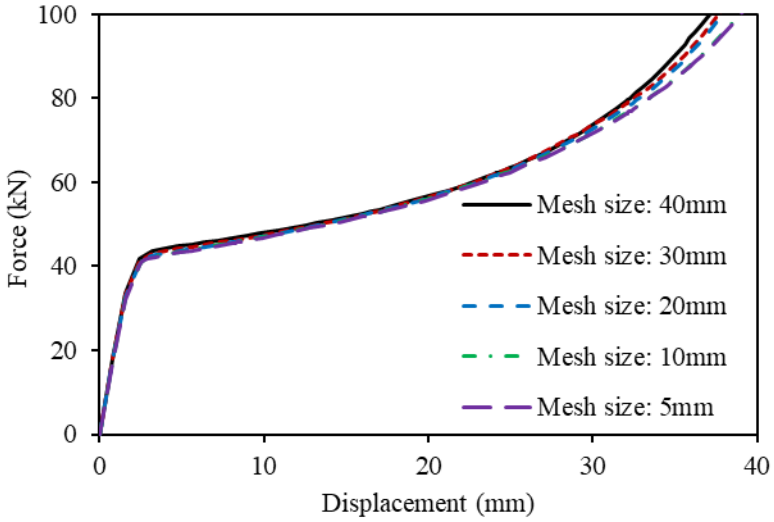

Figure 3-13. Mesh sensitivity analysis

The analytical model is in satisfactory, although not complete, agreement with the Abaqus model; the comparison of two models is shown in Figure 3-10. The initial slopes of the tension and compression curves in the linear-elastic stage are equal. In the plastic stage, as the connection is pulled in tension, the force required increases steadily up to the tension deformation limit is reached, when the connection is effectively straightened, and the four plastic hinges are located on the same line. The slope of the tension curve in the plastic stage increases continuously and becomes almost vertical near to the tension deformation limit, because of the continuous reduction of the lever arm between the applied axial force and the top two plastic hinges (Hinges 3 and 4 in Figure 3-6). For the compression curve, the force required to increase the compression displacement decreases steadily in the plastic stage up to the final compression deformation limit, at which contact, either within the cylindrical section or between the cylindrical section and the end-plate, occurs. This is opposite to the trend of the tension curve due to the increasing lever arm between the applied force and the top two plastic hinges.

3.4.2. Validation of rotation model at ambient temperature

For the analytical rotational model, the connection behaviour is considered as the sum of its components' behaviour. Rotation of the entire connection is simulated by tension and compression of each connection strip. Deformation compatibility of two adjacent connection strips is only piecewise in this analytical model; this ignores the horizontal shear force between adjacent strips. In order to make a more reasonable comparison between the analytical and Abaqus models, two Abaqus connection models were created, which are shown in Figure 3-14. These were used to study the effect of the shear between strips on the rotational behaviour of the whole connection. In the strip model compatibility is maintained between adjacent strips except with respect to horizontal movements, although the ends of each strip are tied so that their movements are in a straight line. As with the component-based analytical model, defined in Figure 3-11, the connection is constrained to rotate about a point at the base of the fin-plate, about which it is also free to move in the vertical direction, although restrained in the axial direction.

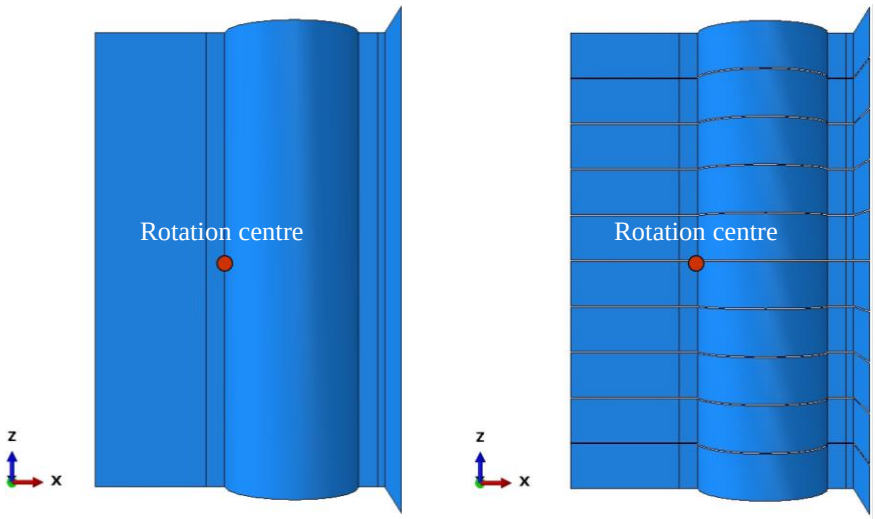

(a) The whole connection piece (b) The strip model

Figure 3-14. Two Abaqus models

The comparison of the two Abaqus models and the analytical model is shown in Figure 3-15. A significant difference can be seen between results from the Abaqus strip model and the analytical model. The difference between the Abaqus strip model and whole connection model indicates that an additional moment is generated by the shear force between adjacent strips in providing rotation compatibility, mainly due to compatibility of the torsional rotations of adjacent strips. This

compatibility is hard to implement in a simple model and it is considered unnecessary to include it; this might be considered using a safety factor at a later stage. The discrepancy between the Abaqus strip model and analytical model will be explained later in Section 3.4.4. In any case, the analytical model gives a more conservative result than either Abaqus model.

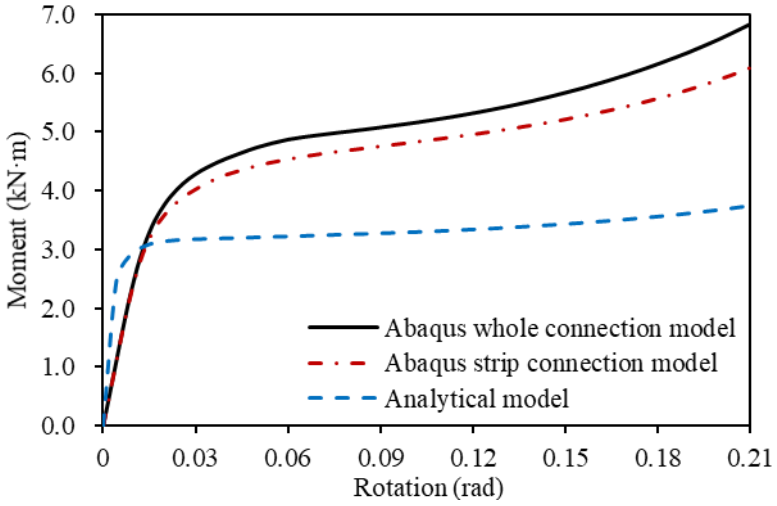

Figure 3-15. Comparison of rotation analytical model against Abaqus models

3.4.3. Validation of analytical models at elevated temperatures

The material properties of the connection at elevated temperatures are calculated according to Eurocode 3 Part 1-2 (CEN, 2005a). For Abaqus simulation, the model is first heated to a pre-defined temperature and then a pure tension, compression or rotation displacement is applied to the model to obtain the force-displacement curve at this temperature value. The comparison of the Abaqus and analytical models over a range of elevated temperatures is shown in Figure 3-16 and Figure 3-17.

It can be seen from Figure 3-16 and Figure 3-17 that all curves are of the same shape, and the difference between analytical and Abaqus models decreases as temperature rises. This indicates that temperature does not influence the deformation mode of the connection. Above 400℃ the force required to produce a certain deformation decreases progressively with increase of temperature. However, it is obvious that this ductile connection can provide satisfactory push-pull ductility at elevated temperatures.

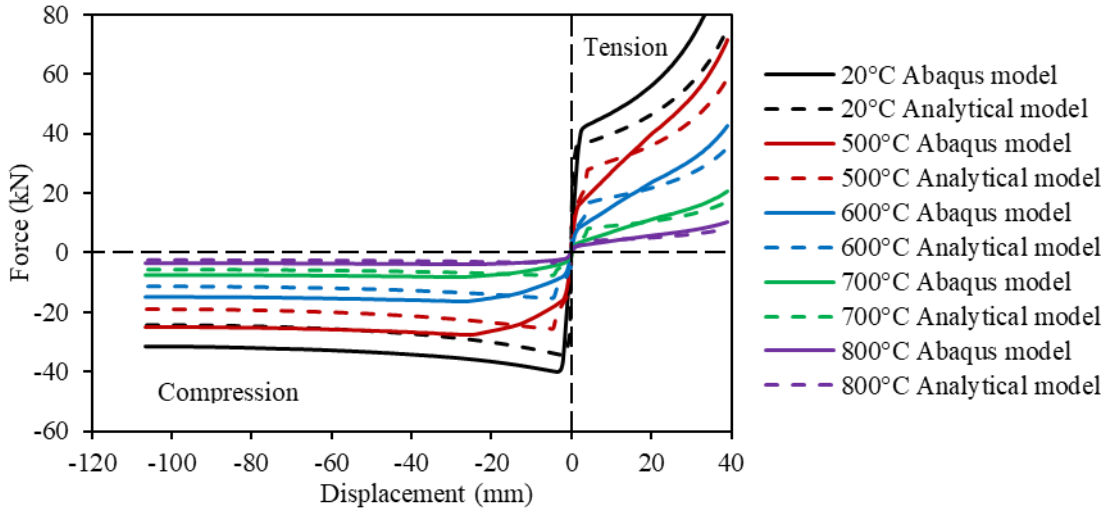

Figure 3-16. Comparison of tension/compression analytical push-pull model against Abaqus model at elevated temperatures

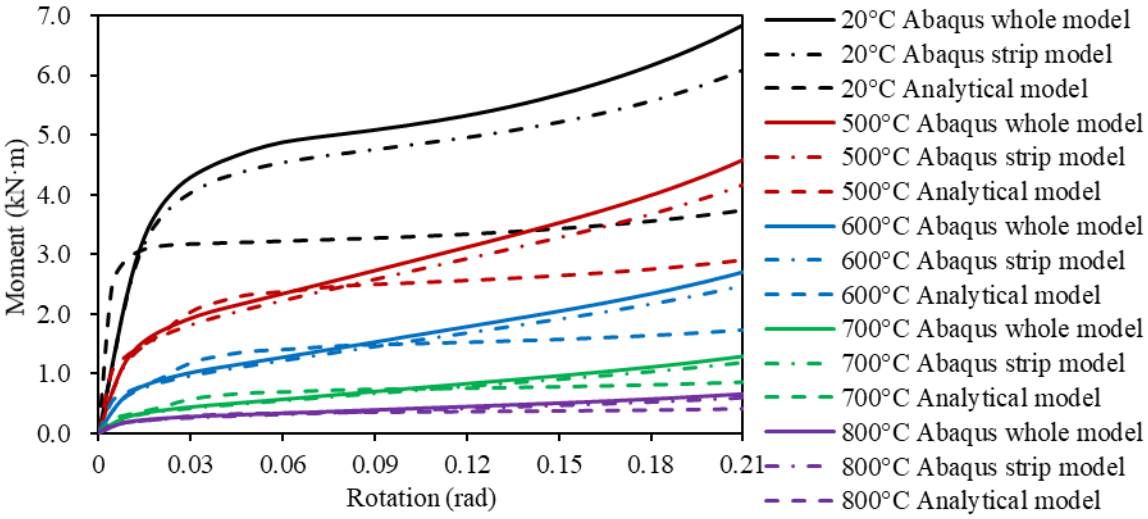

Figure 3-17. Comparison of rotational analytical model against Abaqus model at elevated temperatures

As mentioned above, with a fixed centre of rotation the force equilibrium of the rotational model is not satisfied due to the difference between the resultant forces in the tensile and compressive zones of the connection. Therefore, external axial reaction forces are required to balance the model of the connection during the rotation process at different temperatures; these axial forces, obtained by the analytical and Abaqus models are shown in Figure 3-18.

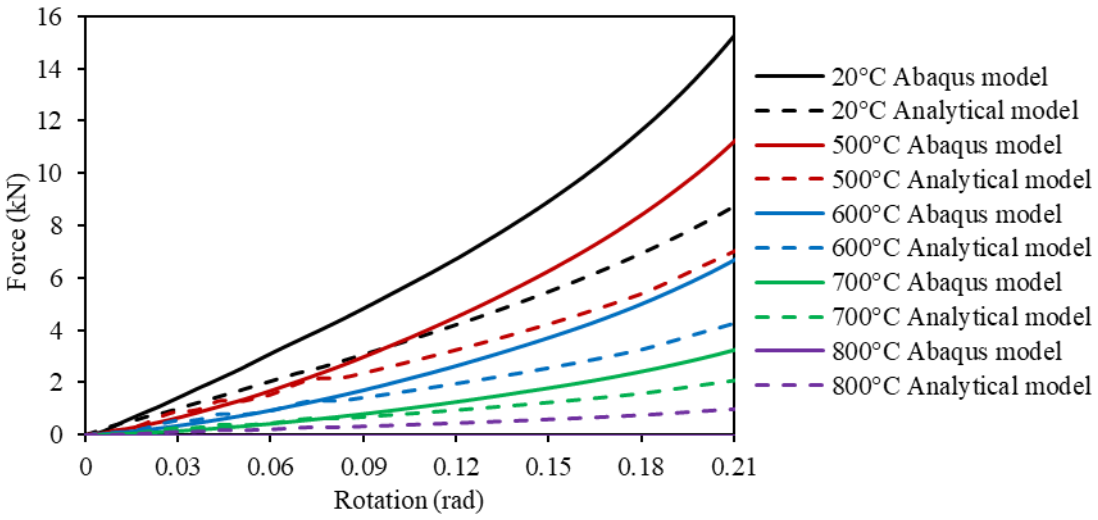

Figure 3-18. Resultant axial forces of the connection during rotation

3.4.4. Analysis of the discrepancy between analytical model and Abaqus models

Differences can be seen between the tension/compression analytical model and the Abaqus model in Figure 3-10 and Figure 3-16. In the initial elastic stage, the analytical model is stiffer than the Abaqus model, which is reasonable due to the simplifications in this phase of the analytical model. For example, the elongation of the connection's cross-section is not considered in the analytical model. Therefore, the deformation of the Abaqus model under any load level is slightly greater than that of the analytical model. In the plastic stage, the Abaqus model becomes the stronger of the two because of the positions of the plastic hinges. In the analytical model, it is assumed that a plastic hinge is generated at a discrete point. However, it can be seen from Figure 3-19 and Figure 3-20 that the end plastic hinge of the Abaqus model is not located at a precise point but has a finite length, which gradually increases and then stabilizes at a certain value as the deformation of the connection proceeds. As described above in the derivation of the analytical model, the position of the plastic hinge is related to the variable α. The change of length of the end plastic hinge in the Abaqus model could be explained as being equivalent to an analytical model with a different initial angle α. Larger plastic hinge lengths cause greater values of the variable angle α.

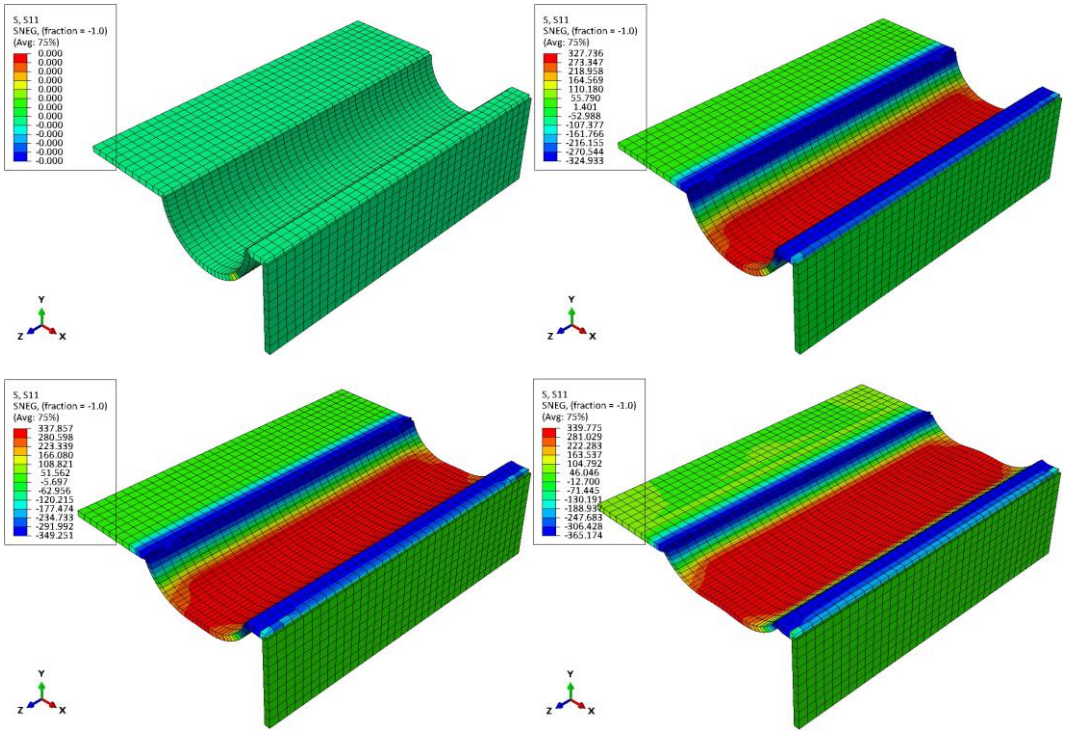

Figure 3-19. Stress distribution of Abaqus tension model

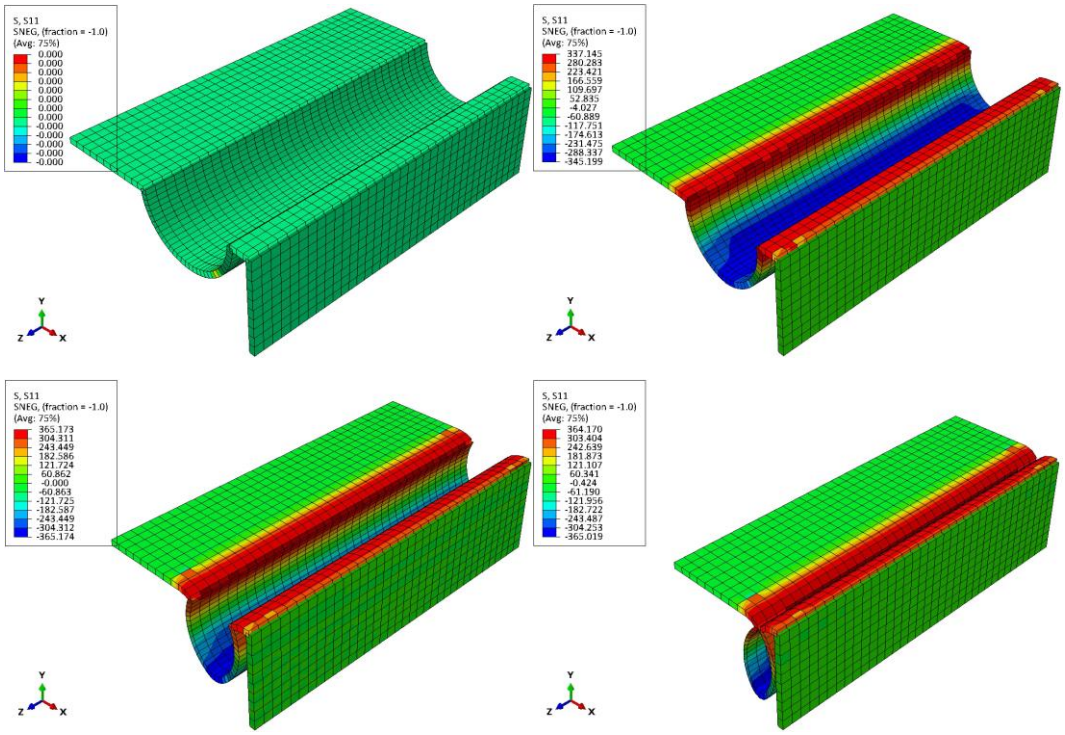

Figure 3-20. Stress distribution of Abaqus compression model

In the tension case, the displacement of the Abaqus model in the plastic stage is slightly lower than that of the analytical model at a certain force value, because the part of the deformed shape

that is straight and parallel to the force direction in the analytical model (between Hinges 3 and 4 in Figure 3-6) has some reverse curvature, as shown in Figure 3-21.

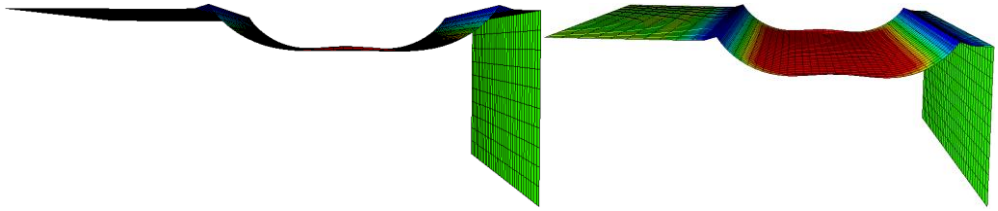

Figure 3-21. Reverse curvature between the two intermediate plastic hinges in tension

The discrepancy between the rotational mechanical and Abaqus models is significant, as has been shown in Figure 3-15 and Figure 3-17. The main reason for this discrepancy seems to be that compatibility of the torsional rotations of the parts of the semi-circular connection strips which are more aligned perpendicular to the fin-plate has been ignored in the mechanical model. As shown in Figure 3-22 (a), the rotational behaviour of the entire connection consists of two actions, namely tension/compression and torsion/bending of each connection strip. The variation of in-plane moment at the end of every strip is shown in Figure 3-22 (b), and the sum of these moments is shown in Figure 3-23 (the blue curve).

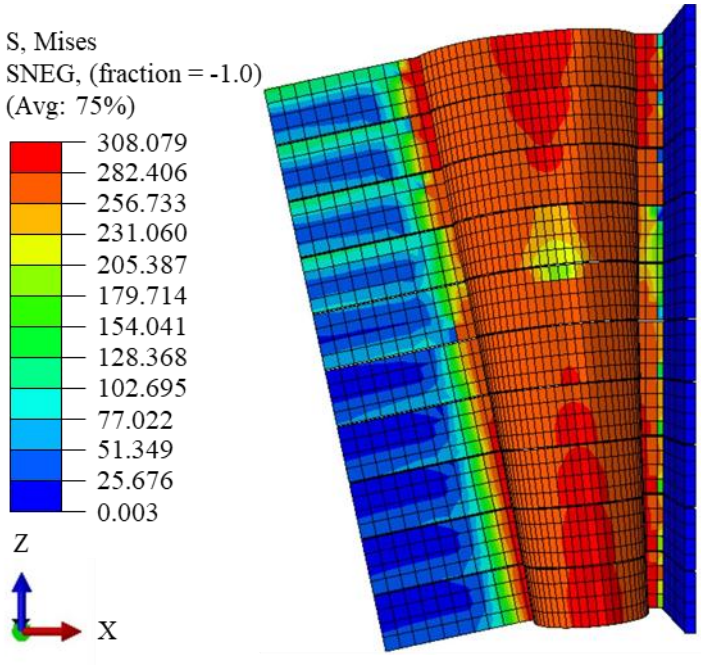

(a) Deformed shape of Abaqus strip model

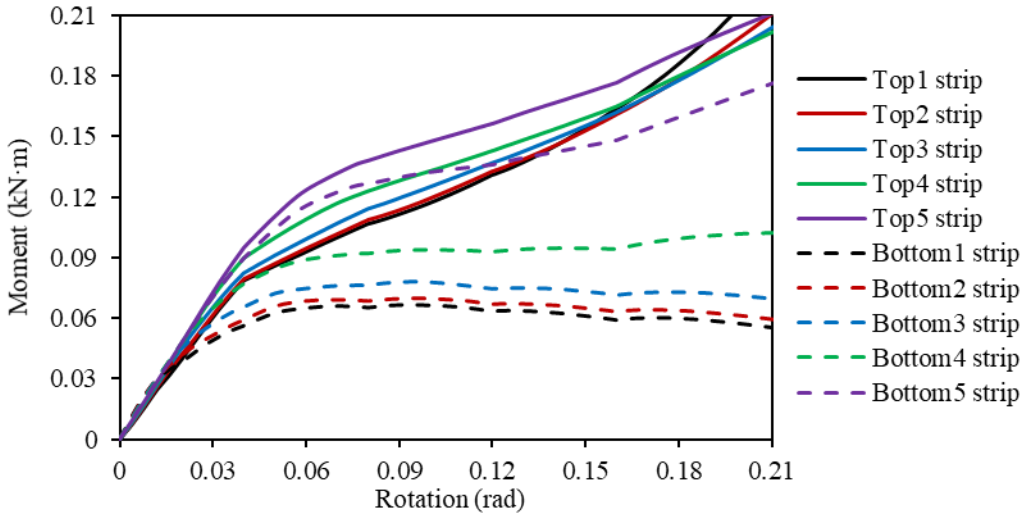

(b) End moments of connection strips

Figure 3-22. Bending of connection strips

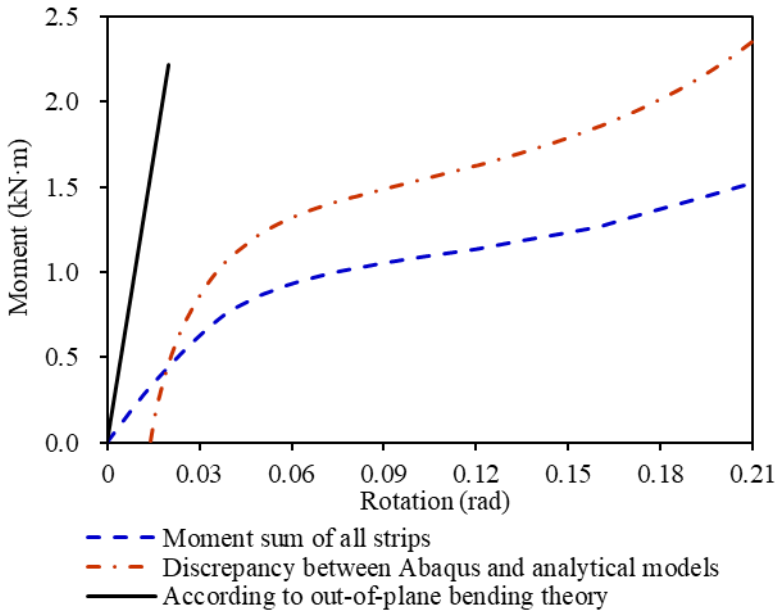

Figure 3-23. Analysis of discrepancy between rotation analytical model and Abaqus model

The red curve shown in Figure 3-23 is obtained by subtracting the analytical model curve in Figure 3-15 from the Abaqus curve. Its initial value is negative, due to the fact that the analytical model is stiffer than the Abaqus model in the initial elastic stage. It can be seen from Figure 3-23 that the sum of the strips' end moments is very close to the difference between the analytical and Abaqus model, which indicates that bending/torsion of strips is the main cause of the difference. In order to illustrate this difference more clearly, the sum of the strips' end moments, shown in Figure 3-23, is added to the original analytical model's curve from Figure 3-15 to form a modified

analytical model curve, shown in Figure 3-24. As can be seen from this figure, the modified curve is very close to the Abaqus strip model curve.

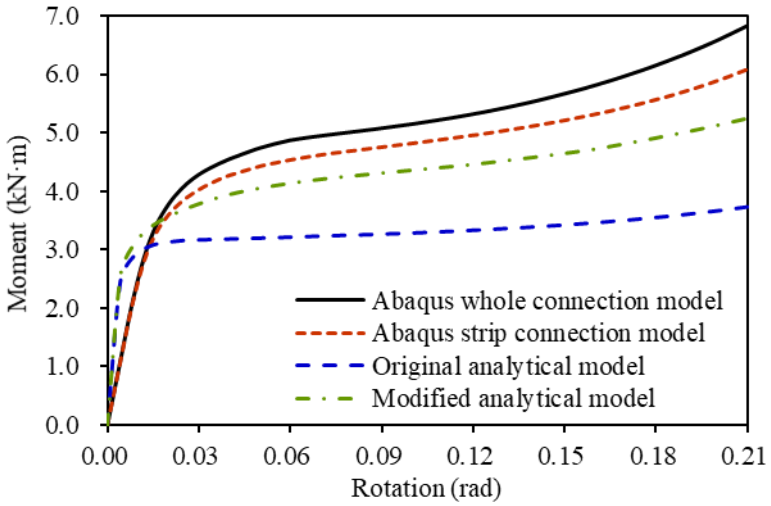

Figure 3-24. Modified rotational analytical model curve

The in-plane bending behaviour of a circular ring has been well studied in the past (Gittleman, 1946, Prescott, 1924). As for out-of-plane bending behaviour, Krahula (1965) proposed a calculation method; the relationship between moment and rotation angle is described as:

$$r\varphi = -A\sin\phi - B\cos\phi + C\alpha\cosh\sqrt{\alpha}\phi + E\alpha\sinh\sqrt{\alpha}\phi + H\sin\phi + \frac{4\kappa H}{M}\cos\phi - H\left[\frac{(\alpha+\beta+1)}{2(\alpha+1)}(\phi\cos\phi + 2\sin\phi) + \frac{2\kappa}{M}\frac{(\alpha+\beta+1)}{(\alpha+1)}(-\phi\sin\phi + 2\cos\phi)\right] \quad (3\text{-}31)$$

Where r is the radius of the ring, φ is the out-of-plane rotation angle, M is the out-of-plane moment, ϕ is the angular coordinate of the cross-section of the ring. The calculation equations for constant α, β and H are documented by Krahula, and are not described here. A, B, C, E, F and κ are six constants determined by the boundary conditions of the circular ring. However, the relationship between angle and moment given by (3-31) is linear-elastic. The black line in Figure 3-23 is calculated by this method, and the slope of this line is very close to the slope of the red line in the elastic stage. However, it is very difficult to study the bending and torsion behaviour of a connection strip by a theoretical method. Each connection strip is pushed or pulled at the same time as it is bent and twisted. This means that the cylindrical section will no longer remain circular in shape, and circular ring bending theory is no longer appropriate. The boundary conditions of the cylindrical section are hard to describe. There is a small curved section between the cylindrical section and the end-plate, so that the boundary conditions of the cylindrical section

at this end cannot be simply treated as fixed-ended or simply-supported. In the context of the moment necessary to apply a significant rotation to the beam-end, the moment generated by applying the same rotation to the connection is small, and so an exact model of aspects such as bending and twisting of connection strips is not very important to this study.

3.5. Validation of the analytical model against experiments

Experiments on this ductile connection have been carried out at model scale by Briggs (2016) and Kalawadwala (2018). In this section the experiments conducted by Kalawadwala are used to test the tension/compression analytical model at ambient temperature, and experiments by Briggs are used to validate the compression analytical model at elevated temperatures.

3.5.1. Validation at ambient temperature

S275 steel was used by Kalawadwala (2018) to produce the test specimens. The dimensions of the specimens are shown in Figure 3-25 (a); the test setup of the ambient temperature tests, shown in Figure 3-25 (b), used a 10kN Shimadzu universal testing machine to apply compressive axial force to the specimen. The force was measured by a load cell. The deformation of the connection specimens during tension and compression tests is shown in Figure 3-26, and the comparison between the analytical model and experiments is shown in Figure 3-27.

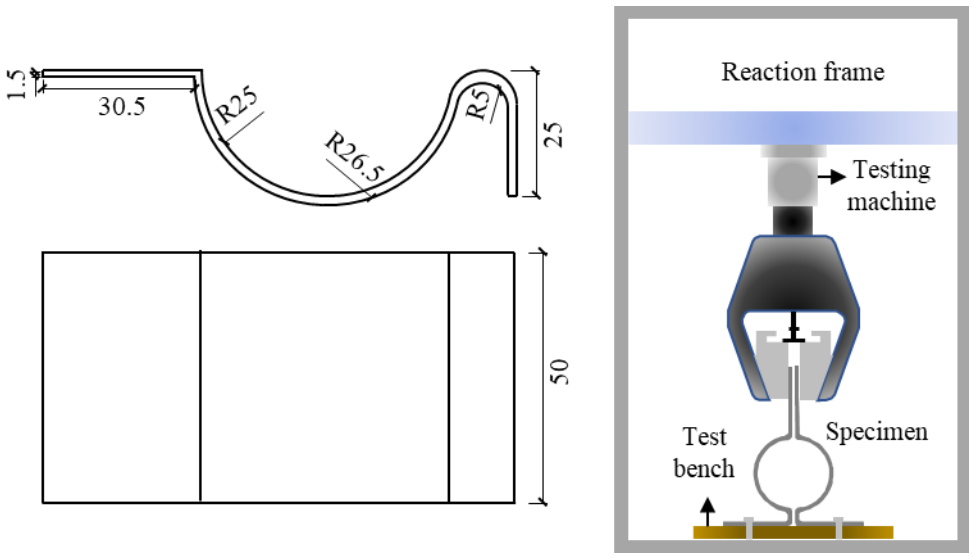

(a) Dimensions of the ambient-temperature test specimens (b) Test setup

Figure 3-25. Ambient-temperature test setup and specimen dimensions

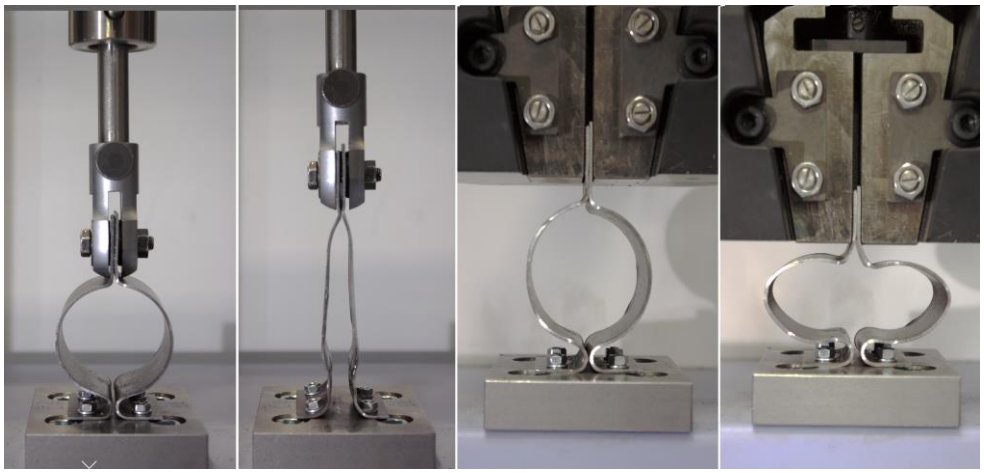

(a) Tension test (b) Compression test

Figure 3-26. Deformation of connection during tests

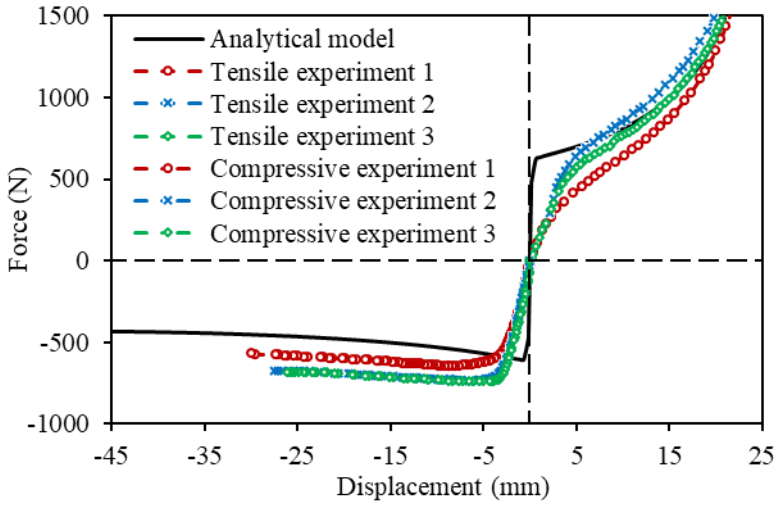

Figure 3-27. Comparison of analytical model against experiment at ambient temperature

As shown in Figure 3-27, the initial stiffnesses of the analytical curves are higher than that of the experimental curves. A potential reason for this is that both the cylindrical section and the low-radius curved section between the cylindrical section and the end-plate contribute to the total displacement during the whole loading process, whereas only the cylindrical section is considered in the analytical models. This simplification was made on the basis that the connection ductility at large deformation phase and the ultimate strength are perhaps more important than the initial elastic stiffness for structural fire engineering analysis, where the prevention of fracture/collapse is the key concern. A satisfactory correlation was obtained in tension between the experimental and analytical model curves. In compression, the test specimen behaved in a stronger manner,

requiring higher force to generate displacement than the analytical model. A potential reason for this is that contact could occur at high deformation between the cylindrical section and the test-bench bolt, as shown in Figure 3-26 (b). This could also enhance the compressive strength of the connection test specimen. These factors have not been considered in the analytical model. However, the general trend of the experimental and analytical curves shows good correlation in both the tension and compression quadrants.

3.5.2. Validation at elevated temperatures

The 3D printing technique was used by Briggs (2016) to produce 316L austenitic stainless-steel specimens. The material properties of 3D printed 316L stainless steel at elevated temperatures had been well studied by Wilkinson (2015). However, Wilkinson's specimens were annealed at between 1050°C and 1120°C to relieve residual stress, whereas Briggs did not follow the same procedure due to equipment limitations. Herliansyah (2015) studied the effect of annealing temperature on 316L stainless steel, and found that annealing can significantly reduce the yield and ultimate strengths, whilst increasing the ductility of the 316L steel. Briggs also conducted three simple material tensile tests, and the comparison of his test results and Wilkinson's material properties are shown in Table 3-1. Differences can be seen between annealed and non-annealed specimens in the table, and Briggs's material properties are used in the analytical model to make a more reasonable comparison with his experiments.

Table 3-1. Comparison of material properties.

Material tests	Yield Strength (MPa)	Ultimate Tensile Strength (MPa)
Test 1	548.7	639.5
Test 2	577.4	671.6
Test 3	572.2	674.3
Average	566.1	661.8
Wilkinson's material properties	325.5	565.1

Since Briggs did not specifically measure Young's modulus in his material tests, the value 299.3GPa obtained by Wilkinson is adopted as the modulus in the analytical model calculation. The dimensions of the specimen are shown in Figure 3-28 (a). The test setup at elevated temperatures is shown in Figure 3-28 (b). A high temperature oven was used to heat the specimens.

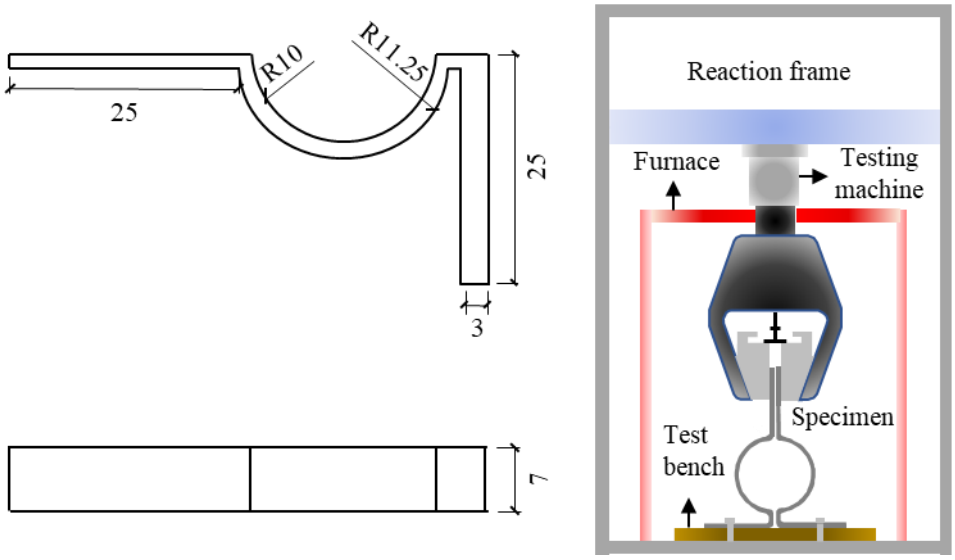

(a) Dimensions of the ambient-temperature test specimens (b) Test setup

Figure 3-28. High-temperature test setup and specimen dimensions

Four temperatures, namely 350°C, 450°C, 550°C and 650°C, were selected to carry out elevated-temperature compression tests. As shown in Figure 3-29, all temperature curves follow the same general trend, showing a slight decrease of compressive force as the compressive displacement increases. The differences between the analytical model and experiments shown in Figure 3-29 may be caused by the uncertainty in the material properties of 316L stainless steel. The large increase of compression force shown in experimental curves beyond -8mm is due to the contact which occurred between the cylindrical section and end-plate. The compression force of the connection under any given displacement should decrease with the increase of temperature. However, an exception can be found in Figure 3-29, for the connection at 450°C has higher resistance than the connection at 350°C. The reason for this may be the heating time of specimen before it was loaded. Specimens at 450°C, 550°C and 650°C were loaded immediately after they reached the required temperature, whereas the specimen at 350°C was held in the oven for a greater period before it was loaded. In general, the experiments at high temperatures show that temperature only affects material properties and does not affect the deformation mode of the connection.

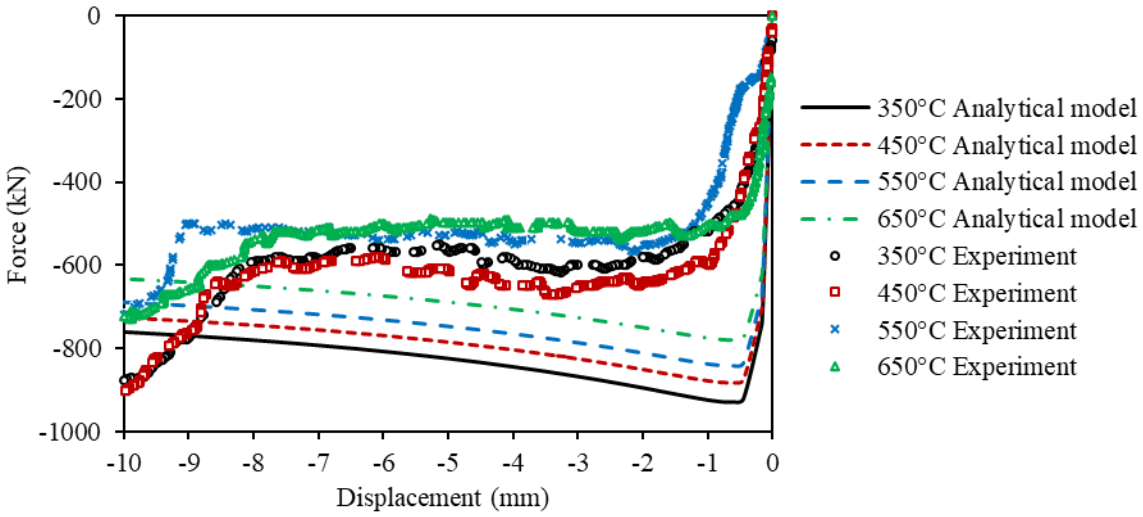

Figure 3-29. Comparison of analytical model against experiment at elevated temperatures

3.6. Case studies for the ductile connection

After the development of the novel ductile connection and its analytical models, which have been described above, preliminary studies using single beam models are now conducted in this section to investigate the structural performance and the failure modes of the new connection.

3.6.1. Simplified single beam model

An isolated 7.5m beam of UKB 533x210x109 section with an appropriately designed ductile connection at its ends is investigated here; the dimensions of the connection are the same as those shown in Figure 3-4.

Simplifications of the FEM model, as shown in Figure 3-30, are listed as follows:

- One half of the model is created to save computational cost, and an axis of symmetry is applied as a boundary at mid-span of the beam.
- The complex contact conditions between bolts and clearance holes lead to non-convergence of the simulation using a static solver, and therefore are not considered in this preliminary study. To avoid complex contacts within the connection zone, the bolts are not modelled, and the fin-plate is directly tied to the corresponding area of the beam web.
- Constraint boundary conditions are applied at the bolt positions of the end-plate,

connecting it to a fixed thick plate representing the column flange.

- Simple hard contacts are defined between the fin-plate and beam web, and between the end-plate and column flange.

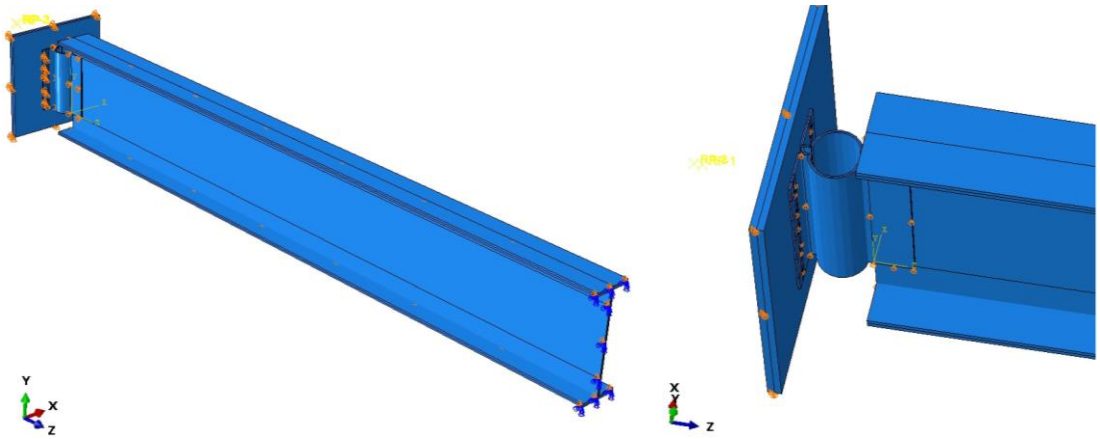

Figure 3-30. Simplified Abaqus model of beam with ductile connection

The element size in the connection model is similar to that used in the half connection model presented in section 3.4. Since the behaviour of the connected beam is not the prime concern of the simulation, its mesh size can be much coarser than that of the connection, to save computational time. External load is first applied to the beam flange at ambient temperature, generating a load ratio of 0.31 with respect to a simply supported beam and then the temperature of the model is gradually increased until the simulation fails to converge. It should be noted that 0.31 is a relatively low load ratio in practical terms. This example serves as a case study in this section. It is assumed that the temperature distribution within the beam and connection is uniform across the depth, and the standard fire curve is used in the model. Lawson (1990a, 1990b) assumed that the temperature of the connection was about 70% of that of the bottom flange at the mid-span of the beam. In order to study the effect of temperature on analytical behaviour of the connection, two cases are simulated, in which the connection temperature is set to 70% and 100% of the beam temperature respectively. The deformation of the connection during the entire simulation process is shown in Figure 3-31. It can be seen that the cylindrical section is initially squeezed due to thermal expansion of the connected beam at temperature up to about 600°C, beyond which the beam develops catenary action, and the rotation angle of the connection increases rapidly with the increase of beam deflection. Eventually, large strains are formed around the top of the cylindrical section, and the connection starts to fail. It can be concluded that the novel connection

can accommodate large deformations induced by the connected beam because the ductility of its cylindrical section allows the fin-plate to move towards and away from the end-plate.

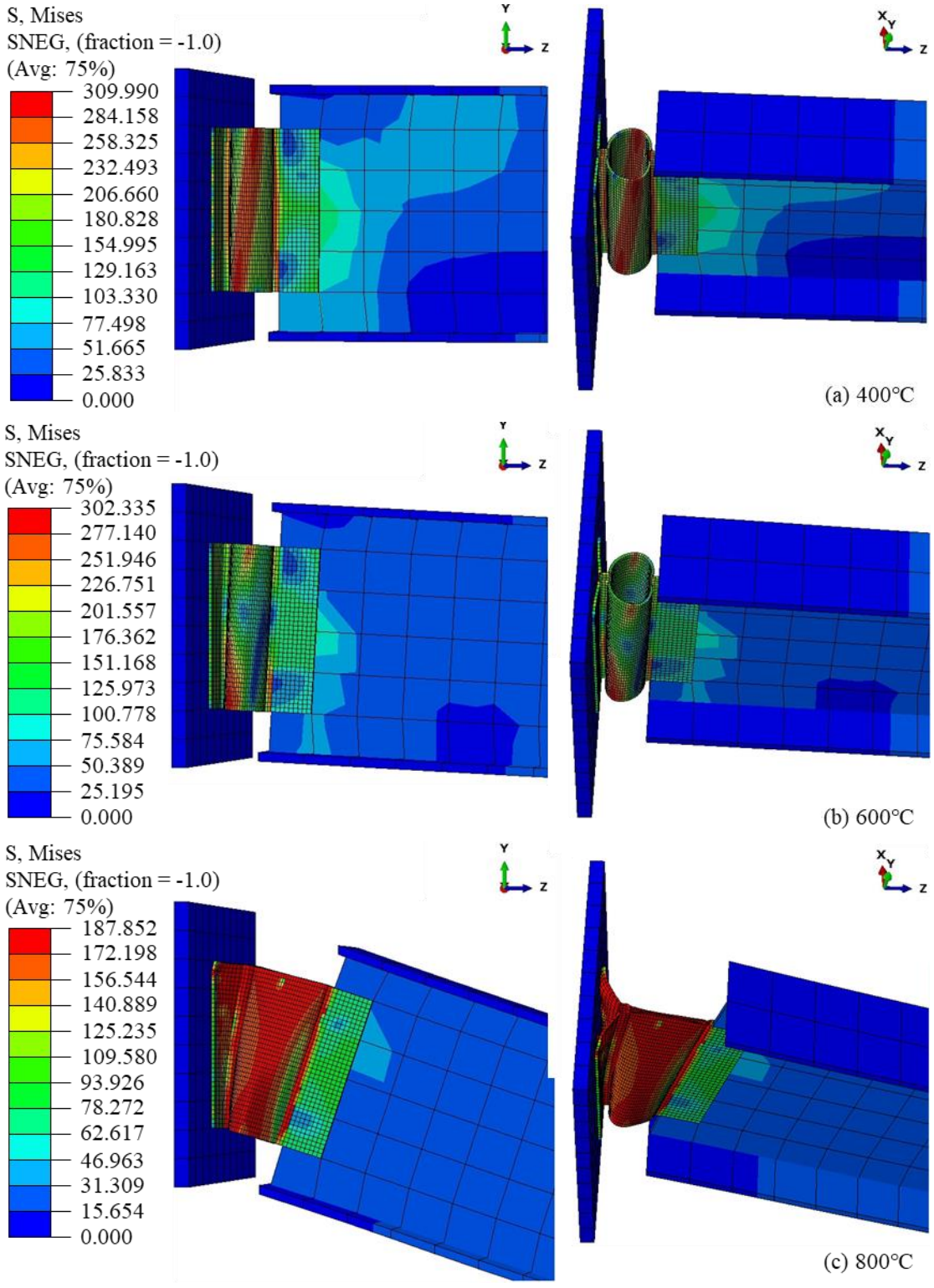

Figure 3-31. Deformation of the connection ($T_C = 70\%T_B$)

Deflections of the mid-span of beams with different boundary conditions are shown in Figure

3-32. It can be seen that curves representing the ductile connection are very close to the solid curve representing the case with simply supported boundaries. The comparison of axial forces (Figure 3-33) shows that the axial force generated in the beam with the ductile connection is significantly reduced due to the high axial ductility created. Thus, the conclusion can be tentatively drawn that the ductile connection behaves more like an idealized pinned joint and has considerable axial ductility to accommodate the deformation of the connected beam in reducing axial forces. This ductile connection will be implemented within Vulcan, and then its ability to reduce the axial force of connected beam will be verified against the Vulcan model. In the cases where the connection temperature is 70% of the beam temperature, the beam deflects less than when the connection temperature is equal to the full beam temperature.

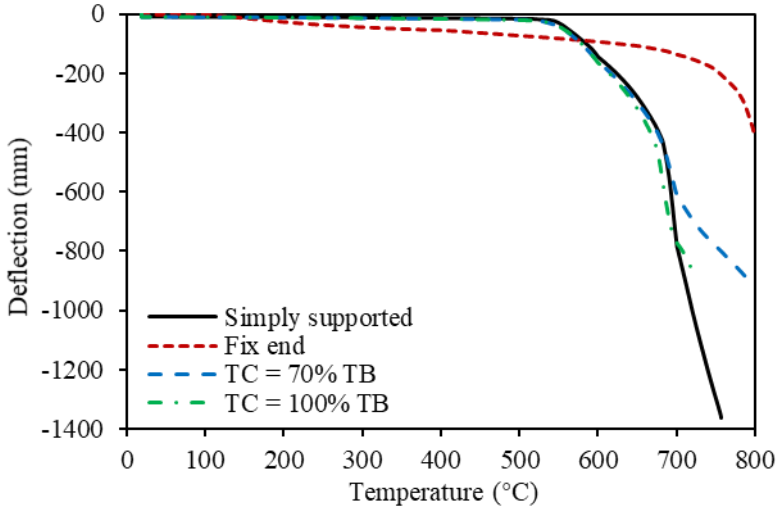

Figure 3-32. Comparison of beam mid-span deflection

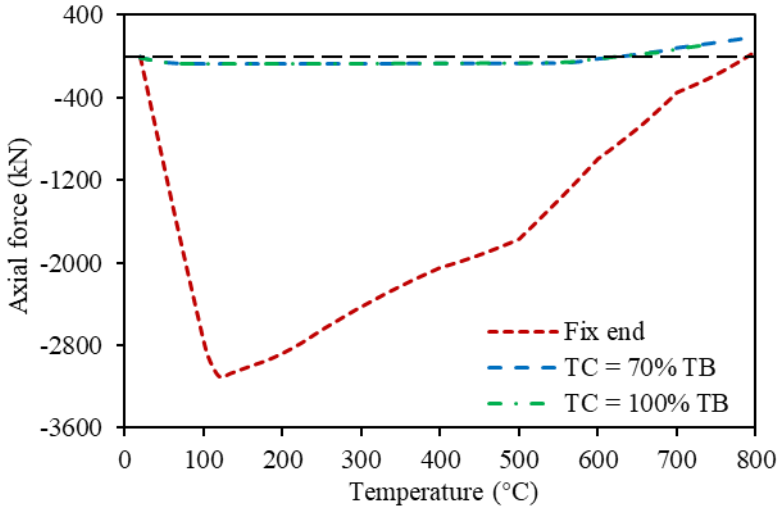

Figure 3-33. Comparison of beam axial forces

To assess the influence of the beam span on the performance of the ductile connection, four different beam spans are adopted. The corresponding beam sections are listed in Table 3-2. Except for the connection depth, the other dimensions of the connections (e.g. plate thickness and cylindrical section radius) are the same in all four cases. The comparative results are show in Figure 3-34 and Figure 3-35, which illustrate the connection rotation and the axial forces generated in the beams of different spans. It can be seen from Figure 3-34 that the ductile connection can rotate a significant angle before failure occurs, which once again demonstrates its good deformability. Figure 3-35 shows that with the increase of beam span, the beam axial force also increases. Reason leads to this may be that the radius of semi-cylindrical section, which is the most critical factor affecting the connection ductility, is insufficient in the case of the relatively long-span beam. Further studies are required to establish guidance on the optimum radius of cylindrical section. In general, the novel connection can be regarded as a ductile connection and can provide satisfactory deformation capacity.

Table 3-2. Parameters of the beams of various spans

Beam Span (m)	6	9	12	15
Beam Section	UKB 356×127×33	UKB 406×178×60	UKB 457×191×98	UKB 610×229×125
Load Ratio	0.4	0.4	0.4	0.4
Connection Depth (mm)	260	290	320	410

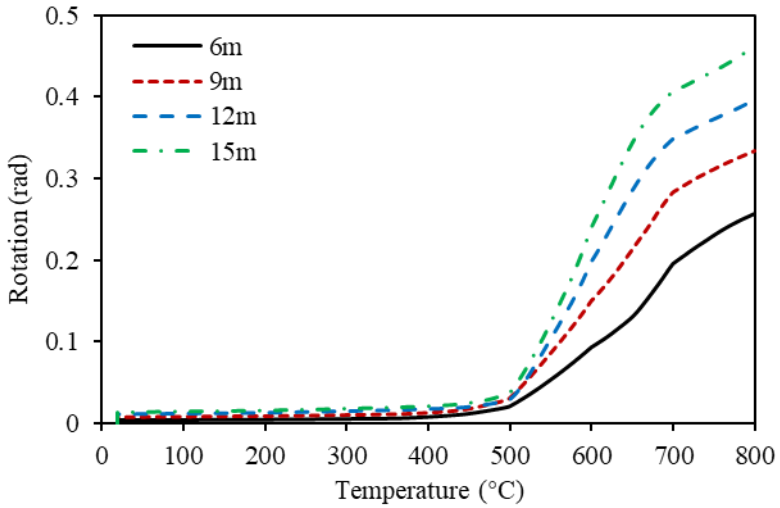

Figure 3-34. Rotation of connections for beams of different spans

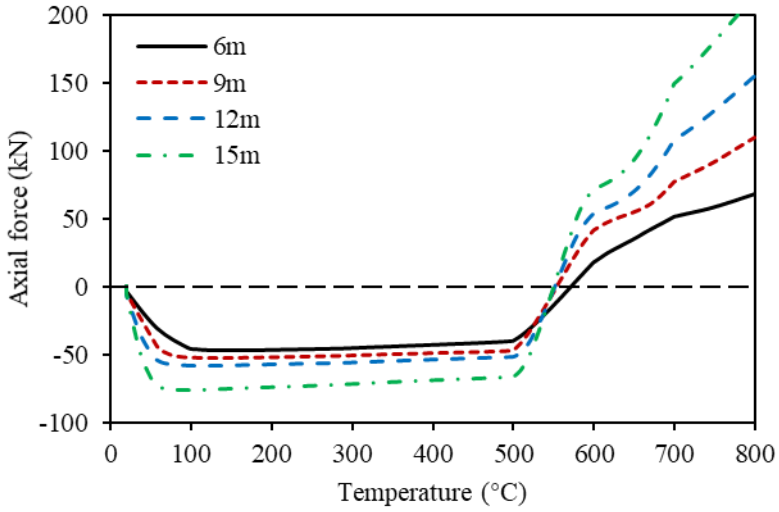

Figure 3-35. Axial force of beams of different spans

3.6.2. Detailed single beam model

As a preliminary study of failure modes of the ductile connections, bolts should be modelled and incorporated into the Abaqus connection model. Therefore, a detailed connection model is built using the 3D solid element C3D8R (Figure 3-36). A thick plate with all degrees of freedom constrained is created to represent the column flange.

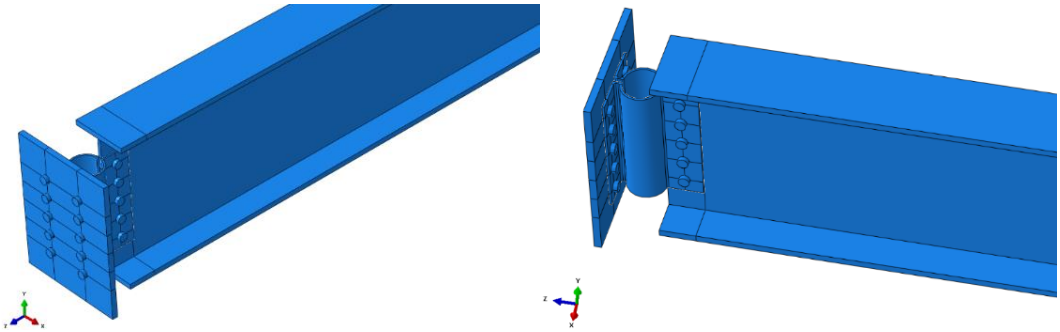

Figure 3-36. Detailed Abaqus model of beam with ductile connection

As mentioned previously, the complex contacts involved in this model may lead to numerical singularities if the Abaqus static solver is used. Therefore, the dynamic explicit solver is adopted here to analyse the model. To solve a quasi-static problem using a dynamic procedure, the loading speed is of most concern. When a dynamic system is subject to a linearly increasing load and the loading duration is longer than the natural period of the system, the response of the system can be regarded as approximately static. Since the total analysis time is proportional to the step time, it is unnecessary and inefficient to use real time as the step time in the simulation. Usually, the real

time is scaled to a very short time period, as long as the response of the model remains static. Yu (2008b) carried out a parametric study to investigate the influence of loading step time on the response of a bolted connection model using the dynamic explicit solver, and concluded that cases with loading time of 1s or 0.1s gave smooth results close to the static analysis results. The simulation of the ductile connection presented here consists of six steps: the first step is to apply external load on the beam at ambient temperature, and the remaining five steps are used to gradually raise the temperature of the model to 800°C. The loading step time is set to 1s, and the time of all heating steps is set to 0.1s. According to the Abaqus/Explicit manual (Hibbitt and Sorensen, 2004), if the kinetic energy to internal energy ratio of the model is less than 10%, the simulation can be considered as quasi-static, whereas responses greater than 10% should be regarded as dynamic and excluded from the results. To make sure that the simulation results are quasi-static, the energy relationship is shown in Figure 3-37. It can be seen from the figure that the kinetic energy is less than 10% of the internal energy, and the maximum ratio of the two reaches 1.4695, at which the connection failure occurs. Therefore, the conclusion can be drawn that the detailed simulation of the ductile connection using the dynamic solver is quasi-static.

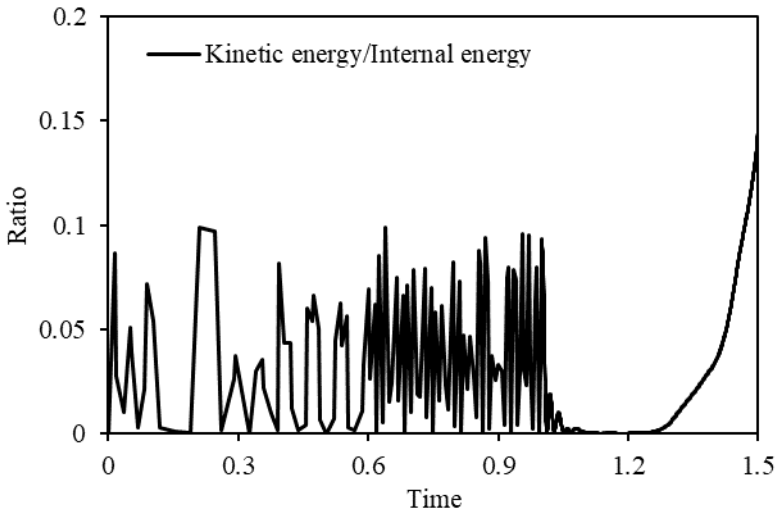

Figure 3-37. The ratio of kinetic energy to internal energy

The mesh of the surfaces where contact may occur needs to be refined in this detailed model. The failure mode of the connection is shown in Figure 3-38. As can be seen from the figure that the end-plate of the connection deforms considerably at the top and is stretched away from the top bolt row. This failure mode, which is the most common and critical failure mode of the ductile connection, is named as bolt pull-out failure, and will be studied in detail and incorporated into

the component-based model of the ductile connection in Chapter 5. The mid-span beam deflection from the detailed connection model is compared with that of the simplified connection model in Figure 3-39. It can be seen from the figure that the deflection of the detailed model is larger than that of the simplified model, which is due to the fact that the constraint provided by the bolts on the end-plate of the ductile connection in the detailed model is weaker than the tie constraint between the end-plate of the ductile connection and the thick plate in the simplified model.

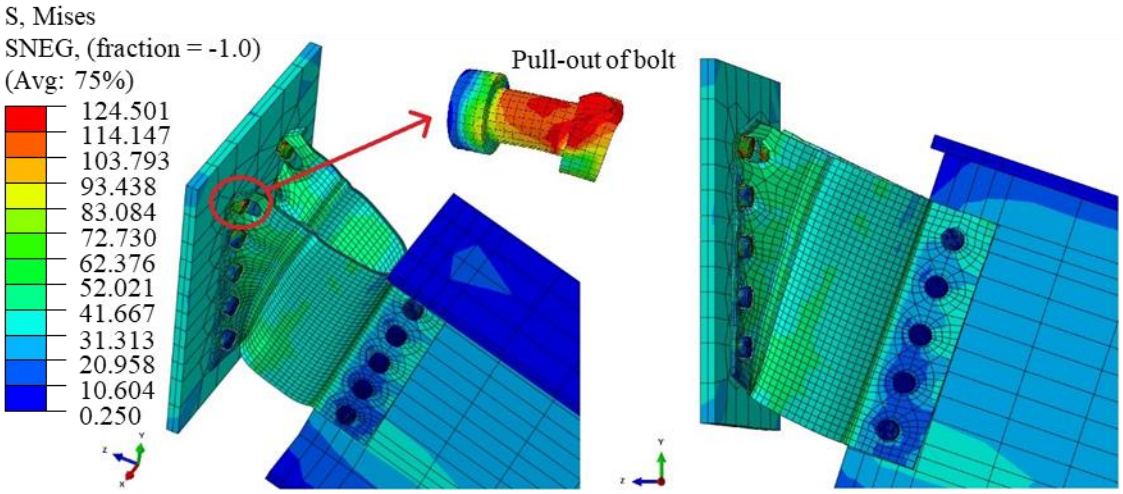

Figure 3-38. Failure mode of the ductile connection

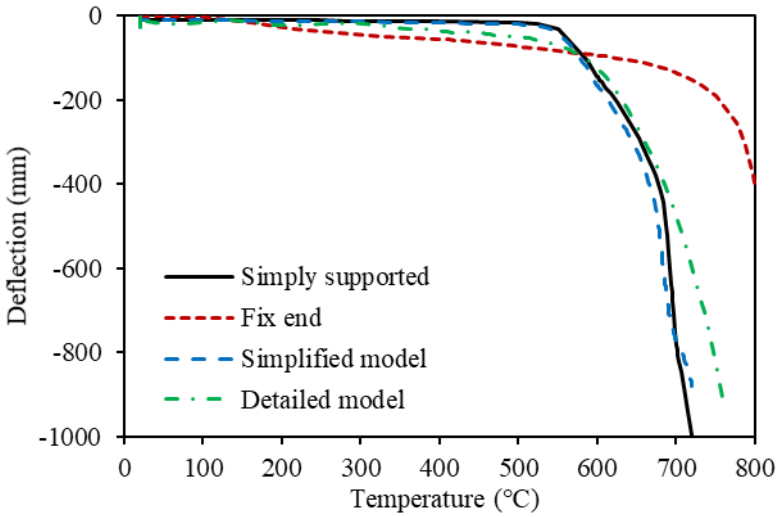

Figure 3-39. Comparison of the deflection

A preliminary parametric study has been carried out using the detailed Abaqus model to study the effects of three parameters on the structural performance of the ductile connection, including the connection thickness, the inner radius of the semi-cylindrical section and the connection height. The endpoints of all curves in Figure 3-40 are determined by the failure of the end-plate as shown

in Figure 3-38.

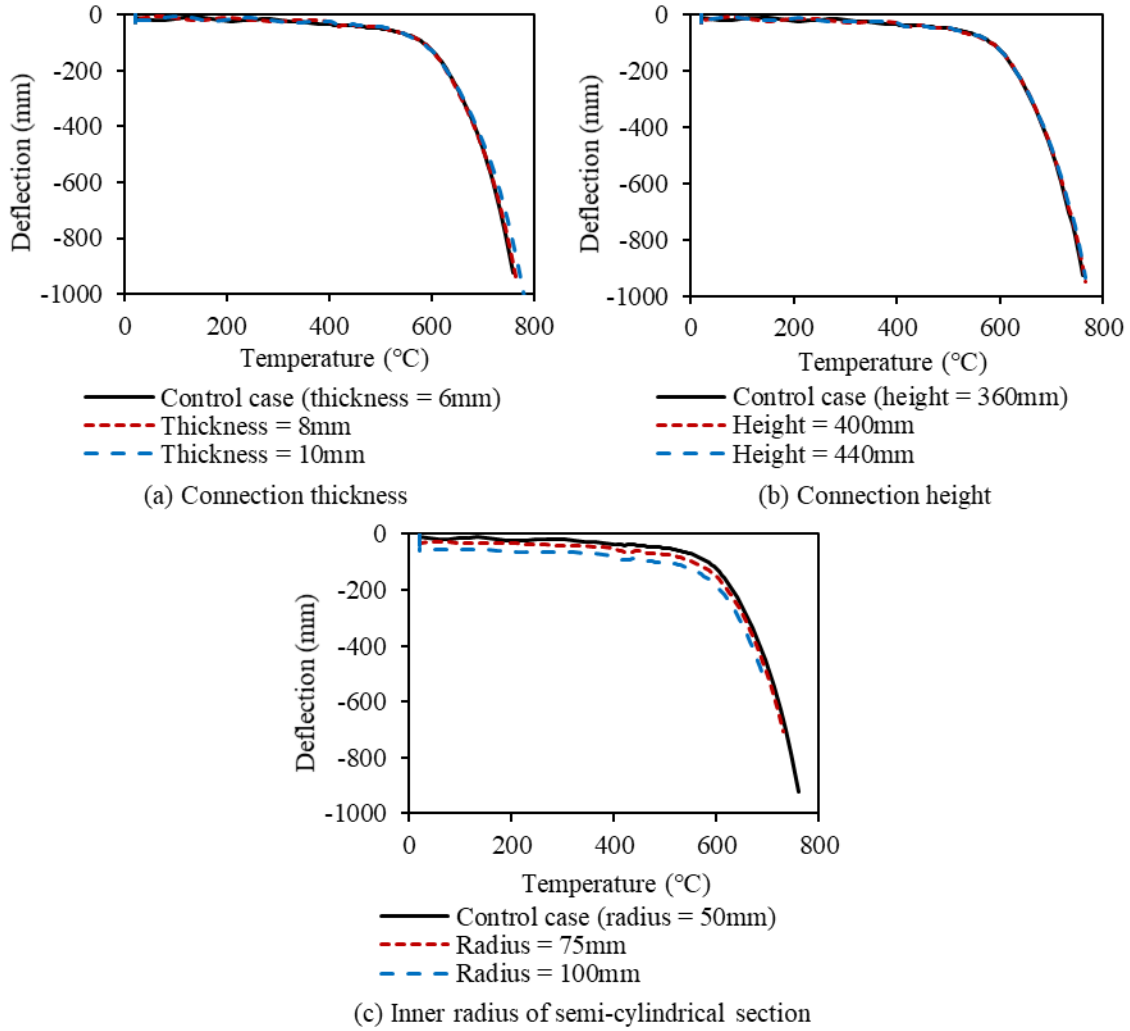

Figure 3-40. preliminary parametric studies

As shown in Figure 3-40 (a), the increase in connection thickness delays the failure of the end-plate and thus allows more deflection of the connected beam. However, excessive increase of plate thickness will reduce the ductility of the connection, which is contrary to the original design intention of the new connection. Therefore, further investigations are needed to determine the criteria for determining the most appropriate connection thickness. The connection height has little effect on its performance (Figure 3-40 (b)), so its value can be determined directly according to the end-plate or fin-plate design criterion provided by Eurocode 3. At any temperature, the larger the inner radius of the semi-cylindrical section, the greater the mid-span deflection of the connected beam., as shown in Figure 3-40 (c). This phenomenon can be explained by the Equations (3-20) - (3-23) for tension and (3-26) - (3-29) for compression derived from the

analytical model of the connection. The larger the radius, the smaller the variable α (shown in Figure 3-7 and Figure 3-9). A large inner radius and a small variable α cause the denominators in Equations (3-20) - (3-23) and (3-26) - (3-29) to increase, which means that as the inner radius of the semi-cylindrical section increases, less force is required for the connection to generate the same deformation. In the case of large inner radius, failure of the endplate will occur at a lower temperature, resulting in a decrease in the final mid-span deflection of the connected beam. However, if the inner radius of the cylindrical section is much less than the $\Delta_{low-temp}$ shown in Figure 3-2 (a), the cylindrical section may buckle at low temperature due to the thermal expansion of the connected beam. In this section, only three values have been tested for each connection dimension, and the results may not represent the effect of a particular dimension on connection performance or failure modes. Therefore, further extensive parametric studies are required to determine the optimal dimensions of the ductile connection.

3.7. Chapter conclusion

This chapter has proposed the design of a novel ductile connection consisting of two connection pieces, each of which takes the form of a fin-plate, an end-plate and a semi-cylindrical section which can provide additional ductility to reduce the probability of brittle failure. Tension/compression analytical models of the ductile connection based on plastic theory and the virtual work principle have been developed. The rotational behaviour of the entire connection is simulated by pure tension or compression of individual connection strips, using the concept of the component-based method. The tension/compression analytical models have been validated against Abaqus simulations and experiments at both ambient and elevated temperatures. Finally, case studies have been carried out using single beam models to test the performance of the ductile connection and its failure mode. The following conclusions can be drawn based on these studies:

- A good consistency can be seen between tension/compression analytical models and Abaqus models at both ambient and elevated temperatures; this indicates that the proposed analytical model is able to predict the tension and compression behaviour of the connection.
- A good correlation has been found between the analytical models and experiments at both

ambient and elevated temperatures in both tension and compression quadrants. It can be concluded from the force-displacement curves at elevated temperatures obtained by the analytical model, the Abaqus model and experiments that temperature does not affect the deformation mode of the connection.

- The discrepancy between the rotational mechanical and Abaqus models is significant. The main reason for this discrepancy is that compatibility of the torsional rotations of the parts of the semi-circular connection strips which are more aligned perpendicular to the fin-plate is ignored in the mechanical model. However, the moment needed to apply a significant rotation to the connection is much lower than the moment required to apply the same rotation to the beam-end. Therefore, an exact model of torsional rotation of connection strips is not very important to this study.
- Through the deformation process of the ductile connection in the simplified Abaqus single beam model, it can be seen that the semi-cylindrical section provides additional ductility to accommodate large axial deformation caused by the horizontal movement of the connected beam. From the comparison of beam mid-span deflections under different boundary conditions, it can be concluded that the ductile connection behaves like an idealized pinned joint.
- From the detailed Abaqus single beam model, the most common and critical failure mode of the ductile connection can be observed. The end-plate of the connection deforms considerably at the top and is stretched away from the top bolt row. This failure mode is named as bolt pull-out failure and will be included into the component-based model of the ductile connection in Chapter 5.

4.

COMPONENT-BASED MODELLING OF THE DUCTILE CONNECTION

4.1. Chapter introduction

The internal forces experienced by connections change, from a combination of shear and axial compressive force due to restraint of the thermal expansion of beams in the initial stage of a fire, to tensile force caused by the eventual catenary action of beams at very high temperatures. Therefore, it is difficult to reproduce such complex loading conditions in experiments, other than in full-scale tests. Compared with experiments, numerical modelling is a more feasible and inexpensive method to investigate the behaviour of connections under the combined action of material degradation and complex internal forces. The finite element method is a reliable technique which enables prediction of the behaviour of connections in a very detailed manner. However, such detailed finite element approaches are not suitable in practical fire engineering design, because of the time-consuming nature of model building and computational costs, particularly where global frame analysis needs to be carried out. An alternative way of conducting large-scale frame analysis in fire is to use the component-based method to simulate connection behaviour in structural frame analysis software. In the case of structural frame, or sub-frame, analysis for fire conditions, it seems the only practically feasible way of taking account of connection behaviour within a 3-dimensional frame analysis.

This chapter presents an improved version of the ductile connection and compares its performance with that of the previous version using a sub-frame model. Five case studies are carried out, in which the ductile connections are applied to sub-frames with different beam spans. The analytical models of the "face-plate" component of the ductile connection, and the face-plate/semi-cylindrical component (FPSC component), in which the semi-cylindrical component and the face-plate component are considered to deform as a whole, based on simple plastic theory are developed. Based on these, two component-based models for the ductile connection have been proposed. The loading and unloading behaviour have been incorporated into individual component behaviour, and the results of the two component-based models are compared and validated against both Abaqus simulations and experiments. Finally, the proposed component-based model is applied to two simple examples, to illustrate how different spring rows contribute to the process of connection deformation.

4.2. Optimized design of the ductile connection

As mentioned in Chapter 3, the basic element of the ductile connection can be manufactured simply by bending a steel plate. In order to facilitate this cold formation, the design proposed in the previous chapter has been modified as shown in Figure 4-1. The sharp intersection between the semi-cylindrical part and the end-plate has been replaced by a curve of higher radius in order to reduce the plastic residual strains induced by bending.

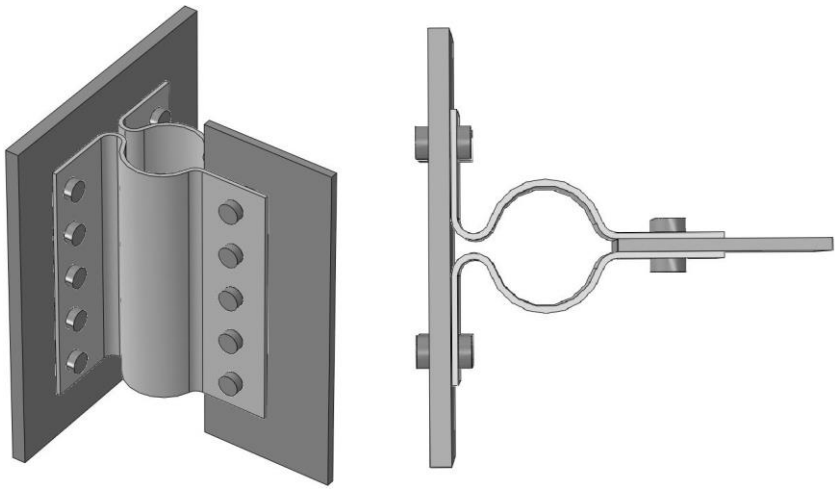

Figure 4-1. Optimized design of the ductile connection

To check whether this change of specification causes unforeseen changes in behaviour, a simple two-storey three-bay plane steel frame, shown in Figure 4-2, has been modelled using Abaqus. The dimensions of the original and modified connections are shown in Figure 4-3. Fire is assumed to occur only on the ground floor of the central bay and the standard fire curve is adopted. The two adjacent cold bays on both sides can, therefore, be simplified as elastic horizontal springs with known axial stiffness, which can be calculated using Equation (4-1). Only half of the central bay is created in the Abaqus model to save computational cost. A uniform line transverse load is applied to the beam's top flange, generating a load ratio of 0.5, which is slightly larger than typical values for the Fire Limit State, with respect to simply supported beams.

$$K = \frac{1}{2 / K_{connection} + 1 / K_{column}} \tag{4-1}$$

in which K_{column} and $K_{connection}$ respectively represent the lateral sway stiffness of a perimeter column and the axial push-pull stiffness of the connections in the outer bays.

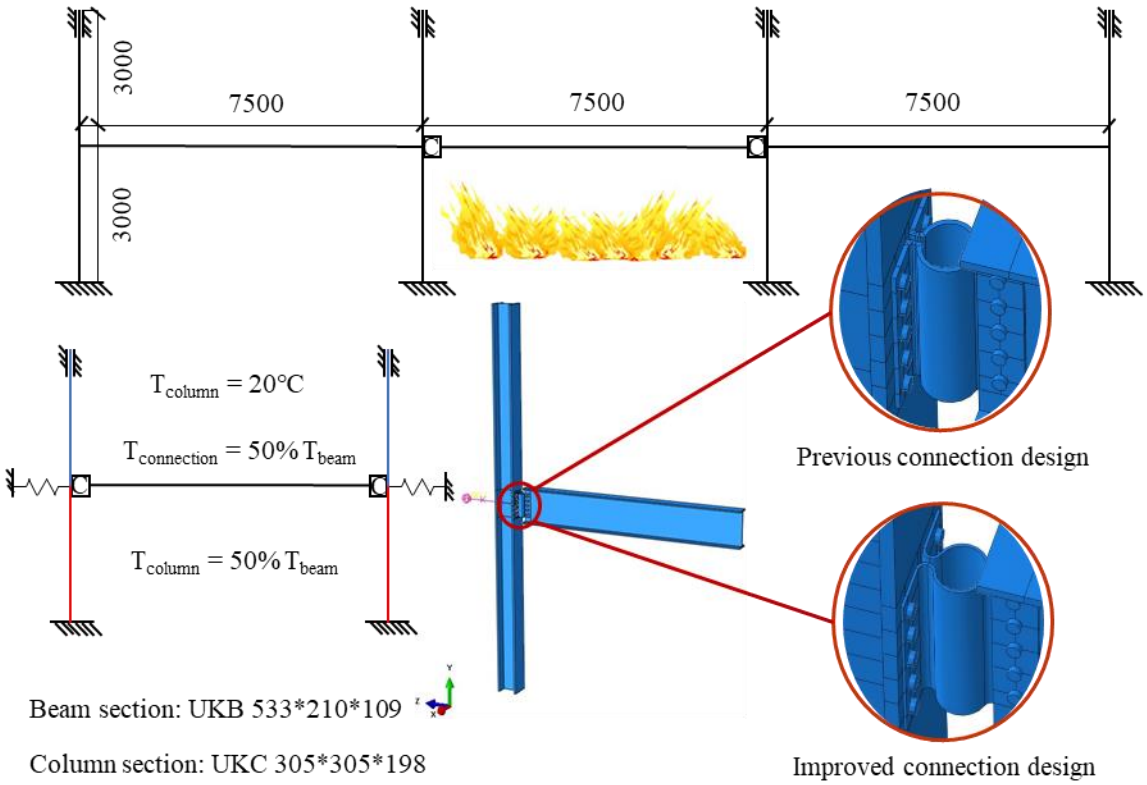

Figure 4-2. Sub-frame model (all dimensions in mm)

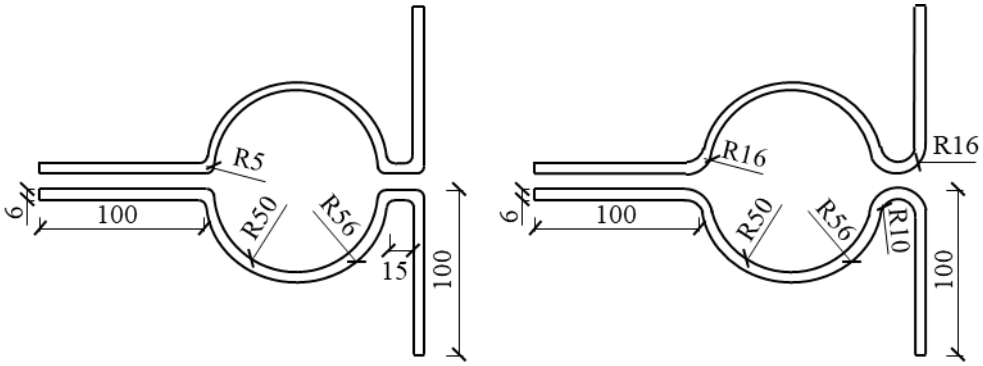

(a) Previous version (b) Improved version

Figure 4-3. Dimensions of the two versions of connection (all dimensions in mm)

Comparing results from the frame with the previous connection design and the same frame with the improved connection design are shown in Figure 4-4 and Figure 4-5. It is assumed that the temperature distribution within the beam is uniform, and the abscissa in Figure 4-4 and Figure 4-5 is the beam temperature. It can be seen from Figure 4-4 that the solid curve representing the mid-span deflection of the beam with the improved design of connections is very close to that of the beam with previous version of connections, represented by the dashed line. The comparison of axial forces (shown in Figure 4-5) shows that the axial force generated in the beam with the

improved version of connections is much smaller than that of the beam with the old version of connections. This indicates the significantly enhanced deformability and ductility of the new design, as expected during the redesigning of the connection. The failure of the two versions of the ductile connection is still controlled by the bolt pull-out failure (Figure 3-38). It can be seen from Figure 4-5 that, when the beam is under catenary action, the tensile axial force of the connection decreases rapidly after reaching the maximum value, indicating that the top row of bolts has been pulled out from the face-plate part of the connection. After that, the excessive deformation around the first row of bolt holes of the face-plate part of the connection leads to the non-convergence of the simulation.

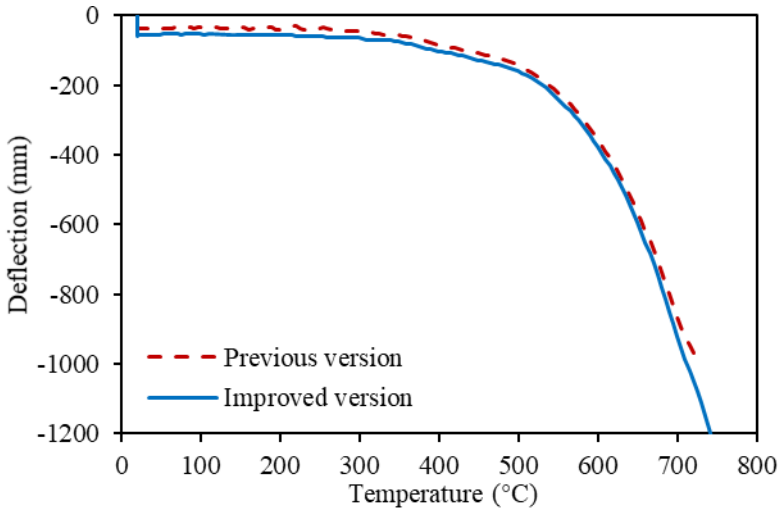

Figure 4-4. Mid-span deflection of beam

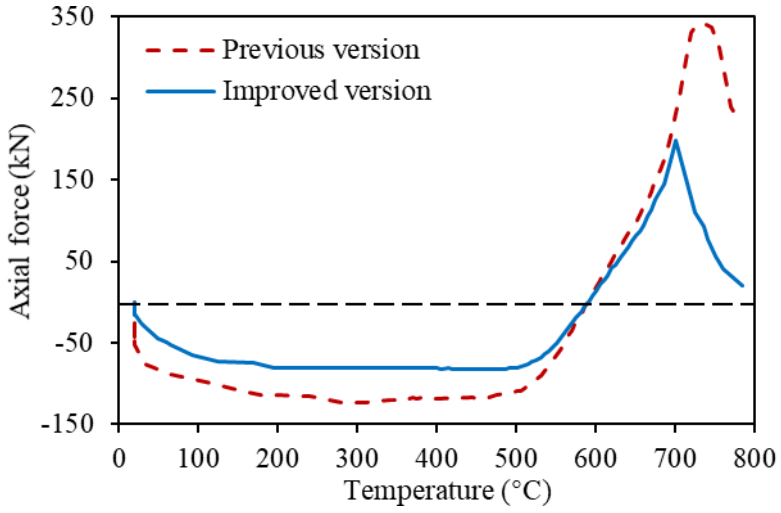

Figure 4-5. Mid-span axial force of beam

4.3. Application of the optimized ductile connection

In this section, the sub-frame shown in Figure 4-2 is used to conduct case studies, as a preliminary demonstration of the optimized ductile connection in building frames. Various beam spans (from 6m to 12m) are considered. A uniformly distributed line load of 42.64 kN/m is applied on the beam and the load ratio of 0.4 is adopted in all cases. The selected beam sizes based on span and load ratio are shown in Table 4-1. A UKC 305 ×305×198 is selected for the columns for all cases. As mentioned previously, the semi-cylindrical section of the connection is critical in providing the required ductility. The radius of this section should not be too small, otherwise, the ductility will be reduced, and the axial force generated in the adjacent structural members will be increased. Therefore, the radius of the semi-cylindrical section should be determined according to the ductility demand of the connected beam during a fire event (as shown in Figure 3-2), which can be calculated using Equations (3-1) - (3-3) proposed in the previous chapter. The diameter of semi-cylindrical section should be larger than the maximum value of $\Delta_{low-temp}$, $\Delta_{high-temp}$ and $\Delta_{high-temp,\max}$. The fin-plate and the end-plate of the ductile connection can be designed based on Eurocode (CEN, 2005a). The dimensions of the ductile connections for all cases are shown in Table 4-2. The connections must be adequate for ambient-temperature Ultimate Limit State conditions. Therefore, the capacities of the connections have all been checked according to the Eurocode (CEN, 2005a), which include shear capacity of the semi-cylindrical section, bolt shear capacity, bolt bearing capacity, shear and bearing capacity of the fin-plate, shear and bearing capacity of the bolt group and shear capacity of the end-plate.

Table 4-1. Beam sizes and ductility demands

Span (mm)	Beam section	Load ratio	$\Delta_{low-temp}$ (mm)	$\Delta_{high-temp}$ (mm)	$\Delta_{high-temp,\max}$ (mm)
6000	UKB 457×152×82	0.40	23.74	7.85	72.90
7500	UKB 533×210×109	0.40	29.61	11.86	76.54
9000	UKB 533×312×151	0.39	35.28	20.00	57.39
10500	UKB 610×305×179	0.40	41.22	24.17	62.78
12000	UKB 610×305×238	0.39	46.88	37.08	39.70

Table 4-2. Connection sizes

Span (mm)	Inner radius of semi-cylindrical section (mm)	Plate thickness (mm)	Fin-plate width × depth (mm)	End-plate Width × depth (mm)	Number of bolt rows
6000	50	6	100×360	100×360	5
7500	50	6	100×360	100×360	5
9000	50	6	100×360	100×360	5
10500	50	6	120×430	100×430	6
12000	50	6	120×430	100×430	6

Mid-span deflections and the axial forces of the beams are shown in Figure 4-6 (a) and (b). In order to compare the performance of the ductile connections with that of the commonly-used end-plate connections, the five sub-frames, whose ductile connections are replaced by end-plate connections, are also simulated using Abaqus. In extreme cases, if the beam is fully restrained in axial direction without buckling, then the axial forces generated in the beams during the initial stage of heating can be simply calculated by the Hooke's law (Equation (4-2)). The comparison results of the axial forces generated in the beams under different axial restraint conditions, the ductile connection, the end-plate connection, and the axial fully restraint without buckling, at the temperature of 400℃ are shown in Table 4-3. It is obvious that the axial compressive forces generated in the beams are significantly reduced by adopting the ductile connections.

$$F_N = E \cdot A \cdot \alpha \cdot T \tag{4-2}$$

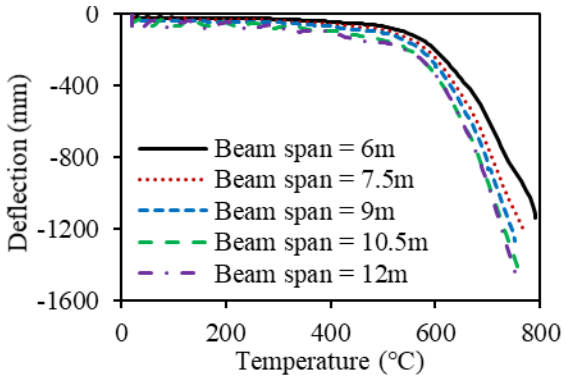

(a) Mid-span deflection of beam

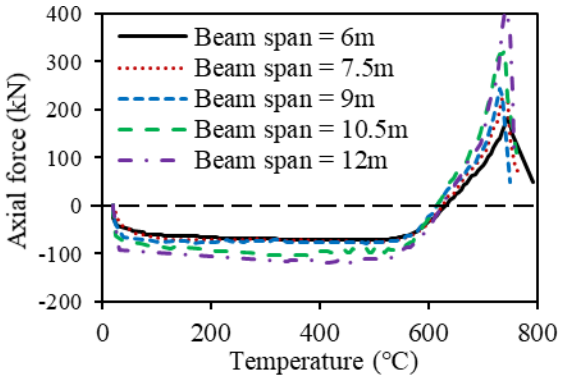

(b) Mid-span axial force of beam

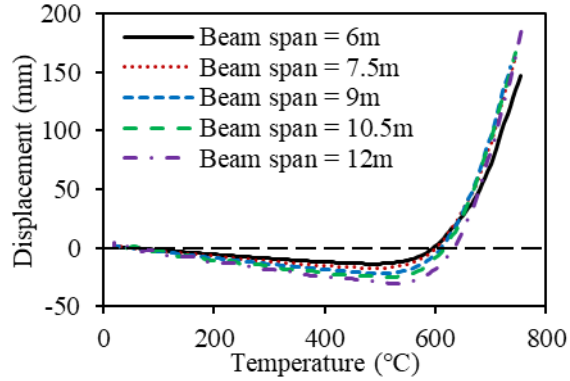

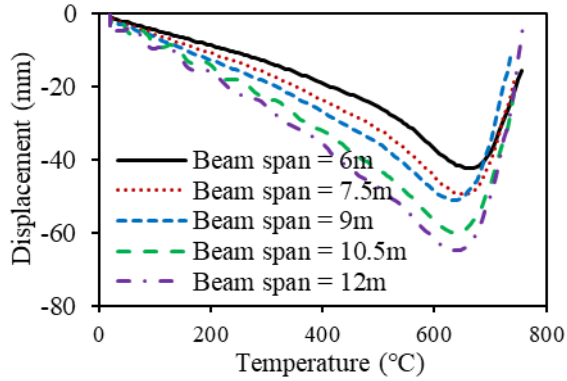

(c) Horizontal displacement of top flange at beam end

(d) Horizontal displacement of bottom flange at beam end

Figure 4-6. Results of case studies

The horizontal displacements of the node on the top flange and the node on the bottom flange at the beam end are shown in Figure 4-6 (c) and (d). These two figures clearly show the deformation capacity of the ductile connection, which can allow the connected beam to fully develop its catenary action at high temperatures. As can be seen from the case studies presented here, the ductile connections are quite suitable for bare-steel frames with different beam spans. It should be noted that the radius of the semi-cylindrical section of the ductile connection is the most important parameter, being based on the demand for push-pull ductility. This should be determined according to the span of beam, its size, applied load and required fire resistance temperature, using Equations (3-1) - (3-3). The ductile connection should also be applicable to composite structures, but the behaviour of connections within a composite floor is quite different from that in a non-composite steel frame, due to the influence of the concrete slab in resisting thermal expansion of the beam. Performance of the ductile connections within composite structures will be studied in Chapters 6 and 7.

Table 4-3. Comparison of the compressive axial forces of the beams at 400°C

Beam span (m)	Axial force (ductile connections)	Axial force (end-plate connections)	Axial force (axial fully restraint)
6	-71.41 kN	-824.42 kN	-3285.01 kN
7.5	-75.52 kN	-985.28 kN	-4348.72 kN
9	-77.18 kN	-1139.47 kN	-6006.87 kN
10.5	-89.52 kN	-1152.98 kN	-7133.16 kN
12	-112.24 kN	-1328.10 kN	-9479.59 kN

4.4. Initial component-based model

The new connection design consists of a fin-plate, a semi-cylindrical section and a face-plate. The active components of the component-based connection model are shown in Figure 4-7. Each spring row of the component-based model consists of five components working in series. Among them, the fin-plate in bearing, beam-web in bearing and bolt in shear constitute the fin-plate component; characterisation of these components has been done previously (Sarraj, 2007). The gap between the compression spring row and the rigid bar is designed to represent the maximum compressive displacement before contact occurs. The two end nodes of the connection element

are located at the intersection points between the reference axes of the beam and column. The vertical shear behaviour, representing the slip between the beam end and the column flange, has not been taken into consideration, although this will be an issue to be investigated since it is relevant to ambient-temperature design. Therefore, the component-based model is assumed to be rigid in the vertical direction.

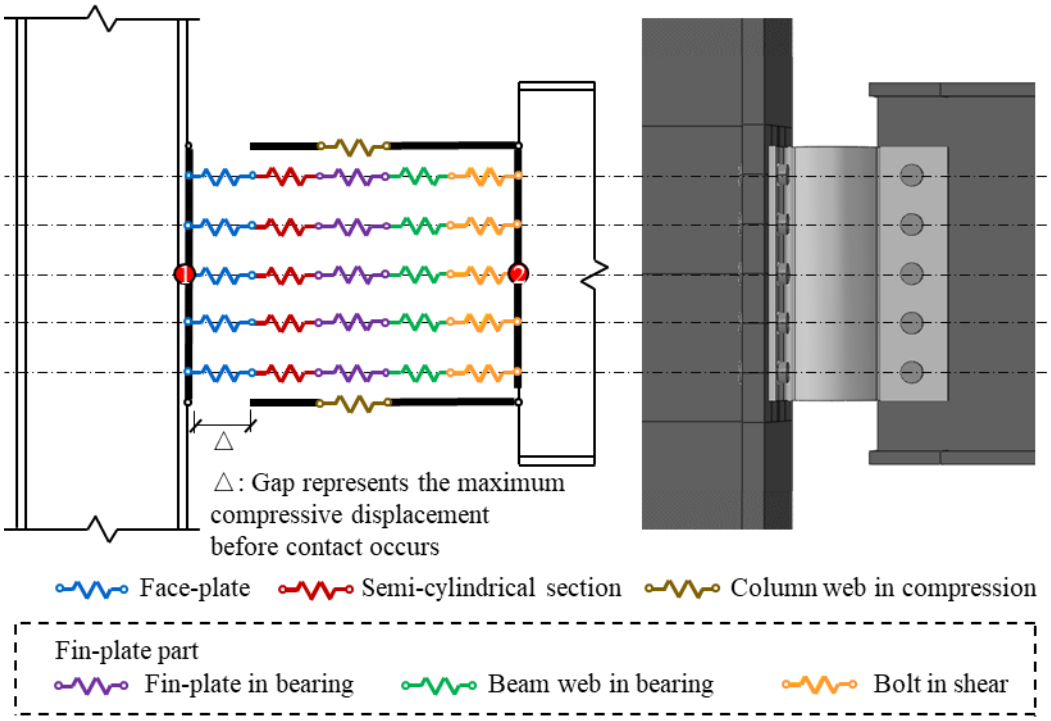

Figure 4-7. First scheme of the component-based model

4.4.1. Analytical model of the semi-cylindrical component

The analytical models of the semi-cylindrical component developed in the previous chapter are directly used here to generate the force-displacement curves of this component (Equations (3-20) - (3-23) for pulling and Equations (3-26) - (3-29) for pushing). It can be seen from these equations that the pulling/pushing force increases with the increase of plate thickness. This means that the ductility of the connection decreases with the increase of plate thickness. However, due to the shear capacity requirements of the ductile connection, the plate thickness should not be too small.

4.4.2. Analytical model of the face-plate component

Simple plastic theory is adopted here to model the plastic behaviour of the face-plate component,

considering both material and geometric nonlinearities. The relationship between the applied force and displacement of the face-plate component is obtained based on the virtual work principle. The calculation of the strain energy of plastic hinges is documented in the previous chapter, and so it is not described here.

The geometric relationship illustrated in Figure 4-8 between the displacements and the rotation angles of the plastic hinges is the key to solving the virtual work equation. It is assumed that the bolt connected to the column flange provides full fixity, and therefore the fixed-point A is located at the edge of the bolt head.

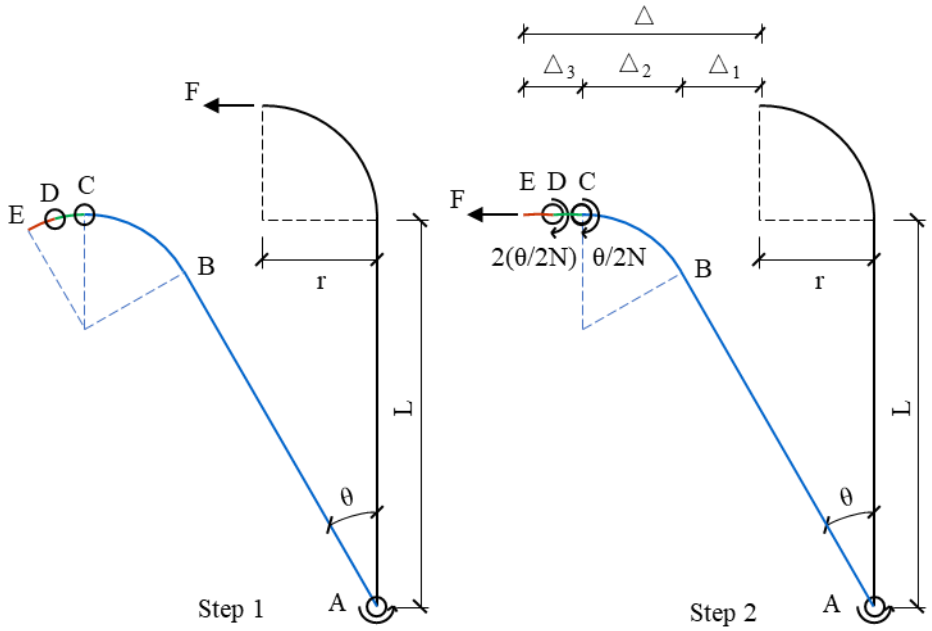

Figure 4-8. Geometric relationships

The deformation of the face-plate can be divided into two steps. The leg of face-plate, represented by AB in Figure 4-8, first rotates by the angle θ. The arc section CE then deforms to a straight horizontal section in the second step. This can be achieved by rotating angles $\theta/4$ and $\theta/2$ at the hinge C and hinge D respectively, if the arc section CE is divided into 2 segments (N=2). For the more general case, if the arc section CE is divided into N segments, the first hinge rotates $\theta/2N$ and the other hinges rotate $2\times(\theta/2N)$ at the second step. The total horizontal displacement can then be calculated as:

$$\Delta = \Delta_1 + \Delta_2 + \Delta_3 = \left(L\sin\theta - r\right) + r\cos\theta + 2Nr\sin\left(\theta/2N\right) \tag{4-3}$$

Then the relationship between the horizontal force and displacement can be obtained by solving the virtual work equation. For bi-linear material at ambient temperature:

$$\text{When } \varepsilon_m \le \varepsilon_y : F = \frac{Eht^2\theta}{12\left[L\cos\theta - r\sin\theta + r\cos\left(\frac{\theta}{2N}\right)\right]} \cdot \frac{4N-1}{2N} \tag{4-4}$$

$$\text{When } \varepsilon_m > \varepsilon_y : F = \frac{ht^2\left[3\theta^2 f_y - \left(12 f_y \varepsilon_y^2 - 8E\varepsilon_y^3\right)\right]}{12\theta^2\left[L\cos\theta - r\sin\theta + r\cos\left(\frac{\theta}{2N}\right)\right]} \cdot \frac{4N-1}{2N} \tag{4-5}$$

where h is the width of web-cleat, E is Young's modulus, ε_m is the maximum strain of plastic hinge, ε_y and f_y are yield strain and stress, respectively.

For tri-linear material at elevated temperatures:

When $\varepsilon_m \le \varepsilon_y$, equation is the same as that in the case of bi-linear material.

$$\text{When } \varepsilon_y < \varepsilon_m \le \varepsilon_u : F = \frac{ht^2\left[E_t\theta^3 + (E-E_t)(3\theta^2\varepsilon_y - 4\varepsilon_y^3)\right]}{6\theta^2\left[L\cos\theta - r\sin\theta + r\cos\left(\frac{\theta}{2N}\right)\right]} \frac{4N-1}{2N} \tag{4-6}$$

$$\text{When } \varepsilon_m > \varepsilon_u : F = \frac{ht^2\left[3\theta^2 f_u + (E-E_t)(3\varepsilon_y\varepsilon_u^2 - \varepsilon_y^3) + 2E_t\varepsilon_u^3 - 3f_u\varepsilon_u^2\right]}{12\theta^2\left[L\cos\theta - r\sin\theta + r\cos\left(\frac{\theta}{2N}\right)\right]} \frac{4N-1}{2N} \tag{4-7}$$

where E_t is tangent stiffness, ε_u and f_u are ultimate strain and stress, respectively.

A sensitivity analysis on the value of N has been carried out at ambient temperature, and the results are shown in Figure 4-9. As shown in this figure, adequate convergence is achieved when N is larger than 10, and this value is, therefore, used in subsequent calculations.

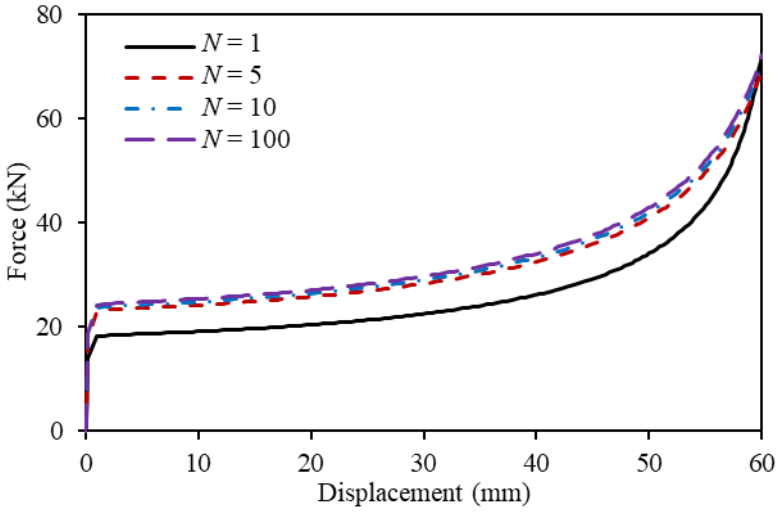

Figure 4-9. Influence of N value on analytical model

4.4.3. Fin-plate component and column web in compression

The fin-plate component of the connection consists of three components, including fin-plate in bearing, beam web in bearing and bolt in shear. Sarraj (2007) carried out a finite element parametric study, based on which, he proposed Equation (4-8) to describe the normalised force-displacement curves of the bearing components using different curve-fit values Ψ and Φ.

$$\frac{F}{F_{b,rd}} = \frac{\Psi\bar{\Delta}}{(1+\bar{\Delta}^{0.5})^2} - \Phi\bar{\Delta} \tag{4-8}$$

where $F_{b,rd}$ is the nominal plate strength and $\bar{\Delta}$ is the normalised bolt hole bearing deformation. Sarraj (2007) also developed a modified Ramberg-Osgood expression, Equation (4-9), to represent the relationship between force and bolt shear deformation. Equations (4-8) and (4-9) are adopted in this work to generate the force-displacement curves of fin-plate in bearing, beam web in bearing and bolt in shear.

$$\frac{F}{K_{v,b}} + \Omega\left(\frac{F}{F_{v,rd}}\right)^m = \Delta \tag{4-9}$$

where $K_{v,b}$ is the shear stiffness of a bolt, and $F_{v,Rd}$ is its shear strength. The index *m* controls the curvature of the response curve. As for the column web in compression, the force-displacement curve proposed by Block (2006) is adopted in this component-based model. This compression curve is divided into elastic and plastic parts, represented by Equations (4-10) and (4-11), respectively.

When $\delta \le \delta_{el}$: $F = \delta k_T$ (4-10)

When $\delta_{el} < \delta \le \delta_u$: $F = F_{el} - c + \frac{b}{a}\sqrt{a^2 - (\delta_u - \delta)^2}$ (4-11)

where k_T is the tangent stiffness of elastic part and is calculated using the parameters *a, b* and *c*. The detailed calculations of k_T, *a, b* and *c* can be found in Reference (Block, 2006).

4.4.4. Loading and unloading process of spring row

When the connection deforms, the forces in each component of a spring row are identical, and the deformation of the whole spring row is the sum of deformations of all components. The resistance

of each spring row is governed by the weakest component in this series.

4.4.4.1. Unloading at constant and changing temperature

Irreversible deformation occurs when the deformation of a component enters the plastic range. Block (2006) and Dong (2015) employed the classic Masing rule (Gerstle, 1988), based on which the unloading curve is obtained by doubling the loading curve in scale and rotating by 180°, to represent this 'memory effect'. However, since the tensive and compressive curves of the semi-cylindrical component are not identical in shape as presented in the previous chapter, the Masing rule is not suitable for this connection. The unloading path of the proposed connection is simplified to be linear, with slope equal to that of the initial linear-elastic part of the loading curve, as shown in Figure 4-10.

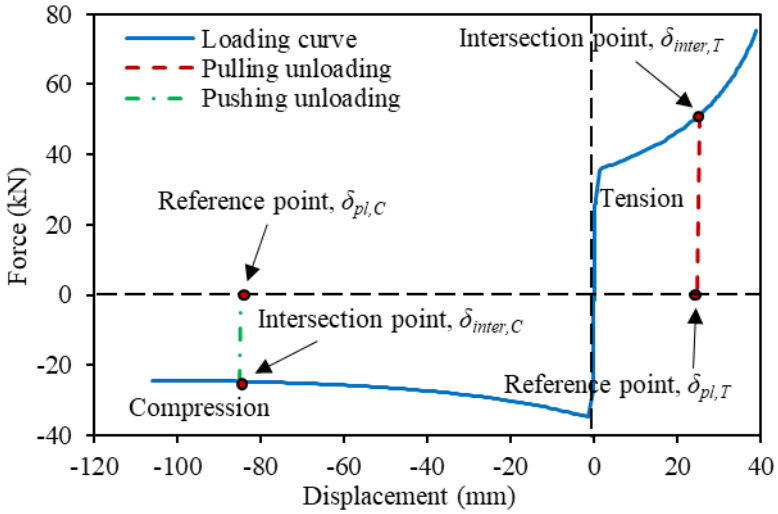

Figure 4-10. Unloading at constant temperature

The intersection between the unloading path and the horizontal-axis is defined as the Reference Point, representing the permanent deformation caused at zero force. The intersection of the unloading path and the loading curve is defined as the Intersection Point. Displacement control is adopted to calculate the force-displacement response of the component-based model. During the calculation process, the displacement of the intersection point δ_{inter} and that of the reference point δ_{pl} at the end of each displacement step is stored. If the applied displacement at an arbitrary step δ is larger than δ_{inter}, the loading path will be followed and the permanent deformation will be updated accordingly. Therefore, both the intersection point and reference point are updated at the

end of this step. If δ is less than δ_{inter} but larger than the δ_{pl}, the unloading path will be followed and the permanent deformation will not change. If δ is less than δ_{pl}, the push-back curve for tension or the pull-back curve for compression will be followed.

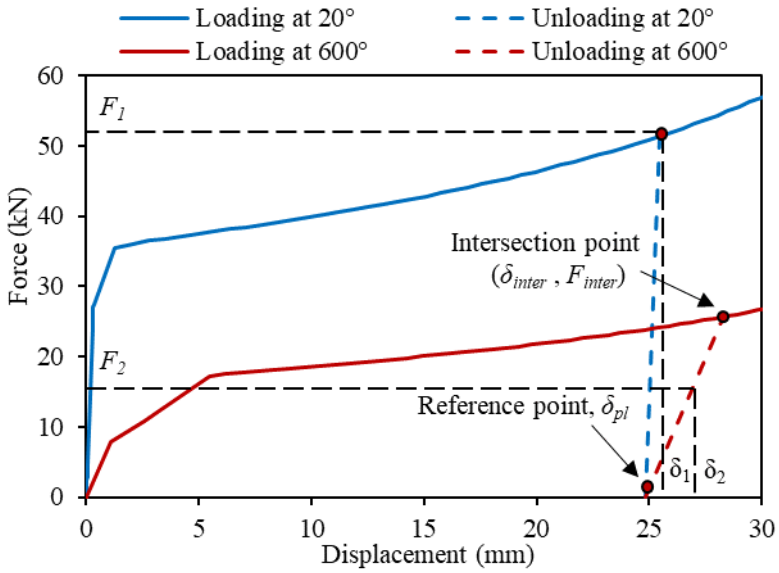

Figure 4-11. Unloading with changing temperatures

When the connection is exposed to fire, its temperature changes continuously, and the force-displacement relationships of the components are temperature-dependent. The 'Reference Point' concept is introduced to generate the unloading curve of each component at changing temperatures. This concept, assuming that plastic strain is not affected by the change of temperature, was initially used by Franssen (1990) to describe the unloading behaviour of composite beams and columns, and by El-Rimawi (1996) to describe the cooling behaviour of steel beams and columns. Bailey (1995) used the concept to incorporate unloading into the simple moment-rotation connection spring element in the early version of Vulcan. Continuing his work, Block (2006) and Dong (2015) also adopted the concept in the development of the end-plate and reverse-channel connection elements. When using this concept to describe the unloading behaviour of a component at changing temperatures, all force-displacement curves at different temperatures unload to the same Reference Point, as shown in Figure 4-11. At 20°C, the semi-cylindrical component is loaded to a displacement δ_1, generating a permanent deformation δ_{pl}. In the next step, it is assumed that the temperature of connection changes to 600°C, and the applied displacement at this step is δ_2. The corresponding force F_2 needs to be calculated in three steps. The first step is to generate the force-displacement curve at 600°C. The second is to calculate the

intersection point (δ_{inter}, F_{inter}) using the displacement at the reference point δ_{pl} of the previous step at 20℃ and the slope of the linear-elastic part of the loading curve at 600℃. The final step is to determine which force-displacement relationship (loading, unloading, push-back or pull-back) should be used for the calculation of force F_2, on the basis of the relationship between δ_2, δ_{inter} and δ_{pl}.

4.4.4.2. Combined loading and unloading curve of each spring row

Figure 4-12 shows the calculation procedure for each spring row. The force-displacement curves of all five components (springs) in each spring row are combined into one force-displacement relationship based on the fact that these springs work in series. At an arbitrary force level, the displacement of the combined force-displacement curve is the sum of the displacements of all components under this force. The loading and unloading process has been described in detail previously. The maximum deformation limit of a spring row during pulling is reached when any component in a row reaches its failure force. In the loading stage, this deformation limit is checked, as shown in the flowchart of Figure 4-12. If the deformation limit is not reached, the force and displacement of this spring row will be output and the corresponding displacement of the Reference Point of each component will be updated. Otherwise, this spring row is considered as having failed and is deactivated. A spring row is pushed back from tension, or pulled back from compression, when the applied displacement in a new displacement step is less than the displacement of the reference point δ_{pl} of the previous step. The combined push-back or pull-back curve needs to be determined. The push-back and pull-back curves of the semi-cylindrical component can be obtained using the compression and tension analytical models developed in Chapter 3, together with the existing deformation of the connection. The push-back curve of the face-plate can be obtained using the same method as the semi-cylindrical section, except that the deformation of the already deformed connection should be considered.

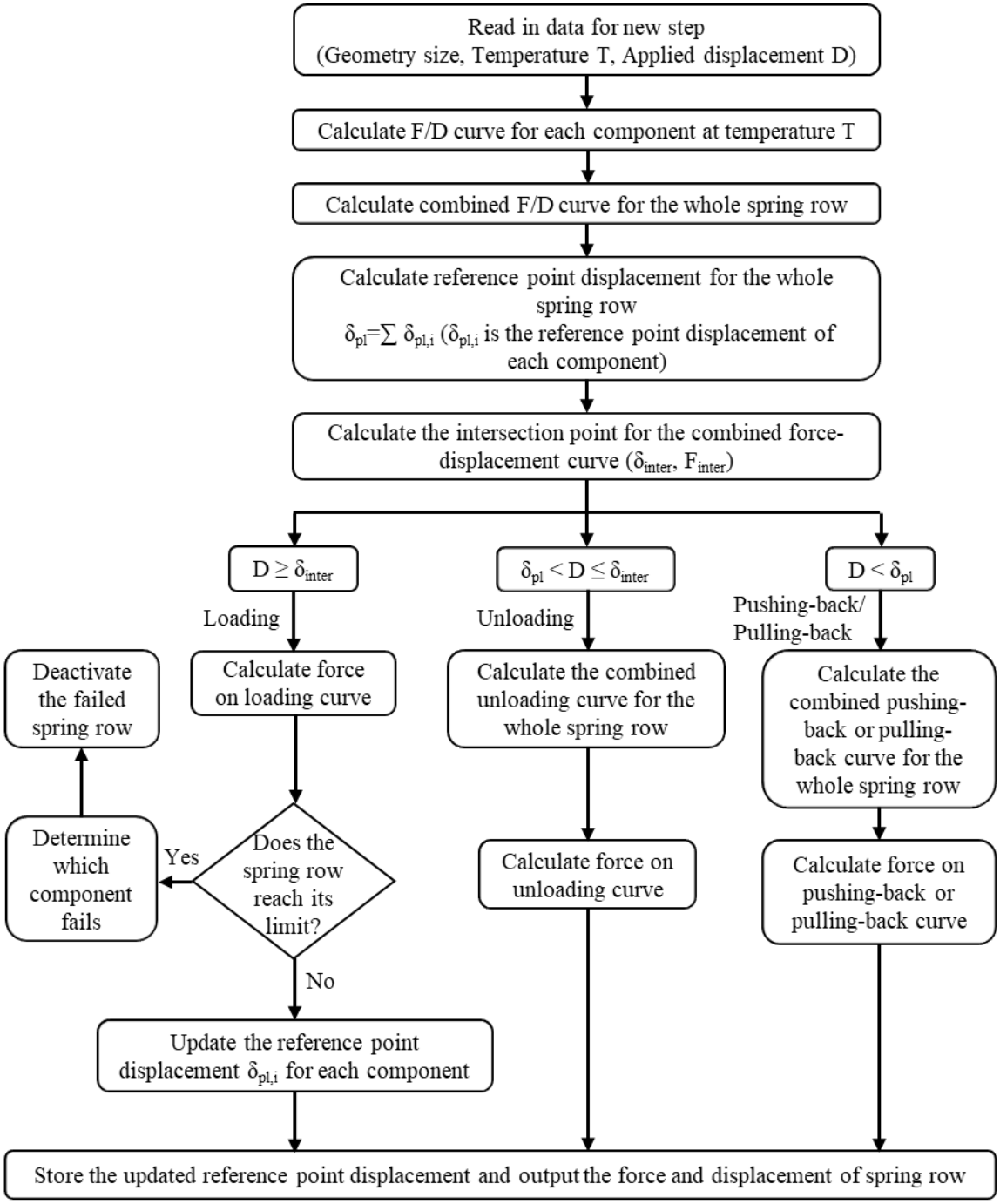

Figure 4-12. Calculation procedure for each spring row

Following this procedure, the complete force-displacement relationship under cyclic load of an example connection of the size shown in Figure 4-3 (b), fabricated in steel of grade S275, is established, as shown in Figure 4-13. The blue loop starts in pulling, and then the connection is unloaded and pushed-back to its original state. As shown in Figure 4-13, during push-back, the force increases sharply when the displacement is around 10mm. This is because the maximum force of the push-back curve of the face-plate component is smaller than that of the push-back

curve of the semi-cylindrical component, and so the face-plate component will be pushed back to its original position first. The push-back of the semi-cylindrical component then causes the sudden increase in force. The red loop starts in pushing. The connection is then unloaded and pulled back to its original shape.

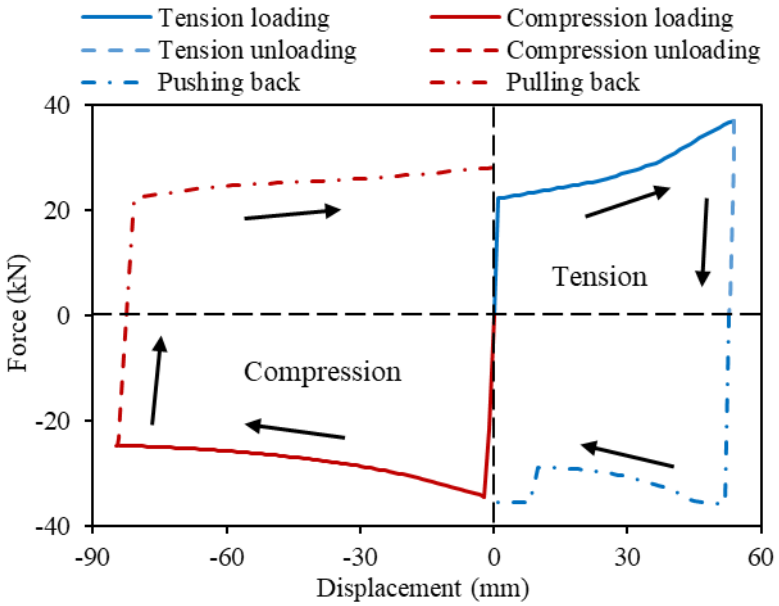

Figure 4-13. Loading and unloading process for a spring row

4.5. Alternative component-based model

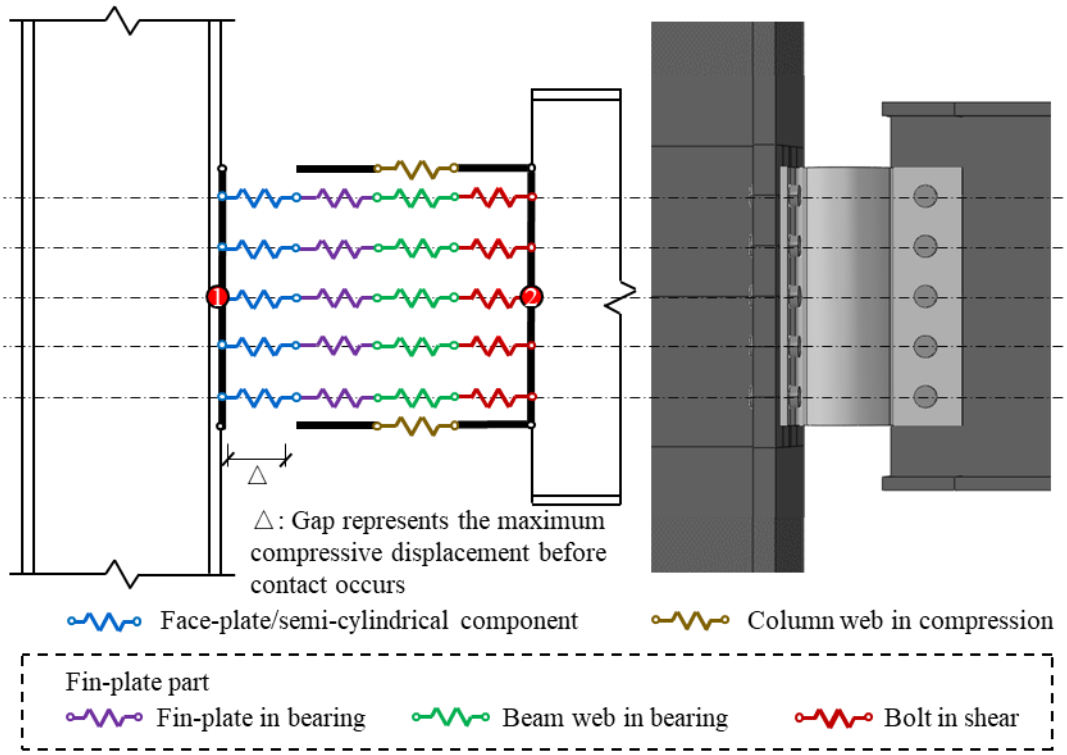

Figure 4-14. Second scheme of the component-based model

In the scheme given in Section 4.4 for the component-based model, the semi-cylindrical section and the face-plate are treated as two separate components, working in series. However, in the actual deformation process, these two parts of the connection interact with each other directly. Therefore, a face-plate/semi-cylindrical (FPSC) component is adopted as an improved scheme for the component-based model. This considers the semi-cylindrical section and the face-plate as a single component, as shown in Figure 4-14. Two deformation cases generally need to be considered when developing the FPSC component, according to the position of the face-plate bolts; these are described below.

4.5.1. Case 1 of the FPSC component

In Case 1, the length of the face-plate leg from the edge of the bolt head to the initial plate bend is larger than the radius of the semi-cylindrical section. It is assumed that five plastic hinges can be formed during the deformation of the component, which are located at the two ends and outer edge (considered as two adjacent hinges) of the semi-cylindrical section, and the edge of bolt head, as shown in Figure 4-15. The position of the bolt is indicated by L_2; this is 99.6mm for the example component. The dimensions of the example FPSC component analysed here are shown in Figure 4-3 (b).

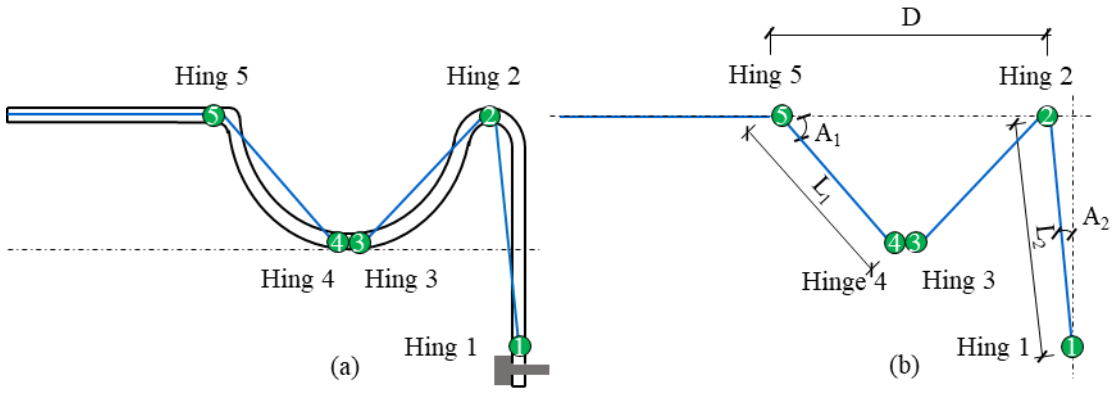

Figure 4-15. Schematic diagram of Case 1

4.5.1.1. Pulling

The pulling of the FPSC component can be divided into two stages. In the first stage, only Hinges

1, 2 and 5 rotate; in the second stage, all the plastic hinges rotate, as shown in Figure 4-16. In both stages, the rotation of one (the "control" hinge) of the five hinges is firstly assumed; the rotations of the other hinges are then calculated. Assuming that the rotation of the control hinge is θ, the sum of the rotation angles of all plastic hinges and the total horizontal displacement are functions of θ. According to the virtual work principle:

$$F \cdot d\Delta(\theta) \cdot d\theta = M_P\left[A(\theta)\right] \cdot dA(\theta) \cdot d\theta \tag{4-12}$$

where $\Delta(\theta)$ is the total horizontal displacement, $M_P\left[A(\theta)\right]$ is the plastic moment, and $A(\theta)$ is the sum of the rotations of all plastic hinges. The calculation of plastic hinge moment has been documented in the previous chapter. The relationship between force and displacement is obtained from:

$$F = \frac{M_P\left[A(\theta)\right] \cdot dA(\theta)}{d\Delta(\theta)} \tag{4-13}$$

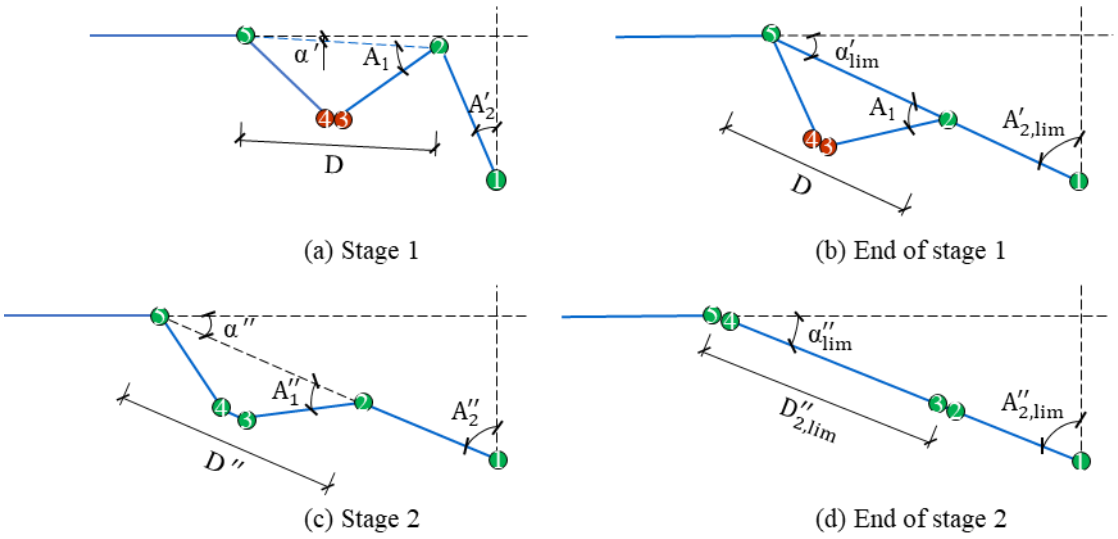

Figure 4-16. Pulling analytical model of Case 1

The key to solving Equation (4-13) is to derive the relationship between the rotation of the control hinge and the total horizontal displacement. Since in the first stage only Hinges 1, 2 and 5 rotate, the distance D between Hinges 2 and 5 remains unchanged during this stage. If the rotation of Hinge 1, the control hinge in Stage 1, is θ, the angle α' can be calculated by Equation (4-14). According to the geometric relationship, the rotations of Hinges 2 and 5 are $(\alpha'+\theta)$ and α', respectively. The total horizontal displacement and its increment can be obtained using Equations

(4-15) and (4-16).

$$\alpha' = \arcsin\left[L_2 \left(\cos A_2 - \mathrm{Cos}(A_2 + \theta) \right) / D \right] \tag{4-14}$$

$$\Delta = L_2 \left(\sin(A_2 + \theta) - \sin A_2 \right) + \sqrt{D^2 - {L_2}^2 \left(\cos A_2 - \mathrm{Cos}(A_2 + \theta) \right)^2} - \mathrm{D} \tag{4-15}$$

$$\mathrm{d}\Delta = \left[L_2 \cos(A_2 + \theta) + \frac{{L_2}^2 \sin(A_2 + \theta)\left[\cos A_2 - \cos(A_2 + \theta) \right]}{\sqrt{D^2 - {L_2}^2 \left[\mathrm{cos}A_2 - \mathrm{Cos}(A_2 + \theta) \right]^2}} \right] d\theta \tag{4-16}$$

Stage 1 switches to Stage 2 when Hinges 1, 2 and 5 form a straight line, as shown in Figure 4-16 (b). Hinges 3 and 4 are then activated, and they will move towards the end hinges as the semi-cylindrical section is stretched. Hinge 2 is the control plastic hinge of Stage 2. Therefore, the rotation of Hinge 2 is firstly assumed, as β. Hinges 1, 2 and 5 always form a straight line. The distance D'' between Hinge 2 and Hinge 5 is calculated with Equation (4-17), using the tensile analytical model of the semi-cylindrical section developed in the previous chapter.

$$D'' = D + 2r\left[n \sin\left(\beta / n \right) + \cos\beta - 1 \right] \tag{4-17}$$

where n is a parameter used to modify the calculation of the tensile deformation of semi-cylindrical section (see detail in previous chapter). According to the geometric relationship, the rotations of Hinges 1, 3, 4 and 5 are $A_2'' - A_{2,\mathrm{lim}}'$, β, β and $\beta + A_2'' - A_{2,\mathrm{lim}}'$, respectively. The horizontal displacement and its increment in this stage can be calculated by Equations (4-18) and (4-19). The end of Stage 2 is when the component is stretched flat, shown in Figure 4-16 (d), and then the component is purely in tension. By substituting the relationship between the rotation of the control hinge and the total displacement into Equation (4-13), the force can be obtained. The first and second schemes of the component-based model are compared against the Abaqus in Figure 4-17.

This figure shows that the second scheme of the component-based model matches the Abaqus results better than the first scheme, due to the application of the FPSC component. The kink in the blue curve representing the second scheme of the component-based model is caused by the transition from the first stage to the second stage.

$$\Delta = \sqrt{\left[D + 2r\left(n \sin\frac{\beta}{n} + \cos\beta - 1 \right) + L_2 \right]^2 - (L_2 \cos A_2)^2} - L_2 \sin A_2 - D \tag{4-18}$$

$$d\Delta = \frac{\left[D + 2r\left(n\sin\frac{\beta}{n} + \cos\beta - 1\right) + L_2\right]\left[2r\left(\cos\frac{\beta}{n} - \sin\beta\right)\right]}{\sqrt{\left[D + 2r\left(n\sin\frac{\beta}{n} + \cos\beta - 1\right) + L_2\right]^2 - (L_2\cos A_2)^2}} \tag{4-19}$$

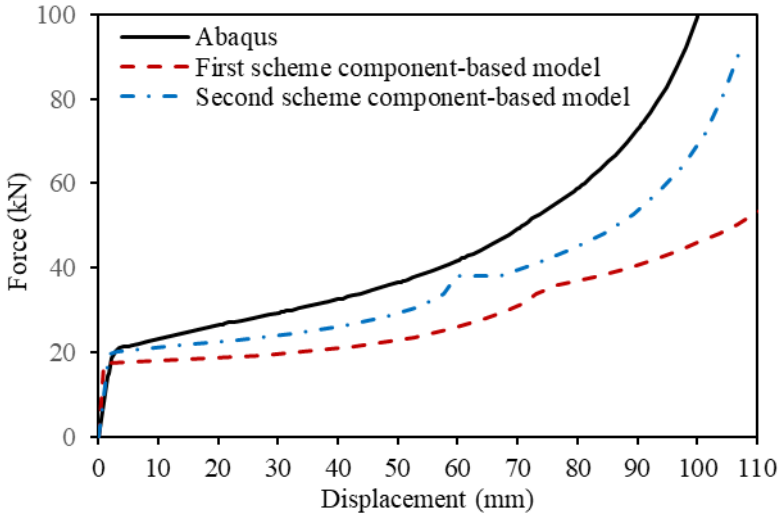

Figure 4-17. Pulling curves of Case 1 connection

4.5.1.2. Push-back

Similarly to the first component-based model, the loading stage (loading, unloading, push-back or pull-back) of the FPSC component in the second scheme is still determined by the flowchart of Figure 4-12. For pushing back, there are two cases: 1) the component is pushed back from Stage 1 of pulling; and 2) the component is pushed back from Stage 2 of pulling.

If the component is pushed back from Stage 1 of pulling, the push-back deformation is the reverse process of the deformation of the first stage of pulling. The force-deformation relationship of the connection when it is pushed back from Stage 1 of pulling, from the Abaqus model and the two component-based model schemes are shown in Figure 4-18. From the comparison shown in Figure 4-18, both the first and second component-based model schemes can produce results which are generally in agreement with the Abaqus simulation. The semi-cylindrical section of the Abaqus model deforms slightly (around 2mm) in the first stage of pulling. This is finally pushed back, causing the sudden kink towards the end of push-back. The second component-based model scheme assumes that the semi-cylindrical section does not deform during the Stage 1 of pulling, and so it cannot model this phenomenon.

The deformation process of the push-back of the connection from Stage 2 of pulling, simulated in Abaqus, is shown in Figure 4-19. This figure shows that the face-plate is pushed back to its original state at first, and then the semi-cylindrical section is pushed back. Therefore, the push-back of connection from Stage 2 of pulling includes two steps as shown in Figure 4-20.

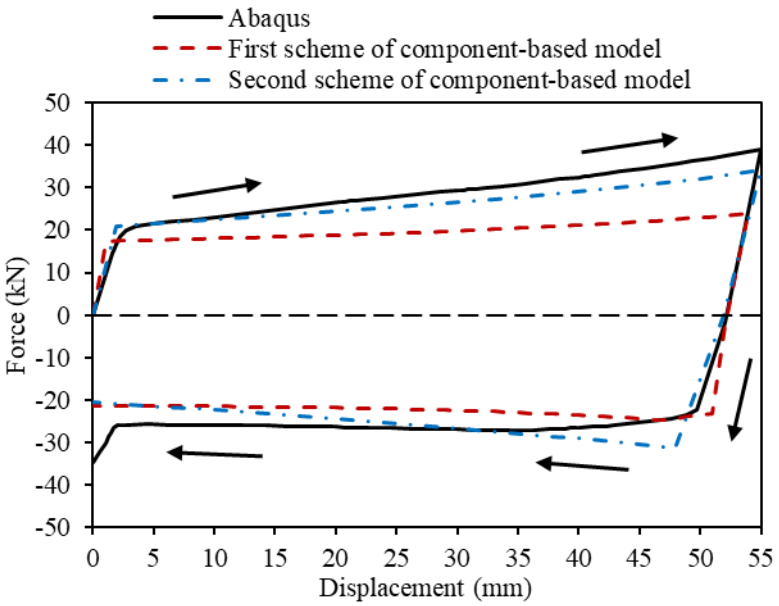

Figure 4-18. Push-back curves of Case 1 connection from Stage 1 of pulling

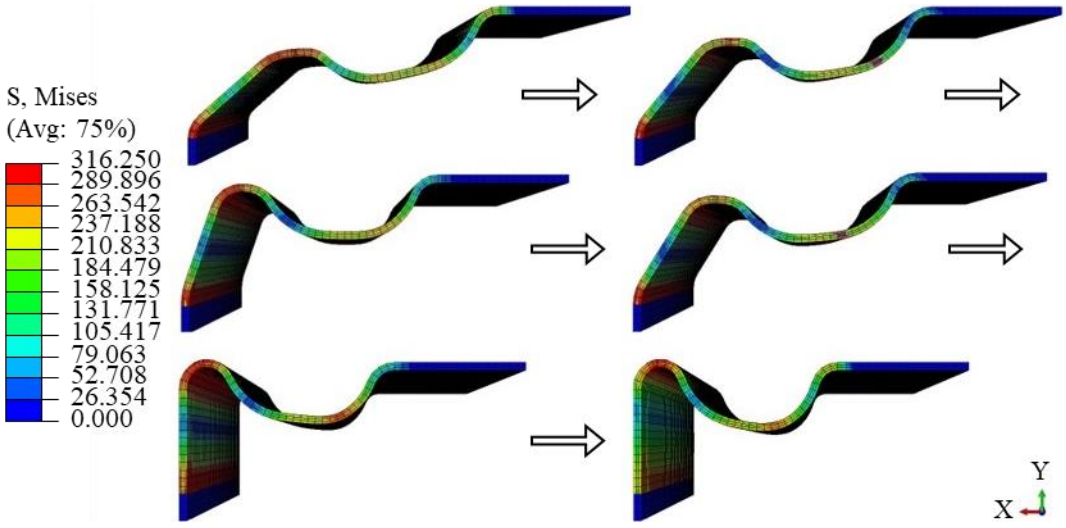

Figure 4-19. Deformation process of pushing back of connection from Stage 2

The initial distance between Hinge 2 and Hinge 5 is related to the displacement D_{ref} at the reference point (when pushing back starts), and is calculated using Equation (4-20). In the first stage of push-back, the control plastic hinge is Hinge 1. Assuming that the rotation of Hinge 1 is θ_c, angle α_c' is calculated from Equation (4-21). Based on geometry, the rotations of Hinge 2 and

Hinge 5 are $90°-\alpha_c'-A_{2,c}'$ and $90°-\alpha_c'-A_{2,c}'-\theta_c$, respectively. The total horizontal displacement and its increment are calculated using Equations (4-22) and (4-23). Stage 1 switches to Stage 2 when Hinge 2 has rotated back to the horizontal line passing through Hinge 5, as shown in Figure 4-20 (c). Stage 2 is the pushing back of the semi-cylindrical section. The analytical model of the semi-cylindrical section in compression developed in the previous chapter can be used here to calculate the force and displacement of the FPSC component.

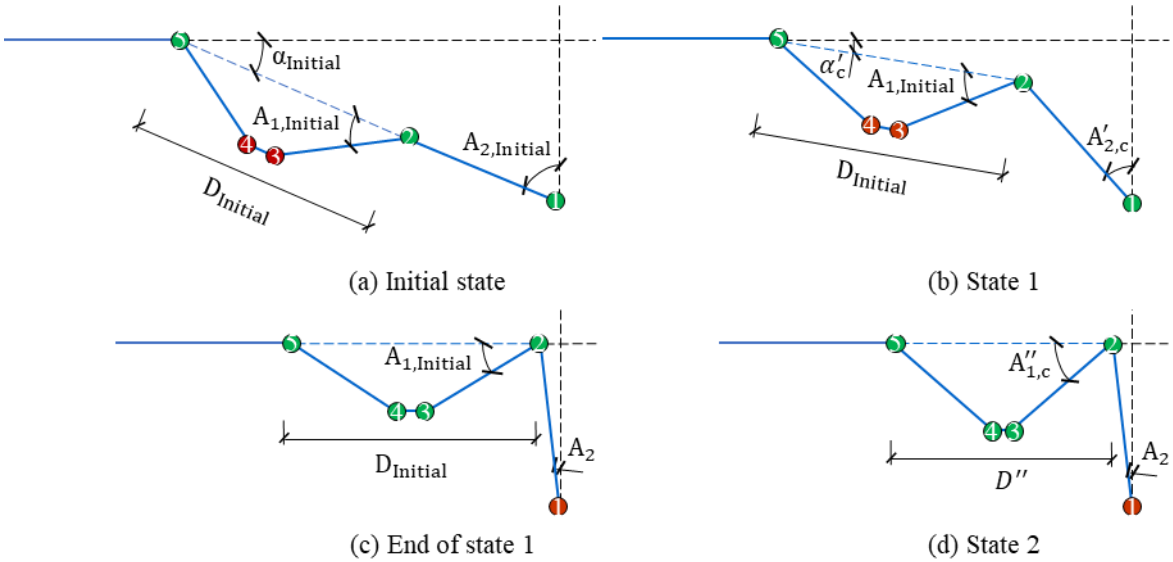

Figure 4-20. Push-back analytical model of Case 1 from Stage 2

The force-displacement relationships of the connection when it is pushed back from Stage 2 of pulling, resulting from the first and second schemes of the component-based and Abaqus models are compared in Figure 4-21. The sudden increase of push-back forces shown in the figure indicates that the face-plate has been pushed-back to its original state, and the semi-cylindrical section has begun to be pushed back. The second component-based model scheme simulates the face-plate being pushed back to its original position earlier than for the other two models. This is because this model assumes that in the first stage of pushing back only the face-plate deforms, whereas the other two models also consider the tiny deformation of the semi-cylindrical section at the same time, which is insignificant.

$$D_{Initial}=\sqrt{(D_{ref}+L_2\sin A_2+D)^2+(L_2\cos A_2)^2}-L_2 \tag{4-20}$$

$$\alpha_c'=\arcsin\left[L_2\left(\cos A_2-\mathrm{Cos}(A_{2,Initial}-\theta_c)\right)/D_{Initial}\right] \tag{4-21}$$

$$\Delta=D_{ref}-\left(D_{ref}+D+L_2\sin A_2-D_{Initial}\cos\alpha_c'-L_2\sin A_{2,c}'\right) \tag{4-22}$$

$$d\Delta = L_2\cos(A_{2,Initial} - \theta_c) - \frac{\left[L_2\cos A_2 - L_2\cos(A_{2,Initial} - \theta_c)\right]\cdot L_2\sin(A_{2,Initial} - \theta_c)}{D_{Initial}\sqrt{D_{Initial}^2 - \left[L_2\cos A_2 - L_2\cos(A_{2,Initial} - \theta_c)\right]^2}} \quad (4\text{-}23)$$

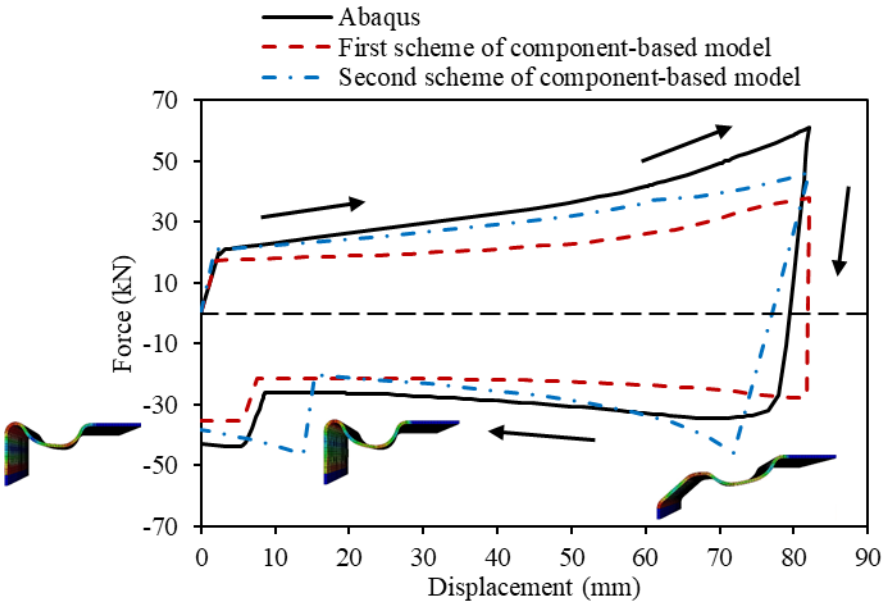

Figure 4-21. Push-back curves of Case 1 connection from Stage 2 of pulling

4.5.2. Case 2 of the FPSC component

Similarly to Case 1, it is assumed that five plastic hinges can be formed during the deformation of the FPSC component, as shown in Figure 4-22. The key difference between Case 1 and Case 2 is that in Case 1 the length L_2 between Hinges 1 and 2 is larger than the radius of the semi-cylindrical section, whereas L_2 is smaller than the radius of the semi-cylindrical section in Case 2. The size of the example connection analysed in this section is shown in Figure 4-3 (b) and the dimension L_2 is equal to 46.6mm.

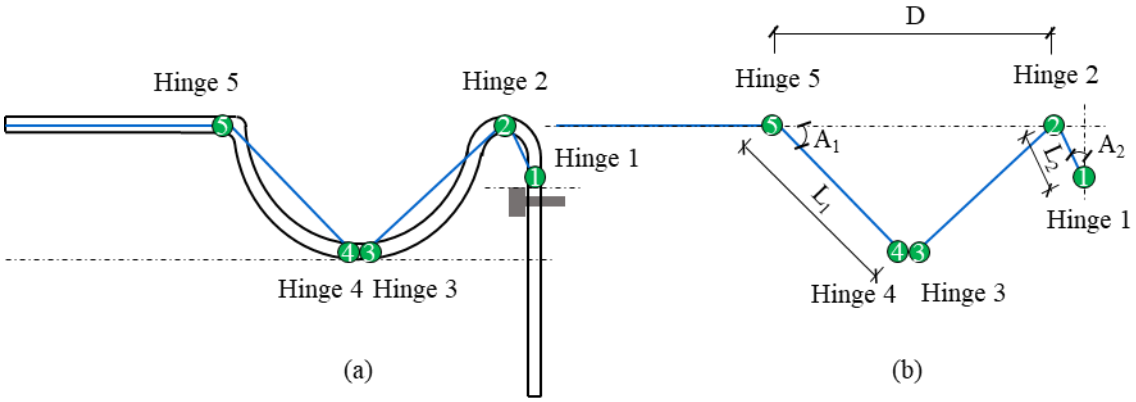

Figure 4-22. Schematic diagram of Case 2

4.5.2.1. Pulling

The pulling of the FPSC component can be divided into two stages. In the first stage, only the semi-cylindrical component is stretched. In the second stage, all the plastic hinges rotate, as shown in Figure 4-23.

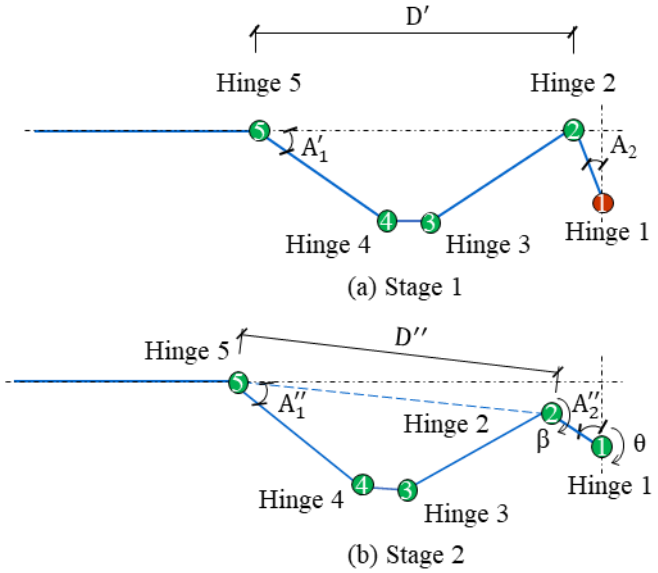

Figure 4-23. Analytical model of Case 2 in pulling

The analytical model of the semi-cylindrical section in tension developed in the previous chapter is adopted here for the first stage of pulling. During the second stage, the behaviour of the hinges is more complex than that of Case 1. Therefore, the procedure shown in Figure 4-24 is followed to calculate the force and displacement of the component. At first, the rotation of Hinge 2 increases to β_i, and the length between Hinges 2 and 5 increases to D'', correspondingly. The force F_{axial} used to stretch the semi-cylindrical section is calculated. β_{max} represents the maximum rotation of Hinge 2 in the second stage, which is equal to A_2 minus the rotation of Hinge 2 in Stage 1. The rotation θ_j of Hinge 1 then increases while D'' remains unchanged. The maximum limit of θ_j, named as θ_{max}, is calculated from Equation (4-24); θ_{max} is reached when Hinges 1, 2 and 5 form a straight line. With the increase of θ_j, the force $F_{i,j}$ increases. However, θ_{max} may not be reached if $F_{i,j}$ is bigger than $F_{axial} \cdot \cos\alpha''$, which is the horizontal component of the force used to stretch the semi-cylindrical section. If $F_{i,j}$ is smaller than $F_{axial} \cdot \cos\alpha''$, the force $F_{i,j}$ and displacement $\Delta_{i,j}$ are output. Otherwise, the semi-cylindrical section will be further stretched, and the rotation

of Hinge 2 will increase to β_{i+1}. As shown in Figure 4-25, the second component-based model scheme leads to a better comparison with the Abaqus result because of the FPSC component.

$$\theta_{\max,i} = \arcsin\left((L_2 \cos A_2)/(D"+L_2)\right) \tag{4-24}$$

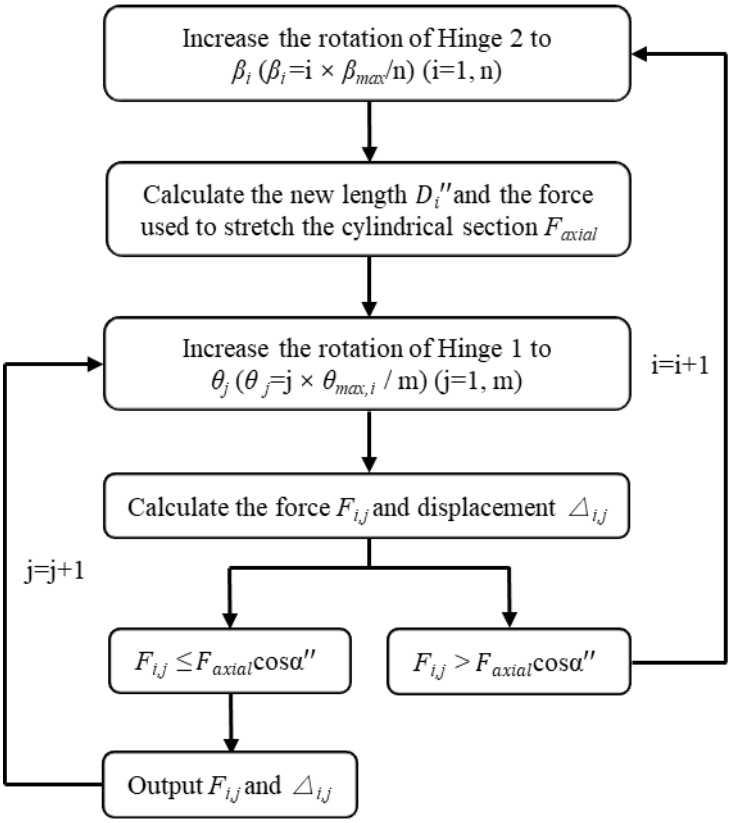

Figure 4-24. Calculation process of Stage 2

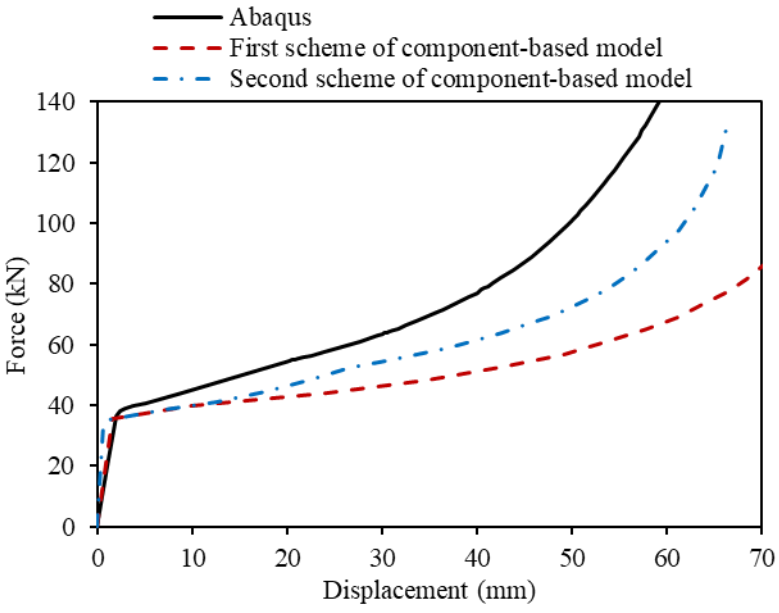

Figure 4-25. Pulling curves of Case 2 connection

4.5.2.2. Push-back

There are two different situations of push-back in Case 2. When the connection is pushed back from the first stage of pulling, the analytical model of the semi-cylindrical section in compression developed in the previous chapter is used to calculate the force and displacement of the FPSC component, as shown in Figure 4-26.

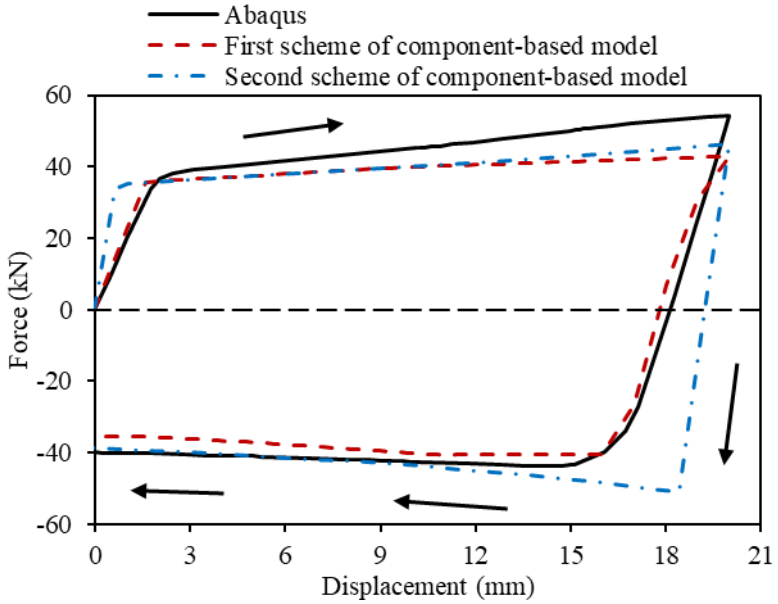

Figure 4-26. Push-back curves of Case 2 connection from Stage 1 of pulling

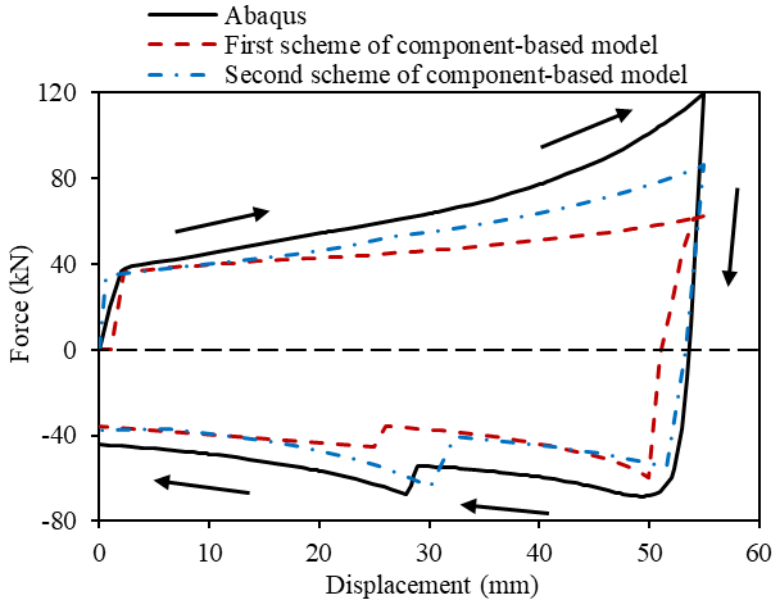

Figure 4-27. Push-back curves of Case 2 connection from Stage 2 of pulling

When the connection is pushed back from the second stage of pulling, the model developed for

Case 1 is also applicable to Case 2. The push-back curve given by Case 2 of the second scheme of the component-based model is plotted in Figure 4-27, and compared with the first model and Abaqus. The resulting curves from the second scheme of component-based model is in better accordance with the Abaqus results.

4.5.3. Pushing and pull-back of the FPSC component

For pushing, when the component is pushed from its initial state, it is assumed that only the semi-cylindrical section deforms in both Cases 1 and 2. Therefore, the analytical model of the semi-cylindrical section in compression developed in previous chapter is adopted for pushing of connection. For pull-back after pushing, the pulling models developed for Cases 1 and 2 can still be used, except that the pre-deformed connection geometry needs to be considered. It should be noted that the choice of Case 1 or 2 for post-pushing pull-back needs to be re-assessed based on the deformed connection geometry. For instance, the appropriate case could be Case 1 for pulling but Case 2 for pulling back.

4.6. Comparison of the two component-based models against experiments

In this section, the experiments on model-scale connections conducted by Kalawadwala (2018) are used for comparison with the two component-based model schemes proposed above. The dimensions of the tested specimens are documented in Chapter 3 and are not repeated here. Kalawadwala conducted three experiments, unloading from different levels of compression; -7.9mm (Experiment 1), -16.6mm (Experiment 2) and -24.0mm (Experiment 3).

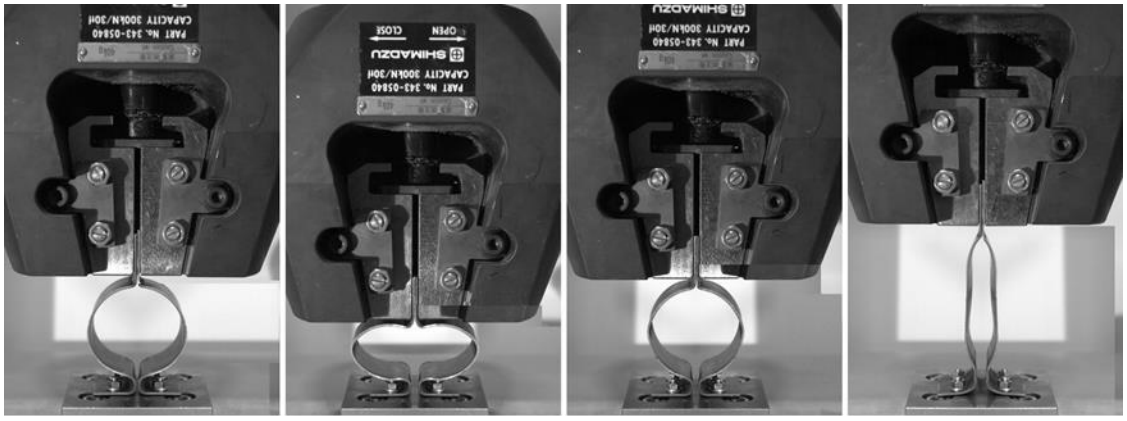

(a) Initial state (b) Pushing (c) Pull-back (d) Pulling

Figure 4-28. Experimental photos

The deformed shapes of the specimens from all three experiments are similar; those of Experiment 3 are shown in Figure 4-28. Figure 4-28 (a) illustrates the initial state of the specimen and (b) shows the deformed shape and the beginning of unloading. Figure 4-28 (c) shows that the specimen is pulled back to its original state. Figure 4-28 (d) shows the specimen when it is eventually stretched flat.

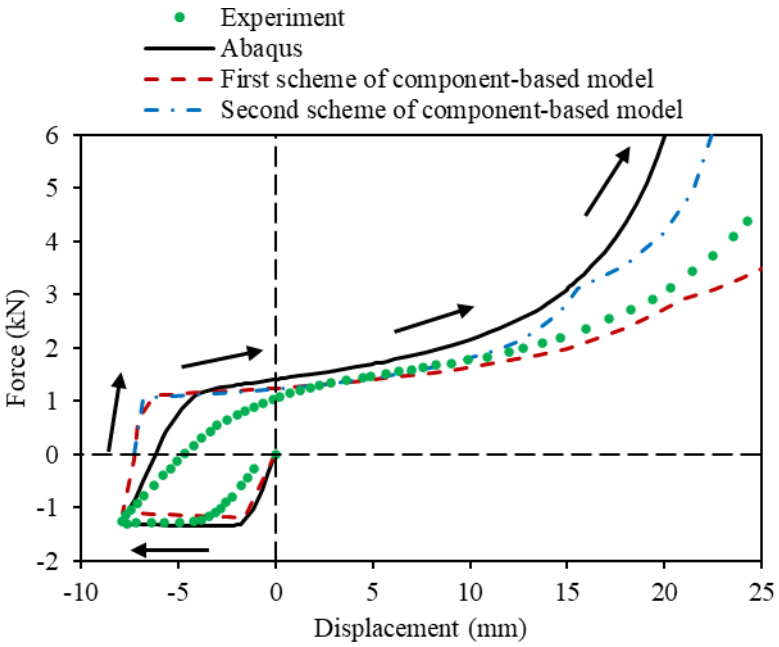

Figure 4-29. Experiment 1 results and modelling

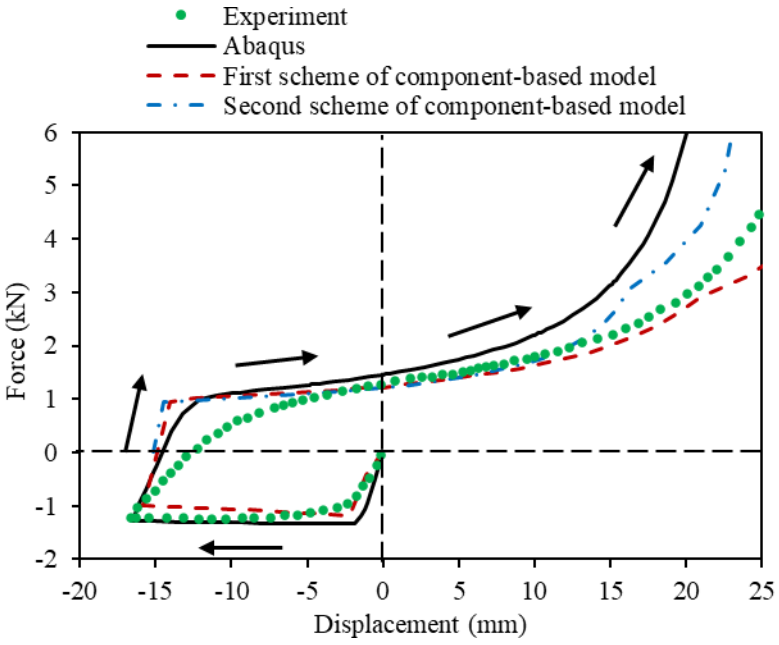

Figure 4-30. Experiment 2 results and modelling

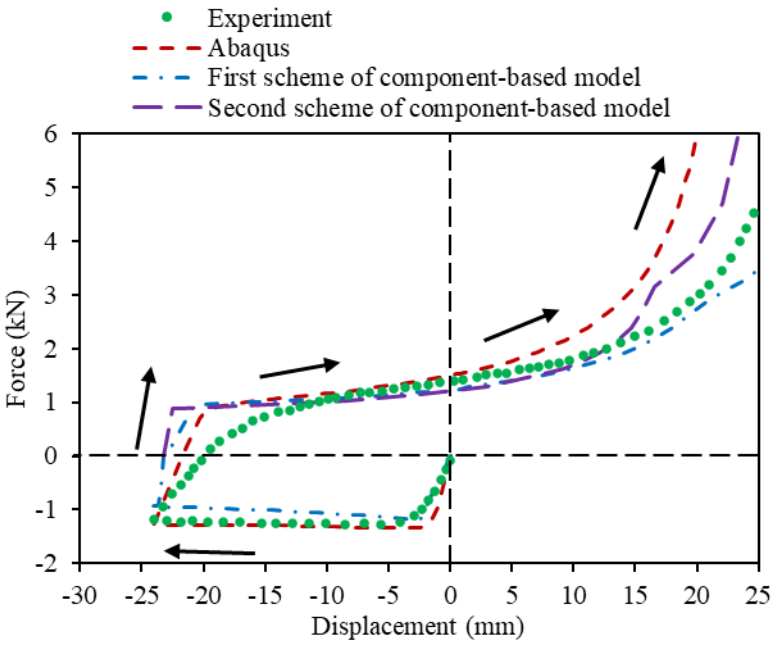

Figure 4-31. Experiment 3 results and modelling

The experimental results, shown in Figure 4-29, Figure 4-30 and Figure 4-31, are compared with the Abaqus model and the two component-based model schemes. These figures show that the slope of the initial linear elastic loading path and that of the unloading path given by the experiments are lower than those given by the Abaqus simulation and the component-based models. This may be because of slip between the clamps of the testing machine and the specimen. The pushing curves of the two component-based models are the same, since both assume that only the semi-cylindrical component deforms during pushing. The results of the second component-based model scheme are closer to the test and Abaqus than those of the first component-based model scheme.

4.7. Example applications of the component-based model

The aim of the research is to implement the component-based model of the ductile connection into global frame analysis. Before this is done, it is important to demonstrate how the model works in simulating isolated connections. Two load cases are discussed in this section. The above sections indicate that the second component-based model scheme delivers the better simulation results of the two, and so it is adopted in this section. As shown in Figure 4-32, a connection of the same dimensions as that shown in Figure 4-3 (b) is divided into five spring rows, each

representing a bolt row. In Load Case 1, a horizontal tensile displacement is applied to the connection first, and then a rotation is applied to the centre line of the connection, with a centre of rotation as shown in the figure. In Load Case 2, a horizontal compressive displacement is applied first, followed by a similarly applied rotation. The results from Abaqus and the component-based model are compared in Figure 4-33. The force-displacement relationships of each spring row of these two cases are shown in Figure 4-34 and Figure 4-36. The force-rotation relationships of each spring row of these two cases are shown in Figure 4-35 and Figure 4-37.

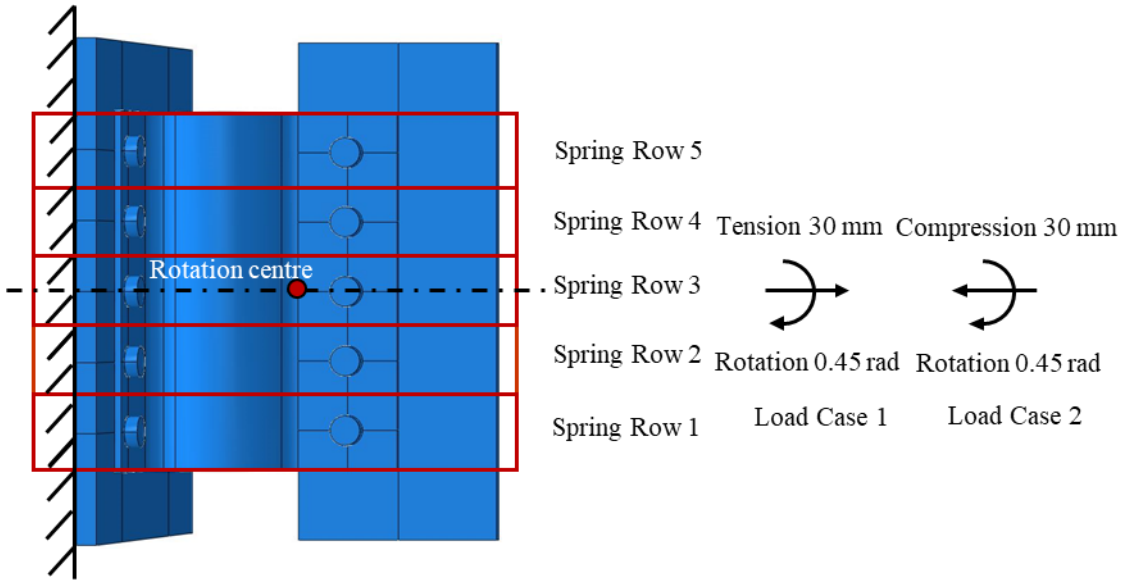

Figure 4-32. Division into 5 component rows for application examples

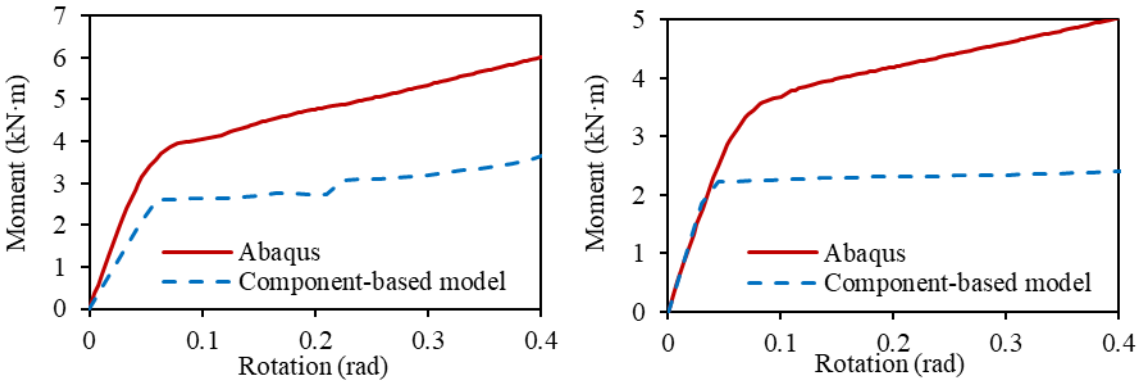

(a) Load Case 1 (b) Load Case 2

Figure 4-33. Comparison of moment generated with Abaqus simulations

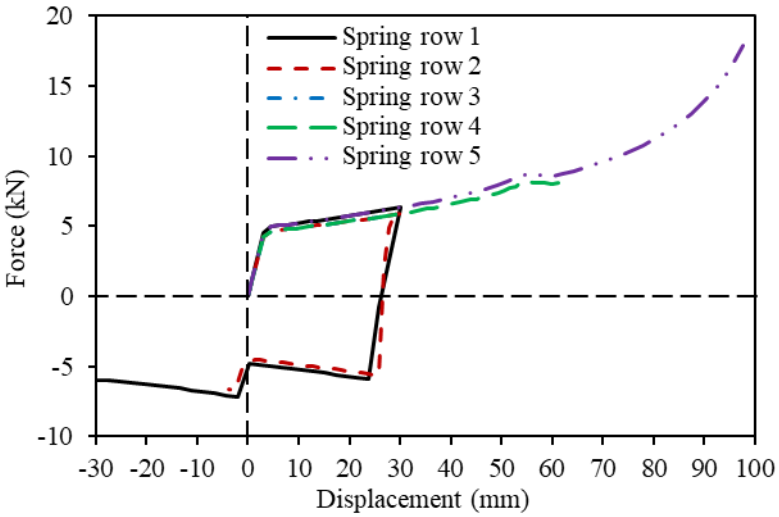

Figure 4-34. Force-displacement relationships of all spring rows in Load Case 1

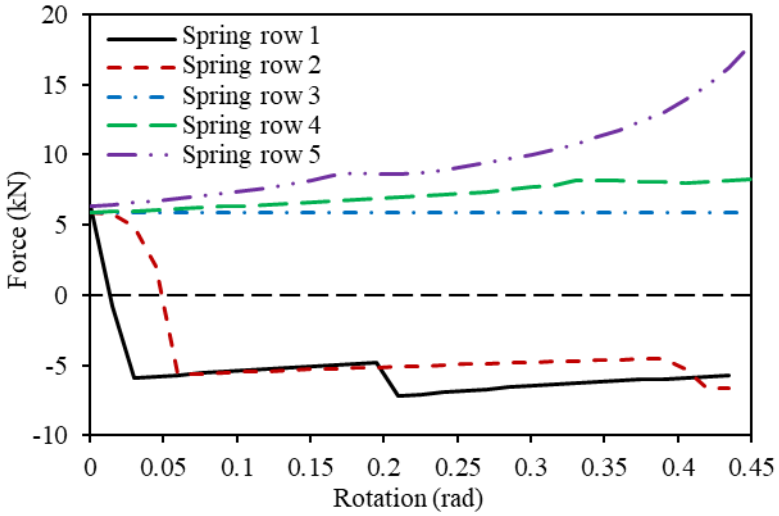

Figure 4-35. Force-rotation relationships of all spring rows in Load Case 1

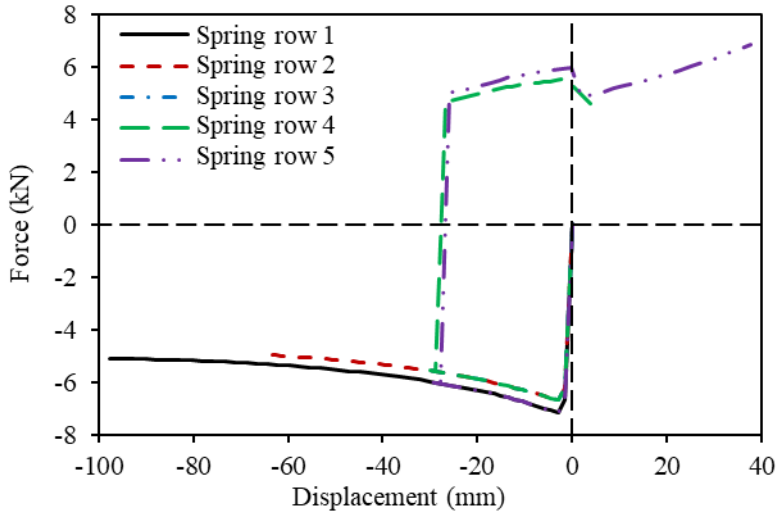

Figure 4-36. Force-displacement relationships of all spring rows in Load Case 2

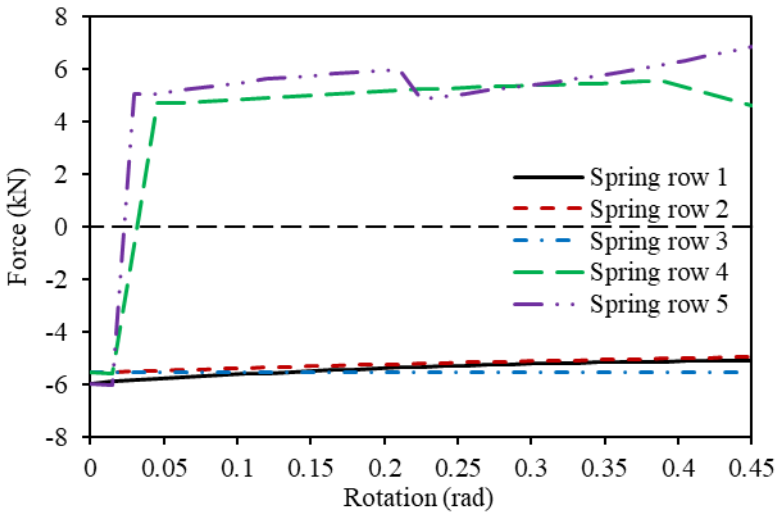

Figure 4-37. Force-rotation relationships of all spring rows in Load Case 2

The discrepancy between the moment-rotation curves of the component-based model and Abaqus is quite large, as shown in Figure 4-33. This discrepancy may be due to the fact that torsion of the semi-cylindrical section and the semi-circular section of the face-plate is ignored in the component-based model. The rotational behaviour of the entire connection consists of two actions, which are pulling/pushing of each spring row and torsion of the semi-cylindrical and semi-circular parts. However, it is very difficult to represent the torsional behaviour using an analytical model, since each bolt row is simultaneously subject to axial push/pull, as well as torsion. In the context of the moment necessary to apply a significant rotation to the beam-end, the moment generated by applying the same rotation to the connection is small, and so an exact model of aspects such as torsion of the connection section is not very important to this study. Deformation of two adjacent spring rows is only piecewise-compatible in the component-based model, which means that the horizontal shear force between adjacent spring rows is ignored. In Load Case 1, all spring rows experience pulling until 30mm, at which stage the rotation is applied. With the increase of rotation, spring rows 1 and 2 undergo unloading, push-back and pushing, as shown in Figure 4-34 and Figure 4-35. The reason for the sudden increase of compressive force in both Spring Rows 1 and 2 at around 0mm displacement is explained in Section 4.5.1, concerning pushing back from Stage 2 of pulling. Since Spring Row 3 is on the centre line of the connection, the applied rotation does not cause additional displacement to this row, and, therefore, the displacement of Spring Row 3 remains 30mm during rotation. Spring Rows 4 and 5 are always in tension (pulling)

because they are above the centre line of the connection. In Load Case 2, all the spring rows are subject to 30mm of compression (pushing) and then Spring Rows 4 and 5 switch to unloading, pull-back and finally pulling, as shown in Figure 4-36 and Figure 4-37. Spring Rows 1 and 2 are always under compression. Spring Row 3, on the connection centre line, maintains the compressive displacement of 30mm during rotation.

4.8. Chapter conclusion

This chapter has introduced an improved design version of the ductile connection, which aims to enhance its practical feasibility of design and ease of fabrication. The performance of the improved connection has been initially compared with that of the previous version using a sub-frame model. Five case studies have been carried out, in which the ductile connections are applied to sub-frames with different beam spans. The first analytical component-based model, including a face-plate component model and a model of the semi-circular ductile part, based on simple plastic theory, has been proposed. The second component-based model, including a FPSC component, in which the semi-cylindrical component and the face-plate component are considered to deform as a whole, has been also developed. The resulting curves of the two schemes of component-based model have been compared against one another, as well as against Abaqus simulations and experiments. Finally, two preliminary application examples have been conducted to investigate the performance of the proposed component-based model. The following conclusions can be drawn based on these studies:

- By comparing the axial force of the beam with the improved connection with that of the beam with the previous connection, it can be found that the improved version produced smaller axial thrust than the previous version, which indicates an enhanced ductility.
- The five case studies illustrate the design requirements of the ductile connection, and demonstrate the satisfactory deformation capacity of the ductile connection by comparing the axial forces generated in the beams with ductile connections with those of the beams with rigid connections.
- The ‘Reference point’ concept is adopted to describe the unloading behaviour of individual components, and this is developed to calculate the complete loading-

unloading-reloading behaviour of the ductile connection.

- The results from the second (FPSC) component-based model are more in line with the behaviour given by Abaqus than those from the first model. Therefore, the second component-based model will be incorporated into the software Vulcan in the following work aimed at facilitating global frame analysis for structural fire engineering design.
- There is some discrepancy between the moment-rotation curves of the component-based model and Abaqus simulations in the preliminary application examples, which is probably due to neglecting the torsion of the semi-cylindrical component parts of the component-based model. However, in a connection whose objective is to act essentially as non-moment-transmitting at ambient temperature and to permit a large amount of axial beam-end movement in fire, the moment resistance is more or less irrelevant, provided that it is low compared with the moment resistances of the connected members. In general, the two simple examples illustrate how different spring rows work in the process of connection deformation

5.

PERFORMANCE OF THE DUCTILE CONNECTION IN STEEL-FRAMED STRUCTURES

5.1. Chapter introduction

In order to simulate the complete behaviour of a structure in fire, from local instability to final collapse, Sun (Sun et al., 2012a, 2012b, Sun, 2012) developed a procedure which combined static and dynamic solvers to make full use of the advantages of each. In this way, Vulcan can use its static solver to simulate the static behaviour of the structure until instability occurs, at which stage the dynamic solver is activated to track the motion of the structure until stability is regained. Combining this with the parallel development of component-based connection models, Vulcan is capable of tracking the behaviour of connections from initial movement, through the fracture of individual components, to eventual failure.

This chapter aims to incorporate the component-based model of the ductile connection into Vulcan. The analytical model of bolt pull-out failure has been added to the component-based model. The tangent stiffness matrix derived by Block (2006) has been used to convert the component-based model of the ductile connection into a connection element, following the principles of the finite element method. A single beam model with these connections at each end has been modelled using both Vulcan and Abaqus, in order to establish whether the component-based model in Vulcan adequately represents the behaviour shown by a detailed FE analysis. Sub-frame models have also been created in order to compare the performance of the ductile connection with that of conventional connection types. Different types of connections are used in these sub-frame models including idealised rigid and pinned connections, and the commonly-used end-plate and web-cleat connection types. In order to model the web-cleat connection using Vulcan, the analytical model developed by Yu (2009d), has been implemented in the software in the same way as the new element. Parametric studies have been carried out, in order to optimize the performance of the ductile connection under the tensile axial forces generated by the eventual catenary action of unprotected beams at high temperatures. Five key parameters including the temperature of the connection, the inner radius of its semi-cylindrical section, the plate thickness, the bolt spacing and the connection material are selected. Finally, the static-dynamic solver has been used to simulate the progressive collapse of a three-storey three-bay plane frame using the ductile connections.

5.2. Incorporation of the component-based model into Vulcan

To integrate the component-based model, shown in Figure 5-1, of the connection into global frame analysis, the component-based model needs to be converted into a connection element and then incorporated into Vulcan. The component-based model proposed in the previous chapter includes the behaviour modes associated with fin-plate connections (bolt and plate shear and bearing), and those of the semi-cylindrical section (plastic bending and tensile fracture). However, the detailed Abaqus simulations in Section 3.6.2 show that bolt pull-out failure from the face-plate zone may be the most critical failure mode in practical designs. Therefore, a simplified model of bolt pull-out failure has been added to each spring row (bolt row) of the component-based model as a separate component, before converting the whole component-based model into a connection element and incorporating it into Vulcan.

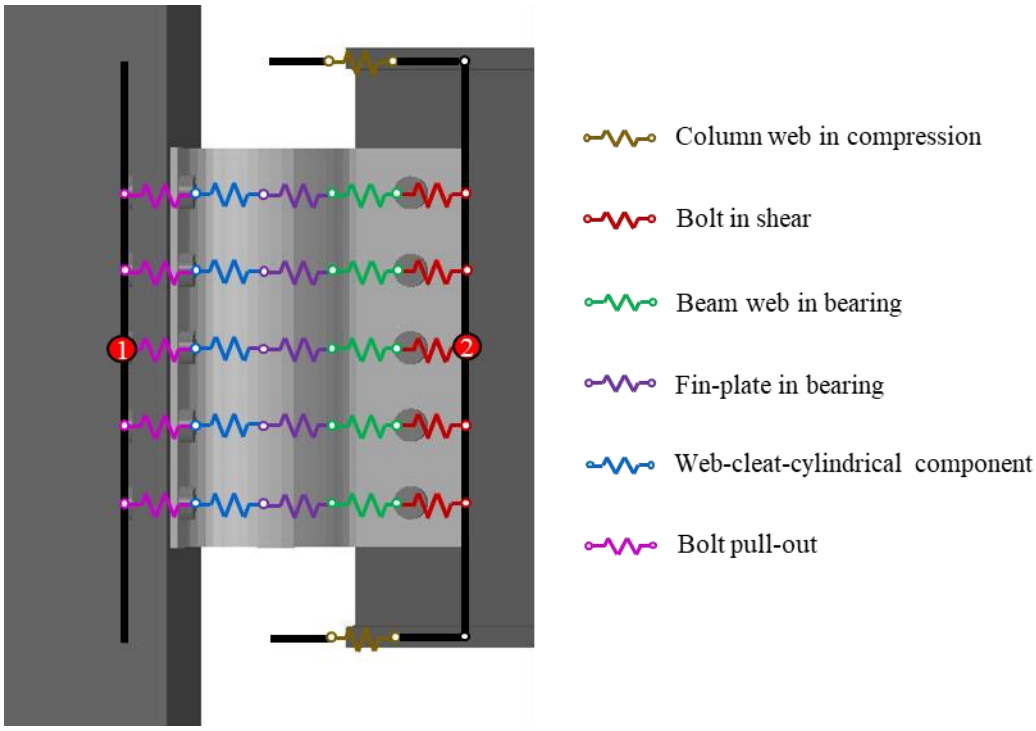

Figure 5-1. Component-based model of the ductile connection

5.2.1. Analytical model of bolt pull-out failure

Dong (2016) developed a simplified 'plastic cone' model to calculate the local deformation of steel plate around a bolt hole during pull-out, as shown in Figure 5-2. According to the virtual work principle, the external work done by the bolt tensile force F in a vertical displacement

increment $d\delta$, should be equal to the increment of internal absorbed work dW_{total}, which includes increments of the plastic work in the circular plastic hinge $dW_{circular}$ and the plastic work induced by circumferential stretching of the cone wall dW_{strip} (Equation (5-1)). The contact between the bolt head and steel plate in the 'cone' model is considered by determining the deformation of the cone wall according to the position and diameter of the bolt head, as shown in Figure 5-2. However, the proposed 'cone' model is just a simplified way of incorporating bolt pull-out failure into the component-based model. The effects of stress concentration, cracking of the steel plate around the bolt hole and the complex contact between the edge of the bolt head and the steel plate when the steel plate is under partial bending and tension are neglected. Equations (5-2) - (5-7) derived by Dong are adapted here to generate the F-D curve of the bolt pull-out component. The plastic work induced by stretching of the cone wall at a given bolt head movement δ can be calculated using Equation (5-2) according to the relationship between ΔL_{strip}, ΔL_y and ΔL_u. The rotation θ of the cone wall relative to its original position is calculated using Equation (5-3) and is shown in Figure 5-2. ΔL_{strip} is the average elongation of a strip of the cone wall circumference, and is given in Equation (5-4). ΔL_y and ΔL_u are respectively the elongation of the cone wall under yield and ultimate load, which can be calculated using Equation (5-5). Equations (5-6) and (5-7) are respectively used to calculate the increment of internal absorbed work dW_{total}, the maximum movement of the bolt head $\delta_{\max}$ and the maximum rotation of the cone wall $\theta_{\max}$. The F-D curves of the other components are obtained using the analytical models developed in the previous chapters. The revised component-based model of the ductile connection is shown in Figure 5-1. The gaps included in the compression spring rows at the upper and lower beam flanges represent the maximum clearance between these flanges and the column-face before contact occurs. Since the vertical shear behaviour has not been taken into consideration, the component-based model is assumed to be rigid in the vertical direction. The loading and unloading behaviour have been incorporated into the individual component characteristics, to enable simulation of the complicated loading conditions experienced by the connection under fire conditions.

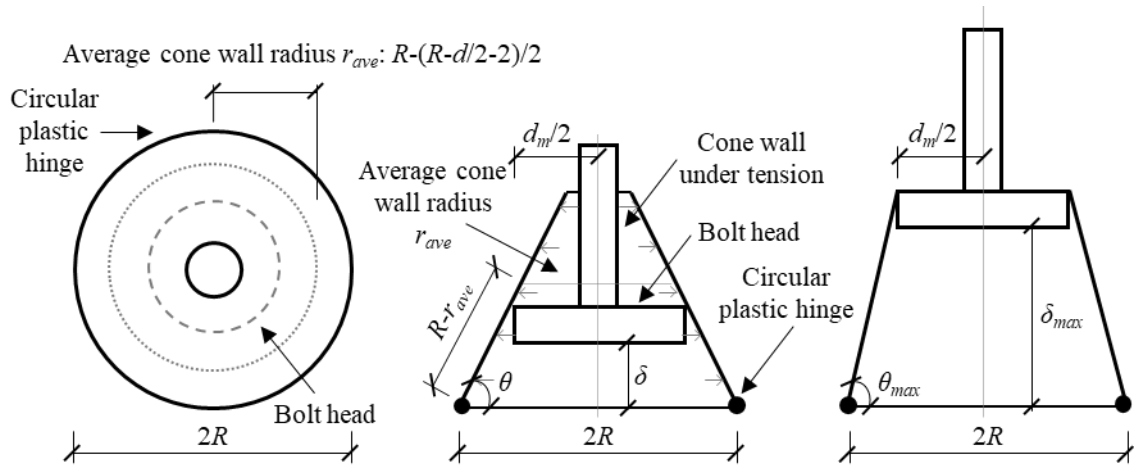

Figure 5-2. Simplified 'cone' model

$$F = dW_{total} / d\delta = d\left(W_{strip} + W_{circular}\right) / d\delta \tag{5-1}$$

$$dW_{strip} = \begin{cases} \dfrac{EA}{L_{strip}} \Delta L_{strip} \cdot d\left(\Delta L_{strip}\right) & \Delta L_{strip} \le \Delta L_y \\ f_y A \cdot d\left(\Delta L_{strip}\right) + \dfrac{E_T A}{L_{strip}} \left(\Delta L_{strip} - \Delta L_y\right) \cdot d\left(\Delta L_{strip}\right) & \Delta L_y < \Delta L_{strip} \le \Delta L_u \\ f_u A \cdot d\left(\Delta L_{strip}\right) & \Delta L_{strip} > \Delta L_u \end{cases} \tag{5-2}$$

$$\theta = \arctan\left(\frac{\delta + t_b}{R - d_m / 2}\right), \quad d\theta = \frac{d\delta}{\left[1 + \left(\dfrac{\delta + t_b}{R - d_m / 2}\right)^2\right]\left(R - d_m / 2\right)} \tag{5-3}$$

$$\Delta L_{strip} = 2\pi\left[R - \left(R - r_{ave}\right)\cos\theta\right] - L_{strip}, \; d\Delta L_{strip} = 2\pi\left(R - r_{ave}\right)\sin\theta \cdot d\theta \tag{5-4}$$

$$\Delta L_y = \frac{f_y L_{strip}}{E}, \; \Delta L_u = \frac{f_y L_{strip}}{E} + \frac{(f_u - f_y) L_{strip}}{E_T} \tag{5-5}$$

$$dW_{circular} = M_p \times 2\pi R \times d\theta = \left(\frac{f_y t^2}{4}\right) \frac{d\delta}{\left[1 + \left(\dfrac{\delta + t_b}{R - d_m / 2}\right)^2\right]\left(R - d_m / 2\right)} \tag{5-6}$$

$$\theta_{\max} = \arccos\left((R - d_m / 2) / (R - d / 2 - 2)\right), \; \delta_{\max} = (R - d / 2 - 2)\sin\theta_{\max} \tag{5-7}$$

in which d is the diameter of the bolt shank, $r_{ave} = R - \left[R - \left(d / 2 + 2\right)\right] / 2$ is the average radius of the cone wall, $L_{strip} = 2\pi r_{ave}$ is the average circumference of the cone wall, A is the average cross-sectional area of the cone wall, t is the thickness of the cone wall, and t_b is the thickness of

the bolt head.

5.2.2. Incorporation into Vulcan

The existing subroutine SEMIJO of Vulcan was originally specified for simple spring elements, including rigid, pinned and semi-rigid connections. This subroutine passes the incremental displacement vector to the connection element and returns the tangent stiffness matrix and force vector to the main program. The properties of the ductile connection element developed in this research are accessible to this subroutine, which was also used by Block (2006) and Dong (2016) for their connection elements. Following the principles of the finite element method, the tangent stiffness matrix derived by Block (2006), represented by Equations (5-8) and (5-9), is adopted here to convert the component-based model of the ductile connection into a connection element. The symbols *i* and *j* in Equation (5-8) represent the two end nodes of the connection element.

$$K_{Connection} = \begin{array}{c} \\ i \\ \\ \\ \\ \\ \\ \\ \\ \\ \\ j \\ \\ \\ \\ \\ \\ \end{array} \begin{array}{c} \begin{array}{cccccccccccc} i & & & & & & j & & & & & \end{array} \\ \begin{array}{cccccccccccc} U & V & W & R_X & R_Y & R_Z & U & V & W & R_X & R_Y & R_Z \end{array} \\ \begin{pmatrix} K_{11} & 0 & 0 & 0 & K_{15} & 0 & -K_{11} & 0 & 0 & 0 & -K_{15} & 0 \\ 0 & \infty & 0 & 0 & 0 & 0 & 0 & -\infty & 0 & 0 & 0 & 0 \\ 0 & 0 & K_{33} & 0 & 0 & 0 & 0 & 0 & -K_{33} & 0 & 0 & 0 \\ 0 & 0 & 0 & \infty & 0 & 0 & 0 & 0 & 0 & -\infty & 0 & 0 \\ K_{51} & 0 & 0 & 0 & K_{55} & 0 & -K_{51} & 0 & 0 & 0 & -K_{55} & 0 \\ 0 & 0 & 0 & 0 & 0 & \infty & 0 & 0 & 0 & 0 & 0 & -\infty \\ -K_{11} & 0 & 0 & 0 & -K_{15} & 0 & K_{11} & 0 & 0 & 0 & K_{15} & 0 \\ 0 & -\infty & 0 & 0 & 0 & 0 & 0 & \infty & 0 & 0 & 0 & 0 \\ 0 & 0 & -K_{33} & 0 & 0 & 0 & 0 & 0 & K_{33} & 0 & 0 & 0 \\ 0 & 0 & 0 & -\infty & 0 & 0 & 0 & 0 & 0 & \infty & 0 & 0 \\ -K_{51} & 0 & 0 & 0 & -K_{55} & 0 & K_{51} & 0 & 0 & 0 & K_{55} & 0 \\ 0 & 0 & 0 & 0 & 0 & -\infty & 0 & 0 & 0 & 0 & 0 & \infty \end{pmatrix} \end{array} \begin{array}{c} \\ \\ \\ \\ \\ \\ \\ \\ \\ \\ \\ \\ \\ \\ \\ \\ \\ \\ \end{array} \begin{array}{c} \\ \\ U \\ V \\ W \\ R_X \\ R_Y \\ R_Z \\ U \\ V \\ W \\ R_X \\ R_Y \\ R_Z \end{array}$$

(5-8)

in which

$$K_{11} = \sum_{i=1}^{n} k_{T,i} + \sum_{i=1}^{2} k_{C,i} \qquad K_{15} = K_{51} = \sum_{i=1}^{n} k_{T,i} \cdot l_{T,i} + \sum_{i=1}^{2} k_{C,i} \cdot l_{C,i}$$

$$K_{33} = k_s \qquad K_{55} = \sum_{i=1}^{n} k_{T,i} \cdot l_{T,i}^2 + \sum_{i=1}^{2} k_{C,i} \cdot l_{C,i}^2 \tag{5-9}$$

in which the subscripts $_T$, $_C$ and $_S$ represent the springs working in tension, compression and shear

respectively, and n is the number of bolt rows. $k_{T,i}$ / $k_{C,i}$ represents the stiffness of ith tension/compression spring row. $l_{T,i}$ $l_{C,i}$ represents the lever arm of the ith tension/compression spring row to the centre of rotation.

During the calculation process, Vulcan provides an incremental displacement of the connection element based on the previous step's stiffness, and then the tangent stiffness matrix is recalculated and the incremental force vector is updated. The updated tangent stiffness matrix and the incremental force vector are returned back to the main program. A convergence check based on out-of-balance forces is carried out to determine whether either the next load or temperature step will be applied to the model or the current load step should be reduced until the convergence criteria are satisfied. As shown in Equation (5-8), the out-of-plane and torsional DoFs are assumed to be connected rigidly and without interaction, since they are in any case of relatively minor importance in steel structures.

5.3. Validation of the connection element against Abaqus

In order to verify whether the connection element in Vulcan adequately represents the behaviour shown by a detailed FE analysis, a single beam (Figure 5-3), with ductile connections at both ends, is modelled using both Vulcan and Abaqus.

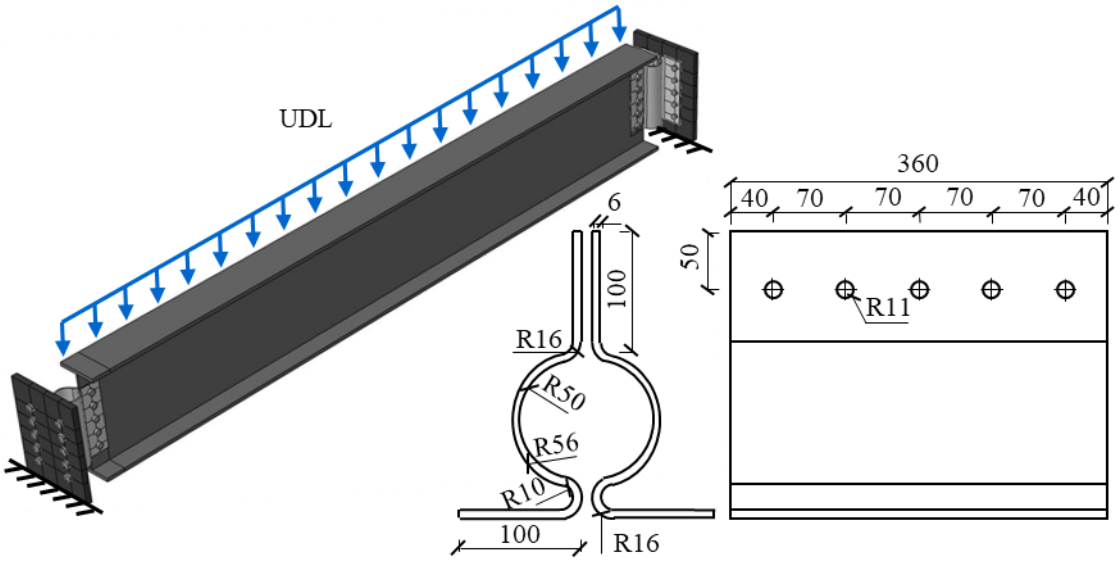

Figure 5-3. Single beam model

It is difficult to verify the single-beam model with connections at the beam ends. Therefore, the

verifications of the beam and connection parts of the model were conducted separately. The connection part of the model has already been validated in previous chapters against push/pull experiments on model-scale specimens with good agreement between the test and modelling results. The beam part of the model is checked against hand calculations for a simply supported beam under increasing distributed loading at different temperatures (20°C and 500°C). The comparison of results is shown in Figure 5-4, indicating that the Abaqus results correlate well with the hand calculations before inelasticity occurs.

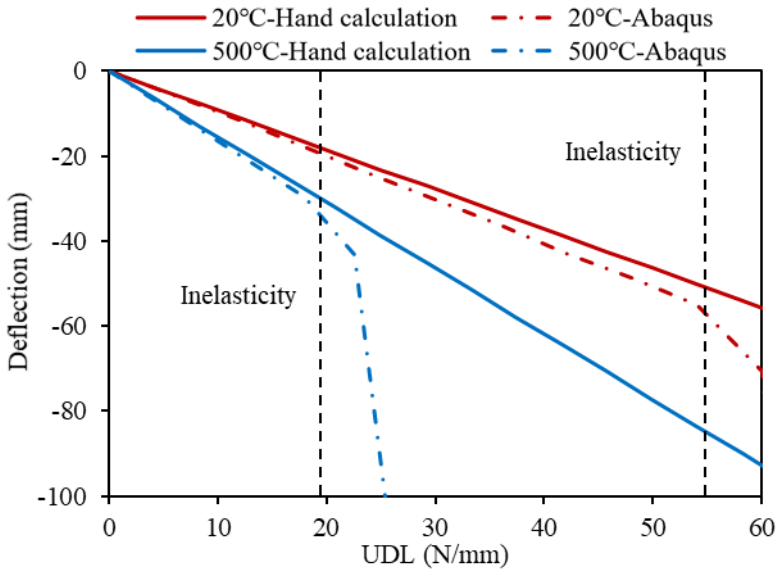

Figure 5-4. Comparison between Abaqus and hand calculation results

A uniformly distributed line load of 42.67 kN/m is applied on the beam model and the load ratio of 0.4 is adopted for all the cases with respect to a simply supported beam. It is assumed that there are five cases in total, as listed in Table 5-1. Comparisons between results from Vulcan and Abaqus are shown in Figure 5-5 - Figure 5-9. As can be seen from Figure 5-5 - Figure 5-7 that the changes of beam span and beam section have little influence on the compressive mid-span beam axial force during the low-temperature stage before 600°C, which is contrary to the results obtained by adopting traditional connection types (as shown in Table 4-3). This is due to the excellent axial deformability of the ductile connection, which can accommodate the thermal expansion of connected beam. It is obvious that the ultimate failure temperature of the connection decreases with the increase of connection temperature relative to that of the beam (Figure 5-6, Figure 5-8 and Figure 5-9), as expected. As shown in Figure 5-5 (a) - Figure 5-9 (a), the mid-span

deflection of the Vulcan model increases rapidly after 500℃, until the slope of the deflection-temperature curve is nearly vertical, indicating the failure of the connection by bolt pull-out. The connected beam then detaches from the column and loses its axial constraint. This is shown by the rapid decreases of the axial tensile forces in Figure 5-5 (b) - Figure 5-9 (b). The failure temperatures predicted by Abaqus in Cases 2 and 5 are higher than those predicted by Vulcan. This is because fracture criteria are not set in the Abaqus models, resulting in unreasonably large deformation rather than fracture. The failure modes of the five cases modelled in Vulcan are all bolt pull-out failures, which are consistent with the simulation results of Abaqus, as shown in Figure 5-10. Except for the final failure stage, the deflection and the axial force predicted by Vulcan are very close to those given by Abaqus, indicating that the ductile connection element adequately represents the behaviour of the connection.

Table 5-1. Parameters for different cases

	Beam span	Beam section	Connection temperature
Case 1	6m	UKB 457×152×82	$T_{connection} = 50\% T_{beam}$
Case 2	7.5m	UKB 533×210×109	$T_{connection} = 50\% T_{beam}$
Case 3	9m	UKB 533×312×151	$T_{connection} = 50\% T_{beam}$
Case 4	7.5m	UKB 533×210×109	20℃
Case 5	7.5m	UKB 533×210×109	$T_{connection} = 100\% T_{beam}$

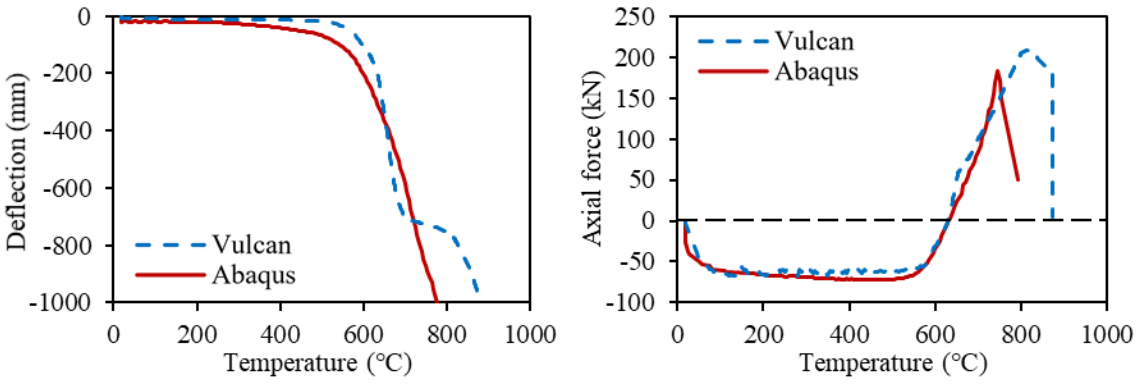

(a) Mid-span deflection of beam (b) Mid-span axial force of beam

Figure 5-5. Comparison results of Case 1

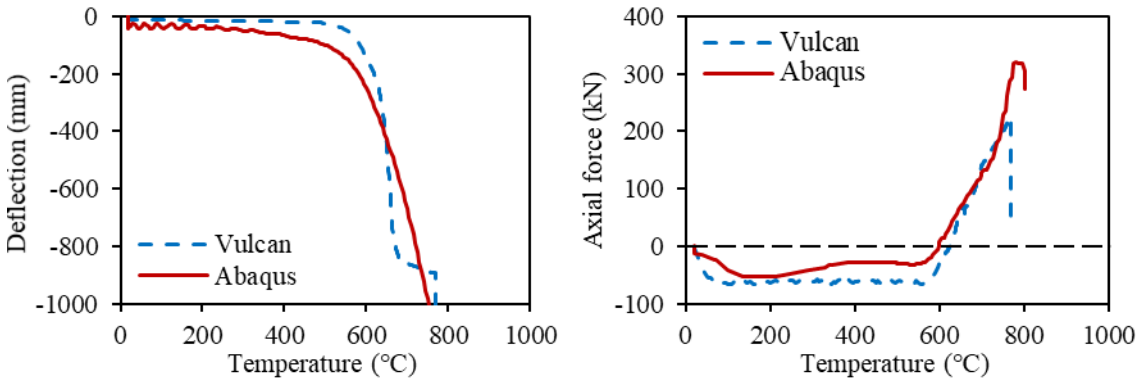

(a) Mid-span deflection of beam (b) Mid-span axial force of beam

Figure 5-6. Comparison results of Case 2

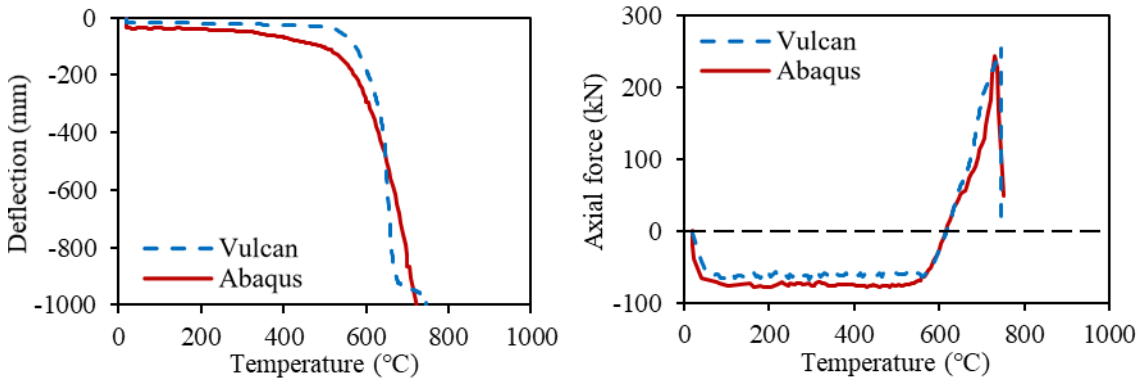

(a) Mid-span deflection of beam (b) Mid-span axial force of beam

Figure 5-7. Comparison results of Case 3

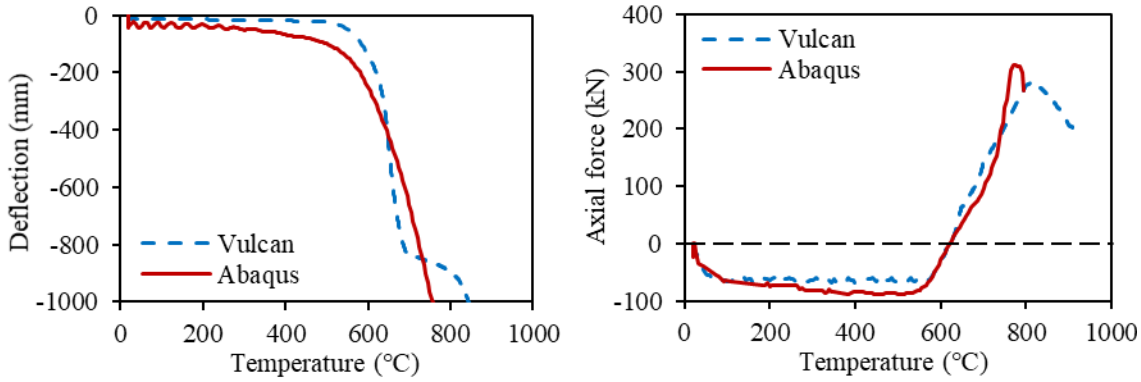

(a) Mid-span deflection of beam (b) Mid-span axial force of beam

Figure 5-8. Comparison results of Case 4

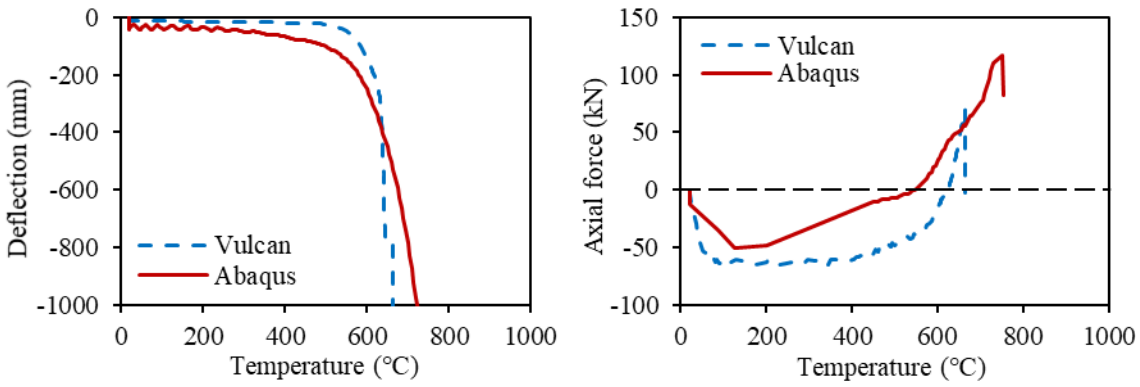

(a) Mid-span deflection of beam (b) Mid-span axial force of beam

Figure 5-9. Comparison results of Case 5

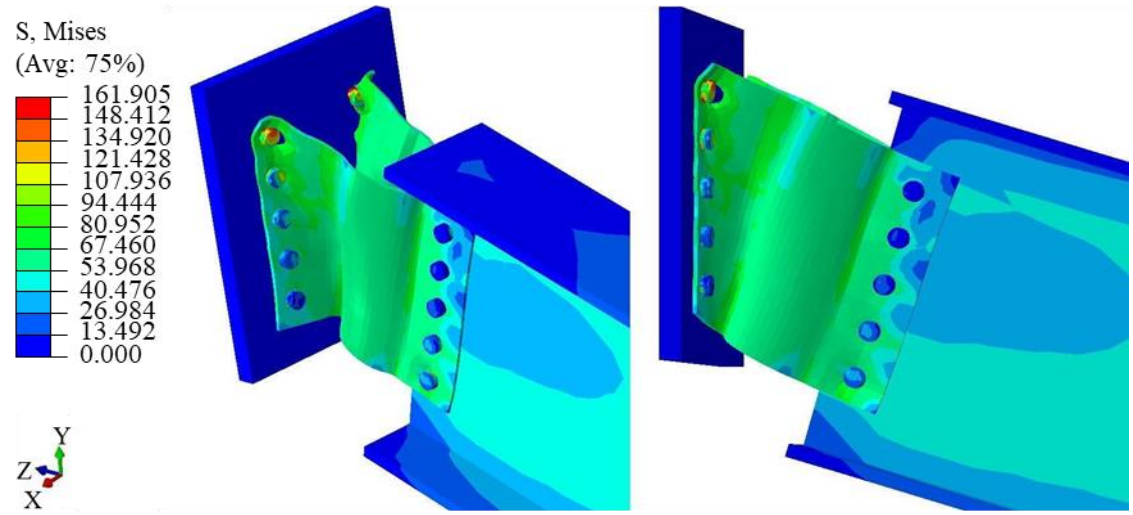

Figure 5-10. Bolt pull-out failure

Figure 5-11 (a), Figure 5-12 and Figure 5-13 (a) show the force-displacement curves of each spring row for Cases 2, 4 and 5. It can be seen that each spring row will undergo different stages as the connection deforms; pushing, unloading of pushing, pulling-back and finally pulling. During the pulling-back stage, a spring row is pulled back to its original state after compressive deformation. In Case 5, since the temperature of the connection is equal to that of the connected beam, the temperature of the connection reaches nearly 600℃ before it enters the pulling-back stage. The mechanical properties of steel degrade rapidly after 400℃, which leads to the decrease of compressive forces shown in Figure 5-13 (a). The force-temperature curves of each spring row in Cases 2 and 5 are shown in Figure 5-11 (b) and Figure 5-13 (b). As expected, the evolution of the axial force of each spring row almost corresponds to the beam's axial force development. In

the initial stage of heating, each spring row is subject to compressive force, due to restraint of the thermal expansion of the connected beam. When the temperature of beam exceeds 600°C, it enters the catenary action phase, and the force of all spring rows becomes tensile. After the deformation limit is reached, the tensile force of each spring row increases rapidly in a pure tension mechanism. Since the failure temperature of the connection in Case 2, which is around 760°C, is higher than that in Case 5, which is around 660°C, the ultimate tensile force of each spring row in Case 2 is higher than that of the corresponding row in Case 5.

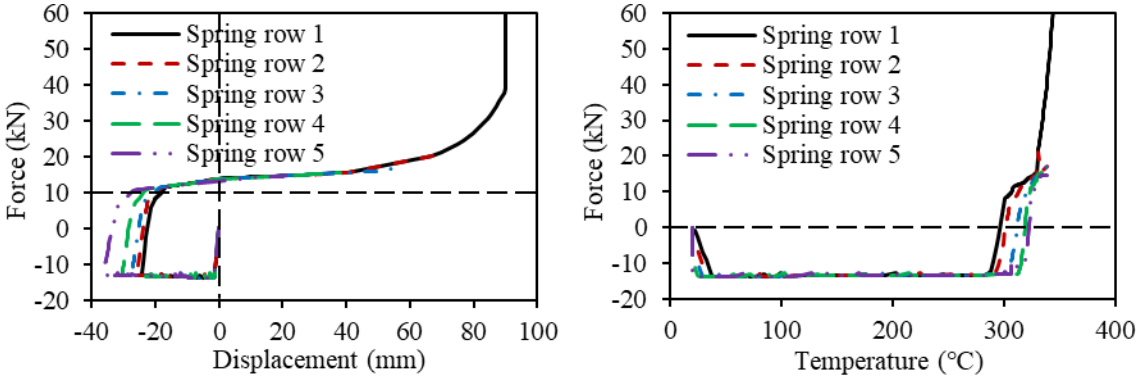

(a) Force-displacement curves (b) Force-temperature curves

Figure 5-11. Results for each spring row of the novel connection in Case 2

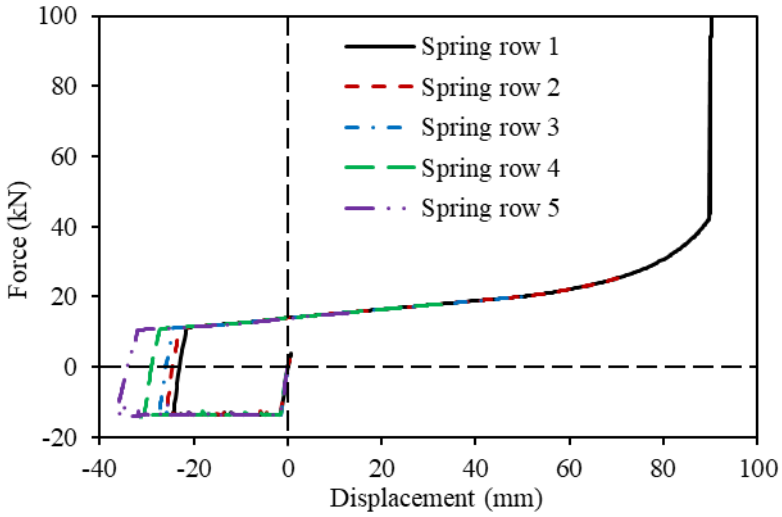

Figure 5-12. Force-displacement curves of each spring row of the novel connection in Case 4

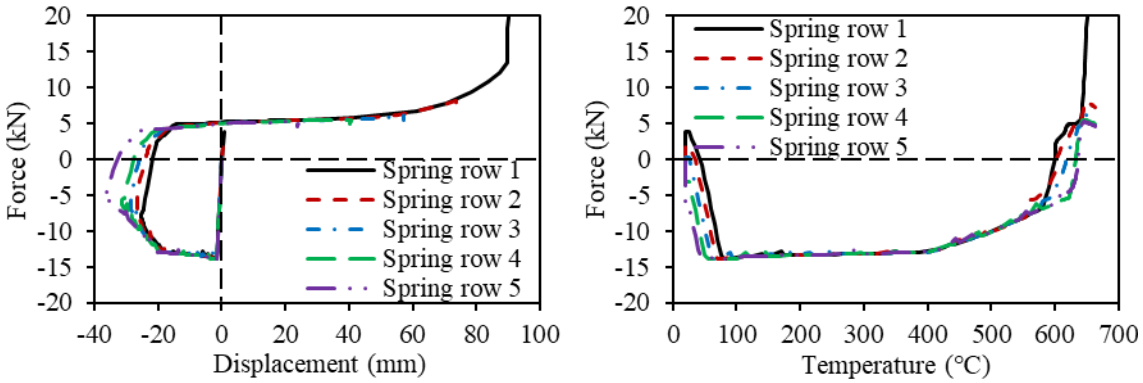

(a) Force-displacement curves (b) Force-temperature curves

Figure 5-13. Results for each spring row of the novel connection in Case 5

5.4. Comparison of the ductile connection with conventional connection types

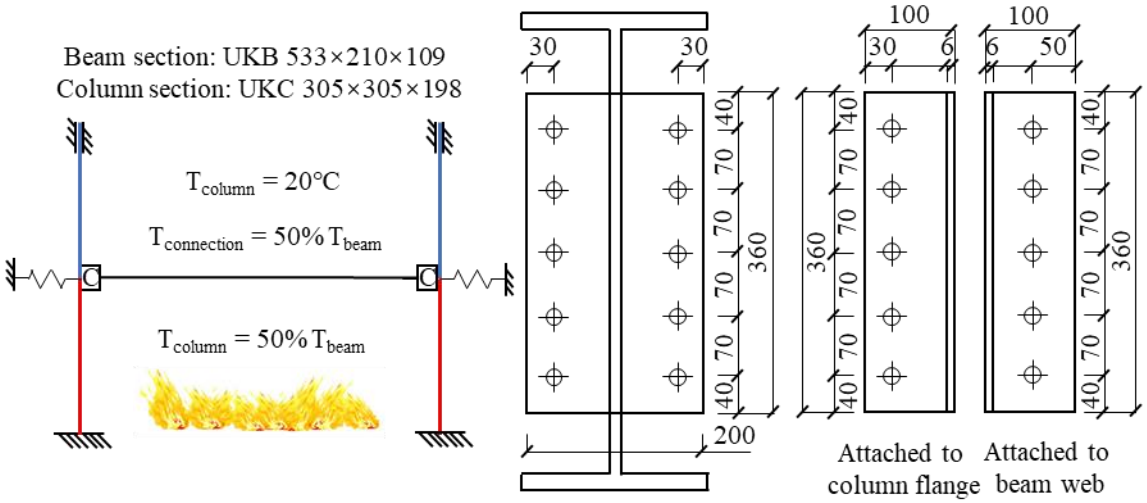

(a) Sub-frame model (b) End-plate connection (c) Web-cleat connection

Figure 5-14. The sub-frame model

The motive behind introducing the ductile connection is to enhance the ductility of connections, so as to accommodate the large deformations generated by the connected beams as their temperatures rise, in order to improve their robustness in fire. To compare the performance of this new connection type with that of conventional connection types, a sub-frame model, shown in Figure 5-14 (a), is used. It is assumed that the connections and columns in the first floor are protected to the same level, and that 50% is a fairly typical ratio of the protected column temperature to the unprotected beam temperature. Therefore, the column and connection temperatures are both set to 50% of the unprotected beam's temperature, and the standard fire

curve is used. Different types of connection have been used in this sub-frame model, including idealised rigid and pinned connections, as well as the commonly-used end-plate and web-cleat connections. An end-plate connection element has already been incorporated into Vulcan by Block (2006) and Dong (2016). Although the Structural Fire Engineering Research Group at the University of Sheffield has done some research on web-cleat connections, including experiments (Yu et al., 2009c) and the derivation of analytical models (Yu et al., 2009d), the web-cleat connection had not yet been incorporated into Vulcan. The web-cleat connection will be implemented in Vulcan in this chapter.

5.4.1. Integration of web-cleat connection element into Vulcan

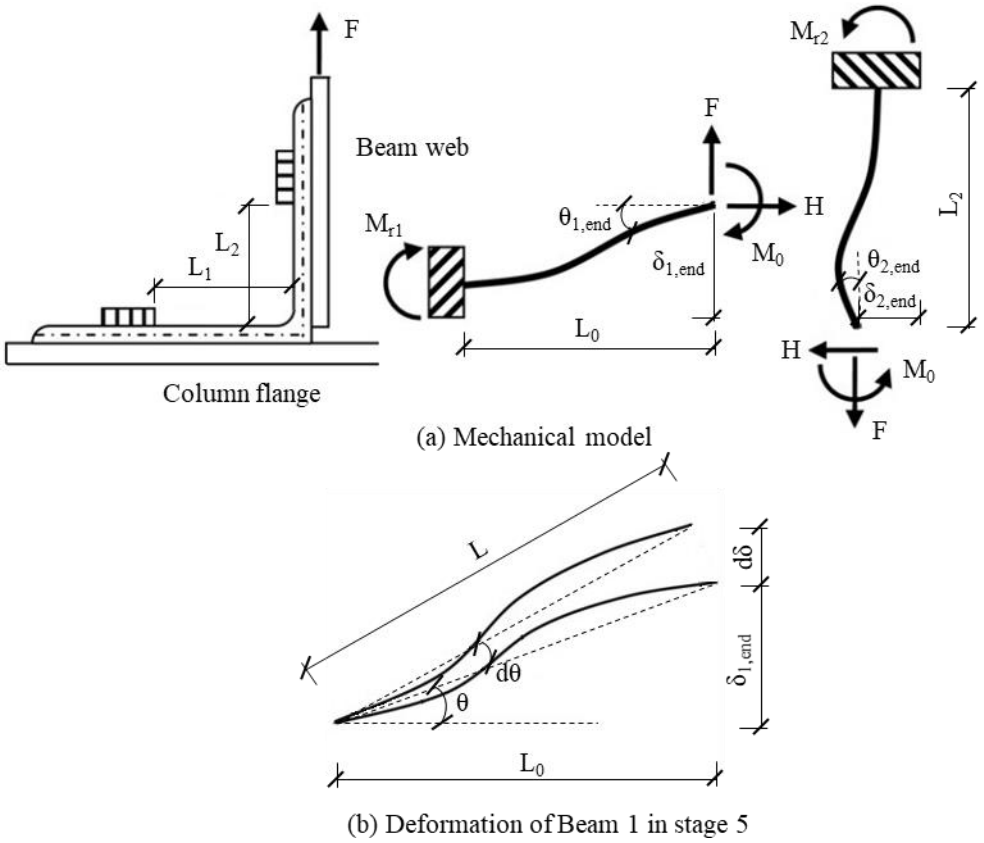

Figure 5-15. The model of web-cleat connection

During the process of developing the mechanical model of a web-cleat connection, Yu (2009d) made three assumptions: (i) the two legs of the web-cleat are considered as two orthogonal cantilever beams connected at the middle of the heel with concentrated forces at their ends; (ii) the bolts attached to the column flange can provide full fixity; and (iii) the bolts connected to the

beam web allow movement in the plane of the web, as shown in Figure 5-15 (a). Plastic hinges are formed at the ends of Beams 1 and 2. Depending on the relative relationships between the moments M_{r1} and M_{r2} (Figure 5-15 (a)) at the beam ends with M_y (yield moment capacity of the plastic hinge) and M_u (ultimate moment capacity of the plastic hinge), the state of the plastic hinge can be divided into five stages. The forces and deformations of the web-cleat are then derived differently depending on the current stage.

Stage 1: ($M_{r1} \leq M_y$)

$$M_y = \frac{wt^2 f_y}{4},\ M_u = \frac{wt^2 f_u}{4} \tag{5-10}$$

$$L_1 = L_0 + \frac{1}{2(EI)^2}\left[\frac{1}{20}F^2 L_0^5 - \frac{F}{4}(FL_0 - M_0)L_0^4 + \frac{1}{3}(FL_0 - M_0)^2 L_0^3\right] \tag{5-11}$$

$$M_0 = \frac{(L_1 - L_0)EI + FL_0^2 L_2 / 3}{L_2^2 / 6 + 2L_0 L_2 / 3} \tag{5-12}$$

$$\delta_{1,end} = \frac{FL_0^3 / 3 - M_0 L_0^2 / 2}{EI} \tag{5-13}$$

in which w and t are respectively the effective width and the thickness of the web-cleat. The meanings of the other parameters in these equations are shown in Figure 5-15 (a). At any applied external force F, L_0 can be found iteratively after substituting Equation (5-12) into Equation (5-11). Once L_0 is obtained, M_0 and the vertical displacement $\delta_{1,end}$ at the end of Beam 1 can be obtained from Equations (5-12) and (5-13), respectively.

Stage 2: ($M_y < M_{r1} \leq M_u$ and $M_0 \leq M_y$)

At this stage, the external force F increases by a small amount $\triangle F$ in each step, and M_0 is used as the controlling incremental parameter. The value of L_0 from the previous step is used as the initial value for each step; it is then updated at the end of the step using Equation (5-17). C_1 is a variable used to simplify Equation (5-17), and is calculated using Equation (5-16). Once F, C_1 and L_0 are known, the vertical deformation $\delta_{1,end}$ can be obtained using Equation (5-18).

$$H = \frac{3EI(L_1 - L_0) + 3M_0 L_2^2 / 2}{L_2^3} \tag{5-14}$$

$$F = \frac{M_0 + M_y - HM_0 L_2^2 / (2EI) + (K_r + HL_0)\left[M_0(L_0 + L_2) - HL_2^2 / 2\right] / (EI)}{L_0 - HL_0^3 / (3EI) + L_0^2 (K_r + HL_0) / (2EI)} \tag{5-15}$$

$$C_1 = M_0(L_0 + L_2) - \frac{1}{2}FL_0^2 - \frac{1}{2}HL_2^2 \tag{5-16}$$

$$L_1 - L_0 = \frac{2F^2L_0^5/15 - 5FM_0L_0^4/12 + (M_0^2 + 2FC_1)L_0^3/3 - M_0C_1L_0^2 + C_1^2L_0}{2(EI)^2} \tag{5-17}$$

$$\delta_{1,end} = \frac{FL_0^3/3 - M_0L_0^2/2 + C_1L_0}{EI} \tag{5-18}$$

Stage 3: ($M_y < M_{r1} \leq M_u$ and $M_y < M_0 \leq M_u$)

In this stage, the two cantilever beams begin to rotate relative to each other, once their end moments have reached their yield values. H and L_0 are still calculated using Equations (5-14) and (5-17), respectively. F and C_1 are obtained from Equations (5-19) and (5-20), respectively. Once these parameters are updated, the vertical deformation $\delta_{1,end}$ can be obtained from Equation (5-18).

$$F = \frac{(M_0 + M_y)EI - HM_0L_2^2/2 + (K_r + HL_0)\left[2(M_0 - M_y)EI/K_r - HL_2^2/2 + M_0(L_0 + L_2)\right]}{EIL_0 - HL_0^3/6 + K_rL_0^2/2} \tag{5-19}$$

$$C_1 = 2(M_0 - M_y)EI/K_r - \frac{1}{2}FL_0^2 - \frac{1}{2}HL_2^2 + M_0(L_0 + L_2) \tag{5-20}$$

Stage 4: ($M_{r1} = M_u$ and $M_y < M_0 \leq M_u$)

In this stage, F and C_1 are updated using Equations (5-22) and (5-23), respectively, and L_0 is still iteratively calculated using Equation (5-17). The vertical deformation $\delta_{1,end}$ can be obtained from Equation (5-21).

$$\delta_{1,end} = \frac{2(M_0 - M_y)EIL_0/K_r - M_uL_0^2/6 + M_0(L_0^2/3 + L_0L_2) - HL_0L_2^2/2}{EI + HL_0^2/6} \tag{5-21}$$

$$F = (M_U + M_0 + H\delta)/L_0 \tag{5-22}$$

$$C_1 = \left(EI\delta_{1,end} - FL_0^3/3 + M_0L_0^2/2\right)/L_0 \tag{5-23}$$

Stage 5: ($M_{r1} = M_u$ and $M_0 = M_u$)

In this stage, both ends of Beam 1 have reached their ultimate moment capacities, and therefore Beam 1 actually rotates as a 'link', as shown in Figure 5-15 (b). The deformation at the end of Beam 1 can be calculated using Equation (5-24).

$$\delta_{1,end} = \delta_{1,end} + Ld\theta\cos\theta \tag{5-24}$$

The mechanical model of a web-cleat connection represented by Equations (5-10) - (5-24) has been incorporated into Vulcan following the same methodology as for the ductile connection element. Equations (5-8) and (5-9) are used to calculate the tangent stiffness matrix of the web-cleat connection element. The Vulcan web-cleat connection element was verified against Abaqus using a single beam model with web-cleat connections at both ends. Temperatures of the web-cleat connections were assumed to be half of that of the connected beam. The mid-span deflection and the axial force of the beam, as obtained by Vulcan and Abaqus, are compared in Figure 5-16. It can be seen from the figure that Vulcan results have a good correlation with Abaqus results before 500 ℃. After that, the beam of the Vulcan model deflects more than that of the Abaqus model (Figure 5-16 (a)). In addition, the compressive connection axial force of the Vulcan model decreases at a higher rate and eventually becomes tensile at a lower temperature than those predicted by the Abaqus model (Figure 5-16 (b)). This is due to the fact that the analytical model of the web-cleat connection is of lower stiffness in plastic phase than that of the detailed FE model (Yu et al., 2009d). Although the comparison is not perfect, given that the component-based modelling is a simplified method, it is sufficient to be used for large-scale frame analysis in fire.

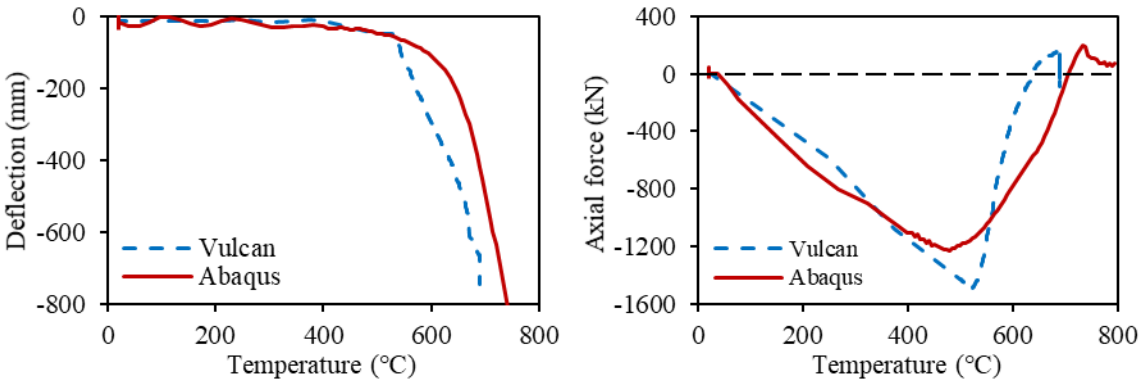

(a) Mid-span deflection of beam (b) Mid-span axial force of beam

Figure 5-16. Comparison results to validate the web-cleat connection element

5.4.2. Comparison of the ductile connection with other connection types

After incorporating the web-cleat connection element in Vulcan, sub-frame models of the geometry shown in Figure 5-14 (a) were created, using different types of connection. It is assumed that fire occurs on the first floor of the sub-frame, and that temperatures of the lower columns and connections are half of that of the beam, whereas the upper columns stay at ambient temperature.

Five different types of connection were selected, including the ductile connection, idealised rigid and pinned connections, and conventional end-plate and web-cleat connections. The dimensions of the ductile, end-plate and web-cleat connections (the latter two designed according to Eurocode 3 Part 1-1 (CEN, 2005a)) are shown in Figure 5-3, Figure 5-14 (b) and Figure 5-14 (c), respectively. It should be noted that the end-plate and web-cleat connections have the same key dimensions as the ductile connection, including the thickness, the width and the depth of the plate, as well as their bolt spacing, to ensure comparability. The behaviour of the beam using these different end connections is compared in Figure 5-17 to Figure 5-19.

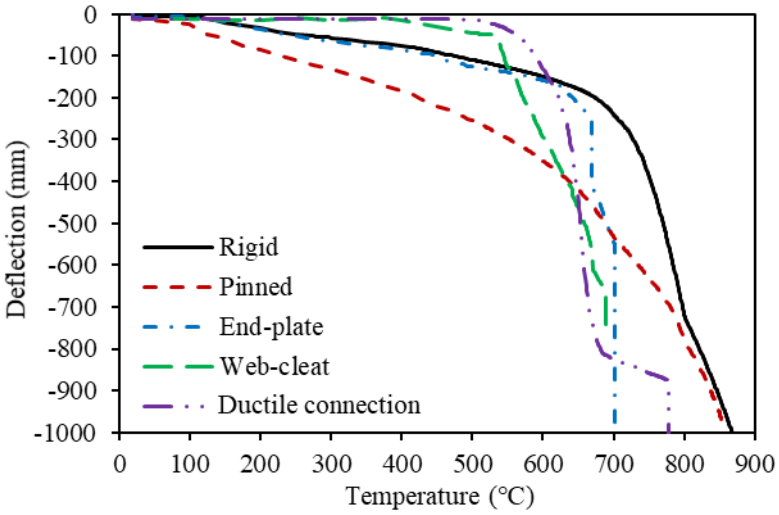

Figure 5-17. Mid-span deflection of beams with various end connections

As shown in Figure 5-17, the mid-span deflection of the beam with the ductile connections is very close to that of the beam with web-cleat connections. The rotations at the beam ends with the ductile connections are much higher than those with end-plate and web-cleat connections (Figure 5-18). The axial force generated in the beam with the ductile connections is very significantly reduced compared to those with all the other connection types, as shown in Figure 5-19. These phenomena indicate that the ductile connection provides much higher axial and rotational ductilities, which successfully accommodate the deformations generated by the connected beams as their temperatures rise. As part of this process, these connections are instrumental in greatly reducing the axial forces to which the surrounding structure is subjected. The failure temperature of the ductile connection under the tensile axial forces generated by the eventual catenary action of the heated beams at high temperatures is much higher than that of end-plate and web-cleat connections. This performance could be further improved by optimizing the design of the ductile

connection, which will be described in the next section.

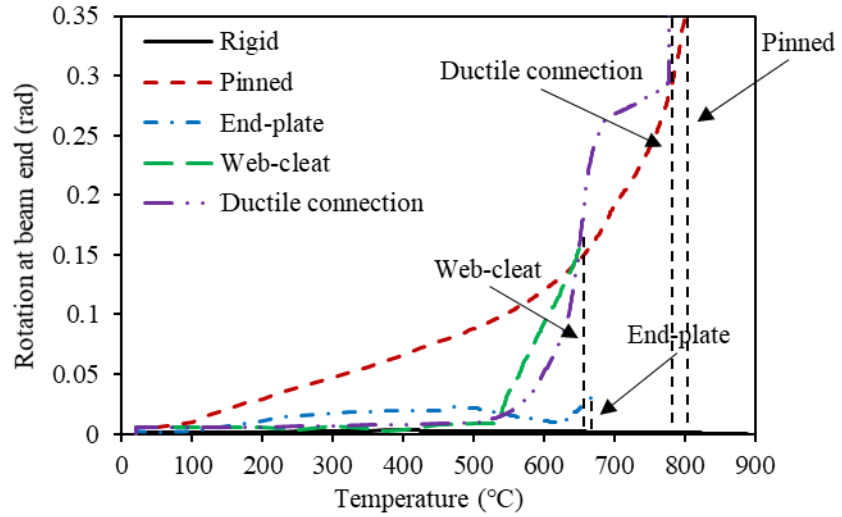

Figure 5-18. Rotations at beam ends for different connection types

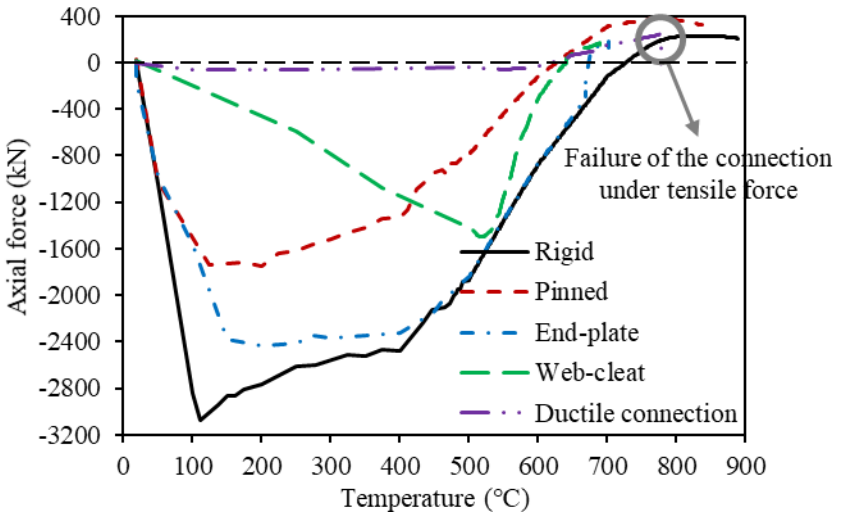

Figure 5-19. Mid-span axial forces of beams with different end connection types

5.5. Optimization of the ductile connection design

In this section, parametric studies are carried out on several key parameters, using the sub-frame shown in Figure 5-14 (a), to optimize the design of the ductile connection in terms of the beam's failure temperature.

It is generally assumed in these studies that the temperature of the connection is equal to half of that of the connected beam in the model used in Section 5.4. Connections tend to experience lower temperatures than the members which they connect during a fire event, due to their smaller section factor, lower exposed surface area, and fire protection measures which tend to imitate those of the

attached column. A sensitivity analysis has been conducted, adopting different relationships between the connection temperature and the beam temperature. The results are shown in Figure 5-20 and Table 5-2. The beam temperature at which the connection fails is increased by 13.9% when its temperature is reduced to 40% of the beam temperature. Further reductions of the connection temperature ratio have little effect on increasing the failure temperature of the beam. This is due to the fact that the temperature of the connection will not exceed 400°C if it is assumed to be lower than 40% of the beam temperature. Therefore, it is a reasonable choice to protect the connection to prevent its temperature exceeding 40% of the beam temperature. Further reducing the connection temperature will only increase the cost of insulation to the connection.

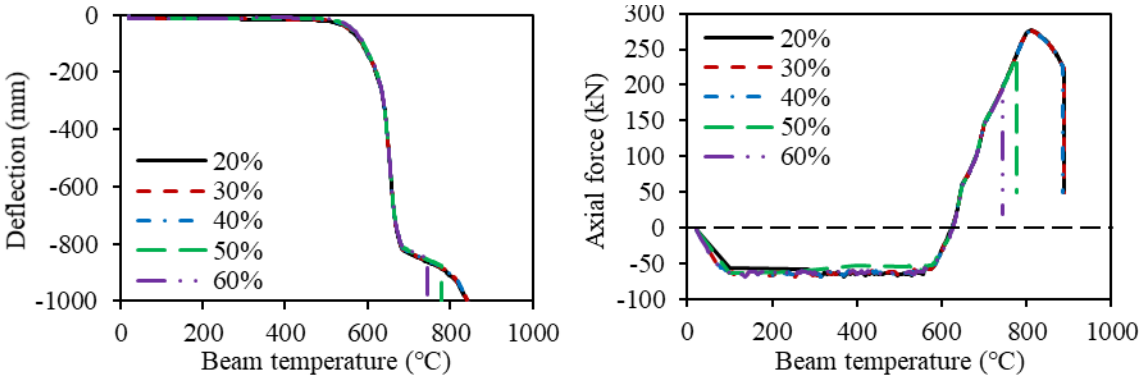

(a) Mid-span deflection of beam (b) Mid-span axial force of beam

Figure 5-20. The effect of different temperature ratio assumptions

Table 5-2. Beam failure temperatures under different temperature ratio assumptions

Connection temperature ratio	Beam failure temperature (°C)	Difference from original design
$T_C = 20\%T_B$	889	14.3%
$T_C = 30\%T_B$	887	14.0%
$T_C = 40\%T_B$	886	13.9%
$T_C = 50\%T_B$*	778	0.0%
$T_C = 60\%T_B$	745	-4.2%

* Control case

In the component-based connection element, if the axial force of a spring row reaches the failure load of the bolt pull-out component, then the spring row is judged to have failed. Therefore, the occurrence of bolt pull-out failure can be delayed by reducing the axial force generated in each spring row. This can be achieved by improving the ductility of the connection, typically by increasing the radius of the semi-cylindrical section. Another way to increase the failure load of the bolt pull-out component is to increase the thickness of plate. The top bolt row experiences the largest tensile displacement when the connection is subject to positive rotation. Moving from the

top bolt row towards the bottom one, the tensile displacement of each bolt row decreases progressively. In order to reduce the maximum tensile displacement, in the top spring row, reducing the vertical bolt spacing could also be effective. Therefore, various inner radii of the semi-cylindrical section, plate thicknesses and bolt spacings have been adopted. The effects of these variations on the mid-span deflection and the axial force of the beam are shown in Figure 5-21 - Figure 5-23 and Table 5-3 - Table 5-5. As shown in Figure 5-21 and Table 5-3, increasing the radius of the semi-cylindrical section can reduce the axial compressive force generated in the beam. However, its effect on the maximum tensile force of the beam in catenary action, and the final beam failure temperature, is negligible. For instance, even when the inner radius of the semi-cylindrical section is increased to 90mm, the beam failure temperature is only 0.9% higher than the control case (inner radius of semi-cylindrical section = 50mm). Increasing the plate thickness can significantly improve the performance of the connection in the catenary tension stage, by enhancing the ultimate failure temperature, as shown in Figure 5-22 and Table 5-4. However, the increase of plate thickness also reduces the ductility of the connection, resulting in larger axial forces generated in the connected beam. For example, the beam failure temperature with a connection of 10mm thickness is 13.2% higher than that of the control case, whereas the maximum compressive axial force increases by 207.2% during the initial heating. Therefore, the plate thickness should not be increased excessively, otherwise, the ductility of the connection will decrease sharply, and this may impose very high forces on adjacent structure. Figure 5-23 and Table 5-5 show that the bolt spacing has little influence on the ultimate failure temperature of the connection. The last parameter studied is the steel grade. In general, the steel grade of the connections is the same as for the beams. However, Figure 5-24 and Table 5-6 indicate that the use of a higher grade of steel for connections is effective in raising the failure temperature.

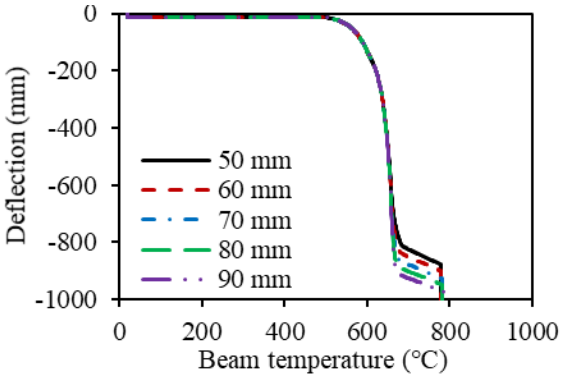

(a) Mid-span deflection of beam

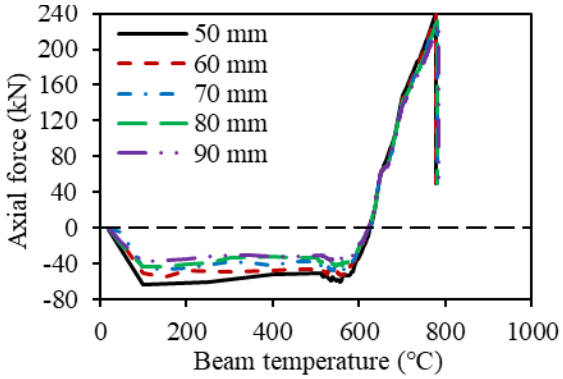

(b) Mid-span axial force of beam

Figure 5-21. The effect of changing the inner radius of the semi-cylindrical section

Table 5-3. Beam failure temperatures with different inner radii of the semi-cylindrical section

Connection temperature ratio	Beam failure temperature (°C)	Difference from original design
50*	778	0.0%
60	779	0.1%
70	781	0.4%
80	782	0.5%
90	785	0.9%

* Control case

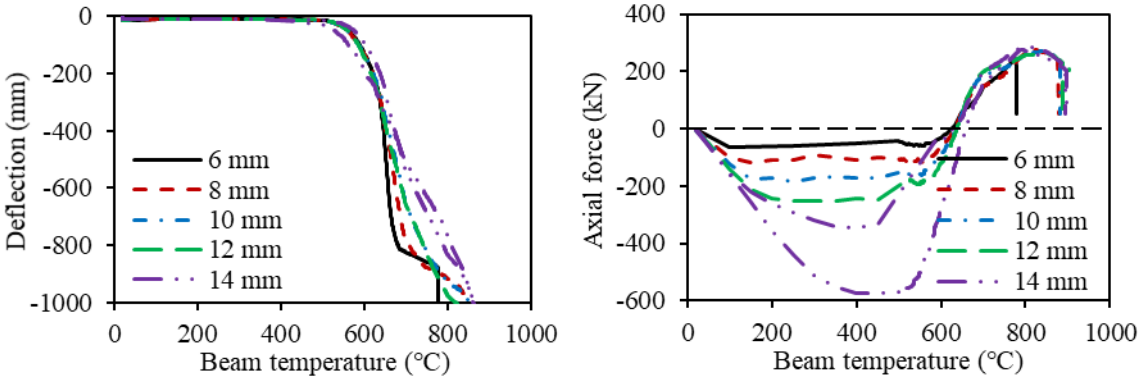

(a) Mid-span deflection of beam (b) Mid-span axial force of beam

Figure 5-22. The effect of changing the plate thickness of connection

Table 5-4. Beam failure temperatures with different connection plate thickness

Plate thickness (mm)	Beam failure temperature (°C)	Difference from original design	Maximum compressive axial force (kN)	Difference from original design
6*	778	0.0%	-59.75	0.0%
8	878	12.9%	-116.48	94.9%
10	881	13.2%	-183.54	207.2%
12	888	14.1%	-253.01	323.4%
14	894	14.9%	-346.81	480.4%

* Control case

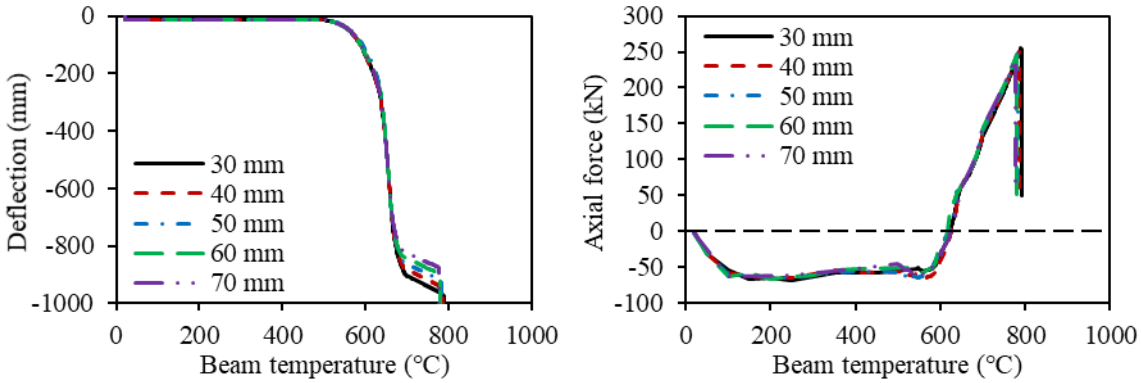

(a) Mid-span deflection of beam (b) Mid-span axial force of beam

Figure 5-23. The effect of different vertical bolt spacing

Table 5-5. Beam failure temperatures with different vertical bolt spacing

Vertical bolt spacing (mm)	Beam failure temperature (°C)	Difference from original design
30	791	1.7%
40	786	1.0%
50	783	0.6%
60	780	0.3%
70*	778	0.0%

* Control case

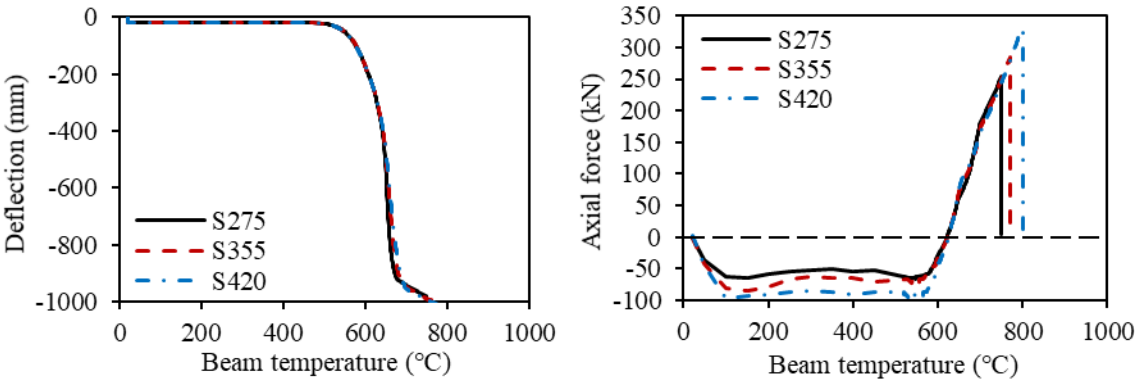

(a) Mid-span deflection of beam (b) Mid-span axial force of beam

Figure 5-24. The effect of different connection materials

Table 5-6. Beam failure temperatures with different connection materials

Steel grade	Beam failure temperature (°C)	Difference from original design
S275	751	0.0%
S355	772	2.8%
S420	800	6.5%

* Control case

In order to test the effectiveness of the connection optimization, a ductile connection of 8mm thickness is adopted in the sub-frame model shown in Figure 5-14 (a). The inner radius of the semi-cylindrical section is 70mm, the temperature of the connection is assumed to be 40% of that of the connected beam, and the vertical bolt spacing is 50mm. Figure 5-25 shows that the optimized ductile connection delivers a much higher failure temperature compared with the original design of the ductile connection (inner radius = 50mm, plate thickness = 6mm, bolt spacing = 70mm, connection temperature = 50% of beam temperature), as well as with the end-plate and web-cleat connections.

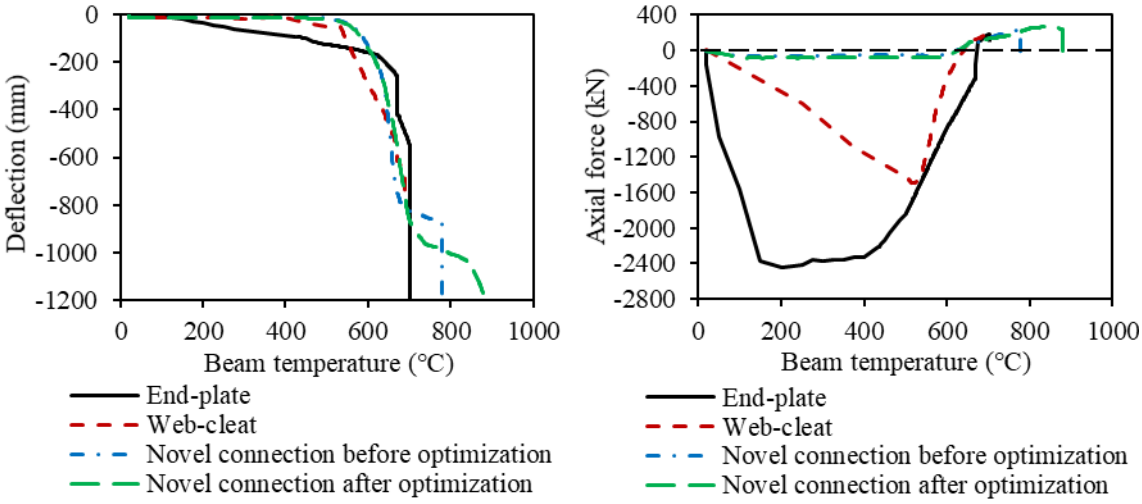

Figure 5-25. Comparison of beam performance with different connection details

5.6. Progressive collapse modelling

Once a connection fractures, the connected beam can be detached from the supporting column, leading to an increase in the column slenderness, which might cause the column to buckle. Connection failures can also trigger the collapse of slabs and the spread of fire into adjacent compartments. These may lead to a sequence of failures resulting in the progressive collapse of the entire structure. In order to effectively model the global behaviour of structures in fire from local instability to overall collapse, a combination of static and dynamic solvers was developed by Sun (Sun et al., 2012a, 2012b, Sun, 2012) and implemented in Vulcan. The static solver is computationally efficient and is used to track the static behaviour of a structure. Once local instability occurs, the dynamic solver is activated to track the motion of the structure until stability is regained, and then the static solver comes back into service. These two solvers are used alternately to analyse the structure under stable and unstable states, respectively. In this section, the static-dynamic solver is used to model the three-storey three-bay plane frame with ductile connections shown in Figure 5-26, to illustrate the progressive collapse of a structure in fire. Although this model is for a non-composite frame, the contributions of the slabs are considered to some extent: 1) the restraint to lateral movement of the beam's top flange provided by the slab is considered by constraining the out-of-plane degrees of freedom of the frame; 2) the transfer of external loads from the slab to the beam is considered by directly converting the external loads into a distributed loading applied to the beam. It is further assumed that fire occurs only in the

ground floor, and the horizontal springs on the outer columns of each floor are used to prevent lateral sway instability of the frame. Only half of the frame is built in the Vulcan model, in order to save computational effort, given that the structure is symmetric. A uniformly distributed line load is applied to the beam on each floor, generating a load ratio of 0.4, with respect to a simply supported beam. A concentrated vertical force of 3000kN is applied on each of the two intermediate columns, representing superstructure loads. The temperatures of the connections and columns at ground floor level are assumed to be half of that of the connected beams.

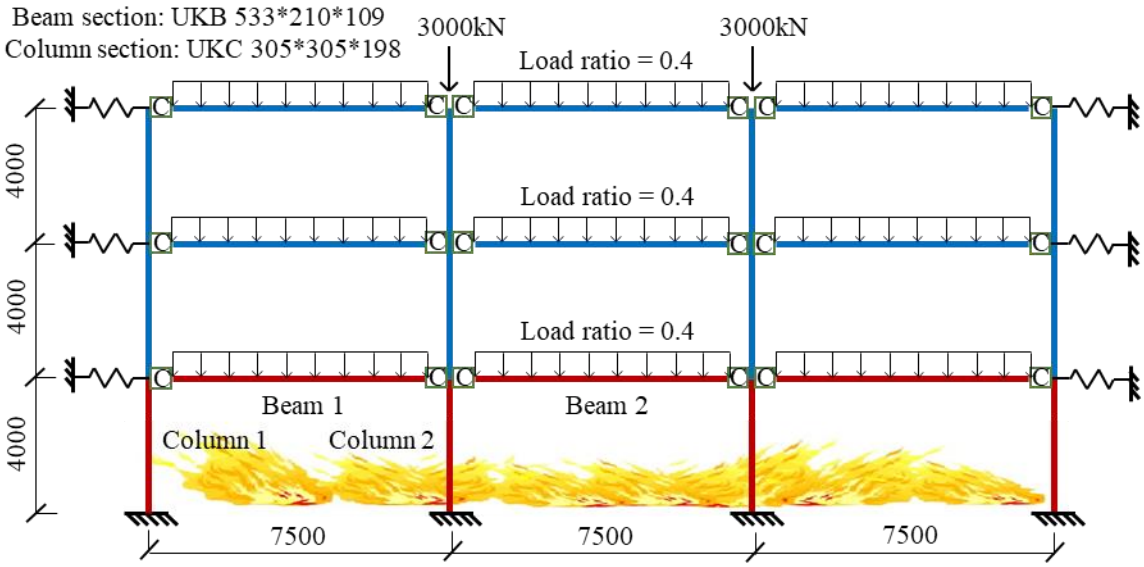

Figure 5-26. The three-storey three-bay frame

The calculation procedure for progressive collapse of the frame is shown in in Figure 5-27. Firstly, input data is read in for a new temperature step. The static solver is used to analyse the model. As soon as one component of a spring row reaches its failure limit, this spring row is considered as failed, and is deleted. When all spring rows in a connection element fail, the connection is considered as failed, and its stiffness matrix is set to zero. Once both connections have failed, the connected beam detaches from the columns. It is then removed from the model by restraining all its degrees of freedom.

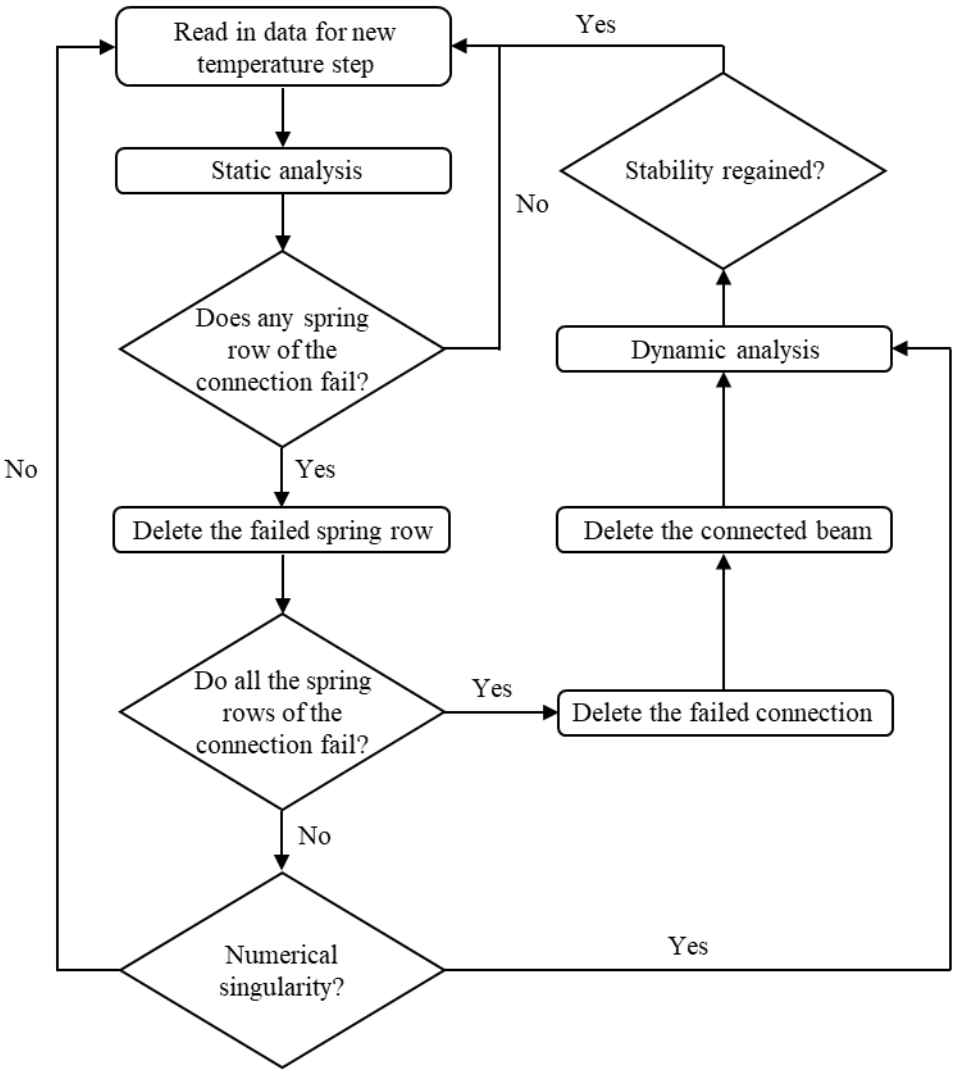

Figure 5-27. Static-dynamic calculation process

Figure 5-28 shows temperature-force and displacement-force curves of the spring rows of the connections at the ends of Beam 2. Spring Row 1 (the top bolt row) undergoes the minimum compressive displacement and maximum tensile displacement, whereas Spring Row 5 (the bottom bolt row) undergoes the maximum compressive displacement and minimum tensile displacement. The force-displacement curve of Spring Row 1 becomes almost vertical as failure occurs. However, the tensile capacity of the spring row cannot be reached because its failure is governed by bolt pull-out. Fortunately, several measures discussed in Section 5.5 can be taken to delay the occurrence of bolt pull-out failure, so as to increase the ultimate failure temperature of the beam. In the ductile connection element, once a spring row fails, the force of this spring row falls to zero. The sequence of failures of the other bolt bows follows very closely, once the top

bolt bow has pulled out at around 390°C. Once all the bolt rows have failed, the entire connection is considered as having failed.

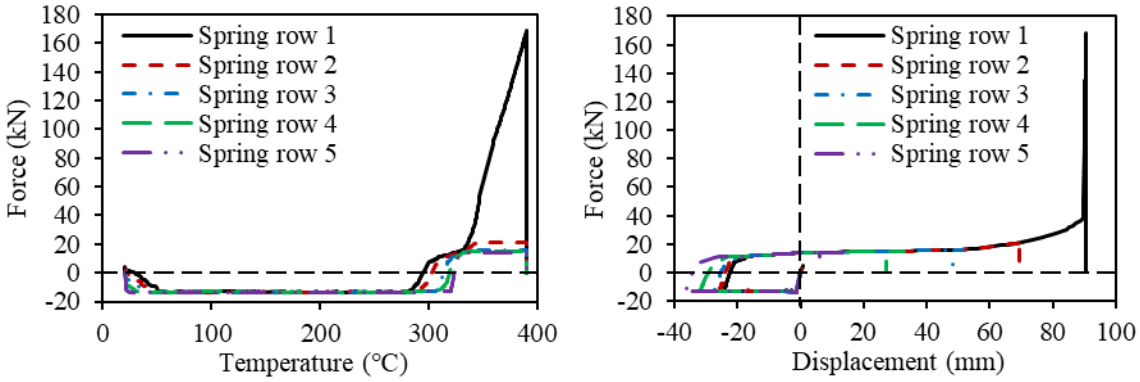

(a) Temperature-Force curve of each spring row

(b) Displacement-Force curve of each spring row

Figure 5-28. Variation of spring row forces of the connection at the end of Beam 2

As can be seen from the progressive collapse of the frame in Figure 5-29 (b), the connections at the ends of Beam 1 and Beam 2 fail when the beam temperature is 688°C, and then Beam 1 and Beam 2 are deleted from the frame (Figure 5-29 (c)). After that, Column 1 and Column 2 continue to be heated, although it is assumed in this case that their upper continuations remain cool, until both of their temperatures reach 550°C, at which point Column 2 begins to buckle due to the increase of its slenderness ratio. Column 1 does not buckle because of its lateral restraint (Figure 5-29 (d) - (f)). The progressive collapse simulation of the frame presented in this section emphasizes the importance of connections for the survival of the entire structure in a fire event.

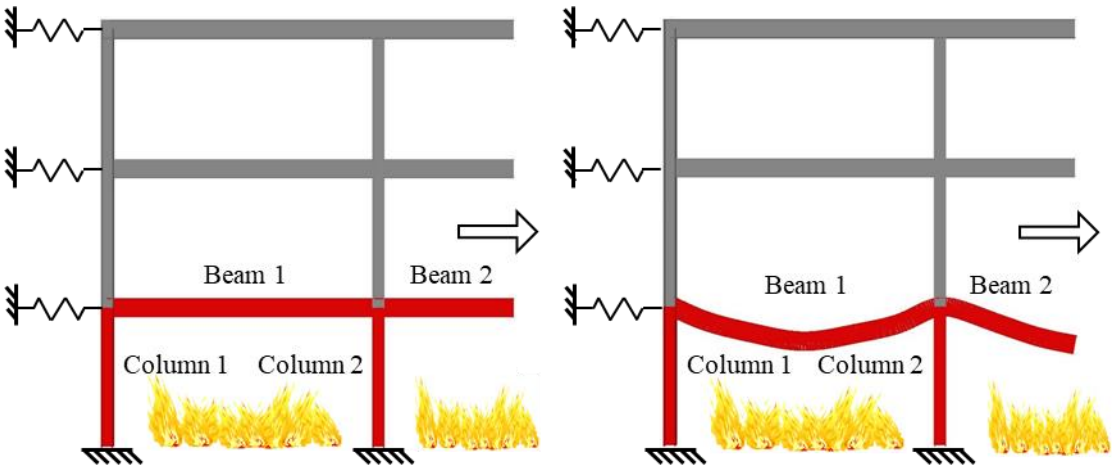

(a) T_{beam}=500°C

(b) T_{beam}=688°C

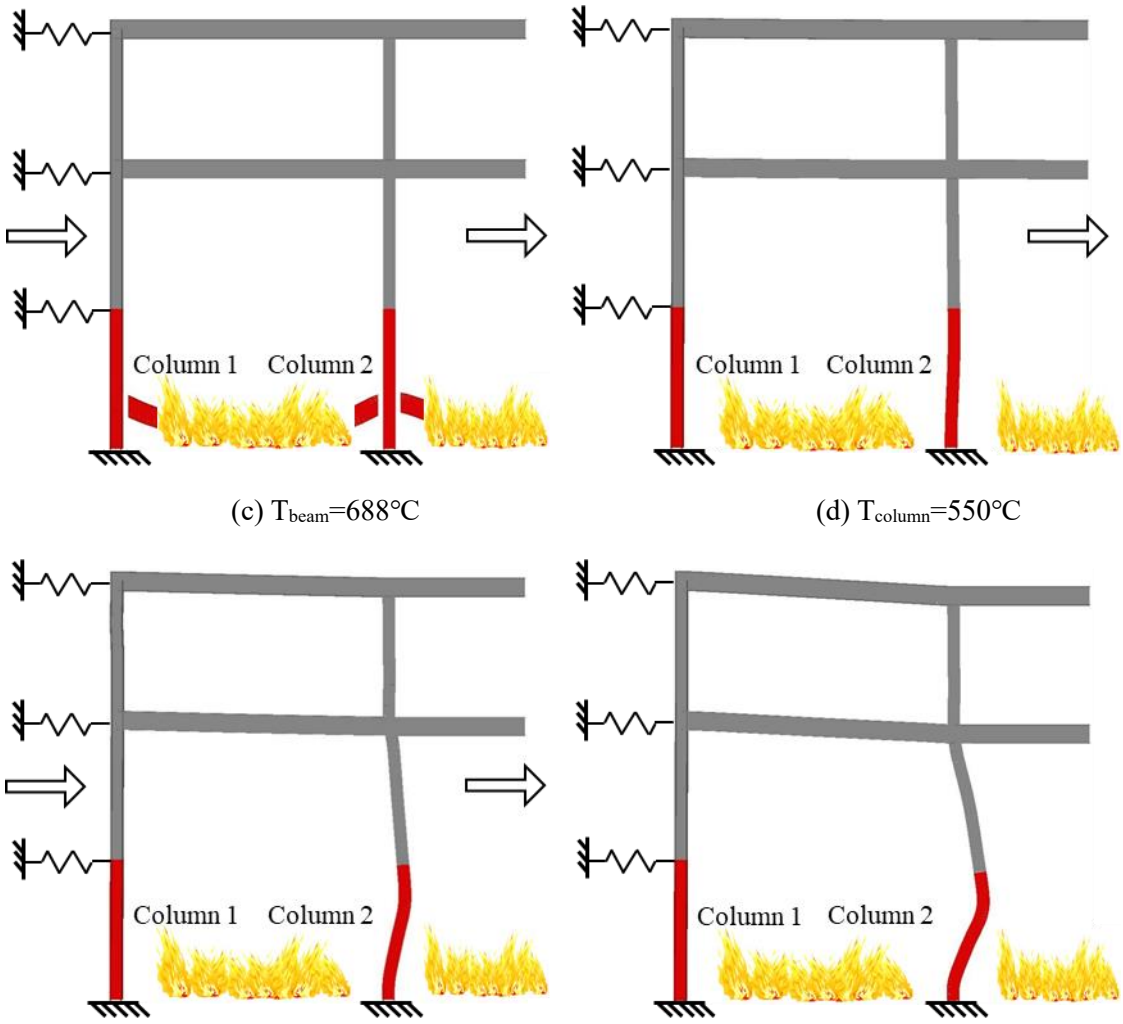

(c) T_{beam}=688°C (d) T_{column}=550°C

(e) T_{column}=550°C (f) T_{column}=550°C

Figure 5-29. Progressive collapse of the frame

5.7. Chapter conclusion

This chapter has described the incorporation of the ductile connection element into the software Vulcan. The bolt pull-out component, represented by the analytical model developed by Dong (2016), has been added to the component-based model of the ductile connection to simulate bolt pull-out failure. The tangent stiffness matrix equations derived by Block (2006) have been used to convert the component-based model into a connection element following the principles of the finite element method. Single beam models with ductile connections at both ends have been modelled using both Vulcan and Abaqus to validate the ductile connection element. The analytical model of a web-cleat connection, developed by Yu (2009d), has been implemented into Vulcan,

following the same method used for the ductile connection element. A sub-frame model was used to compare the performance of the ductile connection with that of conventional connection types. Different types of connection were used in this sub-frame model, including idealised rigid and pinned connections, and conventional end-plate and web-cleat connections. Parametric studies have been carried out to optimize the performance of the ductile connection under the tensile axial forces generated by the eventual catenary action of the unprotected beams at high temperatures. Five key parameters including the temperature of the connection, the inner radius of its semi-cylindrical section, the plate thickness, the bolt spacing and the connection material were selected. Finally, the static-dynamic solver in Vulcan was used to simulate the progressive collapse of a three-storey three-bay frame with ductile connections. The following conclusions can be drawn based on these studies:

- The simulation results obtained by Vulcan single beam models are very close to those of Abaqus single beam models, which indicates that the connection element can adequately represent the behaviour of the ductile connection given by detailed FE modelling.
- By comparing the performance of the ductile connection with other connection types, it can be concluded that the ductile connection can provide much higher ductility to accommodate the deformations generated by connected beams as their temperatures rise.
- It was found from the parametric studies that it is possible to optimize connection thickness, protection level, inner radius of the semi-cylindrical section and connection material in order to delay the occurrence of bolt pull-out failure, and thus enhance a beam's ultimate failure temperature.
- The modelling of the progressive collapse of the three-storey three-bay frame shows that failure of all the spring rows of the heated connection is triggered by the initial failure of the top bolt-row at a certain temperature. When the connection was judged to have failed the connected beam was then removed from the model. A column previously connected to the deleted beam will eventually buckle due to the increase of its slenderness ratio. This progressive collapse simulation emphasizes the importance of connections for the survival of the entire structure in a fire

6.

FIRE PERFORMANCE OF THE DUCTILE CONNECTION IN COMPOSITE CONSTRUCTION

6.1. Chapter introduction

Compared with bare-steel framing, composite construction has higher structural efficiency and lower cost, because it allows the use of smaller steel sections. Therefore, in recent decades, composite structures have been widely used in multi-storey construction. The performance of composite structures at elevated temperatures has been studied by researchers across the world (Wang, 1998, Sanad et al., 2000, Foster et al., 2007, Li et al., 2017). The structural behaviour of connections in composite structures in fire is quite different from that of bare-steel connections, due to the existence and continuity of the composite slab. At elevated temperatures, the composite slab acts as insulation to the top part of the connection, reducing its temperature and thus enhancing its performance. The top flange of a composite beam is likely to experience a much lower temperature than the exposed parts, and this temperature difference may even be as high as 40% (Wainman and Kirby, 1988). Accordingly, the degradation rate of the strength of a composite connection should in general be lower than that of an equivalent bare-steel connection, due to the beneficial effect of this partial temperature reduction. In addition, the composite slab restrains the thermal expansion of the steel beam in the initial stage of a fire, leading to thermal bowing, which also affects the performance of its connections by causing higher early-stage rotations.

The behaviour of the ductile connections in bare-steel structures has already been well studied in the previous chapters, it is appropriate now to investigate their performance in composite structures. In non-composite steel frames, the thermal expansion of a complete beam can be absorbed by plastic deformation of the ductile connections, thus greatly reducing the forces imposed on the surrounding structure. However, in composite construction, unless a large number of shear studs are fractured or highly deformed, the deformation of the ductile connections will mainly be caused by rotation at the column face, which will mainly be caused by thermal bowing of the composite beams. Hence the influence of these connections on the overall frame behaviour is less easily predicted.

This chapter investigates the application of the ductile connections in composite structures. Equations have been proposed to represent the axial ductility demands of the beam at four key positions; the rebar level, the connection top surface, the connection bottom surface, and the beam

bottom flange. In the calculation of ductility demand of the composite beam, the deflection caused by thermal bowing of the composite beam has been included in its total deflection. A reinforcement component, which considers the pull-out of reinforcing bars and the influence of weld points in mesh, has been added to the non-composite ductile connection model to establish a suitable component-based model for the composite ductile connection. This component-based composite ductile connection model has been incorporated into Vulcan, and validated against a detailed Abaqus FE model. Parametric studies using Vulcan have been carried out to study the effect of three parameters on the performance of the ductile connections, including the connection thickness, the inner radius of the semi-cylindrical section and the number of longitudinal reinforcing bars within the effective width of the slab. Since the shear studs are not considered in the component-based composite connection model, an Abaqus model of a plane composite frame has been established to investigate the influence of shear studs on the behaviour of the connection. The method of simulating the composite connection using Abaqus has been validated against experiments carried out by Al-Jabri (1999).

6.2. Ductility demand of composite beam in fire

The deformation of a typical composite beam as its temperature rises is illustrated in Figure 6-1. The connection needs to be able to accommodate the axial displacement caused by the combined effect of the effective shortening of the beam due to deflection and the rotation of the beam end. In a composite beam, as the slab does not expand with the thermal strain of the steel downstand, the steel's thermal expansion is included in the calculation of the thermal curvature of the composite beam. There are four key positions where the axial displacement of the beam end needs to be taken into consideration; the rebar level, the top surface of the connection, the bottom surface of the connection, and the bottom flange of the beam. The top surface of the connection experiences the maximum displacement away from the column-face, whereas internal contact may occur at the connection's bottom surface. In addition, to avoid contact between the beam bottom flange and column flange, which may lead to the buckling of column web, the axial displacement of the beam bottom flange is also considered when determining the ductility demand. The displacements of these four key positions are represented by Δ_r , Δ_{cts} , Δ_{cbs} and Δ_{bbf}

respectively, and can be simply calculated using Equations (6-1) - (6-4). The lever arms used are the distances between each key position and the neutral axis of the composite beam. As mentioned previously, the slab restrains the thermal expansion of the composite beam. This leads to thermal bowing, and the deflection due to thermal bowing needs to be included into the total deflection of the composite beam. The total deflection of the composite beam also includes the deflection caused by external load.

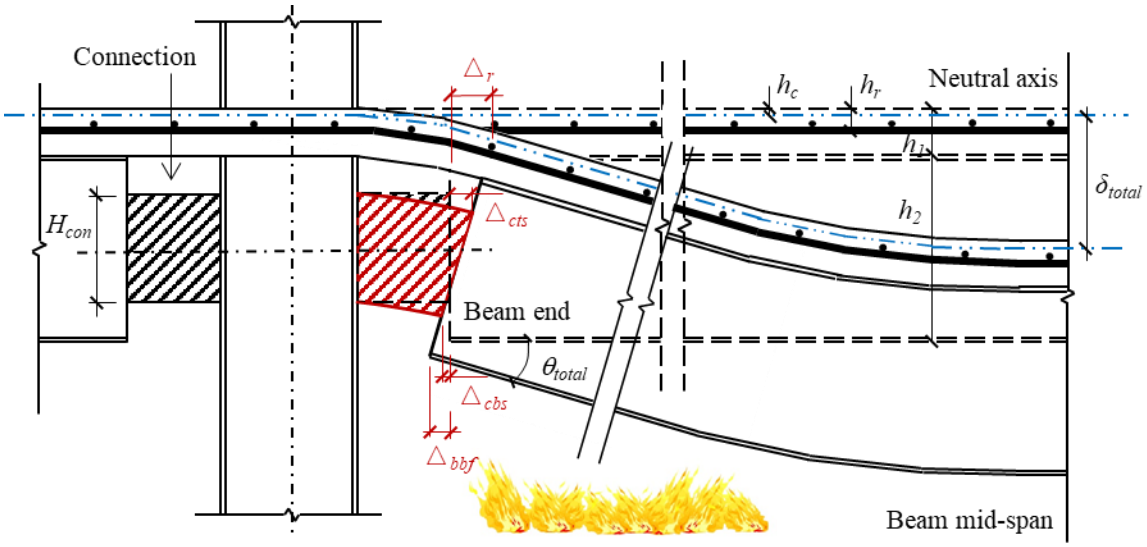

Figure 6-1. Deformation of composite beam in fire

$$\Delta_r = \frac{4}{3}\delta_{total}^{\ 2} / l - \tan(\theta_{total}) \cdot (h_r - h_c) \tag{6-1}$$

$$\Delta_{cts} = \frac{4}{3}\delta_{total}^{\ 2} / l - \tan(\theta_{total}) \cdot \left(h_1 + \frac{h_2 - H_{con}}{2} - h_c\right) \tag{6-2}$$

$$\Delta_{cbs} = \frac{4}{3}\delta_{total}^{\ 2} / l - \tan(\theta_{total}) \cdot \left(h_1 + \frac{h_2 + H_{con}}{2} - h_c\right) \tag{6-3}$$

$$\Delta_{bbf} = \frac{4}{3}\delta_{total}^{\ 2} / l - \tan(\theta_{total}) \cdot (h_1 + h_2 - h_c) \tag{6-4}$$

in which Δ_r, Δ_{cts}, Δ_{cbs} and Δ_{bbf} respectively represent the axial ductility demands of the beam at the rebar level, the connection top surface, the connection bottom surface, and the beam bottom flange. θ_{total} is the total rotation of the composite beam at beam end, and δ_{total} is the total deflection of the composite beam ($\delta_{total} = \delta_{external-load} + \delta_{thermal-bowing}$). l, h_1, h_2 and H_{con} represent the length of the composite beam, the slab depth, the steel beam depth and the connection depth,

respectively. h_c and h_r are the vertical distances from the top surface of the slab to the neutral axis and to the longitudinal rebar, respectively.

To calculate the thermal bowing deflection of the composite beam, several assumptions are made here:

1) the slab is assumed to remain at ambient temperature;
2) the temperature distribution within the beam section is uniform;
3) full shear connection between the slab and steel beam is assumed.

As shown in Figure 6-2 (a), the mechanical strain is obtained by subtracting the thermal strain from the total strain, and is then used to establish mechanical equilibrium.

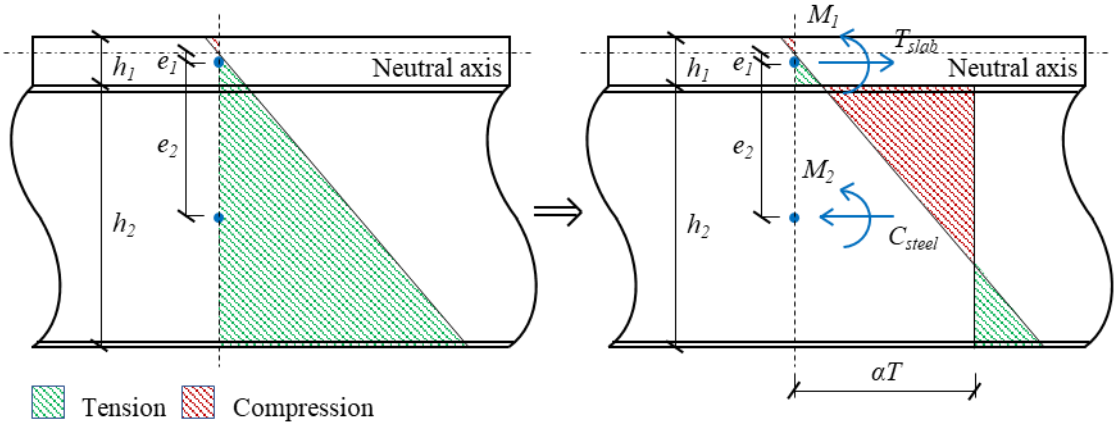

(a) Strain distribution

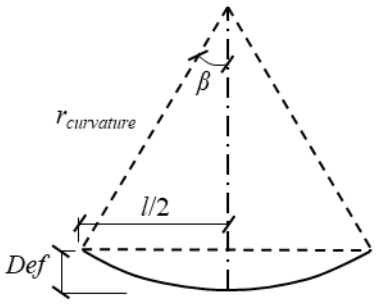

(b) Calculation of deflection

Figure 6-2. Calculation of the thermal bowing deflection of composite beam

Due to the assumption of full shear connection, the curvature of the slab is equal to that of the beam (Equation (6-5)).

$$\frac{M_1}{E_1 I_1} = y'' \qquad \frac{M_2}{E_2 I_2} = y'' \tag{6-5}$$

in which E_1, A_1 and I_1 are the Young's modulus, the cross-section area and the second moment

of area of the slab respectively. E_2, A_2 and I_2 are the Young's modulus, the cross-section area and the second moment of area of the steel section respectively. The tensile force acting at the centroid of the slab T_{slab}, and the compressive force acting at the centroid of the steel section C_{steel} can be obtained using Equation (6-6).

$$T_{slab} = E_1 A_1 y'' e_1 \qquad C_{steel} = E_2 A_2 (\alpha T - y'' e_2) \tag{6-6}$$

in which α is the thermal expansion coefficient. e_1 and e_2 are the vertical distances from the neutral axis to the centroid of the slab and to the centroid of the steel section, respectively.

According to the horizontal force equilibrium, the curvature can be expressed by a formula containing the two distances e_1 and e_2 (Equation (6-7)).

$$T_{slab} = C_{steel} \Rightarrow E_1 A_1 y'' e_1 = E_2 A_2 (\alpha T - y'' e_2) \Rightarrow y'' = \frac{E_2 A_2 \alpha T}{E_1 A_1 e_1 + E_2 A_2 e_2} \tag{6-7}$$

Moment equilibrium is then used to obtain the values of e_1 and e_2, as shown in Equation (6-8).

$$T_{slab} \frac{h_1 + h_2}{2} = M_1 + M_2 \Rightarrow e_1 = \frac{2(E_1 I_1 + E_2 I_2)}{E_1 A_1 (h_1 + h_2)} \quad e_2 = e_1 + \frac{h_1 + h_2}{2} \tag{6-8}$$

Once the curvature is determined using Equation (6-7), the deflection due to thermal bowing is calculated using Equation (6-9). The variables in Equation (6-9) are illustrated in Figure 6-2 (b).

$$\beta = \sin^{-1}\left(\frac{l/2}{r_{curvature}}\right) \qquad Def = r_{curvature}(1 - \cos\beta) \tag{6-9}$$

in which Def is the deflection due to thermal bowing.

An example composite beam of 10m span, subject to a uniform load intensity of 20 kN/m^2 applied on top of the slab is used to demonstrate the determination of ductility demand. The steel downstand of the composite beam is designed as a UKB 533×210×109. The depth and width of the slab are 130mm and 2600mm, respectively. It should be noted that the width used here is the effective width of the concrete flange of the composite beam, which is $b_{eff} = l/4 + b_0$, where b_0 represents the width of the steel flange occupied by shear studs. After the position of the neutral axis of the composite beam is obtained, the thermal bowing deflection and the displacements of the four key positions are calculated using Equations (6-1) - (6-9), and are shown in Figure 6-3. This figure shows that the connection should have an axial deformation capacity of at least

28.1mm in “closing” and 10.7mm in “opening”, in order to meet the ductility demand of the composite beam in fire, if the composite beam is designed to survive to 800℃. The elastic modulus of steel decreases with the increase of temperature. When the temperature reaches 600℃, the elastic modulus of steel decreases considerably, to the same order of magnitude as that of concrete, which leads to the rapid change of thermal bowing deflection slope, as shown in Figure 6-3 (a).

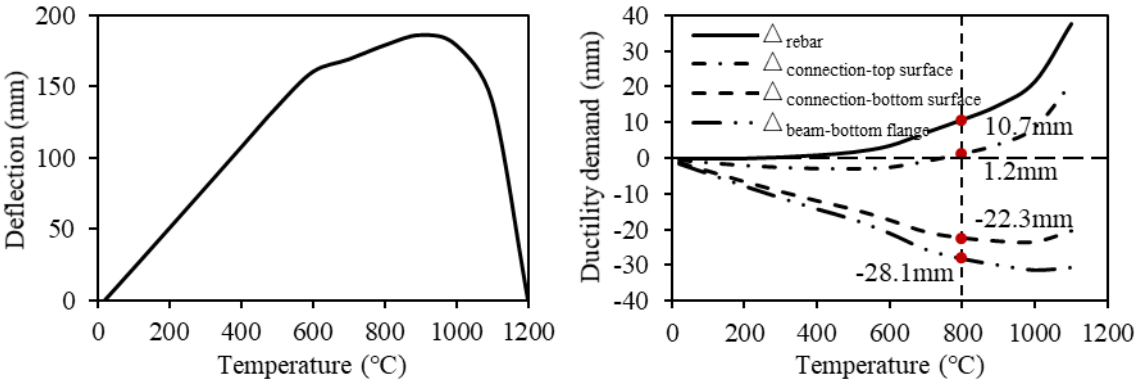

(a) Thermal bowing deflection (b) Ductility demand

Figure 6-3. Determination of ductility demand of the example composite beam

The schematic diagram of applying ductile connections in composite structure is shown in Figure 6-4. As the bare-steel ductile connection, the inner radius of the semi-cylindrical section of the composite ductile connection should be determined according to the ductility demands of composite beam in fire using Equations (6-1) - (6-4).

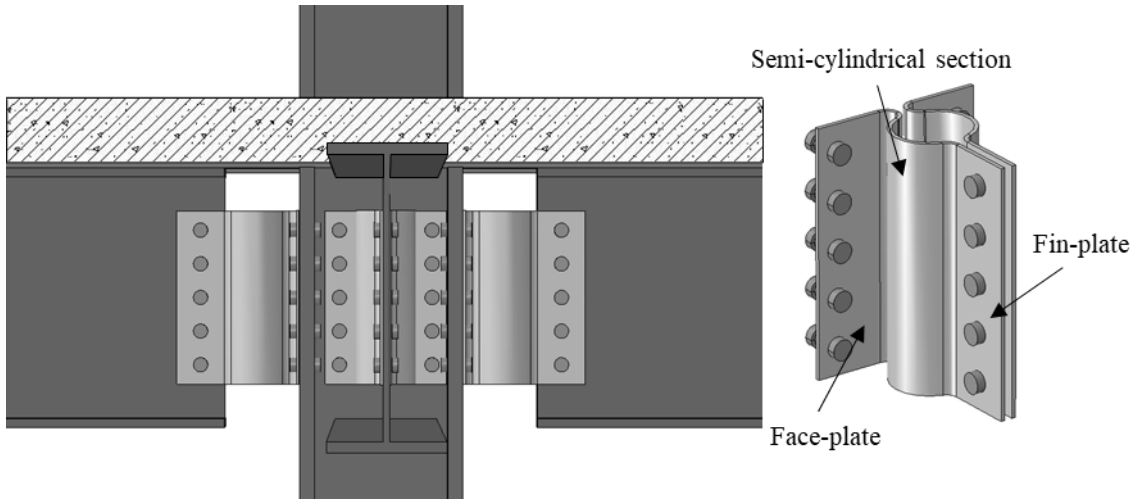

Figure 6-4. Application of ductile connections in composite structure

6.3. Component-based model of the composite ductile connection

Component-based modelling of bare-steel connections has been well studied in recent years. However, few studies have been conducted on the component-based modelling of complete composite connections. Madas (1993) proposed a component-based model of composite end-plate connections for use in the analysis of composite frames under dynamic loading at ambient temperature. In the Madas model, the concrete slab is divided into a finite number of layers and each layer considered is subject to a uniform strain between studs and across the slab's effective width. Al-Jabri (1999) developed a high-temperature composite end-plate connection model by adding two additional components, representing the reinforcement and shear studs, to his steel end-plate component-based connection model. Rassati et al. (2004) developed an ambient-temperature component modelling approach for the simulation of composite connections, which is capable of accounting for the influence of partial interaction between the slab and beam, and the cracking and crushing of the slab. Li et al. (2012a) developed a component model, which includes bolts in tension, reinforcement in tension, end-plate in bending, column flange in bending and column web in compression, to predict the initial stiffness and the ultimate moment capacity of composite connections in fire. However, the component-based models reviewed above are mainly for composite end-plate connections, and cannot be directly applied to the composite ductile connection. In addition, the full load-deformation characteristics of the connection, including the axial deformation of each spring row in the process of connection deformation, are needed to investigate the performance of the ductile connection as part of a composite structure; these are not available in existing models. It was, therefore, decided to develop a component-based model of the composite ductile connection in this research.

A component-based model of the non-composite ductile connection has already been developed in previous chapters and has been implemented into the Vulcan software for global frame analysis. Using the same method as the bare-steel ductile connection, the composite ductile connection will be implemented into Vulcan as a 2-noded spring element. Since the connections are within the hogging bending moment zone, and the tensile strength of concrete is negligible, the concrete in tension is ignored. In the following section, a reinforcement component will be added to the non-composite ductile connection model to establish a suitable model of the ductile connection in a

composite structure. This component-based composite ductile connection model will be incorporated into Vulcan, and several case studies will be carried out to test its performance.

6.3.1. Reinforcement component

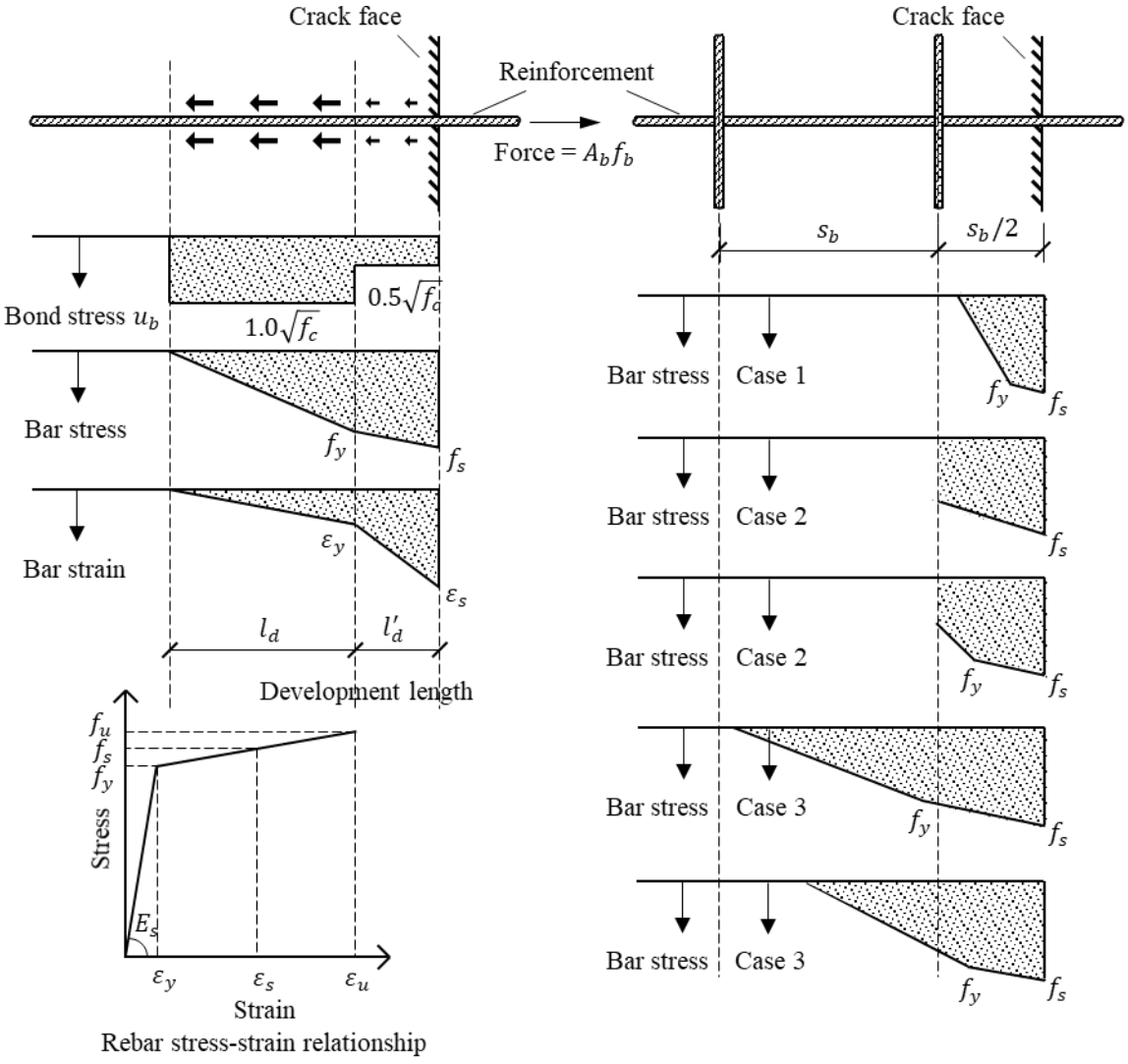

(a) Rebar slip model (Sezen and Setzler, 2008)

(b) Different cases considering the anchorage of the welds

Figure 6-5. Model of the rebar component

Depending on its effective depth within the slab, the reinforcement above the connection may be subject either to tensile or compressive strain due to the combination of hogging moment and thermally-induced rotation. In the case where the reinforcement strain becomes tensile, as the tensile strength of the concrete is very low, cracks usually occur, leading to reinforcement pull-

out within these cracks. The part of the rebar within the crack width is under uniform stress, which is equal to its ultimate strength. However, the part of the rebar within the embedded length is subject to stresses lower than those within the crack width, due to the surface bond stress. The further away from the crack-face, the smaller the stress is. Sezen and Setzler (2008) considered the pull-out of the rebar at concrete cracks when modelling the lateral deformation of a column caused by rebar slip in the anchorage zone. Their simple model of rebar slip, shown in Figure 6-5 (a), was verified against 12 tests conducted by Sezen (2004) and by Lynn and Moehle (1996).

In this model, a bilinear stress-strain relationship is assumed for the rebar, with a shallow gradient between the yield and ultimate stress points. The bond stress within the embedded length is assumed to be locally constant, at either u_b and u_b'. When the rebar strain is lower than the yield strain, the bond stress is $u_b = 1.0\sqrt{f_c}$, but when the rebar strain is above yield, the bond stress is $u_b' = 0.5\sqrt{f_c}$. This assumption is reasonable because only high rebar strain (above yield) and the resulting high slip at the rebar perimeter can cause real damage to the adjacent concrete. The slip of the rebar can be calculated using Equations (6-10) and (6-11). In the extreme case of rebar fracture within the crack, $f_s = f_u$ and $\varepsilon_s = \varepsilon_u$. In the context of Figure 6-5,

$$l_d = f_y d_b / 4u_b \qquad l_d' = (f_y - f_s) d_b / 4u_b' \tag{6-10}$$

in which u_b and u_b' are the bond stresses when the rebar strain is lower than the yield strain and higher than the yield strain, respectively. l_d and l_d' are the development lengths of elastic zone and post-yield zone, respectively. f_y and f_u are the yield stress and ultimate stress of rebar. f_s is the rebar stress between f_y and f_u. d_b is the diameter of the rebar.

The total slip of the rebar from the crack-face, assuming that it is anchored in the concrete either side of the crack is

$$slip = \varepsilon_y l_d / 2 + (\varepsilon_s + \varepsilon_y) l_d' / 2 \tag{6-11}$$

where ε_y and ε_u are the yield strain and ultimate strain of rebar.

Burgess and Sahin (2018) further considered the contribution of the weld points on the transverse reinforcing bars in the mesh when calculating the crack width at which rebar fractures using the

simple slip model presented above. In fact, the weld points on the transverse bars at regular spacing s_b can provide physical anchorages to the longitudinal bars. The strength of each weld should be at least 25% of the bar strength in accordance with Eurocode 2 (CEN, 2004a). If the rebar stress at a weld point exceeds the strength of the weld, then the weld will fracture. The distance from the crack-face to the next weld point is then used as the development length. In this case, the pull-out of the rebar will increase suddenly when weld fracture occurs. Considering different combinations of development length, rebar stress and weld strength, three typical cases are shown in Figure 6-5 (b). The first weld is positioned at a distance of $s_b / 2$ from the crack face, and the subsequent welds are at a regular spacing s_b. In Case 1, the development length of the rebar does not go beyond the first weld; this is likely to occur to deformed bars with very high bond stress. If the development length reaches the first weld-point, there are two possible scenarios, according to the relationship between the rebar stress and the weld strength.

1) Case 2: If the rebar force is less than or equal to the weld strength, the first weld does not fracture, but becomes a positive anchorage point. The development length and crack width are both reduced compared to when weld points are neglected;
2) Case 3: If the rebar force exceeds the weld strength, the first weld fractures and the remaining anchoring force is borne by the bond stress developed beyond the broken weld. For bars with low bond stress, such as plain circular bars, there may be more welds broken before sufficient anchorage is accumulated.

According to Burgess's study (Burgess and Sahin, 2018), for plain rebars the bond stresses are reduced to $u_b' = 0.15\sqrt{f_c}$ and $u_b = 0.3\sqrt{f_c}$, where f_c is the concrete strength. For deformed bars, the two values ($u_b' = 0.5\sqrt{f_c}$ and $u_b = 1.0\sqrt{f_c}$) mentioned earlier remain valid. The weld strength is assumed to be 25% of the rebar strength according to Eurocode 2 (CEN, 2004a).

The force-slip curve of a bar is generated by using the rebar slip model considering the weld anchorage described above. If the concrete crack occurs in the middle of the slab and there is enough length on both sides of the crack to develop the anchorage, the crack-width should be twice the slip from a single crack face. The tensile force of the rebar is obtained by multiplying the rebar stress by its cross-sectional area. Taking deformed and smooth A252 meshes at 200mm

× 200mm spacing as two examples, the properties of these two meshes and their weld fracture predictions are listed in Table 6-1.

Table 6-1. Properties of deformed and smooth A252 meshes and the weld fracture predictions

Rebar type	Diameter	Ductility class	Strengths (MPa)		Ultimate strain	Weld fractures		
			f_y	f_u	ε_u	1st	2nd	3rd
Deformed A252	8mm	C	435	500	0.075	Y	N	N
Smooth A252	8mm	C	435	500	0.12	Y	Y	Y

The calculated force-slip curves are shown in Figure 6-6 (a). This figure shows that only the first weld of the deformed A252 breaks, whereas three successive welds break for the smooth A252 bar. The location of the concrete crack must be determined when the rebar component is incorporated into the component-based model of the connection. Based on the results of the tests conducted by Al-Jabri (1999), it is assumed that the crack occurs on the outer surface of the column flange, as shown in Figure 6-6 (b).

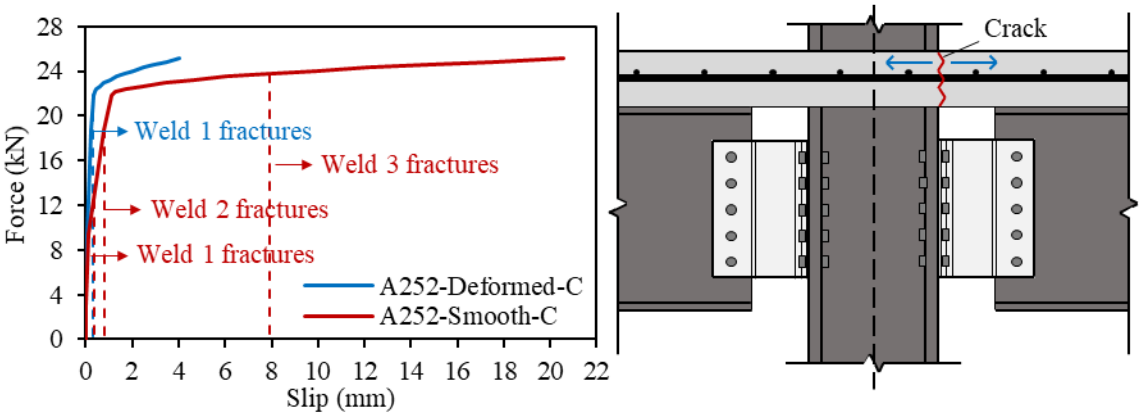

(a) Force-slip curves of two different types of meshes

(b) Development length of rebar component

Figure 6-6. Rebar component

The development length on the right side of the crack is assumed to be limited by the first three weld points, since previous research indicates that the rebar development length usually does not exceed the third weld point (Burgess and Sahin, 2018). The development length on the left side of the crack is assumed to be limited by the first weld point and the centre line of the column section, depending on whether the first weld point fractures. The slip on the left and right sides of the crack should be calculated separately. The sum of the slips on both sides is the crack-width, or the total displacement of the rebar component.

6.3.2. Incorporation of the composite component-based model into Vulcan

The rebar component described above has been added to the component-based model of the bare-steel connection to form the component-based model of the composite ductile connection. As shown in Figure 6-7 (a), the proposed component-based model includes components representing the face-plate and semi-cylindrical section, the column web in compression, bolt pull-out, rebar, fin-plate in bearing, beam web in bearing and bolt in shear. The gap between the compression spring row and the column face is designed to represent the maximum compressive displacement before internal contact occurs. The component-based model is then converted into a connection element, following the principles of the finite element method. The method is introduced in detail in Chapter 5, and so is not repeated here.

The 2-D composite frame model shown in Figure 6-7 (b) is used to test the performance of the composite connection element. The height of the upper and lower columns is 3m, and the beam span is 10m. The rebar is assumed to be anchored to the centre line of the column section for both the inner and outer column cases. For an inner column, the inherent symmetry of deflection about the column line makes this assumption generally valid. For the outer column case, the rebar is assumed to be anchored, generally by a hook, to the column, which would be normal good design practice. In order to reduce the size of the model to save computation cost, only half of the frame is modelled, and symmetric boundary conditions are applied at the mid-span of the beam and slab. The bottom of the column is fully restrained, and the top can only move vertically. It is further assumed that fire only occurs in the lower storey, and the standard fire curve is adopted. Lawson (1990a, 1990b) assumed that the temperature of the connection was about 70% of that of the beam bottom flange at the beam mid-span. This assumption applies to bare-steel structures. Since the concrete slab can act as an insulation to the connection, it was decided to further reduce the connection temperature to half of the beam temperature in the 2-D composite sub-frame model. Columns in steel-framed structures are invariably protected, and so the temperature of the lower column is set to be equal to the connection temperature, assuming that they are protected to the same level. The slab and the upper column are assumed to remain at ambient temperature. Full shear connection is assumed between the slab and beam, and this is modelled by shared nodes between the slab and beam elements. In order to verify the developed connection element, an

Abaqus 2-D composite frame model is also established. The Abaqus modelling approach is described in Section 6.4, including material characteristics, contact settings, etc. The only difference is that the shear studs in the Abaqus model are not modelled in detail in this section. Full shear connection is achieved by fully tying the bottom of the slab and the top flange of the steel beam. The deformations of the ductile connection at different temperatures obtained from the Abaqus model is shown in Figure 6-8 for a perimeter column connection. As can be seen from this figure, the proposed ductile connection exhibits satisfactory deformability.

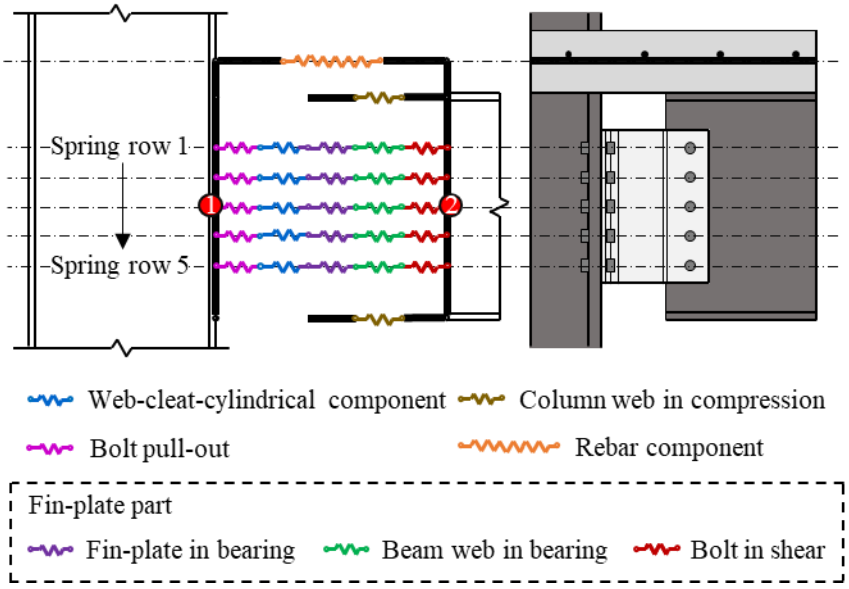

(a) The component-based model of composite ductile connection

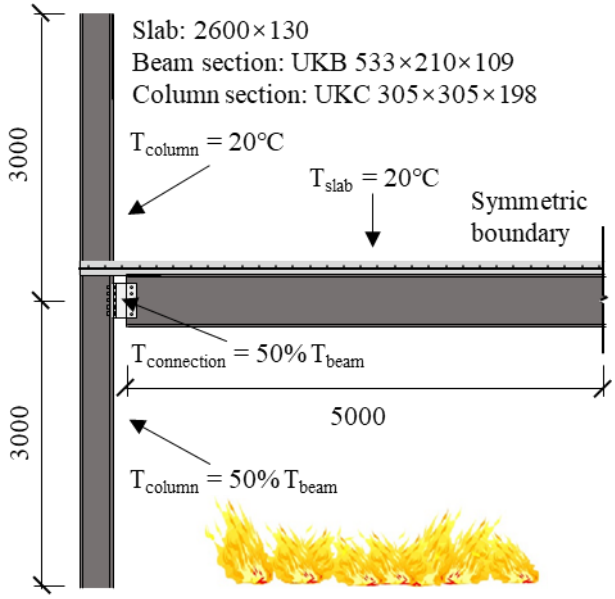

(b) The 2-D composite frame model

Figure 6-7. The component-based model and the 2-D composite frame model

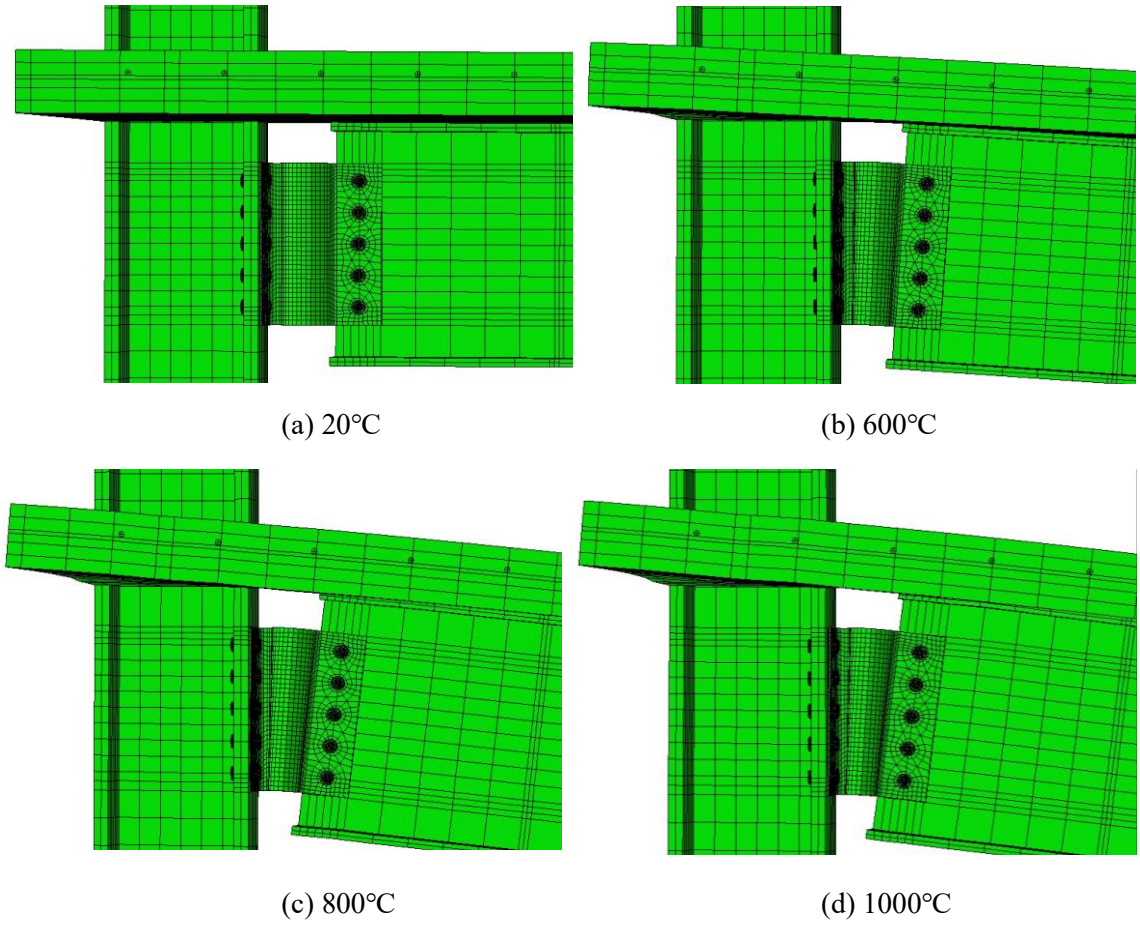

(a) 20°C (b) 600°C

(c) 800°C (d) 1000°C

Figure 6-8. Deformation of the ductile connection at different temperatures; connection to a perimeter column

The results of the Abaqus and Vulcan models are compared in Figure 6-9. Looking at the mid-span deflections and end rotations shown in Figure 6-9 (a) and (b), the Abaqus model appears to be stiffer than the Vulcan model at temperatures above 200°C. These differences can be explained by two different aspects of the respective models:

1) In its plastic phase, the push-pull analytical model of the semi-cylindrical section used in the component-based model of the ductile connection is softer than the detailed Abaqus connection model, as shown in Figure 6-9 (d);
2) The discrete concrete cracking and the pull-out of rebars are only introduced in the Vulcan connection element; they are not considered in the Abaqus model, making the composite slab of the Abaqus model apparently stronger than that of the Vulcan model.

The differences between the Abaqus and Vulcan models occur above 200°C, since all the spring rows of the Vulcan connection element are within their linear-elastic phase below 200°C, and the

difference between the push-pull analytical model used in Vulcan and the detailed Abaqus model in the linear-elastic range is small (Figure 6-9 (d)). The comparison of the connection axial forces obtained from the Vulcan and Abaqus models is shown in Figure 6-9 (c), which shows that above 200℃ the connection axial force of the Abaqus model is larger than that of the Vulcan model. This is also due to the fact that the Abaqus detailed connection model is more rigid than the push-pull analytical model in the plastic stage. At around 690℃, the compressive axial force of the connection in the Vulcan model decreases rapidly and changes temporarily into tension at about 800℃. Above this temperature, the connection axial force becomes compressive again. During heating, the behaviour of the connection is affected by the combined effects of thermal expansion and material degradation. In the beam temperature range 700℃ - 800℃, the change of steel crystal structure causes a pause in the beam's thermal expansion, which resumes when the transition is complete. This can be seen (Figure 6-9 (b)) to cause a temporary change of direction in the connection rotation. This causes the connection spring rows to reverse direction, causing their forces to change rapidly into tension because of the rather stiff nature of the elastic unloading curves. When the thermal expansion re-commences, the connection force again rapidly changes to compression, as shown in Figure 6-9 (c). Figure 6-10 (a) and (b) show the temperature-force and temperature-displacement curves of each spring (component) row in the Vulcan model, indicating that the decrease in connection rotation leads to unloading of all the spring rows. Among all the five spring rows, the reduction in the compressive displacement of the bottom spring row (Row 5) is the largest, whereas the displacement reduction of the top spring row (Row 1) is the smallest. Therefore, Row 5 enters the so-called pulling-back stage, and its force temporarily changes into tension, whereas Row 1 is within the unloading stage before the compressive displacement increases again, and its force remains as compressive.

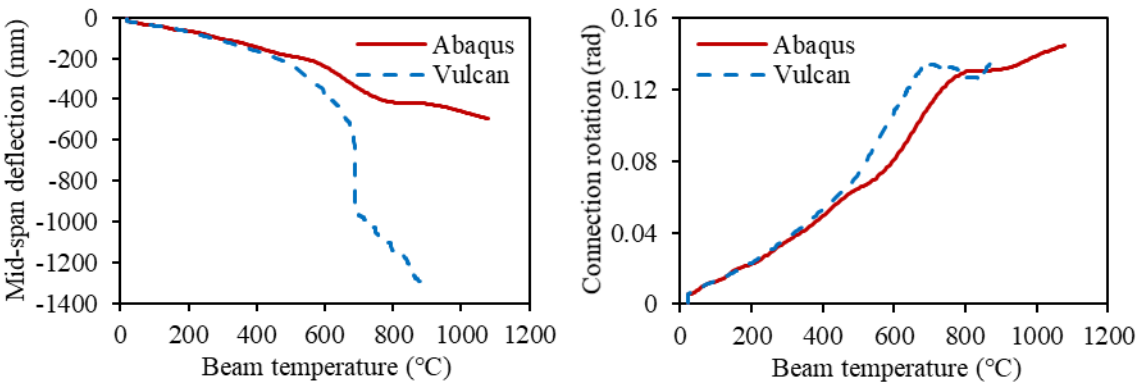

(a) Mid-span deflection

(b) Connection rotation

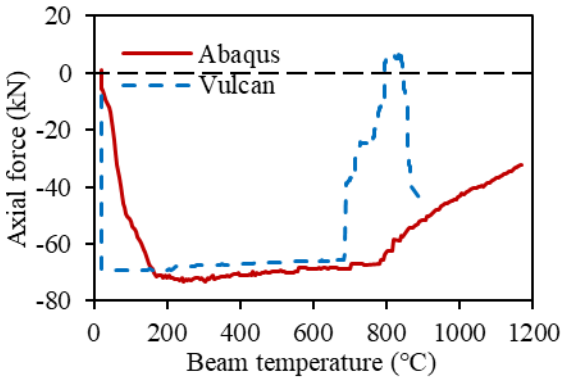

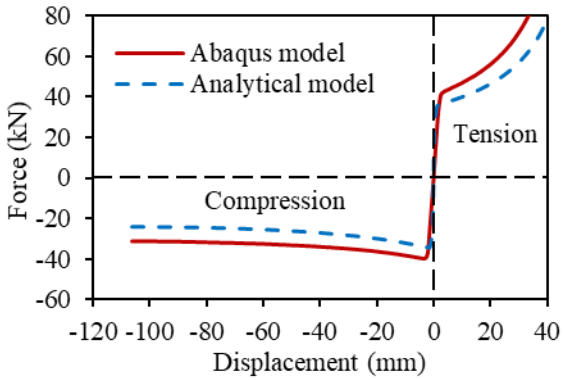

(c) Axial force of connection

(d) Comparison between the push-pull curve of Abaqus model and that of analytical model

Figure 6-9. Comparison between Vulcan and Abaqus

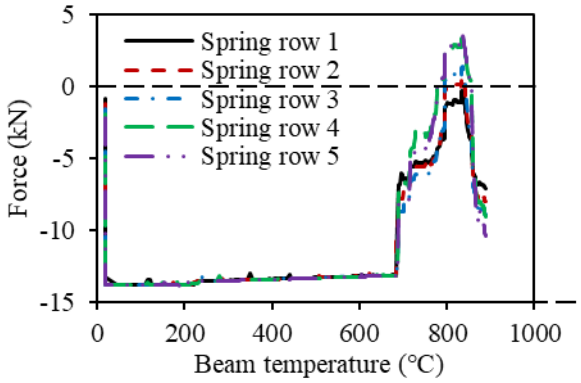

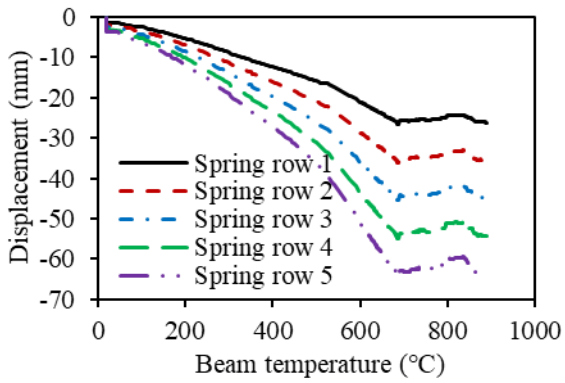

(a) Temperature-force curves

(b) Temperature-displacement curves

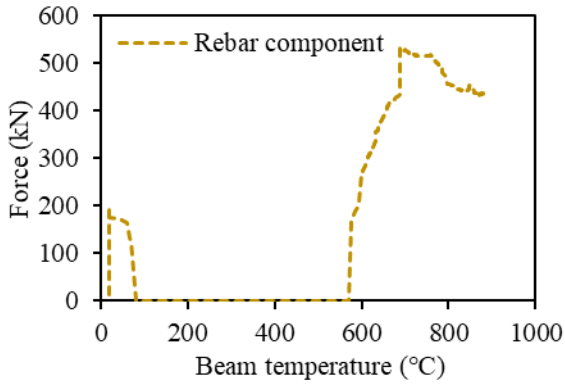

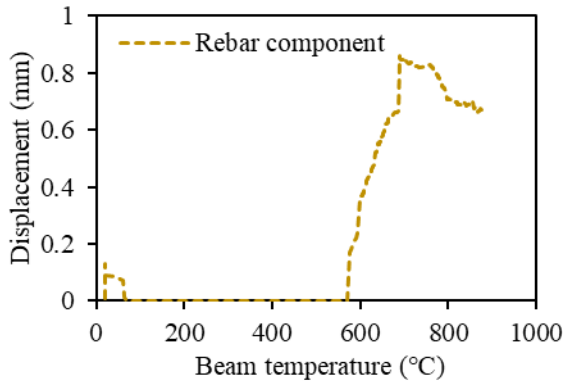

(c) Temperature-force curve of rebar

(d) Temperature-displacement curve of rebar

Figure 6-10. Temperature-force and temperature-displacement curves of each spring row and rebar component

Figure 6-10 (c) and (d) show the temperature-force and temperature-displacement curves of the rebar component of the Vulcan model, which works only in tension. It is temporarily active at

ambient temperature due to the hogging moment applied to the connection; it then remains inactive until about 600°C, since the beam's thermal expansion compensates for the tensile displacement of the rebar component. After the activation of the rebar component, the discrepancy between results from the Vulcan and Abaqus models begins to increase, as shown in Figure 6-9 (a) and (c). At 689°C, the force in the rebar component increases almost vertically; this is caused by a sudden increase of beam deflection (shown in Figure 6-9 (a)), as all the spring rows enter the unloading stage, which is manifested by the sudden decrease of the compressive forces of all the spring rows, as shown in Figure 6-10 (a). Most Vulcan results show a slight oscillatory pattern, which is caused by the large unloading stiffness of the connection element. It is assumed that the unloading stiffness of the spring row in the connection element is the same as the initial elastic loading stiffness, and the initial elastic loading stiffness of the ductile connection is very large. This leads to a sudden change of the spring force when unloading occurs, which is manifested by the slight oscillatory pattern of the Vulcan result curves. In addition to this, the concrete model used in the slab elements models cracking at different levels within the elements. This causes the tensile stresses at various locations to vanish abruptly as the loading or heating proceeds. In general, the performance of the Vulcan composite connection element is satisfactory compared with the detailed model in Abaqus, indicating that the Vulcan composite connection element which has been developed can be used to investigate the effect of utilising the ductile connection within a composite structure in fire conditions. However, the rather large unloading path used in the current component-based models can lead to a sudden change of the spring row force when unloading occurs, which is one of the main reasons for the differences between the results of the Vulcan composite connection element and those of the Abaqus connection model. Therefore, a softer unloading path is needed to further improve the composite connection element in the future.

6.3.3. Parametric studies using Vulcan

In this section, the 2-D composite frame model shown in Figure 6-7 (b) is used for a series of parametric studies. The effects of three parameters (the connection thickness, the inner radius of the semi-cylindrical section and the number of longitudinal bars within the effective width of the slab) are studied. As shown in Figure 6-11, an increase in connection thickness leads to a decrease

in connection ductility. Frames experience lower mid-span beam deflection, smaller connection rotation, larger connection axial force, larger rebar component force, and smaller axial displacement at the beam end, as their plate thickness increases. As mentioned previously, the inner radius of the semi-cylindrical section is a key parameter, determining the connection's axial deformation capacity, and should be determined on the basis of the ductility demands obtained using Equations (6-1) - (6-4).

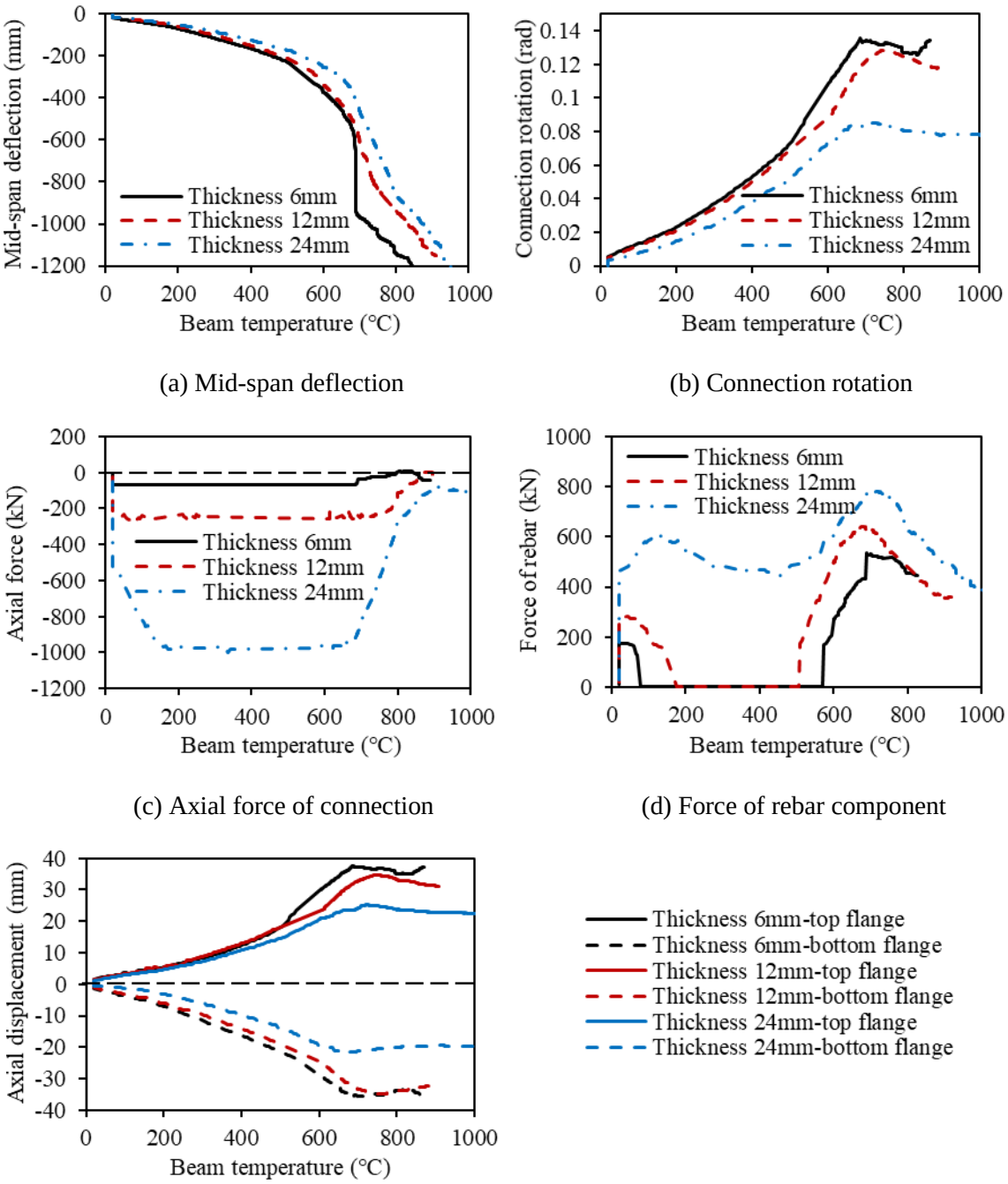

(a) Mid-span deflection

(b) Connection rotation

(c) Axial force of connection

(d) Force of rebar component

(e) Axial displacement at beam end

Figure 6-11. Different connection thickness

The effect of the semi-cylindrical section's inner radius on the connection's behaviour is shown in Figure 6-12. This figure shows that connections with larger inner radii have higher axial ductility, which can significantly reduce the forces in the connection and reinforcing bars, compared with connections of smaller inner radii. However, the influence of the cylindrical section radius on the mid-span beam deflection, connection rotation and beam end axial displacement are not obvious below about 500°C. Above 500°C, the mid-span beam deflection and connection rotation of the composite frame models with larger cylindrical section radius are smaller than those of the same frame with smaller radii. Although increasing the cylindrical section radius can effectively improve the axial deformation capacity of the ductile connection, it should be noted that an excessive increase in this radius may hinder the installation of bolts in the face-plate part of the connection, and may lead to hard contact between the semi-cylindrical section and the face-plate. Therefore, the limitation on the dimensions of the various parts of the ductile connection does not generally depend on the analytical aspects of its behaviour, but on the constraints of practical construction.

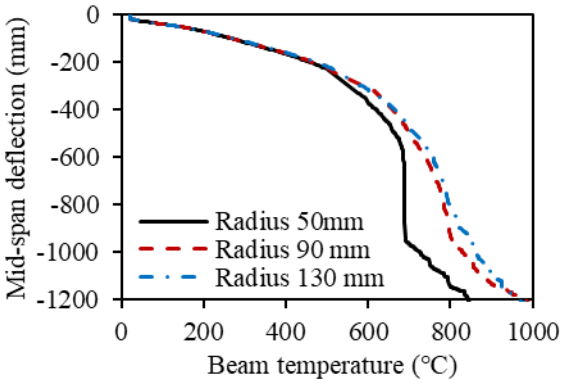

(a) Mid-span deflection

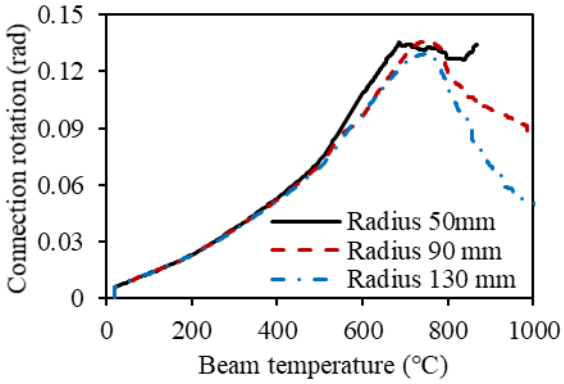

(b) Connection rotation

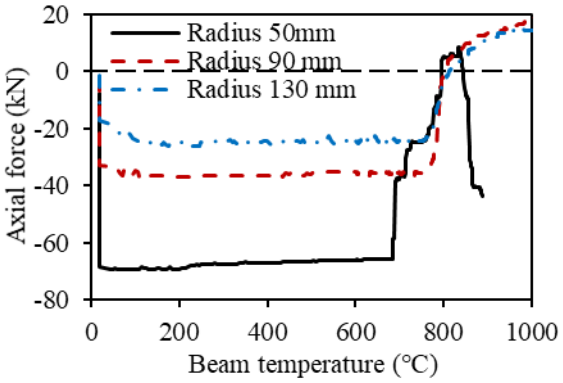

(c) Axial force of connection

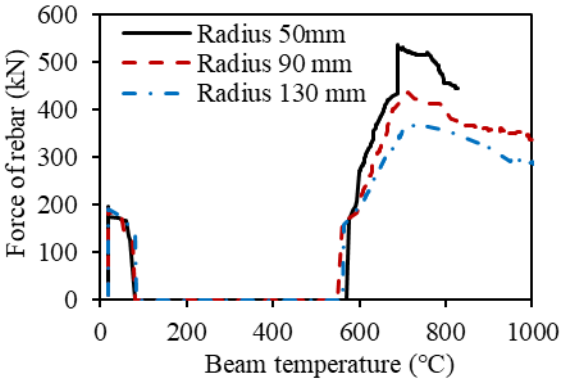

(d) Force of rebar component

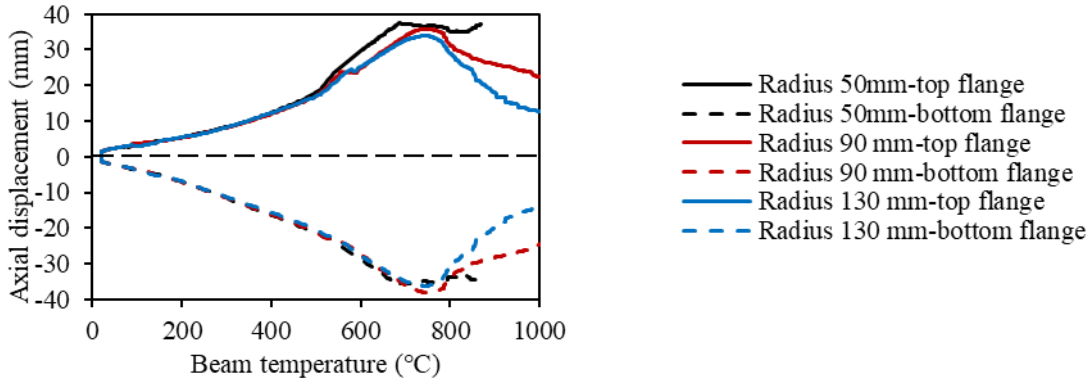

(e) Axial displacement at beam end

Figure 6-12. Different inner diameter of the semi-cylindrical section

The difference between the component-based model of the bare-steel ductile connection and that of the composite version is the introduction of the rebar component. Therefore, the effect of the number of longitudinal bars on the behaviour of the composite connection is also worth attention. In general, composite ductile connections with fewer longitudinal bars are prone to premature failure. It can be seen from Figure 6-13 (a) and (b) that the mid-span beam deflection and connection rotation of the composite frame model with 7 bars increase rapidly at 688°C. This is caused by the failure of the rebar component (Figure 6-13 (d)). The connection axial force of this model changes suddenly from compression to tension at 688°C, when the bars fail, and then carries on increasing in tension from this point (Figure 6-13 (c)). At the same time, the axial displacement of the beam bottom flange at beam end changes from compressive to tensile, which is a first indication of run-away failure of this model.

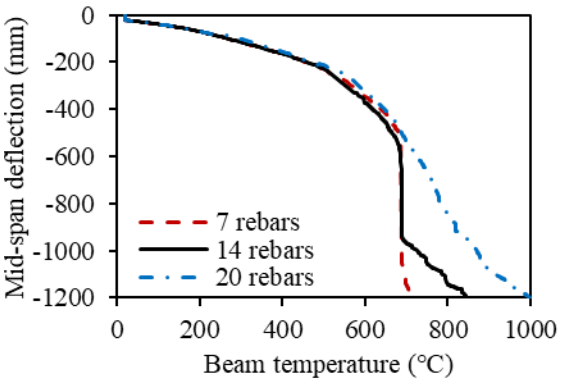

(a) Mid-span deflection

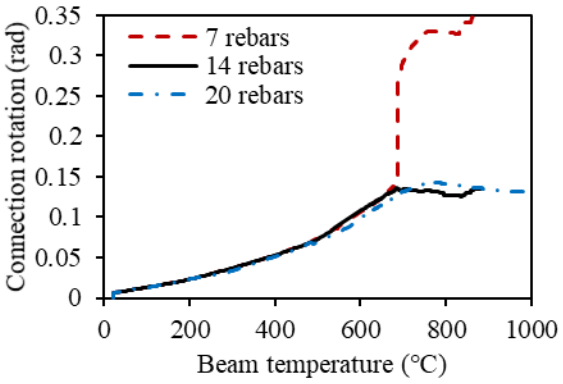

(b) Connection rotation

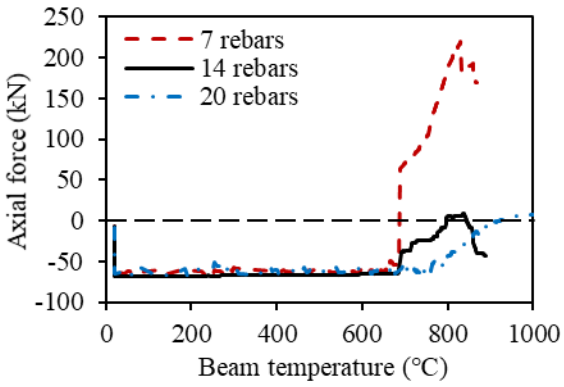

(c) Axial force of connection

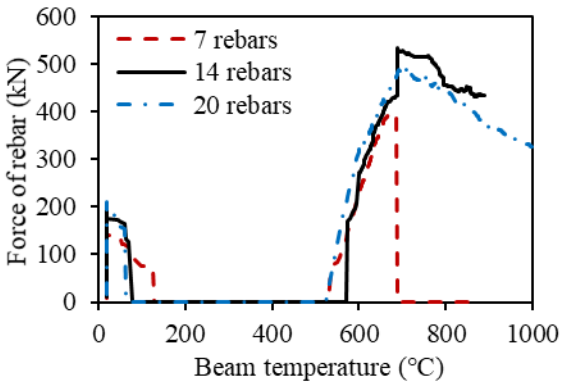

(d) Force of rebar component

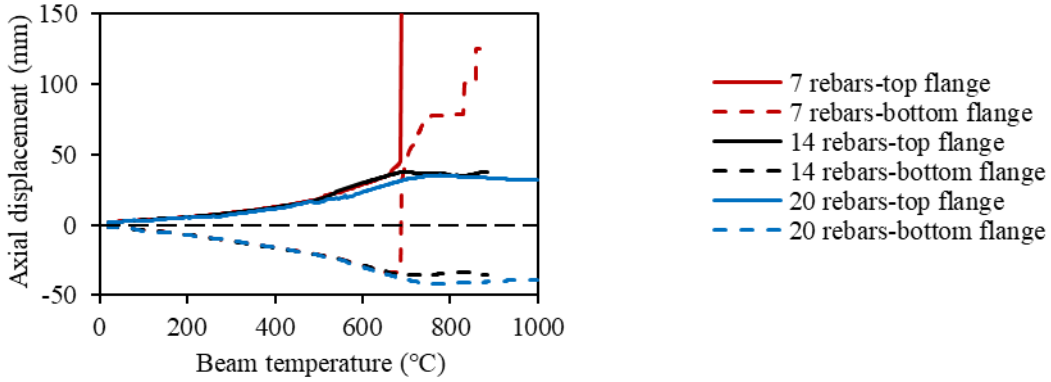

(e) Axial displacement at beam end

Figure 6-13. Different number of longitudinal rebars

Figure 6-14 shows the temperature-force and temperature-displacement curves of each spring row of this model. Row 1 fails at 831°C, at which point the forces in the remaining spring rows increase suddenly. Among these, the force increase in Row 2 is the largest, and this spring row fails at a slightly higher temperature (859.5°C). The failure of Rows 1 and 2 results in an increase of connection rotation and the axial displacement at the beam end in a stepped manner, as well as a stepped decrease in connection axial force, as shown in Figure 6-13. Although increasing the number of longitudinal bars can effectively delay the failure of the composite ductile connection, the additional cost of doing so should also be considered. In addition, the spacing of rebars should not be less than the minimum spacing specified in the Eurocode. The minimum spacing of reinforcing bars should be greater than the reinforcing bar size, the maximum aggregate size + 5mm or 20mm (CEN, 2004b). In the immediate vicinity of the connection the spacing has to be sufficient to bypass the column with an adequate clearance.

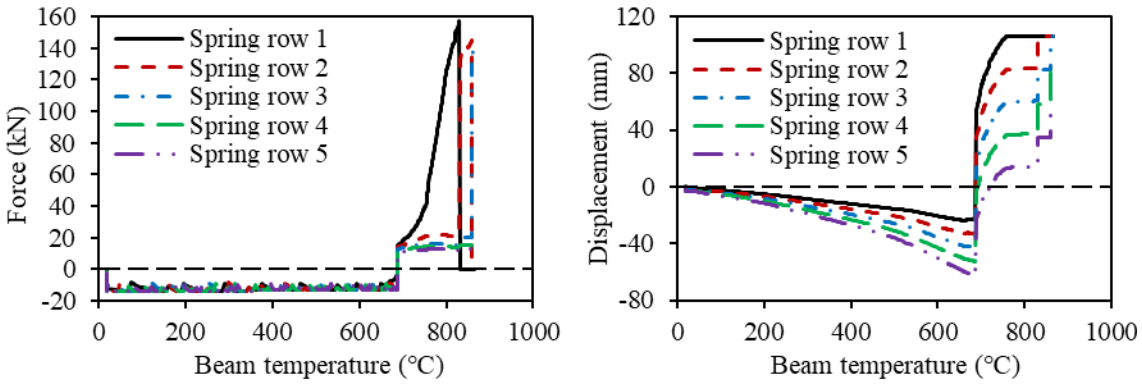

(a) Temperature-force curves (b) Temperature-displacement curves

Figure 6-14. Result curves of each spring row in the model with 7 rebars

6.4. Abaqus sub-frame model

The function of shear studs is to connect the slab and steel beam, transmitting the horizontal shear force between the two. The moment capacity of the composite beam can be reduced if partial-strength shear connection is applied. Therefore, shear studs are very important components in composite structures. It is therefore useful to investigate the influence of shear studs on the performance of the composite ductile connection. However, the shear studs are not included in the Vulcan composite connection element, and so it was decided to establish a composite frame model (Figure 6-7 (b)) in Abaqus to study the influence of shear studs. The behaviour of the steel decking on which the concrete is cast cannot be guaranteed in a fire. The thin steel deck heat much more quickly than the concrete, and usually separates from it under the influence of its own local thermal expansion. The steel deck is of little importance at high temperatures, and is therefore neglected to simplify the Abaqus model, and to save computational cost.

6.4.1. Concrete material model

The nonlinear behaviour of uniaxially compressed concrete at different temperatures is represented by a series of stress-strain curves as shown in Figure 6-15. In compression, the stress-strain relationship given by EC2 (CEN, 2004a) is used, in which a linear descending branch is adopted for each curve. As for concrete in tension, it is assumed that the tensile stress increases linearly with respect to strain until concrete cracking occurs, after which the stress decreases

linearly to zero, and the strain corresponding to zero stress is taken as 10 times the cracking strain, as suggested by the Abaqus user's manual (Hibbett et al., 1998). In this work, the tensile strength of concrete is set to be 10% of the compressive strength (Pi et al., 2006), and the total tensile strain of concrete is assumed to be 0.1 (Liang et al., 2005). The Concrete Damage Plasticity model in Abaqus, which is suitable for materials with different tensile and compressive strengths, is adopted for concrete solid elements in this model. This material model combines the concepts of isotropic damaged elasticity and isotropic tensile and compressive plasticity to represent the inelastic behaviour of concrete. The yielded parts of the tensile and compressive stress-strain curves of concrete are entered separately into the model. The material dilation angle and eccentricity parameter are taken as 20° and 0.1, respectively. The ratio of biaxial to uniaxial compressive strength is taken as 1.16. The stress-strain relationship of carbon steel without consideration of strain-hardening specified in Eurocode 3 Part 1-2 (CEN, 2005b) at elevated temperatures is adopted to simulate beam, column and ductile connection. This is widely used, although it is an implicit-creep model based on transient testing. The current analysis does not consider the effects of high-temperature creep explicitly.

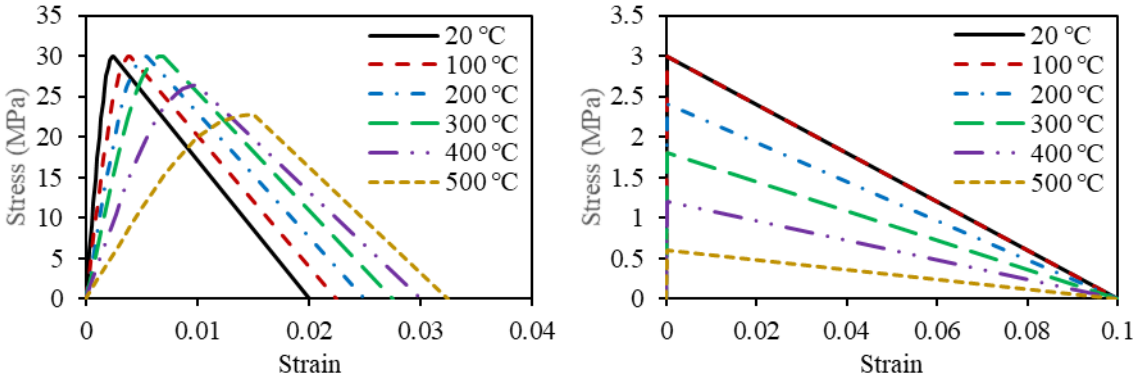

(a) Compressive stress-strain curves (b) Tensile stress-strain curves

Figure 6-15. Concrete material model

6.4.2. Interaction and boundary conditions

In order to reduce the model size and to save computational cost, only a quarter of each model was built, as shown in Figure 6-16 (a).

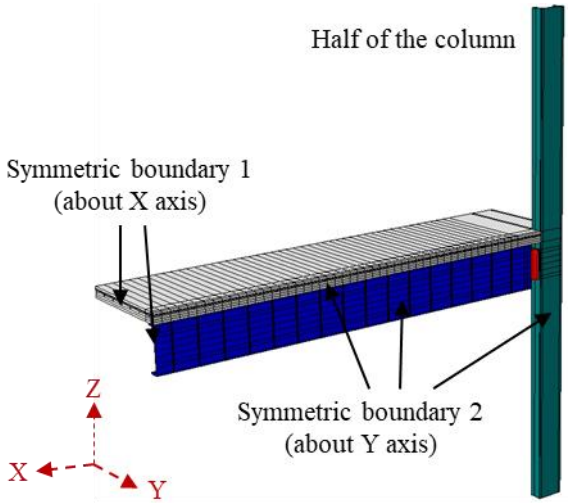

(a) Boundary conditions

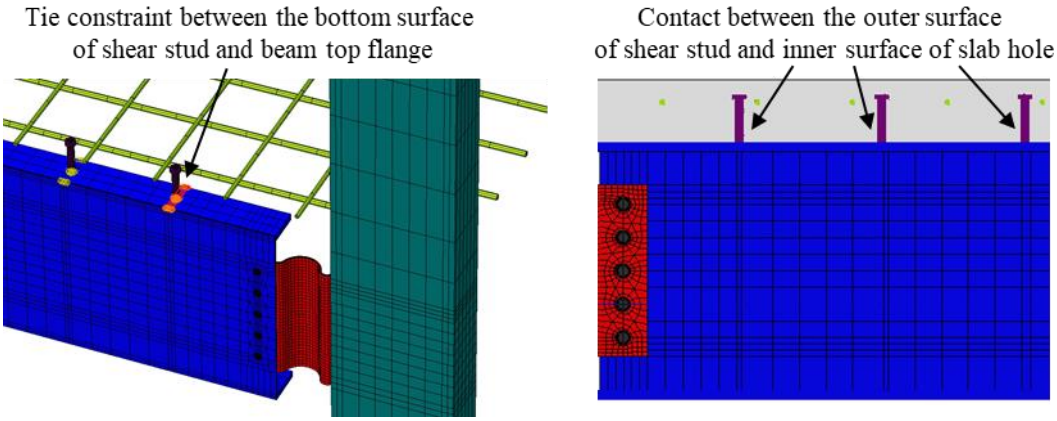

(b) Method of simulating shear studs

Figure 6-16. The Abaqus composite frame model

The X-Z plane is assumed as a plane of symmetry throughout the model, and the Y-Z plane is assumed as a plane of symmetry at the mid-span of the composite beam. Since the purpose of these Abaqus models is to investigate the influence of shear studs on the performance of the composite ductile connection, detailed shear studs are modelled using solid elements. The bottom surface of the shear stud is tied to the steel section's top flange. A cavity is created in the slab at the position of each stud, and then hard contact between the outer surface of the stud and the inner surface of the cavity is established. Other contacts, such as contact between the slab bottom surface and steel section top flange, and those between the connection surface and beam web and the bolt shank and bolt hole, are all included in these Abaqus models. All the reinforcing bars are embedded in the slab. The slab is connected to the column using a tie constraint in the Abaqus frame model.

6.4.3. Validation against experiments

Limited research exists on the performance of composite connections in fire, and there is limited experimental evidence for comparison. The experiments used to validate the modelling methodology are a series of tests carried out by Al-Jabri (1999). Al-Jabri used a cruciform test arrangement with a furnace wrapping the connection zone to conduct these high-temperature experiments. His Group 5 (FLC-5) tests are selected for this validation. The experimental setup of FLC-5 consists of a pair of UKB 610x229x101 sections connected to a UKC 305x305x137 column by 10mm thick flexible end-plates with 14 M20 Grade 8.8 bolts, as shown in Figure 6-17 (a). The Abaqus model is shown in Figure 6-17 (b).

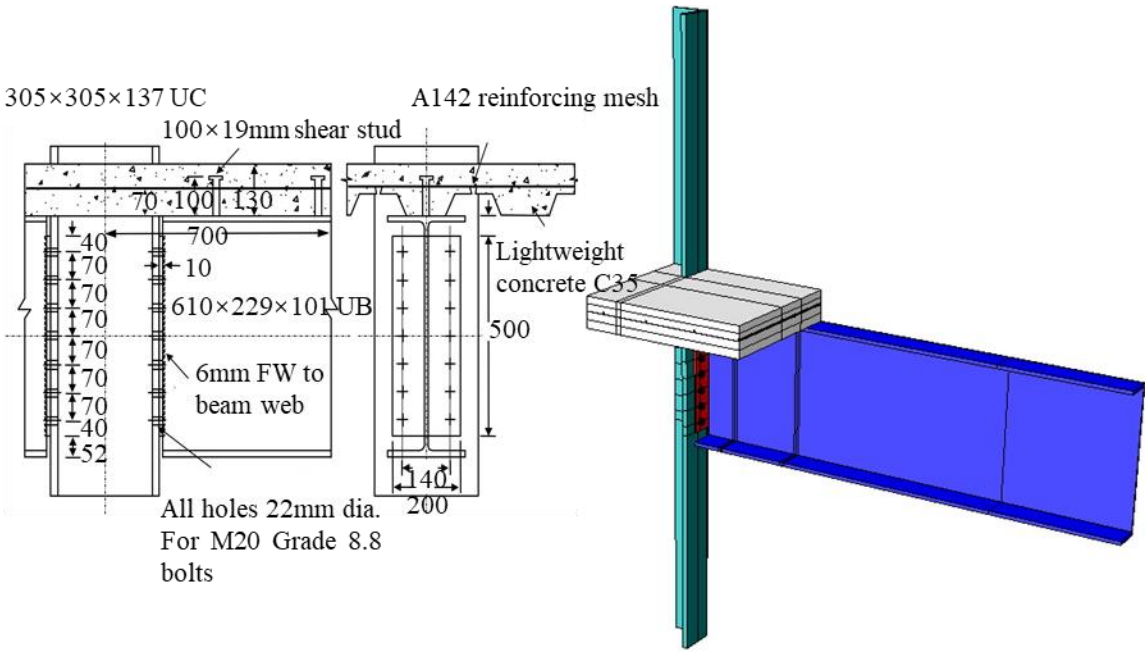

(a) Experimental setup of FLC-5 (Al-Jabri, 1999) (b) Abaqus model

Figure 6-17. The Group 5 tests (FLC-5)

Two tests (FLC-5-2 and FLC-5-3) from this series were modelled. The difference between these two tests is in the applied moment. In FLC-5-2, a moment of 80 kN·m was applied at a distance of 1370mm from the column flange surface, whereas in FLC-5-3, the applied moment increased to 134 kN·m. The comparison between the experimental results and Abaqus simulation results is shown in Figure 6-18. This figure shows that the overall trend of the connection rotation-beam temperature curves obtained from the experiments is very similar to those obtained from the Abaqus models. However, the temperatures at which run-away failure occurs in the experiments

are lower than those of the Abaqus models. This is because, in the tests, run-away failure was caused by longitudinal splitting of the slab. This kind of cracking might cause the shear studs to separate from the slab, essentially turning the composite beam to non-composite, and eventually leading to a sudden increase in the connection rotation. Since such localised cracking is not considered in the Abaqus models, the beams in these models always remain composite. This may explain why the connection rotations of the Abaqus models are lower than those of the experiments. Other than this, the comparisons between the modelling and test results are satisfactory, validating the simulation method of the Abaqus models.

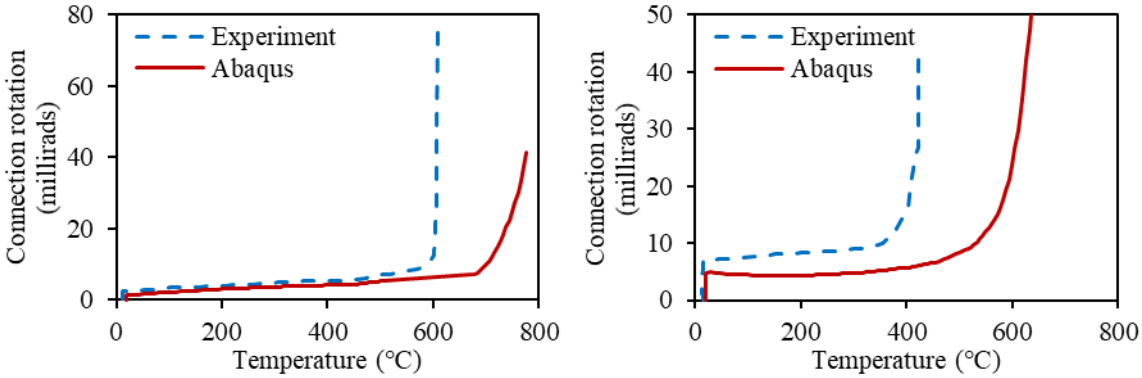

(a) FLC-5-2 (b) FLC-5-3

Figure 6-18. Comparison between experimental results and Abaqus results

6.4.4. Parametric studies using Abaqus model

In this section, the Abaqus model shown in Figure 6-16 (a) is used to conduct parametric studies on the influence of the shear studs on connection performance. It is assumed that the temperatures of beam web and top flange are 90% of the temperature of the beam bottom flange. The lower column and the connection are protected to the same level, and their temperatures are therefore set to 60% of the temperature of the beam bottom flange, whereas the upper column is assumed to remain at 20°C. The temperature of the slab bottom surface is assumed to be the same as that of the beam top flange, and its top surface is assumed to remain at 20°C throughout the analysis. The temperature distribution through slab depth is assumed to be linear.

As mentioned previously, the moment capacity of the composite beam could be reduced in cases of partial shear connection. Three different shear stud spacings are selected here, and their corresponding degrees of shear connection are listed in Table 6-2.

Table 6-2. Degrees of shear connection corresponding to different shear stud spacings

Spacing of shear studs (mm)	Degree of shear connection
200	106.84%
500	42.74%
1000	21.37%

The comparative results for the composite frame models with different shear stud spacings are shown in Figure 6-19. It can be seen that the variation of stud spacing has negligible influence on the beam mid-span deflection, connection rotation, axial force in the connection and axial displacements of the top and bottom flanges of the steel section at the beam end. The only significant difference is in the beam end slip, as shown in Figure 6-19 (d). In this figure the slip is defined as positive when the steel section's top flange moves away from the column-face and the lower surface of the slab moves towards the column-face. If the degree of shear connection is low, the connection between the slab and steel section is weak, then they will bear the external loads more like two unconnected members. In this case, under the action of external loads at ambient temperature, the bottom surface of the slab will stretch, while the top flange of the steel section will contract, resulting in a positive beam end slip. Therefore, the composite beam with the largest stud spacing (1000mm) experiences the largest initial positive beam end slip at ambient temperature. With increase of temperature, the steel beam expands more than concrete due to the non-uniform temperature distribution, leading to the observed change in beam end slip from positive to negative. Compared with the other two cases, the composite beam with the smallest stud spacing (200mm) experiences the smallest negative beam end slip, because the slab provides the highest constraint to the thermal expansion of the steel beam among the three cases.

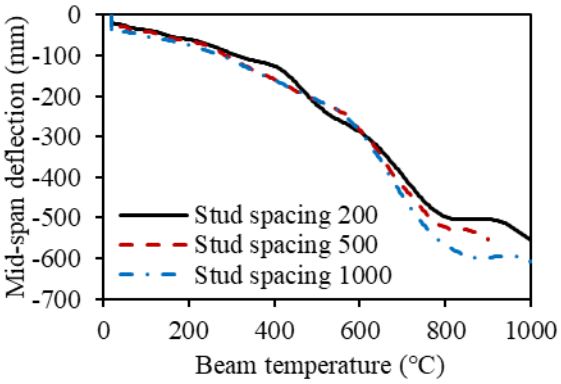

(a) Mid-span deflection

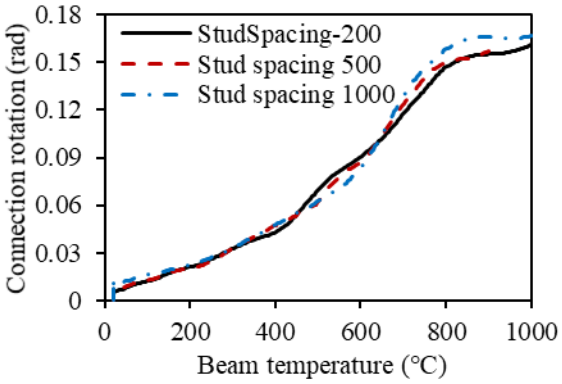

(b) Connection rotation

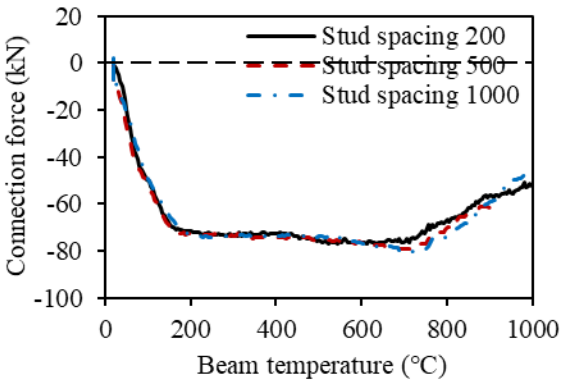

(c) Axial force of connection

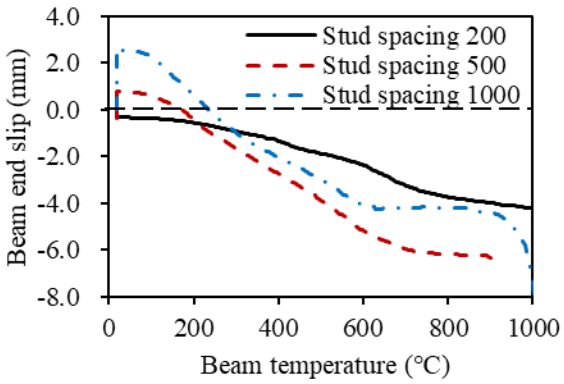

(d) Beam end slip

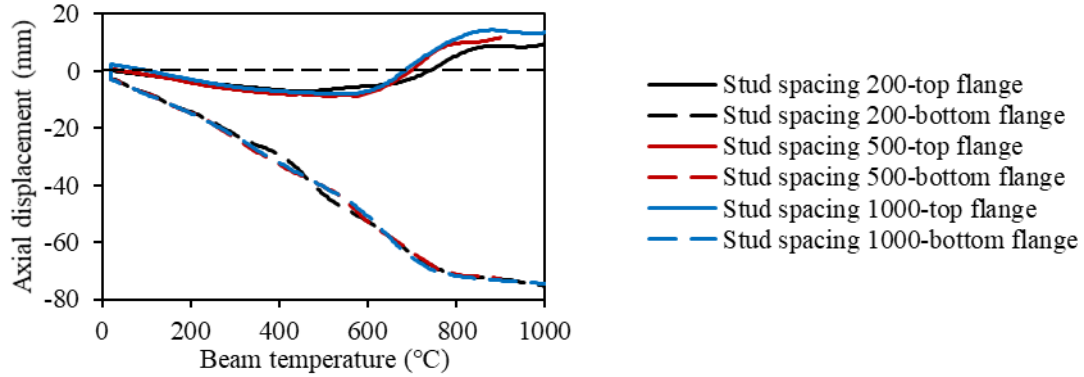

(e) Axial displacement at beam end

Figure 6-19. Comparison of the composite frame models with different stud spacings

6.5. Chapter conclusion

This chapter has studied the influence of the ductile connection on the behaviour of composite beams in fire conditions. Four equations have been proposed to calculate the axial ductility demands of the composite beam at four key positions of the cross-section; the reinforcement layer, the connection top surface, the connection bottom surface, and the beam bottom flange. The deflection caused by the thermal bowing of the composite beam was included within the beam's total deflection in order to consider the effect of the concrete slab. A component-based model of the composite ductile connection has been established by adding the reinforcement component to the bare-steel ductile connection model developed in Chapters 4 and 5. The component-based composite ductile connection model has been converted into a connection element following the principles of the finite element method, and incorporated into the software Vulcan. A 2-D composite frame model with ductile connections has been modelled using both Vulcan and

Abaqus; the latter has used a detailed model of the connection's geometry using solid elements. Parametric studies on three design parameters were carried out, including the connection thickness, the cylindrical section radius and the number of longitudinal bars in an effective width. Since the shear studs are not considered in the component-based composite ductile connection model, detailed Abaqus composite framed models were created to investigate the effect of shear studs on the performance of the composite ductile connection under different stud spacings. The Abaqus modelling approach was validated against the experiments previously conducted by Al-Jabri. The following conclusions can be drawn based on these studies:

- The proposed reinforcement component can consider the pull-out of longitudinal bars across a discrete crack above the connection, and the physical anchorages provided by the weld points to transverse bars in the welded mesh.
- The comparison between Vulcan and Abaqus results shows that although the connection in the Abaqus model is stiffer than that in the Vulcan model, the proposed component-based composite ductile connection model can efficiently represent the behaviour of the composite ductile connection without going to the extent of creating a full model using solid elements.
- It was found from the parametric studies that thinner plate thickness and larger cylindrical section radii lead to higher axial ductility, which significantly reduces the axial force carried by the connection. Lower numbers of longitudinal reinforcing bars tend to lead to early failure.
- The variation of stud spacings has little influence on the beam's mid-span deflection, connection rotation, connection axial force or the axial displacements of the top and bottom flanges of the steel section at the beam end. The only substantial difference is in the end slip between the steel section and the concrete slab. Composite beams with lower degrees of shear connection experience an initially positive end slip at ambient temperature, which becomes negative as the steel section temperature rises due to the thermal expansion

7.

THREE-DIMENSIONAL MODELLING OF COMPOSITE FRAMES WITH DUCTILE CONNECTIONS

7.1. Chapter introduction

In the previous chapter, the component-based model of the composite ductile connection has been developed, and isolated composite beam models with ductile connections have been created to carry out parametric studies. However, structural elements in a composite steel-framed floor system always interact with each other and work as a whole. The influence of the out-of-plane structure, particularly slabs, on the connection performance cannot be accounted for by isolated composite beam models. Elghazouli et al. (2000) created 3-D high-temperature grillage composite floor models using the non-linear numerical modelling software ADAPTIC, in which all the slabs, beams and columns were represented by cubic elasto-plastic beam-column elements. These models were validated against two of the Cardington full-scale fire tests. Lamont et al. (2004) used Abaqus to simulate a small generic composite steel frame and compared the structural performance of the frame under two different single-floor compartment fire scenarios. Suwondo et al. (2019) studied the progressive collapse of composite steel frames exposed to fire after earthquake, using a 3-D Abaqus composite building model, in which connection failures were not considered and all the connections were simplified either as ideally rigid or pinned.

Simulating a full 3-D composite frame in commercial finite element software (e.g., Abaqus) is extremely time-consuming, since it involves a huge number of elements and usually requires a dynamic explicit solver. In addition, to allow for reasonable computing times, most researchers had to use idealised connections when building 3-D composite frame models. Vulcan is a specialist software designed for high-temperature global frame analysis. It is capable of simulating the behaviour of 3-D composite structures at elevated temperatures, considering both geometric and material non-linearities. It was, therefore, decided in this research to use Vulcan to conduct the 3-D modelling in fire conditions.

This chapter presents 3-D modelling of composite frames with ductile connections in fire. A single floor panel within a composite frame has been designed according to the typical frame layout adopted in the Cardington fire tests (Lennon et al., 1999, Wald et al., 2004). The 3-D models of this composite frame compartment with different connection types, including the ductile connection, idealised rigid and pinned connections, as well as conventional end-plate and web-

cleat connections, have been created using Vulcan. In order to further save computational cost, the 3-D composite frame compartment model has been reduced to a quarter of the original size by applying planes of symmetry at as many boundaries as possible. These models have also been used to investigate the influence of unconnected length between slab and beam on the connection performance in this research.

7.2. Comparison of the ductile connection with conventional connection types

Due to the contribution of composite slabs, the connection performance in a composite structure is very different from that of a bare-steel structure. When building a composite frame model, the influence of the out-of-plane structure on the performance of the composite connections must be taken into consideration. In this section, 3-D composite frame models with different types of connections are created using Vulcan to compare the performance of ductile connection with other connection types.

7.2.1. 3-D composite frame model

On the basis of the typical frame structure adopted in the Cardington full-scale fire tests (Lennon et al., 1999, Wald et al., 2004), an internal compartment of a composite frame is designed as shown in Figure 7-1. The sections adopted for primary and secondary beams are selected as UKB 356×171×51 and UKB 305×165×40, respectively. The column section is selected as UKC 305×305×198. The thickness of the composite slab is 130mm and A142 mesh is adopted. It should be noted that the composite connection element already includes rebar component, therefore the slab elements above the connections in the models do not contain reinforcement to avoid repetition. It is assumed that fire occurs on the lower floor, including beneath adjacent floor panels, and the standard fire curve is used. The beams on the column grid and the columns themselves are protected to the same level, whereas the central secondary beam is unprotected. The temperatures of all the gridline beams and lower columns are set to 70% of the central secondary beam's temperature, and the upper columns remain at ambient temperature. The temperature of each connection is equal to the temperature of the beam to which it is connected. Taking the permanent load as 3.65 kN/m^2 and the imposed load as 3.5 kN/m^2, the combined load applied on

the slab in the fire limit state should be 3.65+3.5×0.5=5.4 kN/m^2. The detailed dimensions of the ductile connections used in the composite frame are shown in Figure 7-2.

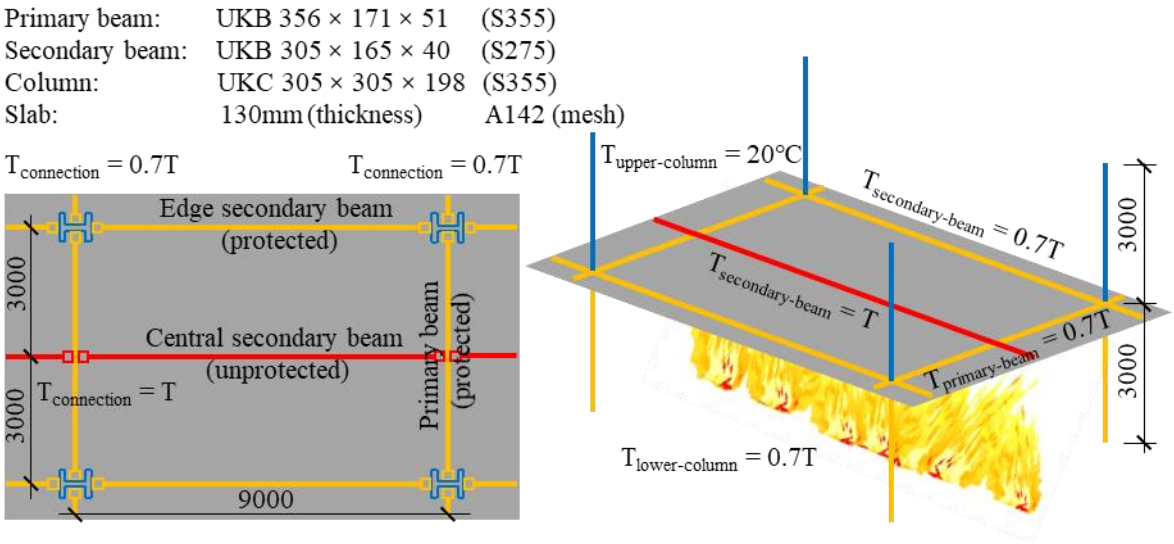

Figure 7-1. Design of the internal compartment of a composite frame (unit: mm)

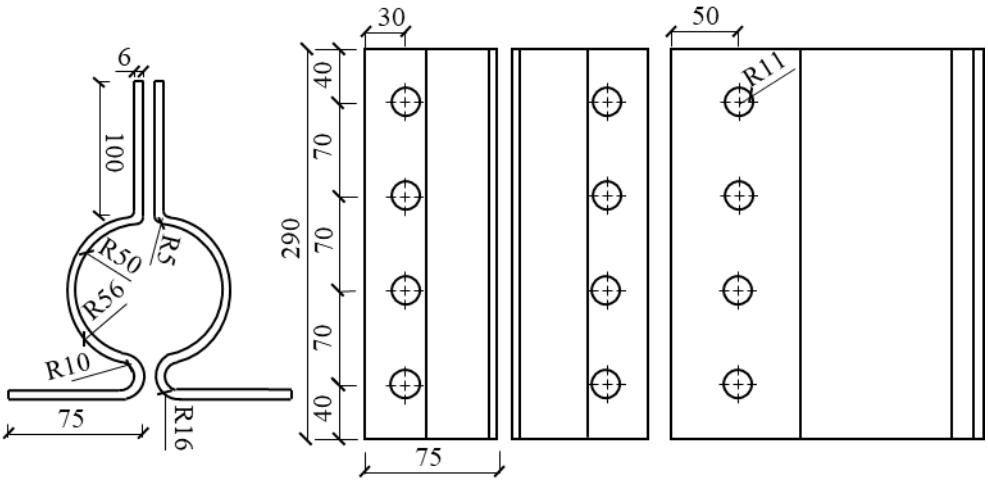

Figure 7-2. Detailed dimensions of the ductile connection (unit: mm)

7.2.2. Comparison of the ductile connection with other connection types

The 3-D composite frame models (Figure 7-1) with different types of connections, including ideally pinned and rigid connections, and the conventional end-plate and web-cleat connections, have been created using Vulcan to compare the structural performance using these connection types. Full shear connection is assumed between the slab and beams, and this is modelled by sharing the nodes between the slab and beam elements. To save computational cost, only a half

of the models is built, and planes of symmetry are applied to the boundaries of each model. The component-based model of bare-steel end-plate connections has already been incorporated into Vulcan by Block (2006), and the component-based model of bare-steel web-cleat connections has been incorporated into Vulcan in this research as described in Chapter 5. Rebar components have now been added to these two models, to model the whole composite joint zone including either end-plate connections or web-cleat connections.

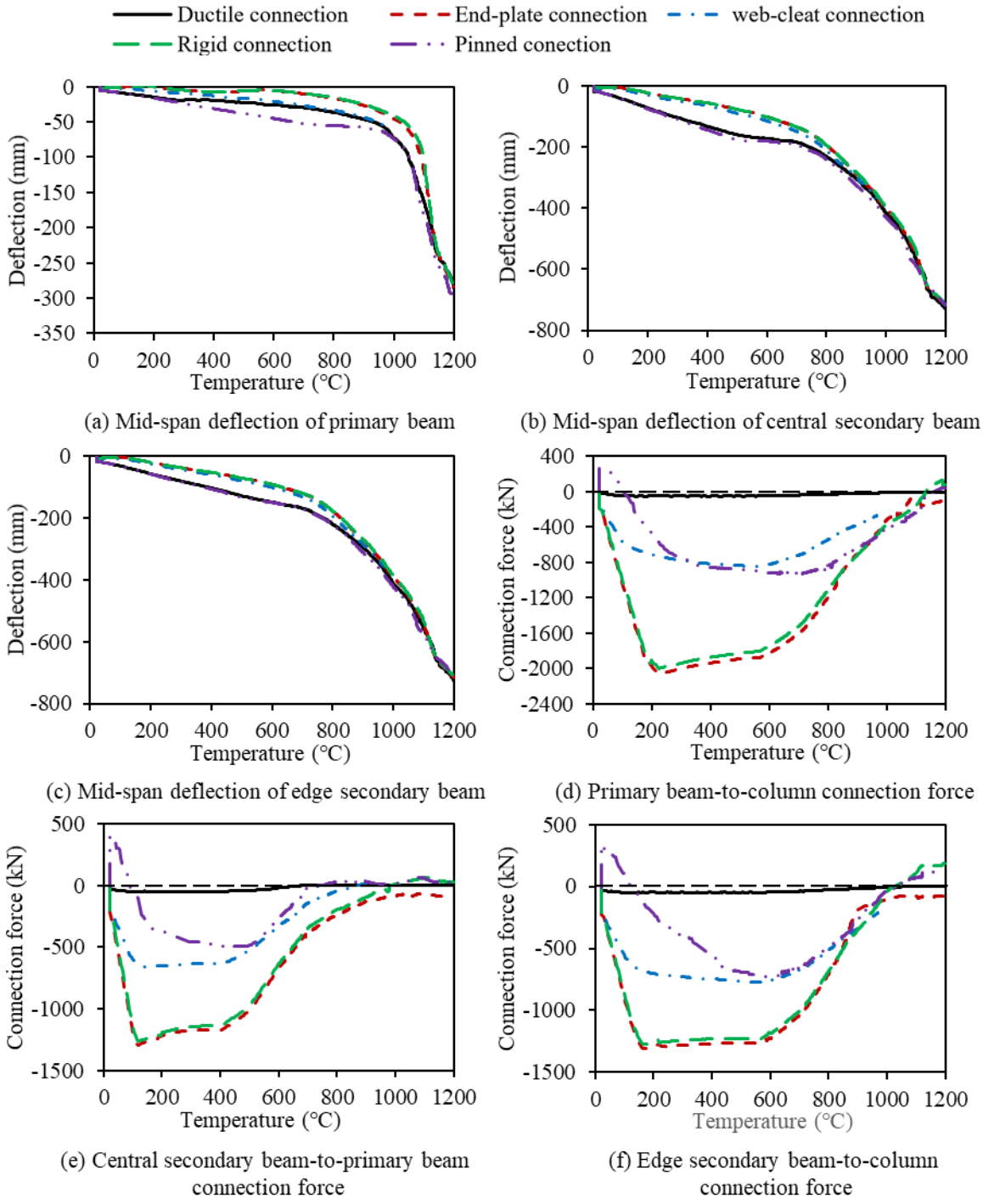

(a) Mid-span deflection of primary beam

(b) Mid-span deflection of central secondary beam

(c) Mid-span deflection of edge secondary beam

(d) Primary beam-to-column connection force

(e) Central secondary beam-to-primary beam connection force

(f) Edge secondary beam-to-column connection force

Figure 7-3. Comparative results (central secondary beam temperature)

The results of the comparison are shown in Figure 7-3 (a) - (c), which shows that altering the connection type has little effect on the mid-span deflections of the primary, central secondary and edge secondary beams. At the same temperature, the deflections of the beams with ductile connections and ideally pinned connections are generally larger than those of the beams with the other connection types. Compared with the other connection types, the axial forces generated in the ductile connections are considerably reduced, as shown in Figure 7-3 (d) - (f). This indicates that the proposed ductile connection can provide satisfactory deformability to accommodate the axial displacement applied by the connected beam in fire without increasing axial force levels markedly.

In order to further illustrate the deformation capacity of the ductile connection, the axial displacements at the ends of beams with different connection types are compared and shown in Figure 7-4. In this figure, the negative value represents compressive displacement, and the positive value represents tensile displacement. It is obvious that the axial displacements at the beam ends with ductile connections are much larger than those of the other connection types, and their values are not even of the same order of magnitude. Looking at the development of the axial displacements at beam ends with ductile connections as temperature increases, the observed increase in the compressive displacements at the beam ends are probably mainly due to the thermal expansion of the steel beam. When the temperature of the central secondary beam exceeds 500℃, the increase in beam curvature caused by the reduced steel strength compensates for the compressive displacement at beam end, resulting in a decrease of the compressive displacement, as shown in Figure 7-4 (b). At around 800℃, the axial displacement at the end of the central secondary beam becomes tensile, indicating that the beam is entering the catenary action stage. After this stage, the tensile axial displacement of the central secondary beam basically remains unchanged and does not continue to increase. It is well known that, at 800℃, the strength of steel has dropped to about 10% of its original strength, and the steel beam has lost most of its flexural load carrying capacity. In this model, the slab is assumed to be kept at ambient temperature, and the concrete has some tensile strength, albeit very low. Therefore, the external load originally borne by the central secondary beam is now largely taken by the tensile membrane action of the concrete slab, and so the tensile axial displacement of the central secondary beam does not increase further. The edge secondary beam is protected, so its axial displacement decreases much

later than that of the central secondary beam. Since the section size of the primary beam is relatively large, and its span is relatively short compared with the secondary beams, the compressive displacement at the end of the primary beam keeps increasing during the whole analysis.

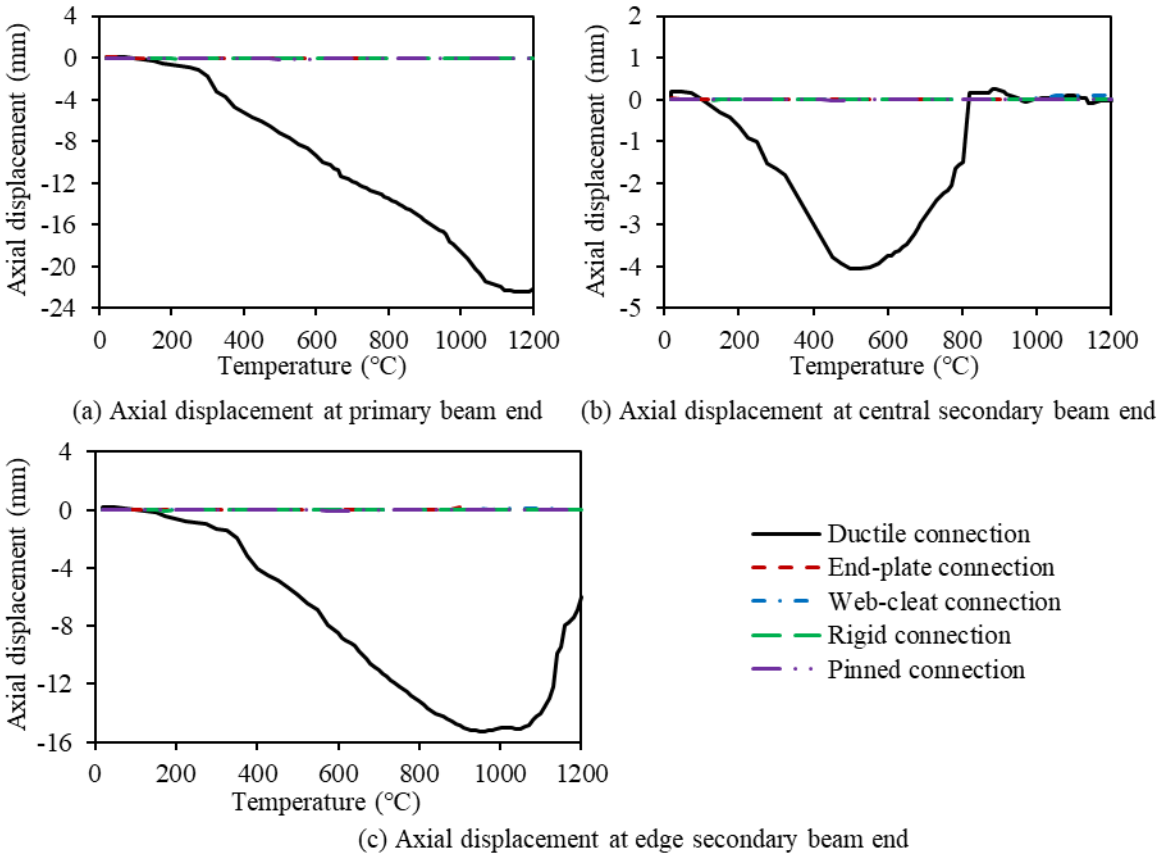

Figure 7-4. Axial displacements at beam ends (central secondary beam temperature)

The deformation of the 3-D composite frame model with ductile connections is shown in Figure 7-5. This figure shows that the ductile connection can provide very high axial ductility, thus accommodating the net contraction of the beam during the high-temperature catenary stage, without fracturing the connection. Figure 7-6 - Figure 7-8 illustrate the force-temperature and displacement-temperature curves for each spring row and rebar component of the primary beam-to-column connection, the central secondary beam-to-primary beam connection, and the edge secondary beam-to-column connection. It is shown in Figure 7-6 that, until about 1100°C, the primary beam has been in the thermal expansion stage, and the compressive displacement of each spring row of the primary beam connection continues to increase. Compared with the primary beam, the edge secondary beam has a smaller cross section and a longer span. Therefore, the edge

secondary beam enters the catenary action stage at a lower temperature (around 900℃) compared to the primary beam. The compressive displacement of each spring row begins to decrease after exceeding this temperature, as shown in Figure 7-8. The central secondary beam is designed to be unprotected, and has a higher temperature than the other beams, resulting in its entering the catenary action stage at a lower temperature compared with the edge secondary beam. At around 700℃, the force in each spring row of the central secondary beam connection becomes tensile, indicating that this spring row has entered the 'pulling-back' stage. The 'pulling-back' stage refers to the pre-compressed connection being pulled back towards its original state as each spring row is gradually pulled back towards its original length. During this period, the tensile force in each spring row also gradually decreases, due to the degradation of the connection's material properties as its temperature rises. The displacement of the rebar component in Figure 7-6 (d), Figure 7-7 (d) and Figure 7-8 (d) represents the crack-width of the concrete slab above the connection, which is determined by the rebar type (the development length of rebar), the weld-point locations of the mesh and the position of the crack. In the connection element, the displacements and rotations of the two connection element nodes are used to determine the axial separation at the rebar level under the plane section assumption, and the rebar component is only activated under tension. Figure 7-6 (d), Figure 7-7 (d) and Figure 7-8 (d) show that the rebar components of all the three connections are temporarily activated below 100℃ due to the hogging moment applied to the connection. Beyond this point, the rebar components of the primary beam and edge secondary beam connections remain inactive, since the beam's thermal expansion compensates for the tensile displacement of the rebar component, whereas the rebar component of the central secondary beam connection is activated again at about 800℃. This confirms that the neutral axis of bending moves during a fire event, as expected. At ambient temperature, the neutral axis of bending is below the rebar. It then moves upward with the increase of temperature in the initial heating stage. When the beam enters the catenary action stage at very high temperatures, the beam has lost most of its bearing capacity and the neutral axis moves below the rebar again, causing the rebar component to be re-activated. In general, compared with other types of connection, the ductile connection exhibits considerable axial deformability in composite frames, which can significantly reduce the forces generated in the connections and prevent premature fracture of connections in fire.

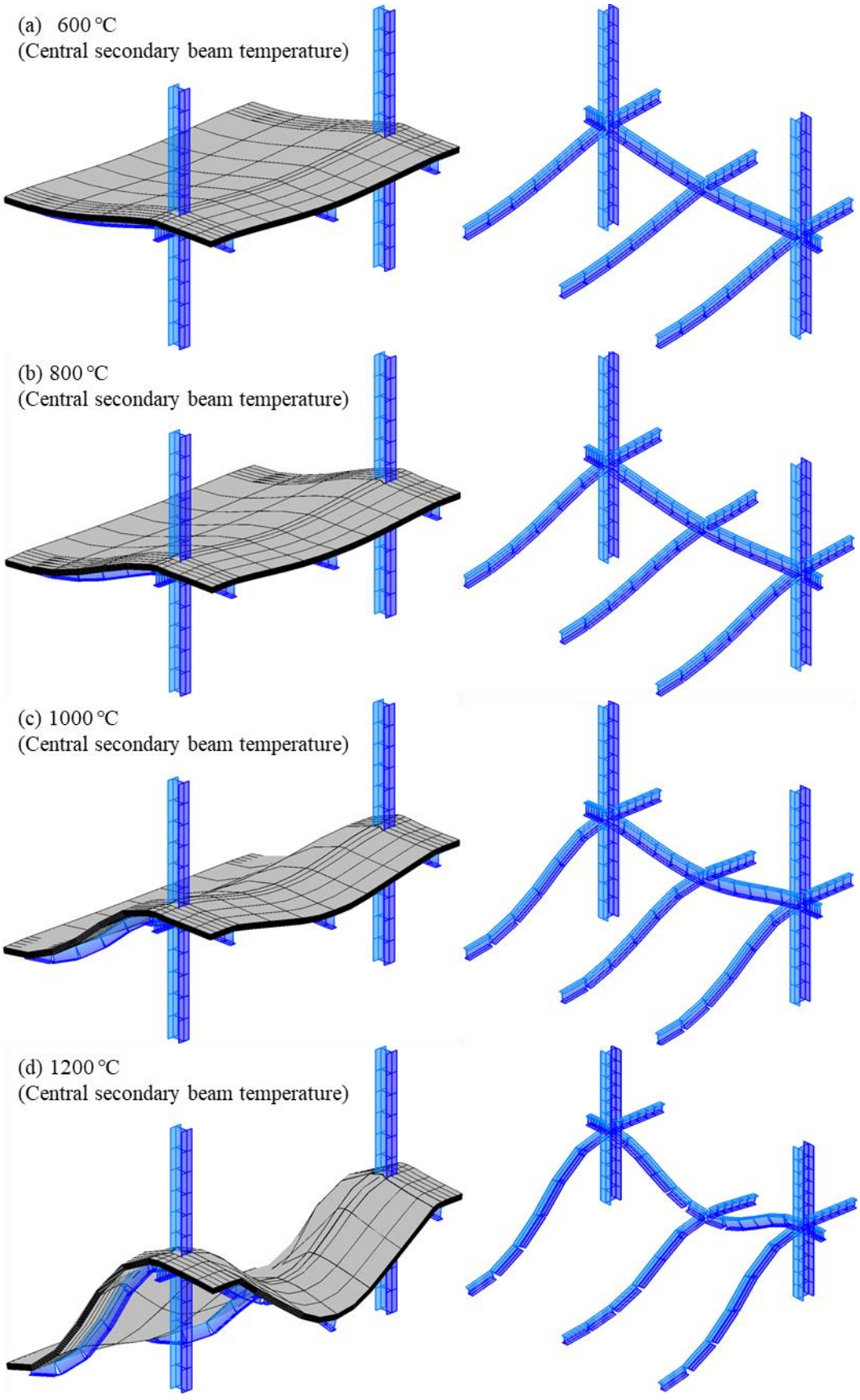

Figure 7-5. Deformations of the 3-D composite frame model (central secondary beam temperature)

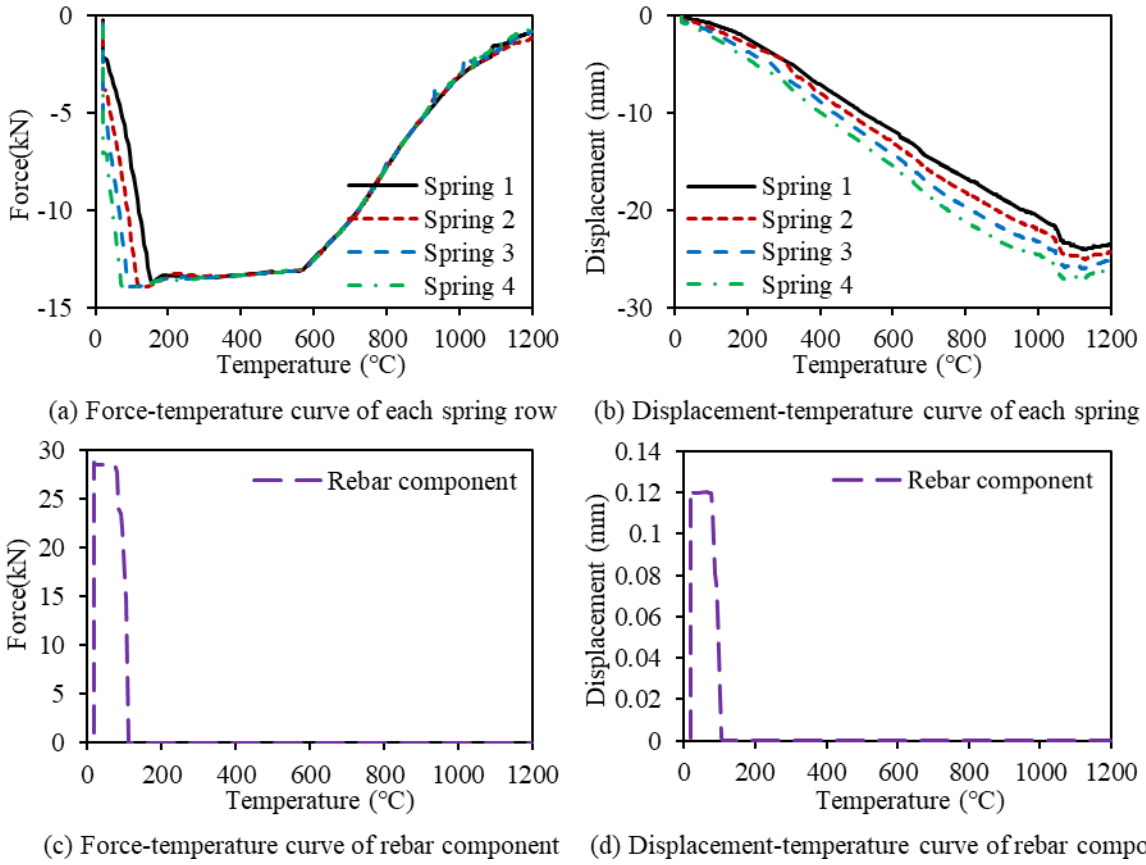

(a) Force-temperature curve of each spring row (b) Displacement-temperature curve of each spring row

(c) Force-temperature curve of rebar component (d) Displacement-temperature curve of rebar component

Figure 7-6. Primary beam-to-column connection (central secondary beam temperature)

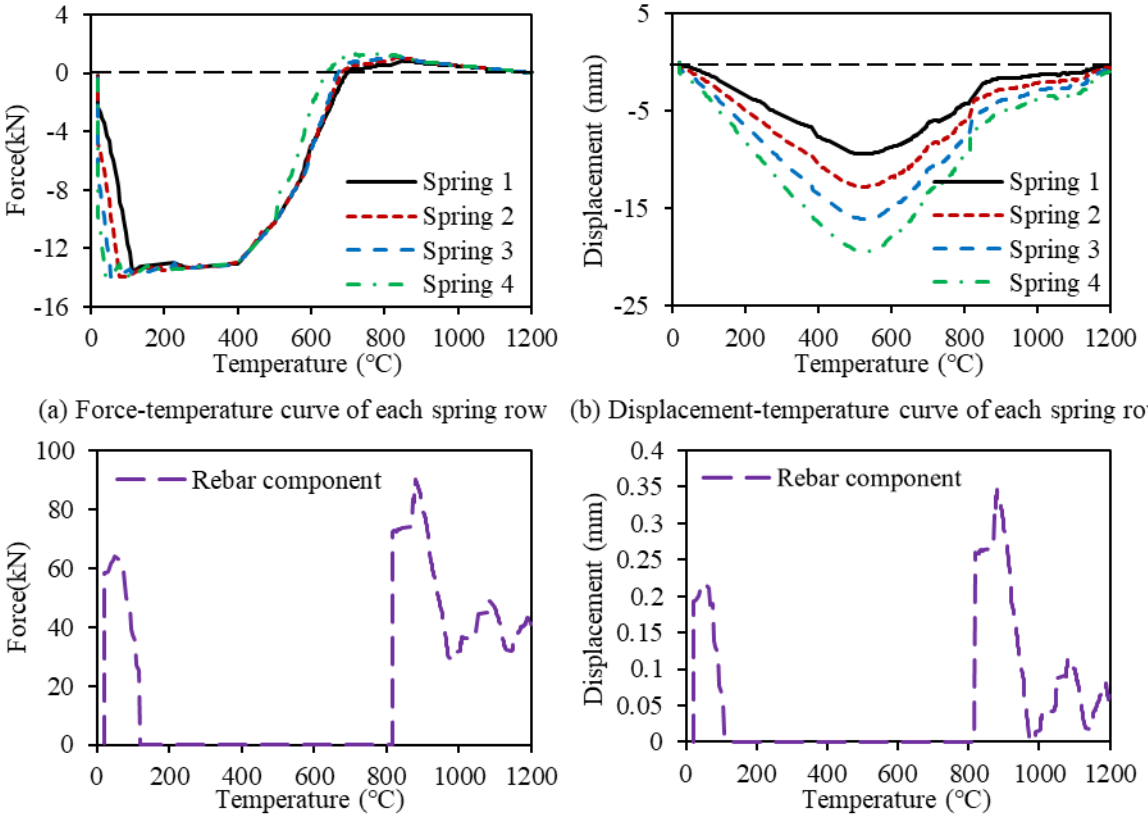

(a) Force-temperature curve of each spring row (b) Displacement-temperature curve of each spring row

(c) Force-temperature curve of rebar component (d) Displacement-temperature curve of rebar component

Figure 7-7. Central secondary beam-to-primary beam connection (central secondary beam

temperature)

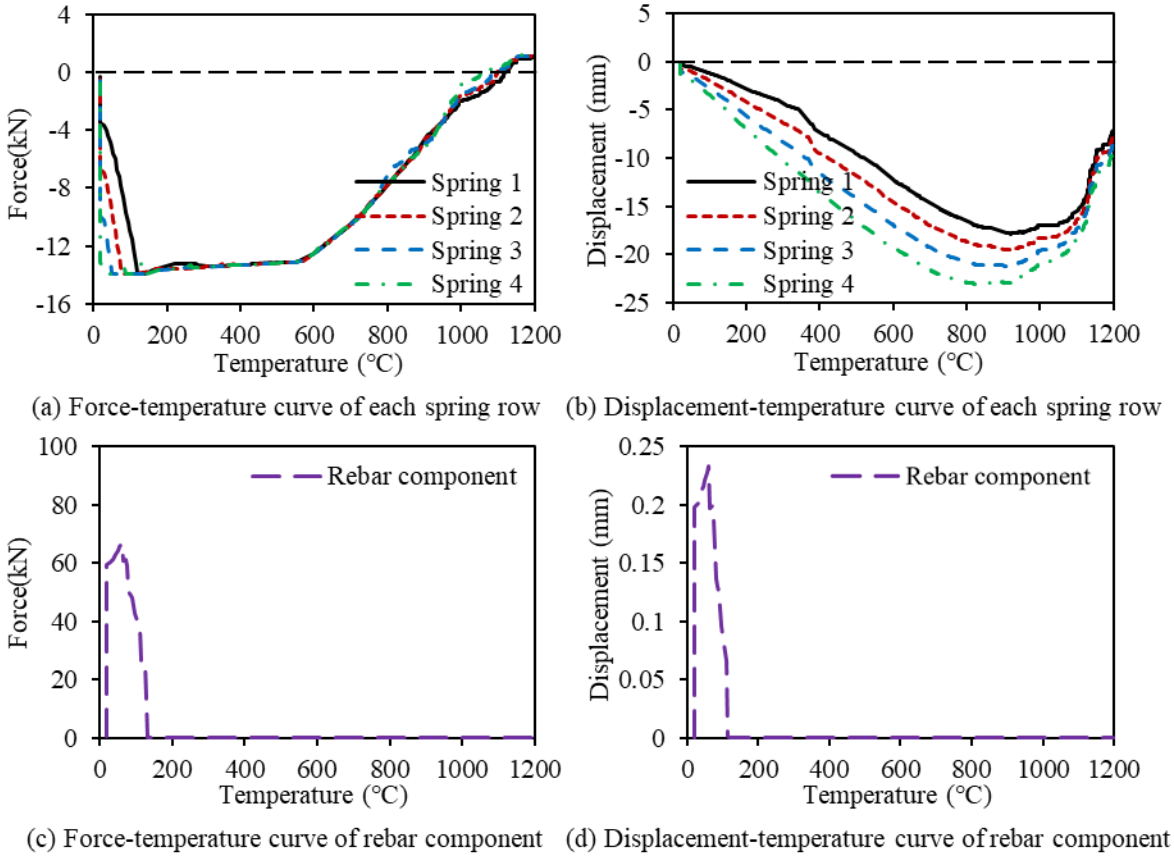

(a) Force-temperature curve of each spring row (b) Displacement-temperature curve of each spring row

(c) Force-temperature curve of rebar component (d) Displacement-temperature curve of rebar component

Figure 7-8. Edge secondary beam-to-column connection (central secondary beam temperature)

7.3. Influence of distribution of shear studs on connection performance

Shear studs are usually uniformly distributed along a beam span. The maximum sagging moment usually occurs at the mid-span, whereas the maximum relative slip between the steel section and slab occurs at the beam ends. Therefore, if the shear studs are concentrated in the central zone of the beam span, allowing the steel beam to move freely relative to the slab at its ends, it might be expected that the thermal bowing deformation of the composite beam would be reduced. It might also be expected that the end-slip would increase (negatively), but this should easily be accommodated by the ductile connection without generating a large axial force. In order to verify this idea, the 3-D composite frame model shown in Figure 7-1 is used in this section to investigate the impact of the shear stud distribution on the performance of the composite ductile connection. The 3-D model shown in Figure 7-1 is a large model of a huge number of elements, which takes nearly a month to run. It was, therefore, decided to build a quarter of the original model and apply

planes of symmetry at the boundaries, as shown in Figure 7-9. The section sizes of the primary, edge secondary, and central secondary beams, the column and connections remain unchanged. It should be noted that due to the boundary conditions applied, only half of the beam and connection sections, and a quarter of the column section, are included in the actual model. Taking full shear connection as the control case (Figure 7-9 (a)), the shear studs of all secondary beams are concentrated in the central zone of the beam span in the comparative models with different unconnected lengths △. These are 250mm, 500mm, 1000mm, and 1500mm, as shown in Figure 7-9 (b). The primary beams in all models are fully shear-connected, since the primary beam is protected and has shorter span and larger section compared with the secondary beams.

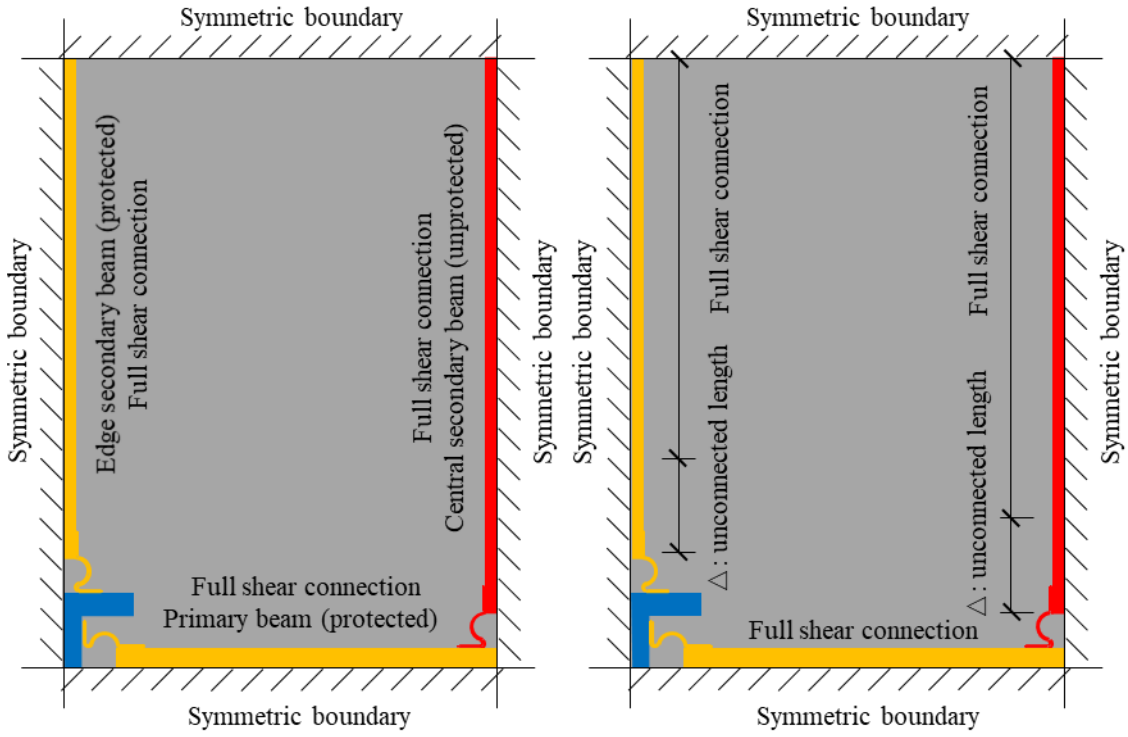

(a) Full shear connection model

(b) Model with a certain length of beam and slab unconnected

Figure 7-9. Models with different unconnected lengths

It is to be expected that the longer the unconnected length of the beam, the larger the relative slip at the beam end. Figure 7-10 shows that the effect of the unconnected length on the end slip is negligible in the edge secondary beam, whereas, it is very obvious in the central secondary beam. At a certain temperature, the central secondary beam of the largest unconnected length (1500mm) experiences the largest negative end slip among all the central secondary beams analysed. Note here that the end slip is negative when the beam end moves towards the column relative to the

slab. As the temperature rises to about 1000°C, the negative end slip begins to decrease, indicating that the beam is beginning to move away from the column as it enters the catenary action stage. The comparative results of the models with different unconnected lengths are shown in Figure 7-11. This figure shows that the mid-span deflections and the axial connection forces of the primary beam, the edge secondary beam and the central secondary beam are only slightly affected by the unconnected length. Figure 7-10 (a) shows that the edge secondary beams with different unconnected lengths generate almost the same end slip. It should be noted that the primary beams in all models are fully connected to the slab. Therefore, it is reasonable to conclude that the distribution of shear studs along the secondary beam has little effect on the behaviour of the primary beam and the edge secondary beam. As for the central secondary beam, different unconnected lengths do generate different relative slip at the beam end (Figure 7-10 (b)), whereas the connection axial force is not significantly affected. The reasoning behind this is illustrated in Figure 7-12. This figure shows the force-displacement curves of a spring row of the ductile connection at different temperatures, indicating that, at a certain temperature, the compressive force of the spring row reaches its peak value soon after it enters compression. After passing its peak, the curve remains almost horizontal until the maximum compressive displacement is reached, at which internal contact occurs within the semi-cylindrical section. Therefore, even though different end slips are applied to the connections, the connection axial forces are almost the same.

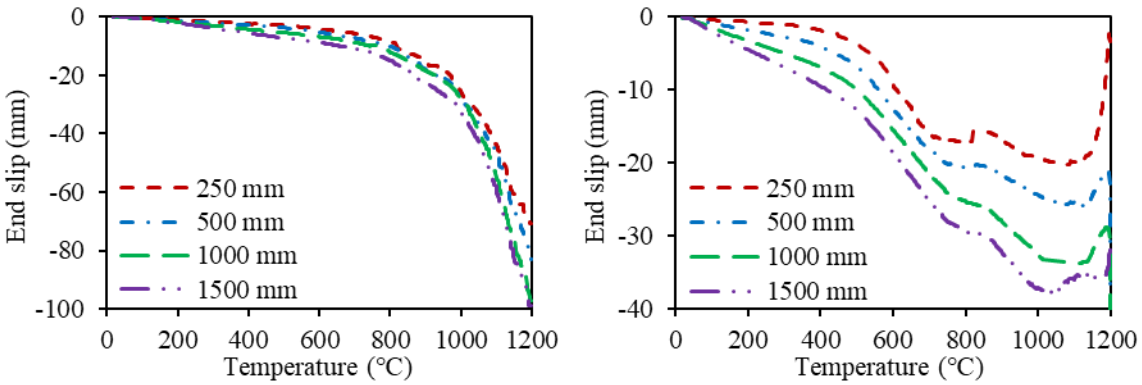

(a) Relative slip at the end of edge secondary beam

(b) Relative slip at the end of central secondary beam

Figure 7-10. Relative end slip at beam end with ductile connection (central secondary beam temperature)

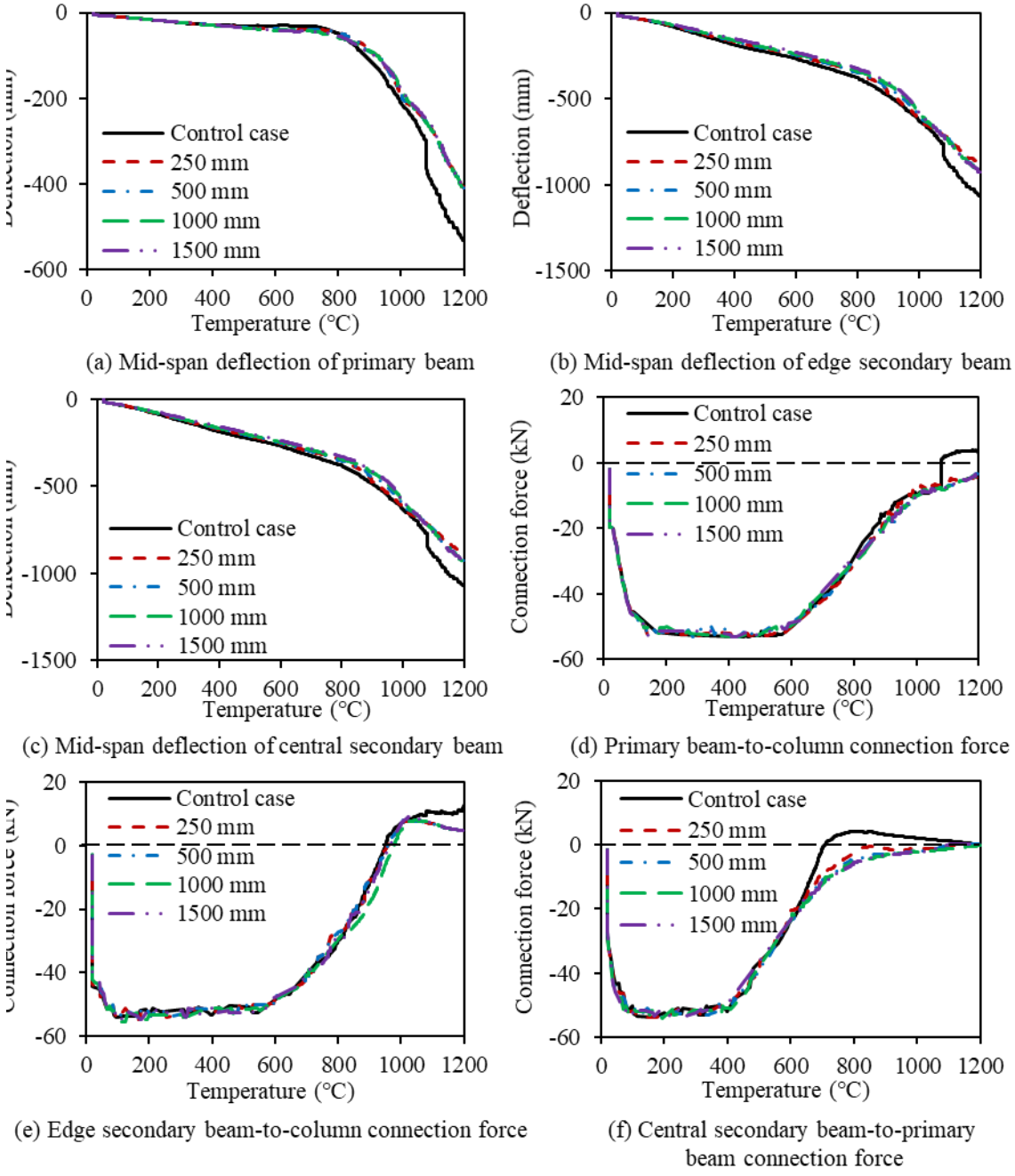

(a) Mid-span deflection of primary beam

(b) Mid-span deflection of edge secondary beam

(c) Mid-span deflection of central secondary beam

(d) Primary beam-to-column connection force

(e) Edge secondary beam-to-column connection force

(f) Central secondary beam-to-primary beam connection force

Figure 7-11. Comparative results of models with ductile connections (central secondary beam temperature)

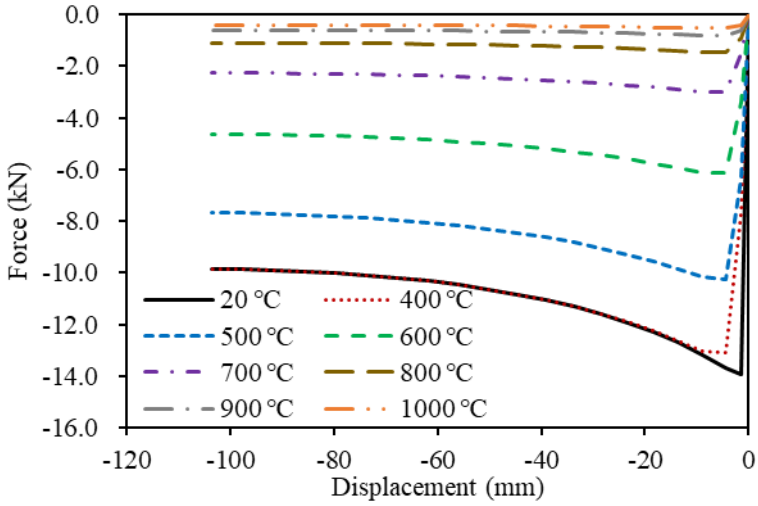

Figure 7-12. Compressive force-displacement curves of a spring row at different temperatures

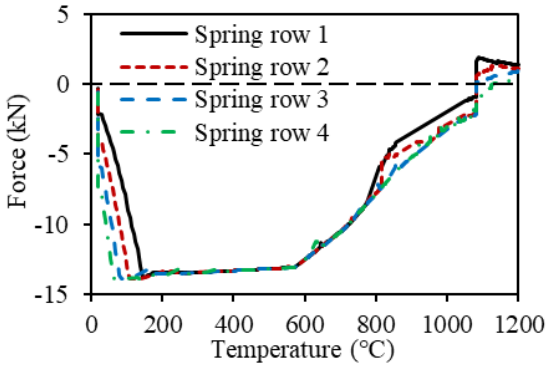

(a) Temperature-force curves (control case)

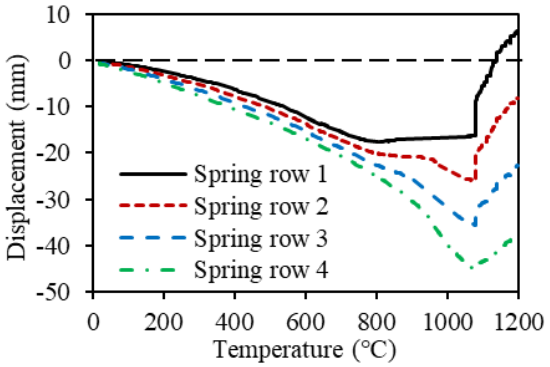

(b) Temperature-displacement curves (control case)

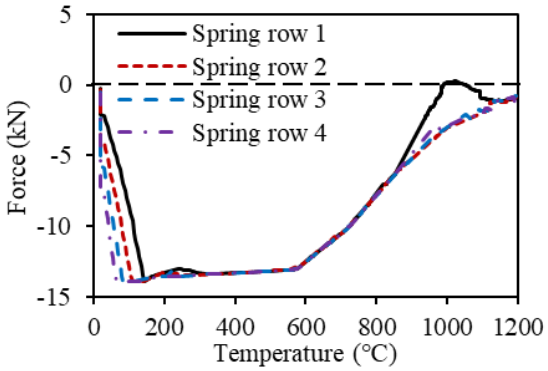

(c) Temperature-force curves (1000 mm)

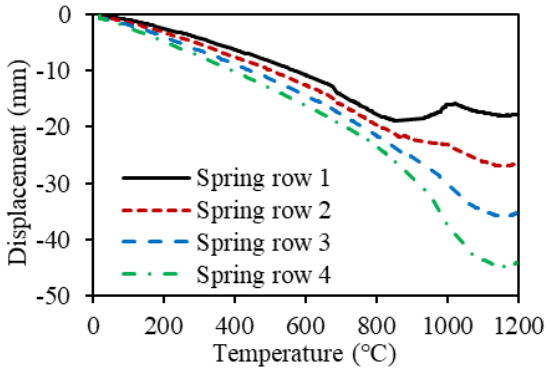

(d) Temperature-displacement curves (1000 mm)

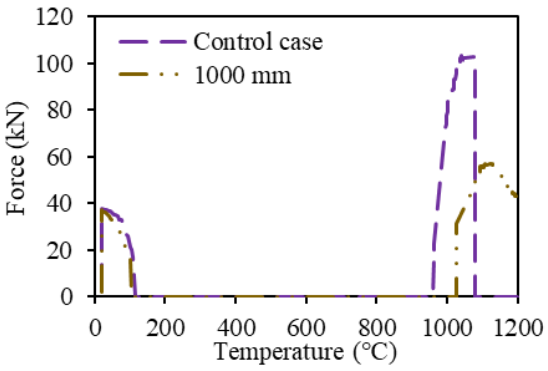

(e) Temperature-force curves of rebar component

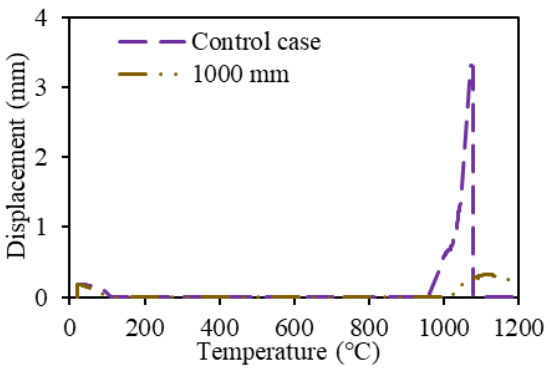

(f) Temperature-displacement curves of rebar component

Figure 7-13. Spring row curves of the primary beam-to-column connection

Although the influence of the unconnected length on the connection axial force is very low, the axial forces in the primary beam and central secondary beam connections of the control case (fully connected) are slightly different from those of the other cases of various unconnected lengths. Figure 7-11 (d) shows that the primary beam connection force of the control case experiences a rapid change at 1081°C, which is not observed in the other cases. To understand the reasoning behind this observation, the temperature-force, and temperature-displacement relationships of all spring rows of the control case, and those of the model with 1000mm unconnected length, are compared in Figure 7-13. Figure 7-13 (e) and (f) show that the rebar component of the connection in the control case reaches its maximum strength at 1081°C, and then its force and displacement immediately drop to 0, indicating the failure of the rebar component. At that time, the tensile force originally borne by the rebar component is transferred to the four spring rows, leading to the sudden decrease in the compressive displacements of all spring rows (Figure 7-13 (b)). Correspondingly, the spring row forces change rapidly from compression to tension (Figure 7-13 (a)), resulting in the total axial force of the whole connection also changing rapidly from compression to tension (Figure 7-11 (d)). On the contrary, the maximum force experienced by the rebar component of the connection of the model with 1000mm unconnected length is far lower than its ultimate strength (Figure 7-13 (e) and (f)), and so the rebar component does not fracture, explaining why the curves of the spring row forces and displacements are relatively smooth in this case (Figure 7-13 (c) and (d)). As for the connection between the central secondary and primary beams, Figure 7-11 (f) shows that the compressive connection force of the control case decreases faster than in the other cases from about 650°C, and that it becomes tensile at about 700°C. Since full shear connection is adopted in the central secondary beam of the control case, less beam-end displacement (since the thermal expansion of the beam is more restrained by the slab) and larger thermal bowing curvature of the composite beam is seen, compared with the other cases. As a result, the compressive displacements of all spring rows in the control case begin to decrease at a lower temperature (about 600°C) than in the other cases, as shown in Figure 7-14 (b). In the control case, when the compressive displacement of a spring row is reduced to a certain extent, the spring row enters the "pulling-back" stage, and the force in the spring row reverses

into tension, as shown Figure 7-14 (a). In contrast, the compressive displacements of all the spring rows in the model with 1000mm unconnected length continue to increase up to about 1188℃ (Figure 7-14 (d)), due to the lower restraint to thermal expansion and lower thermal bowing compared to the control case. For the same reason, the decrease in compressive spring row force of this model is mainly caused by the heat-induced material degradation (Figure 7-14 (c)) and so it is much slower than that of the control case. In general, the influence of unconnected length on the axial forces in ductile connections is very low, which also reflects the high axial deformability of the ductile connection

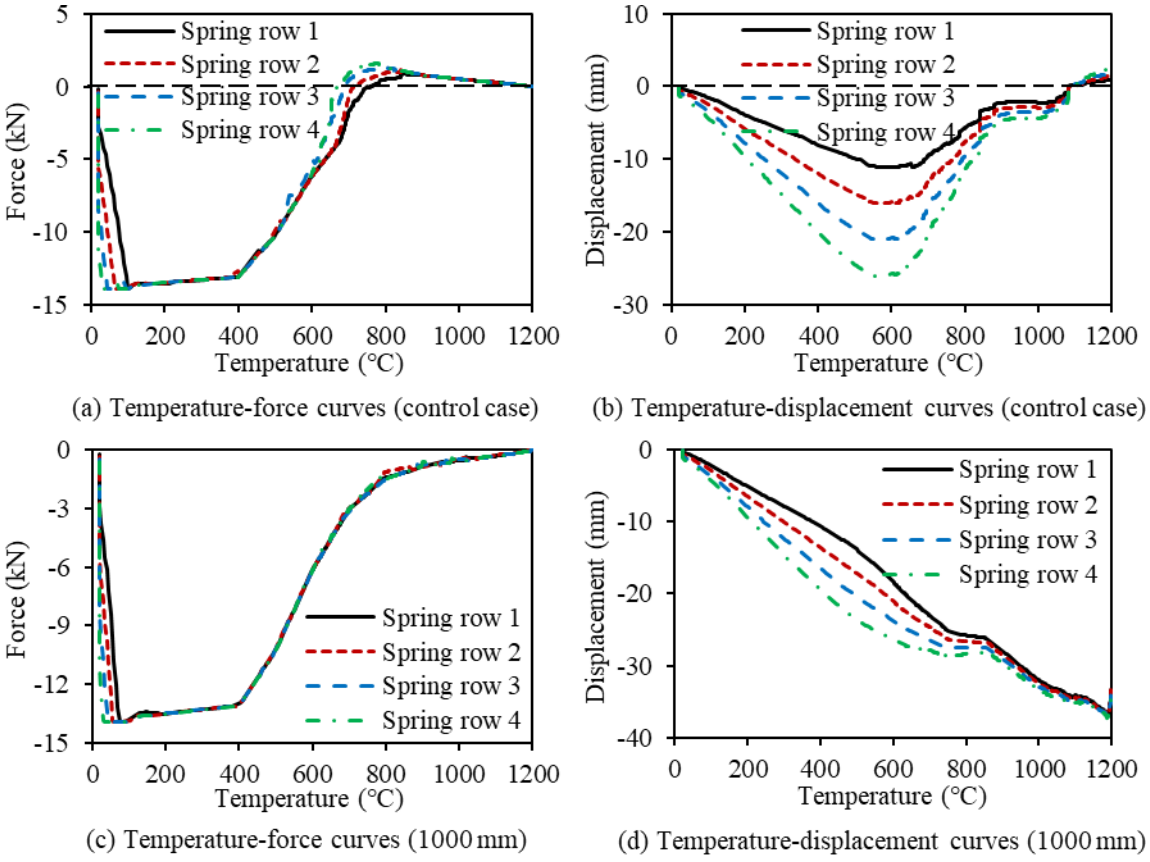

(a) Temperature-force curves (control case)

(b) Temperature-displacement curves (control case)

(c) Temperature-force curves (1000 mm)

(d) Temperature-displacement curves (1000 mm)

Figure 7-14. Spring row curves of the central secondary beam-to-primary beam connection

To compare the observed behaviours, the models with rigid connections and different unconnected lengths were also built and analysed. Similarly to the models with ductile connections, the influence of the unconnected length on the relative end slip of the edge secondary beam is negligible, whereas the end slip of the central secondary beam increases with the increase of the unconnected length, as shown in Figure 7-15. Another similarity is that the mid-span deflections of the primary, edge secondary and central secondary beams, and the axial connection

force of the primary beam, are only slightly affected by the unconnected length (shown in Figure 7-16 (a) - (d)). In contrast to the models with ductile connections, the influence of the unconnected length on the axial connection forces of the edge and central secondary beams with rigid connections are obvious, as shown in Figure 7-16 (e) and (f).

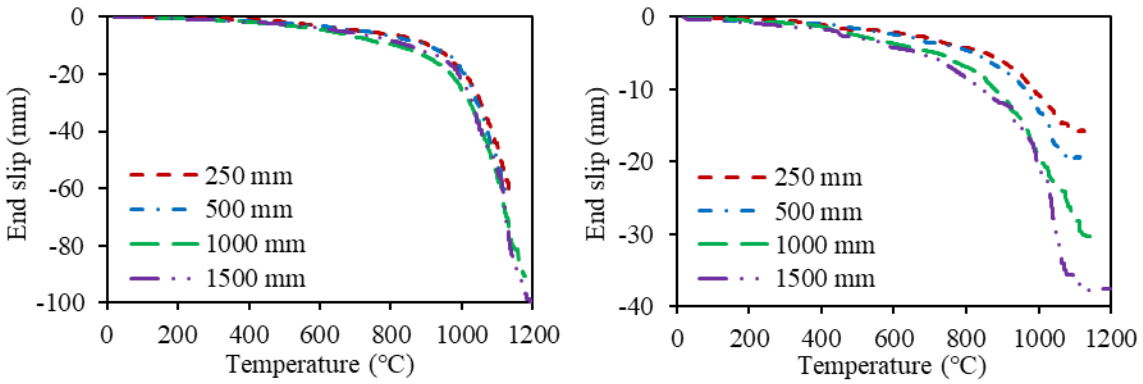

(a) Relative slip at the end of edge secondary beam

(b) Relative slip at the end of central secondary beam

Figure 7-15. Relative end slip at beam end with rigid connection (central secondary beam temperature)

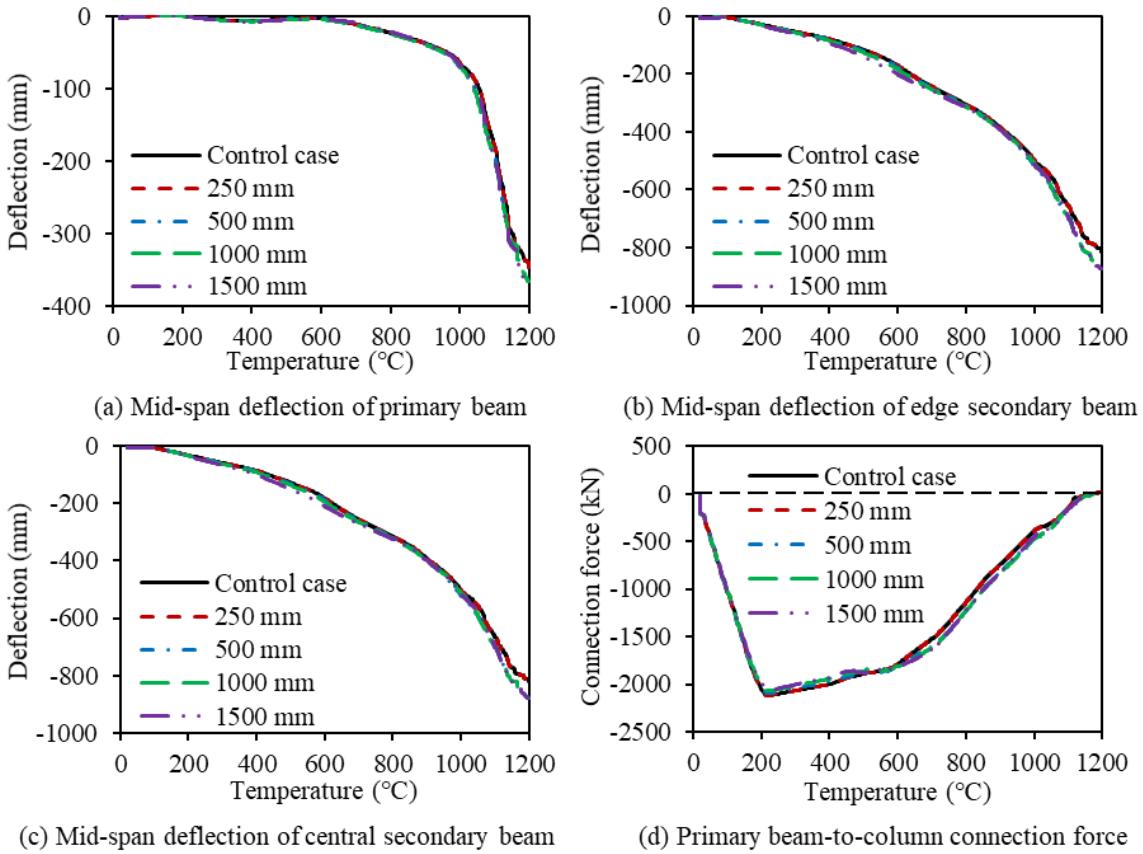

(a) Mid-span deflection of primary beam

(b) Mid-span deflection of edge secondary beam

(c) Mid-span deflection of central secondary beam

(d) Primary beam-to-column connection force

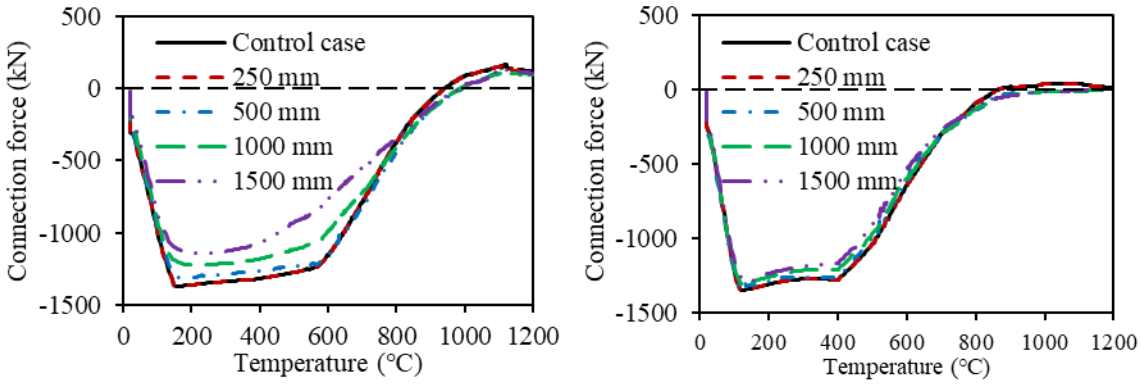

(e) Edge secondary beam-to-column connection force

(f) Central secondary beam-to-primary beam connection force

Figure 7-16. Comparative results of models with rigid connections (central secondary beam temperature)

7.4. Chapter conclusion

This chapter investigates the fire performance of the ductile connection in composite structures. The influence of the out-of-plane structure on the connection performance is important since the structural elements in a composite frame always interact with each other and work as a whole. Therefore, 3-D models of a fire compartment of a typical composite frame, designed based on the Cardington fire test buildings, have been established using Vulcan. Different types of connections were used in these models, including the ductile connection, idealised rigid and pinned connections, and conventional end-plate and web-cleat connections, to compare their performance in composite structures subject to fire.

In order to further reduce computational costs, the 3-D composite frame compartment model has been reduced to a quarter of its original size by applying symmetry at the boundaries and reducing the sections of beams and connections by half. A series of such models has been built to investigate the influence of unconnected length between the slab and beam on the connection performance. For comparison, frame models with rigid connections have also been created. The following conclusions can be drawn based on these studies:

- Compared with other connections, the axial forces generated in the ductile connections are considerably reduced, indicating that the proposed ductile connection can provide satisfactory deformability to accommodate the axial displacement applied by the

connected beam in fire. Therefore, the ductile connection can effectively prevent the local buckling of the beam in the initial stage of a fire, and the brittle fracture of the connection at high temperatures.

- Although the unconnected length will affect the beam end slip, the influence on the ductile connection axial force is almost negligible. This is due to the inherent mechanical properties of the ductile connection, and also reflects its excellent axial deformation capacity.
- It was found that unconnected length affects both the relative slip at the beam end and the axial force generated in the rigid connection.

8.

CONCLUSIONS AND RECOMMENDATIONS FOR FUTURE WORK

8.1. Main conclusions

Connections play the key role in maintaining structural integrity and stability of steel and composite framed structures under exposure to fire. The internal forces experienced by connections vary with the different stages of a fire event. In the initial heating stage of a fire, the thermal expansion of a beam generates compressive forces on its connections, which may lead to the buckling of the beam's bottom flange or the column web. When the temperature rises to a high level, catenary action of the beam occurs, and connection forces change to tension, which may cause the fracture of parts of the connection, Including welds, or the failure of bolts. During the cooling stage of the fire, the thermal contraction of the beam superposes tensile forces on the connections, which further increases the possibility of connection fracture and bolt failure. However, conventional connection types lack the ductility to accommodate the axial deformation of the connected beam under fire conditions. In order to prevent connection failures and improve structural robustness in fire, a novel connection with high ductility has been proposed in this research project, and its fire performance within 2-D and 3-D bare-steel and composite frames has been investigated. The research work can basically be divided into three parts, as described below.

8.1.1. Design of the novel ductile connection

Equations have been derived to quantify the axial deformations of bare-steel beams at both their top and bottom flanges. Equations have also been derived to represent the axial ductility demands of composite beams at four key positions, including the rebar level, the connection top surface, the connection bottom surface, and the beam bottom flange. All these equations should be taken as important design criteria for bare-steel or composite connections in fire.

An initial specification of the novel ductile connection has been proposed, in which it consists of two identical parts, each of which includes a fin-plate which is bolted to beam web, an end-plate which is bolted to column flange or web, and a semi-cylindrical section between these two parts to provide additional ductility. The basic elements of the connection can be simply manufactured by deforming a steel plate. However, the sharp intersection between the semi-cylindrical part and

the end-plate is not practicable in the cold formation process. Therefore, in the improved shape of the connection, it was decided to use curves with an acceptable radius to replace the original sharp intersections. This bent part, together with the end-plate, is referred to as the face-plate. A simple two-storey three-bay plane steel frame has been modelled using Abaqus, to compare the performance of these two versions of the ductile connection. The following conclusions came out of these studies:

- The equations representing the axial ductility demands of bare-steel and composite beams under fire conditions should be used to determine the minimum value of the inner radius of the semi-cylindrical section.
- Comparative results showed that the axial force generated in the beam with the improved version of the ductile connection is much smaller than that of the beam with the original version, indicating that the improved design further enhances the deformation capacity and ductility of the ductile connection.

8.1.2. Development of the component-based models of the novel ductile connection

Compared with experiments or detailed finite element modelling, using the high-temperature component-based model of the connection in the structural finite element software Vulcan is a more practical and effective way for large frame analysis to investigate the connection performance within a real structure. In the component-based approach, the connection is divided into a series of components represented by springs with known characteristics. The accuracy of the component-based model mainly depends on the accuracy of representation of the characteristics of the connection components. The ductile connection consists of a fin-plate, a face-plate and a semi-cylindrical section. Some research work conducted by researchers from the Structural Fire Engineering Research Group at the University of Sheffield has been directly applied to some components of the ductile connection. For example, the equations derived by Sarraj (2007) have been used to obtain the properties of the bolts in shear, the fin-plate in bearing and the beam web in bearing. The force-displacement curve of the column web in compression developed by Block (2006) has been adopted in the component-based model as the compression spring, which is activated after the beam flange contacts the column flange. The plastic ‘cone’

model developed by Dong (2016) has been modified to represent the bolt pull-out component, since pull-out of bolts from the face-plate zone is the main failure mode of the ductile connection observed in the Abaqus simulations.

Apart from the components mentioned above, the most important component of the ductile connection – the semi-cylindrical section has been characterized by analytical models based on simple plastic theory. It is assumed that four plastic hinges are formed during the deformation of the semi-cylindrical section, and the relationship between applied force and displacement is obtained by using the virtual work principle. Experiments and detailed Abaqus simulations at both ambient and elevated temperatures have been conducted to validate the tensile and compressive analytical models of the semi-cylindrical section. Following the same method, the analytical model of the face-plate has also been developed. An initial component-based model of the ductile connection has been proposed, which includes components representing bolts in shear, fin-plate in bearing, beam web in bearing, column web in compression, bolt pull-out, semi-cylindrical section and face-plate. It is assumed that the unloading stiffness of each component at constant temperature is equal to its initial elastic loading stiffness. The 'Reference Point' concept has been used to describe the unloading of each component at changing temperatures.

The semi-cylindrical section and the face-plate are treated as two different components, deforming separately in the initial component-based model. However, by observing the deformation process of the ductile connection in Abaqus simulations, it was found that these two parts interact directly with each other. Therefore, an improved component-based model was proposed, in which the semi-cylindrical section and the face-plate are considered to deform as a whole (FPSC) component. Analytical models of the FPSC component were developed, in which two cases were considered according to the geometric relationship between the length of the face-plate leg and the radius of the semi-cylindrical section. The two component-based models were compared and validated against both experiments and Abaqus simulations.

The component-based model of the composite ductile connection was established by adding a reinforcement component to the bare-steel ductile connection model. This rebar component is based on the simple rebar slip model developed by Sezen and Setzler (2008), and can consider the pull-out of reinforcing bars and the influence of weld points in the mesh. The component-based models of the bare-steel and composite ductile connections were converted into connection

elements according the principles of finite element method, and incorporated into Vulcan. Single beam models and sub-frame models with ductile connections were created using both Vulcan and Abaqus, to check the performance of the ductile connection elements. The following conclusions and discussions came out of these studies:

8.1.2.1. Conclusions

- The tensile and compressive analytical models of the semi-cylindrical section correlate well with both experiments and Abaqus simulations at both ambient and elevated temperatures.
- The Masing rule cannot be used to describe the unloading of the ductile connection since the tensile and compressive loading curves of the semi-cylindrical section/FPSC component are not identical in shape. Therefore, the unloading path of the ductile connection is simplified as linear, and its slope is equal to that of the initial linear-elastic part of the loading curve. However, the large stiffness of the unloading curve leads to the sudden change of spring row force when unloading occurs, as shown in Figure 4-13.
- The concept of "Reference Point" is used to describe the unloading of components in the component-based models at varying temperatures, which means that the force-displacement curves of a component at different temperatures unload to the same reference point (the intersection point between the unloading curve and the abscissa).
- The force-displacement curves of all the components in a spring row are combined into one force-displacement curve since these components work in series. The complete loading-unloading-reloading behaviour has been incorporated into each spring row of the component-based model.
- Results from the second scheme of component-based model are more in line with Abaqus simulation results than those from the first scheme of component-based model. It was therefore decided to convert the second scheme of component-based model into a connection element and incorporate it into Vulcan.
- Results from the Vulcan bare-steel single beam models are in good agreement with those from Abaqus models, indicating that the developed bare-steel ductile connection element

can adequately represent connection behaviour given by detailed finite element simulations.

- The proposed rebar component can consider the pull-out of longitudinal reinforcing bars above the connection, and the anchorage provided by the weld points in the mesh. In the development of the rebar component, it is assumed that the concrete crack of the slab occurs on the outer surface of the column flange, and the development lengths on both sides of the crack are determined by the first three weld points or the first weld point and the centreline of the column section, respectively. The rebar slips on both sides of the crack should be calculated separately and added together as the displacement of the whole reinforcement component.
- The comparison between Vulcan composite sub-frame model and Abaqus composite sub-frame model shows that although the connection in Abaqus model is stiffer than that in Vulcan model, the developed composite connection element can efficiently represent the behaviour of the ductile connection within composite structures. The differences between Vulcan and Abaqus results can be explained mainly in two aspects: 1) the compressive analytical model of the FPSC component used in the component-based model of the ductile connection is softer than the detailed Abaqus model; 2) the concrete crack and the pull-out of reinforcing bars are not considered in the Abaqus model, making the composite slab in Abaqus model stronger than that in Vulcan model.

8.1.2.2. Discussions

- It was mentioned in Section 8.1.2.1 above that the large unloading stiffness of the component-based model leads to a sudden change of spring row force when unloading occurs, and the slight oscillation of the Vulcan result curves involving force (force-displacement curve or force-temperature curve). This indicates that the simplified linear unloading path with the initial elastic loading stiffness is too stiff. When a connection has already been compressed to a certain extent, the loading stiffness when it is loaded again is lower than that when it is loaded from its initial shape. This can be confirmed by inspecting the experimental curves presented in Chapter 4. Therefore, a softer unloading

path is needed to further improve the component-based models. It should also be noted that the softer unloading path will affect the location of the 'reference point'.

- Although the component-based model has a good balance between accuracy and efficiency compared with the detailed FE modelling, its defect is also obvious. In the component-based model, different components of a spring row work in series, and only the tension and compression of each component are considered. However, the interaction through continuity between adjacent upper and lower spring rows, and the bending / torsion of individual components (especially the FPSC component) cannot at present be taken into account in the component-based model, which is one of the main reasons for the differences between Vulcan results and Abaqus results.
- It is assumed that a discrete concrete crack occurs through the concrete slab at the outer surface of the column flange in the development of the rebar component of the composite connection model. This is appropriate for composite slabs with light reinforcement, as is typical of normal composite slabs, in which the main design function of the mesh is to inhibit cracking in setting concrete. However, discrete concrete cracks may not occur in composite slabs with reinforcement which is normal for in-situ reinforced concrete slabs, for which the reinforcing bars will not be pulled out, but cracking is distributed over a finite length. In this case, the proposed rebar component is not applicable.

8.1.3. Investigation of the fire performance of the novel ductile connection within bare-steel and composite structures

Having developed and validated the bare-steel and composite ductile connection elements, Vulcan can now be used to carry out global frame analysis to investigate the effect of the ductile connection on the behaviour of continuous structures.

2-D bare-steel sub-frame models have been built using Vulcan with different connection types, including the ductile connection, idealised pinned and rigid connections, and the commonly-used end-plate and web-cleat connections, in order to compare the effect on structural performance of using the ductile connection with the other connection types. A series of parametric studies have been carried out using these 2-D bare-steel sub-frame models to investigate the influence of five

key parameters of the connection on the resulting performance. These are; the connection temperature, the radius of the semi-cylindrical section, the connection thickness, the vertical bolt spacings and the connection material. The progressive collapse of a three-storey three-bay plane bare-steel frame with ductile connections has also been modelled using the static-dynamic solver in Vulcan.

Parametric studies have also been carried out using Vulcan 2-D composite sub-frame models to investigate the effects of three parameters of the composite ductile connection. These are; the connection thickness, the radius of the semi-cylindrical section, and the number of longitudinal reinforcing bars within the effective width of the slab. Since shear studs are not considered in the Vulcan composite ductile connection element, Abaqus composite sub-frame models have been built to study the influence of shear stud spacings on the performance of the composite ductile connection. In order to take into account the influence of out-of-plane structure on the behaviour of the composite connection, 3-D models of an internal compartment of a composite frame, which is designed according to the typical frames used in the Cardington fire tests (Lennon et al., 1999, Wald et al., 2004), have been created using Vulcan. Different connection types have been adopted in the 3-D composite frame models to compare their fire performance using the ductile connection with that using other connection types. The 3-D Vulcan composite frame models have also been used to investigate the influence of the unconnected length between slab and beam at the beam ends on the connection behaviour. The following conclusions and discussions came out of these studies:

8.1.3.1. Conclusions

- Compared with the axial forces generated in the bare-steel beams with other connection types, the axial force generated in the beam with ductile connections is significantly reduced. This phenomenon indicates that the proposed ductile connection can provide satisfactory ductility in bare-steel structures to accommodate the axial deformation generated by the connected beam under exposure to fire.
- The ultimate failure temperature of the bare-steel beam with ductile connections under high-temperature catenary action stage is much higher than that of the beam with end-

plate and web-cleat connections. The failure temperature can even be further improved by optimizing the design of the ductile connection.

- Taking protection measures to reduce the temperature of the connection can improve its final failure temperature. It is reasonable to keep the connection temperature not to exceed 40% of the beam temperature. Further reducing the connection temperature will only increase the cost and has little effect on improving its failure temperature.
- Increasing the inner radius of the semi-cylindrical section can reduce the axial compressive force generated in the connection, but it has little effect on the final failure temperature of the connection.
- Increasing the thickness of the connection can significantly enhance its failure temperature, but it can also reduce the ductility of the connection. Therefore, the connection thickness cannot be increased excessively, otherwise the ductility of the connection will decrease sharply, and the axial compressive force applied to the adjacent structural members will increase dramatically, which is contrary to the original design intention of the ductile connection.
- Changing vertical bolt spacing has little effect on the connection failure temperature.
- The use of higher-grade steel for the connection could effectively improve its failure temperature.
- In the progressive collapse simulation of the plane bare-steel frame, the static solver was used first to analyse the model. Once a component in a spring row of the connection element reaches its failure limit, then the spring row is considered to have failed, and is deleted from the connection element. After all the spring rows of the connection element fail, the connection is considered to have failed, and is deleted from the model by setting its stiffness matrix to zero. The connection failure leads to the detachment of the connected beam from the adjacent column, and the dynamic solver is then activated to trace the motion of the structure.
- The progressive collapse modelling of the plane frame once again emphasizes the importance of the connection in the survival of the structure under exposure to fire.
- The parametric studies using the 2-D composite sub-frame models show that the ductility of the composite ductile connection can be improved by thinner connection thickness and

larger inner radius of the semi-cylindrical section. In addition, composite ductile connections with fewer longitudinal reinforcing bars within the effective width of slab are prone to early failure.

- Changing shear stud spacings has little influence on the performance of the composite ductile connection.
- The results from the comparison of the performance of different connection types using the Vulcan 3-D composite frame models show that, compared with other connection types, the axial force generated in the ductile connection is significantly reduced, indicating that the ductile connection can also provide excellent ductility in composite structures to accommodate the beam deformation in fire.
- Although the unconnected length between beam and slab at the beam end affects the beam end slip, its influence on the axial force of the composite ductile connection is negligible, which is due to the inherent mechanical properties of the ductile connection. On the contrary, when rigid connections are adopted in the frame models, the unconnected length affects both the beam end slip and the axial force in the connection.

8.1.3.2. Discussions

- Although increasing the radius of the semi-cylindrical section can reduce the axial compressive force generated in the connection, a semi-cylindrical section with too large a radius may hinder the installation of bolts. The ductility demand equations for determining the lower limit of the radius have been given in this research project. However, further investigation is needed to provide a criterion for determining the upper limit of the radius. The criterion could be stated by considering the geometric relationship between the bolt position, the bolt size and the size of the semi-cylindrical section. Further research is also needed to determine the upper and lower limits of the connection thickness.

- The shear capacity of the semi-cylindrical section at ambient temperature can be checked using Equation (3-5). The deformation pictures of the ductile connection from the Abaqus sub-frame models show that the semi-cylindrical section will not undergo shear failure at

high temperatures. The plate thickness is identical to that in the fin-plate section, carries the same vertical shear, but has no cut-out for the bolt holes; so, it is not the preferred location for shear failure. Therefore, in the practical application of the ductile connection, the shear capacity of the semi-cylindrical section will not be a problem.

- The progressive collapse modelling of the plane frame shows that failure of the connection starts from the bolt pull-out failure at the top bolt-row. Once the top bolt-row fails, the sequence of failures of the remaining bolt-rows occurs immediately thereafter. The tensile capacity of a spring row cannot usually be achieved, since its failure mode is controlled by the bolt pull-out. However, several measures can be taken to delay the occurrence of the bolt pull-out failure according to the parametric studies (e.g., using higher grade steel for connection, increasing connection thickness, reducing connection temperature, increasing the bolt size, etc.). In addition, stiffeners can be placed around the bolt holes on the face-plate part to locally stiffen the connection around the bolt holes, in order to prevent large deformation. Further research is needed to test the feasibility and effectiveness of this method.

8.2. Recommendations for future work

8.2.1. Component tests

Understanding the response of connection components to load reversal and temperature change is very important to simulate the temperature-dependent component behaviour in a connection within an interacting structure. The force-displacement curves of the FPSC (face-plate-semi-cylindrical) section under complete tension-compression loading cycles at different temperatures have already been obtained by the analytical models, and validated against detailed Abaqus simulations in this research project. However, the simple experiments carried out in this research focus on the unidirectional loading of the FPSC component. Therefore, it is necessary to carry out experiments under tension-compression loading cycles to further validate the developed analytical models. Since the behaviour of the FPSC component under tension is quite different from that of the component under compression, two loading schemes are suggested, including

tension-compression-tension and compression-tension-compression. The point has already been made that force reversal tends to occur when the connection is highly distorted, and so the reversal stiffness is not necessarily related to the initial loading stiffness. In this way, the force-displacement curve of the component under a complete loading cycle can be obtained. Ambient temperature tests using the universal testing machine (shown in Figure 8-1 (a)) should be carried out first. Then a barrel-furnace can be used to wrap the universal testing machine platens and the specimen to conduct high-temperature tests, as shown in Figure 8-1 (b). Both transient tests, in which the specimen is loaded first and then its temperature is increased at a prescribed rate to a certain value, and steady-state tests, in which the specimen is heated to a specified temperature first and then external load is applied to the specimen, can be attempted. The specimens used in the tests could be divided into several groups, with the dimension of the specimens in any group being identical. However, a key parameter, such as plate thickness, radius of the semi-cylindrical section and bolt gauge, should be varied between different groups of specimens.

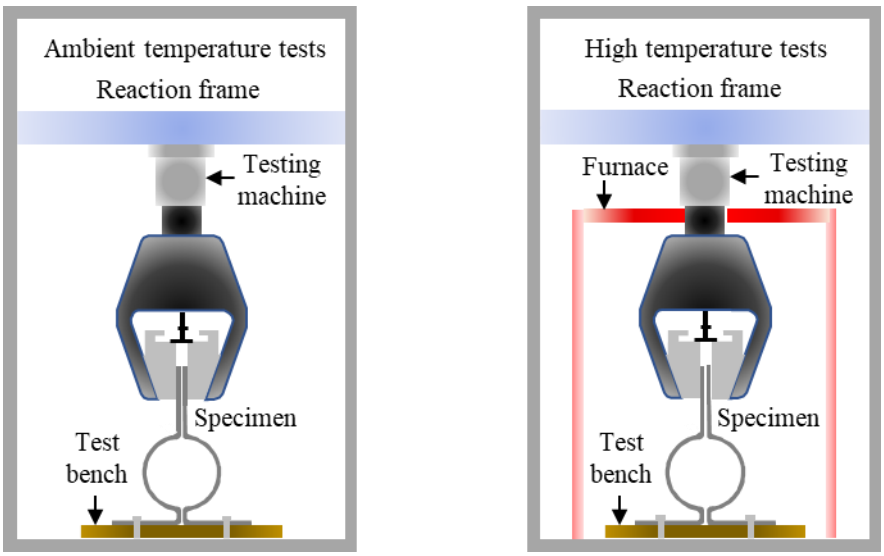

(a) Ambient-temperature test setup (b) High-temperature test setup

Figure 8-1. Component test setup

8.2.2. Connection tests under multi-directional actions

The proposed component-based models of the ductile connection have only been validated against Abaqus simulations in this research project. Experiments on a range of complete ductile connections are definitely needed to further check whether they behave in the way that would be

predicted by the proposed component-based models. The electric furnace and loading apparatus used in several previous projects (Yu et al., 2008a, 2009b, 2009c, 2010, Dai et al., 2009, Huang et al., 2013) at the University Sheffield could be modified to allow the connection to be subjected to normal, shear and moment actions at the same time, as shown in Figure 8-2. It can be seen from the figure that a column-and-stub-beam test specimen is assembled in the oven, with the cantilever stub passing through the cut-out in the wall, which would require modification to both the furnace and the existing test rig. Digital cameras and image recognition software can be used to record connection deformations.

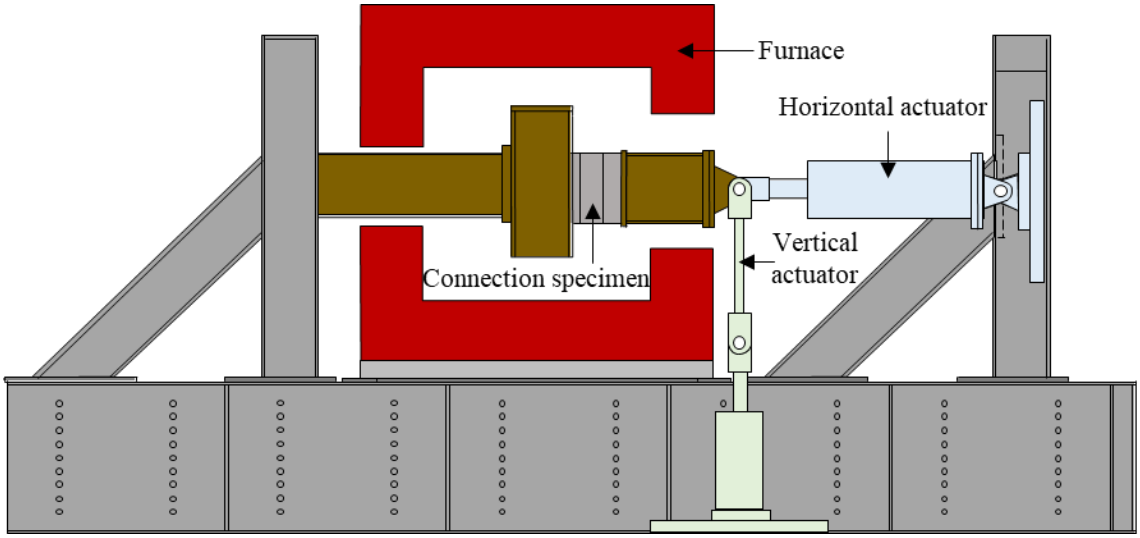

Figure 8-2. Connection test setup

It is recommended that connection tests be carried out at both ambient and elevated temperatures. For high-temperature tests, a steady-state test scheme is suggested, since it is a controllable situation and there is no need to try to reproduce the transient temperature distribution generated during a real fire accident. The two actuators are used to apply loading cycles on the connection specimen at constant temperature. The horizontal actuator generates a gradually increasing axial compressive force on the connection, followed by reversal through to tension, while the vertical actuator continuously increases its deflection at a controlled rate. Although the loading cycles generated by the two actuators are rather artificial and cannot fully reflect the loading conditions experienced by the connection in the real structure under fire, the actuators can make the connection experience all the relevant force changes to be experienced in the fire. Therefore, the recorded experimental results can be used to test the performance of the component-based models

of the ductile connection.

8.2.3. Softer unloading path in the component-based model

The unloading path used in the component-based models in this research project has been simplified as linear, and its stiffness has been set to be equal to the initial elastic loading stiffness. In this way, the unloading stiffness is quite large, resulting in a sudden change of the spring row force when unloading occurs. This is one of the main reasons for the discrepancies between the results obtained using the composite ductile connection elements and those obtained by the detailed Abaqus composite connection model. The large unloading stiffness probably leads to the slight oscillation mode of Vulcan results, especially manifested in the result curves involving forces. The evidence from the experimental curves (Figure 4-29 - Figure 4-31) indicates that the unloading stiffness is lower than the initial loading stiffness. Results from the component tests recommended in Section 8.2.1 can be used to establish the relationship between the initial loading stiffness and the unloading stiffness.

8.2.4. Geometry of the section between the fin-plate and the face-plate

The section between the fin-plate part and the face-plate part can provide additional ductility for the ductile connection, and is designed as a semi-cylindrical section in this research project. As mentioned previously, the radius of the semi-cylindrical section should be determined according to the ductility demands of beam in fire, which can be calculated using Equations (3-1) - (3-4) for bare-steel connections, and Equations (6-1) - (6-4) for composite connections. From these equations, it can be found that the ductility demands of the beam in the two directions of tension and compression are not equal, which means that the section between the fin-plate and the face-plate should not necessarily be semi-circular, but could be elliptical. It is therefore recommended to change the geometry of the section between the fin-plate and the face-plate into an elliptical general shape, and to compare the performance of the ductile connection as a function of the ratio of the major to minor dimensions of the ellipse.

8.2.5. Improved design guidance on the practical application of the connection

Equations have been derived in this research project to determine the lower limit of the radius of the semi-cylindrical section. The fin-plate part and the face-plate part of the ductile connection are designed according to the Eurocode (CEN, 2005a). As mentioned previously in Section 8.1.3.2, further research is needed to determine the upper limit of the radius of the semi-cylindrical section, as well as the lower and upper limits of the connection thickness. Once these studies are completed, an improved guidance document can be produced on the practical applications and detailed design of the ductile connection.

8.2.6. Performance of the ductile connection in the cooling stage of fire

In the cooling stage of a fire, the thermal contraction of the beam can superpose large tensile forces on connections, which may lead to the shear failure of the bolts and the fracture of the connection section. For the ductile connection, large tensile force can also lead to bolt pull-out failure. In this research project, only the performance of the ductile connection during the heating stage of a fire has been studied. It is therefore recommended to further investigate the behaviour of the ductile connection in the cooling stage using Vulcan sub-frame models.

LIST OF REFERENCES

AL-JABRI, K., BURGESS, I., LENNON, T. & PLANK, R. 1999. The performance of frame connections in fire. *Proceedings Eurosteel,* 99, pp.519-22.

AL-JABRI, K. S. 1999. *The behaviour of steel and composite beam-to-column connections in fire.* PhD Thesis, The University of Sheffield.

ANG, K. & MORRIS, G. 1984. Analysis of three-dimensional frames with flexible beam–column connections. *Canadian Journal of Civil Engineering,* 11(2), pp.245-254.

ASFP, Fire Protection for Structural Steel in Buildings (The Yellow Book), 3th Edition revised Jan 2004. 3th Edition ed. 2004: ASFP - Association for Specialist Fire Protection

BAILEY, C. G. 1995. *Simulation of the structural behaviour of steel-framed buildings in fire.* PhD Thesis, The University of Sheffield.

BAILEY, C., NEWMAN, G. & ROBINSON, J. 2006. *Fire safe design: A new approach to multi-storey steel-framed buildings*. Steel Construction Institute.

BAKER, J. 1934. Second report, London: Steel Structures Research Committee, Department of Scientific and Industrial Research.

BHATT, P. 1999. *Structures*. Addison-Wesley Longman Limited.

BLOCK, F. M. 2006. *Development of a component-based finite element for steel beam-to-column connections at elevated temperatures.* PhD Thesis, The University of Sheffield.

BRIGGS, J. 2016. *Experimental investigation of the performance of a modified 3D printed 316L stainless steel structural connection at elevated temperatures.* MSc Dissertation, The University of Sheffield.

BURGESS, I., DAVISON, J. B., DONG, G. & HUANG, S.-S. 2012. The role of connections in the response of steel frames to fire. *Structural Engineering International,* 22(4), pp.449-461.

BURGESS, I. & SAHIN, M. 2018. Tensile membrane action of lightly-reinforced rectangular composite slabs in fire. *Structures,* Vol. 16, pp.176-197.

CEN 2002. *BS EN 1991-1-2, Eurocode 1: General Actions - Part 1-2: Actions on Structures Exposed to Fire*. London: British Standards Institution.

CEN 2004a. *BS EN 1992-1-2, Eurocode 2: Design of concrete structures - Part 1-2: General*

rules — Structural fire design. London: British Standards Institution.

CEN 2004b. *BS EN 1992-1-1, Eurocode 2: Design of concrete structures: Part 1-1: General rules and rules for buildings.* London: British Standards Institute.

CEN 2005a. *BS EN 1993-1-8, Eurocode 3: Design of steel structures - Part 1-8: Design of joints.* London: British Standards Institute.

CEN 2005b. *BS EN 1993-1-2, Eurocode 3: Design of steel structures - Part 1–2: General rules — Structural fire design.* London: British Standards Institute.

CEN 2005c. *BS EN 1994-1-2, Eurocode 4: Design of composite steel and concrete structures - Part 1-2: General rules — Structural Fire Design.* London: British Standards Institute.

DAI, X., WANG, Y. & BAILEY, C. 2009. An experimental study of structural behaviour of joints in restrained steel frames in fires. In *International conference, Application of structural fire design*.

DAI, X., WANG, Y. & BAILEY, C. 2010. Numerical modelling of structural fire behaviour of restrained steel beam–column assemblies using typical joint types. *Engineering Structures,* 32(8), pp.2337-2351.

DONG, G. 2016. *Development of a General-Purpose Component-based Connection Element for Structural Fire Analysis.* PhD Thesis, The University of Sheffield.

DONG, G., BURGESS, I., DAVISON, B. & SUN, R. 2015. Development of a general component-based connection element for structural fire engineering analysis. *Journal of Structural Fire Engineering,* 6, pp.247-254.

EL-RIMAWI, J. 1989. *The behaviour of flexural members under fire conditions.* PhD Thesis, The University of Sheffield.

EL-RIMAWI, J., BURGESS, I. & PLANK, R. 1996. The treatment of strain reversal in structural members during the cooling phase of a fire. *Journal of constructional steel research,* 37(2), pp.115-135.

EL-RIMAWI, J., BURGESS, I. & PLANK, R. 1997. The influence of connection stiffness on the behaviour of steel beams in fire. *Journal of constructional steel research,* 43(1-3), pp.1-15.

ELGHAZOULI, A., IZZUDDIN, B. & RICHARDSON, A. 2000. Numerical modelling of the structural fire behaviour of composite buildings. *Fire Safety Journal,* 35(4), pp.279-297.

EN, B. 1990. BS5950 part 8: Code of practice for fire resistant design. *Br. Stand. Institute, London, UK*.

FOSTER, S., CHLADN , M., HSIEH, C., BURGESS, I. & PLANK, R. 2007. Thermal and structural behaviour of a full-scale composite building subject to a severe compartment fire. *Fire Safety Journal,* 42(3), pp.183-199.

FRANSSEN, J.-M. 1990. The unloading of building materials submitted to fire. *Fire safety journa*l*,* 3, pp.213-227.

GANN, R. G., GROSSHANDLER, W. L., LEW, H. S., BUKOWSKI, R. W., SADEK, F., GAYLE, F. W., GROSS, J. L., MCALLISTER, T. P., AVERILL, J. D. & LAWSON, J. R. 2008. Final Report on the Collapse of World Trade Center Building 7. Federal Building and Fire Safety Investigation of the World Trade Center Disaster (NIST NCSTAR 1A).

GAO, Y., YU, H. & SHI, G. 2013. Resistance of flush endplate connections under tension and shear in fire. *Journal of Constructional Steel Research,* 86, pp.195-205.

GARLOCK, M. E. & SELAMET, S. 2010. Modeling and behavior of steel plate connections subject to various fire scenarios. *Journal of Structural Engineering,* 136(7), pp.897-906.

GERSTLE, K. H. 1988. Effect of connections on frames. *Journal of Constructional Steel Research,* 10, pp.241-267.

GITTLEMAN, W. 1946. Bending Moments in a Circular Ring by the Column Analogy. *Aircraft Engineering and Aerospace Technology,* 18, pp.122-125.

HERLIANSYAH, M. K., DEWO, P., SOESATYO, M. H. & SISWOMIHARDJO, W. 2015. The effect of annealing temperature on the physical and mechanical properties of stainless steel 316L for stent application. In *2015 4th International Conference on Instrumentation, Communications, Information Technology, and Biomedical Engineering (ICICI-BME)* (pp.22-26). IEEE.

HIBBETT, KARLSSON & SORENSEN 1998. *ABAQUS/standard: User's Manual*. Hibbitt, Karlsson & Sorensen.

HIBBITT, K. & SORENSEN 2004. *ABAQUS/Explicit: User's manual*. Hibbitt, Karlsson, and Sorensen.

HORNE, M. R. 2014. *Plastic Theory of Structures: In SI/metric Units*. Elsevier.

HU, Y., DAVISON, B., BURGESS, I. & PLANK, R. 2009. Component modelling of flexible end-

plate connections in fire. *International Journal of Steel Structures,* 9(1), pp.1-15.

HU, Y., DAVISON, J., BURGESS, I. & PLANK, R. 2008. Experimental study on flexible end plate connections in fire. In *Proceedings of 5th European conference on steel structures, Graz, Austria* (pp. 1007-1012).

HUANG, S.-S., DAVISON, B. & BURGESS, I. W. 2013. Experiments on reverse-channel connections at elevated temperatures. *Engineering structures,* 49, pp.973-982.

HUANG, Z., BURGESS, I., PLANK, R., VULCAN, REISSNER, M. & BRE 1999a. Three-dimensional modelling of two full-scale, fire tests on a composite building. *Proceedings of the Institution of Civil Engineers-Structures and Buildings,* 134(3), pp.243-255.

HUANG, Z., BURGESS, I. W. & PLANK, R. J. J. S. J. 1999b. Nonlinear analysis of reinforced concrete slabs subjected to fire. 96(1), pp.127-135.

HUANG, Z., BURGESS, I. W. & PLANK, R. J. 2000. Three-dimensional analysis of composite steel-framed buildings in fire. *Journal of structural engineering,* 126(3), pp.389-397.

HUANG, Z., BURGESS, I. & PLANK, R. 2002. Modelling of six full-scale fire tests on a composite building. *Structural Engineer,* 80(19), pp.30-37.

HUANG, Z., BURGESS, I. W. & PLANK, R. J. 2009. Three-dimensional analysis of reinforced concrete beam-column structures in fire. *Journal of structural engineering,* 135(10), pp.1201-1212.

JASPART, J.-P. 2000. General report: session on connections. *Journal of Constructional Steel Research,* 55(1-3), pp.69-89.

JONES, S., KIRBY, P. & NETHERCOT, D. 1980. Effect of semi-rigid connections on steel column strength. *Journal of Constructional Steel Research,* 1(1), pp.38-46.

KALAWADWALA, S. 2018. *Investigation of the performance of innovative connection under hazard loading.* MSc Dissertation, The University of Sheffield.

KRAHULA, J. L. 1965. Out-of-Plane Bending of a Uniform Circular Ring. In *International Association for Bridge and Structural Engineering* (Vol. 25).

KRUPPA, J. 1976. Resistance au feu des assemblages par boulons haute resistance. *CTICM, Puteaux*.

LAMONT, S., USMANI, A. S. & GILLIE, M. 2004. Behaviour of a small composite steel frame structure in a “long-cool” and a “short-hot” fire. *Fire safety journal,* 39(5), pp.327-357.

LAWSON, R. 1990a. Behaviour of steel beam-to-column connections in fire. *Structural engineer,* 68, pp.263-71.

LAWSON, R. 1990b. *Enhancement of fire resistance of beams by beam to column connections*. Steel Construction Institute UK.

LENNON, T. & JONES, L. 1995. Elevated temperature composite connection moment rotation tests. *Internal Rep., Building Research Establishment, Watford, England*.

LENNON, T., MOORE, D. & BAILEY, C. 1999. The behaviour of full-scale steel-framed buildings subjected to compartment fires. *The Structural Engineer,* 77(8) pp.15-21.

LESTON-JONES, L. C. 1997. *The influence of semi-rigid connections on the performance of steel framed structures in fire.* PhD Thesis, The University of Sheffield.

LESTON JONES, L., JONES, L., BURGESS, I., LENNON, T., PLANK, R. & BRE 1997. Elevated-temperature moment-rotation tests on steelwork connections. *Proceedings of the Institution of Civil Engineers-Structures and Buildings,* 122(4), pp.410-419.

LI, G.-Q., CHEN, L.-Z., LI, J.-T. & LOU, G.-B. 2012a. Modeling of end-plate bolted composite connection in fire considering axial force effects. *Journal of Constructional Steel Research,* 76, pp.133-143.

LI, G.-Q., ZHANG, N. & JIANG, J. 2017. Experimental investigation on thermal and mechanical behaviour of composite floors exposed to standard fire. *Fire Safety Journal,* 89, pp.63-76.

LI, J.-T., LI, G.-Q., LOU, G.-B. & CHEN, L.-Z. 2012b. Experimental investigation on flush end-plate bolted composite connection in fire. *Journal of Constructional Steel Research,* 76, pp.121-132.

LIANG, Q. Q., UY, B., BRADFORD, M. A. & RONAGH, H. R. 2005. Strength analysis of steel–concrete composite beams in combined bending and shear. *Journal of Structural Engineering,* 131(10), pp.1593-1600.

LIU, T. 1996. Finite element modelling of behaviours of steel beams and connections in fire. *Journal of Constructional Steel Research,* 36(3), pp.181-199.

LIU, T. 1998a. Effect of connection flexibility on fire resistance of steel beams. *Journal of Constructional Steel Research,* 45(1), pp.99-118.

LIU, T. 1998b. Three-dimensional modelling of steel/concrete composite connection behaviour

in fire. *Journal of Constructional Steel Research,* 1(46), pp.319-320.

LIU, T. 1999. Moment-rotation-temperature characteristics of steel/composite connections. *Journal of Structural Engineering,* 125(10), pp.1188-1197.

LYNN, A. & MOEHLE, J. 1996. Seismic evaluation of existing reinforced concrete. *Journal of Prestressed concrete Institute,* 17.

MACLEOD, G. 2018. The Grenfell Tower atrocity: Exposing urban worlds of inequality, injustice, and an impaired democracy. *City,* 22(4), pp.460-489.

MADAS, P. J. 1993. Advanced modelling of composite frames subject to earthquake loading.

MCALLISTER, T. & CORLEY, G. 2002. *World Trade Center Building performance study: Data collection, preliminary observations, and recommendations*, Federal Emergency Management Agency.

MONCARZ, P. D. & GERSTLE, K. H. 1981. Steel frames with nonlinear connections. *Journal of the Structural Division,* 107(8), pp.1427-1441.

NETHERCOT, D. & ZANDONINI, R. 1989. Methods of prediction of joints behaviour: beam-to-column connections, Structural Connection: stability and strength, edited by Narayanan, R. Elsevier Applied Science, London and NY.

NEWMAN, G. M., ROBINSON, J. T. & BAILEY, C. G. 2000. *Fire safe design: A new approach to multi-storey steel-framed buildings*, Steel Construction Institute.

PI, Y.-L., BRADFORD, M. A. & UY, B. 2006. Second order nonlinear inelastic analysis of composite steel–concrete members. I: Theory. *Journal of structural engineering,* 132(5) pp.751-761.

POGGI, C. & ZANDONINI, R. 1985. Behaviour and strength of steel frames with semi-rigid connections. In *Connection Flexibility and Steel Frames, ASCE Convention* (pp.57-76). Chen Wai-Fah.

PRESCOTT, J. 1924. *Applied elasticity*, Longmans, Green and Co.

PUCINOTTI, R., BURSI, O., FRANSSEN, J.-M. & LENNON, T. 2011. Seismic-induced fire resistance of composite welded beam-to-column joints with concrete-filled tubes. *Fire safety journal,* 46(6), pp.335-347.

QIANG, X., BIJLAARD, F. S., KOLSTEIN, H. & JIANG, X. 2014a. Behaviour of beam-to-column high strength steel endplate connections under fire conditions–Part 1:

Experimental study. *Engineering Structures,* 64, pp.23-38.

QIANG, X., BIJLAARD, F. S., KOLSTEIN, H. & JIANG, X. 2014b. Behaviour of beam-to-column high strength steel endplate connections under fire conditions–Part 2: Numerical study. *Engineering structures,* 64, pp.39-51.

QIANG, X., JIANG, X., BIJLAARD, F. S., KOLSTEIN, H. & LUO, Y. 2015. Post-fire behaviour of high strength steel endplate connections—Part 1: Experimental study. *Journal of Constructional Steel Research,* 108, pp.82-93.

RAHNAVARD, R. & THOMAS, R. J. 2018. Numerical evaluation of the effects of fire on steel connections; Part 1: Simulation techniques. *Case Studies in Thermal Engineering,* 12, pp.445-453.

RAMBERG, W. & OSGOOD, W. R. RAMBERG, W. & OSGOOD, W. R. 1943. *Description of stress-strain curves by three parameters* (No. NACA-TN-902).

RASSATI, G., LEON, R. T. & NO , S. 2004. Component modeling of partially restrained composite joints under cyclic and dynamic loading. *Journal of Structural Engineering,* 130(2), pp.343-351.

RATHBUN, J. C. 1936. Elastic properties of riveted connections. *Transactions of the American Society of Civil Engineers,* 101(1), pp.524-563.

ROMSTAD, K. M. & SUBRAMANIAN, C. V. 1970. Analysis of frames with partial connection rigidity. *Journal of the Structural Division,* 96(11), pp.2283-2300.

SANAD, A., ROTTER, J., USMANI, A. & O'CONNOR, M. 2000. Composite beams in large buildings under fire—numerical modelling and structural behaviour. *Fire Safety Journal,* 35(3), pp.165-188.

SARRAJ, M. 2007. *The behaviour of steel fin plate connections in fire.* PhD Thesis, The University of Sheffield.

SARRAJ, M., BURGESS, I., DAVISON, J. & PLANK, R. 2007. Finite element modelling of steel fin plate connections in fire. *Fire Safety Journal,* 42(6-7), pp.408-415.

SEZEN, H. 2004. Seismic behavior and modeling of reinforced concrete building columns.

SEZEN, H. & SETZLER, E. J. 2008. Reinforcement slip in reinforced concrete columns. *ACI Structural Journal,* 105(3), p.280.

SHERBOURNE, A. N. & BAHAARI, M. R. 1997. Finite element prediction of end plate bolted

connection behavior. I: Parametric study. *Journal of Structural Engineering,* 123(2), pp.157-164.

SOMMER, W. H. 1969. *Behaviour of welded header plate conections.* PhD Thesis, University of Toronto.

SPYROU, S. 2002. *Development of a component based model of steel beam-to-column joints at elevated temperatures.* PhD Thesis, The University of Sheffield.

SUN, R., HUANG, Z. & BURGESS, I. 2012a. The collapse behaviour of braced steel frames exposed to fire. *Journal of Constructional Steel Research,* 72, pp.130-142.

SUN, R., HUANG, Z. & BURGESS, I. 2012b. Progressive collapse analysis of steel structures under fire conditions. *Engineering Structures,* 34, pp.400-413.

SUN, R. R. 2012. *Numerical modelling for progressive collapse of steel framed structures in fire.* PhD Thesis, The University of Sheffield.

SUWONDO, R., CUNNINGHAM, L., GILLIE, M. & BAILEY, C. 2019. Progressive collapse analysis of composite steel frames subject to fire following earthquake. *Fire safety journal,* 103, pp.49-58.

TAIB, M. & BURGESS, I. 2013. A component-based model for fin-plate connections in fire. *Journal of Structural Fire Engineering,* 4, pp.113-122.

WAINMAN, D. & KIRBY, B. 1988. *Compendium of UK standard fire test data: Unprotected structural steel*, British Steel Corporation, Swinden Laboratories.

WALD, F., DA SILVA, L. S., MOORE, D., LENNON, T., CHLADNA, M., SANTIAGO, A., BENEŠ, M. & BORGES, L. 2006. Experimental behaviour of a steel structure under natural fire. *Fire Safety Journal,* 41(7), pp.509-522.

WALD, F., SILVA, S., MOORE, D. & LENNON, T. 2004. Structural integrity fire test. In *Proceedings Nordic Steel Conference*..

WANG, Y.-C. 1998. Composite beams with partial fire protection. *Fire Safety Journal,* 30(4), pp.315-332.

WANG, Y., DAI, X. & BAILEY, C. 2011. An experimental study of relative structural fire behaviour and robustness of different types of steel joint in restrained steel frames. *Journal of Constructional Steel Research,* 67, pp.1149-1163.

WILKINSON, H. 2015. *Catastrophic Fire-Testing of 3D Printed Stainless Steel*. MSc

Dissertation, The University of Sheffield.

YU, H., BURGESS, I., DAVISON, J. & PLANK, R. 2008a. Experimental investigation of the tying capacity of web cleat connections in fire. In *The 5th European conference on steel structures*..

YU, H., BURGESS, I., DAVISON, J. & PLANK, R. 2008b. Numerical simulation of bolted steel connections in fire using explicit dynamic analysis. *Journal of Constructional Steel Research,* 64(5), pp.515-525.

YU, H., BURGESS, I., DAVISON, J. & PLANK, R. 2009a. Development of a yield-line model for endplate connections in fire. *Journal of Constructional Steel Research,* 65(6), pp.1279-1289.

YU, H., BURGESS, I., DAVISON, J. & PLANK, R. 2009b. Experimental investigation of the behaviour of fin plate connections in fire. *Journal of Constructional Steel Research,* 65(3), pp.723-736.

YU, H., BURGESS, I., DAVISON, J. & PLANK, R. 2009c. Tying capacity of web cleat connections in fire, Part 1: Test and finite element simulation. *Engineering Structures,* 31(3), pp.651-663.

YU, H., BURGESS, I., DAVISON, J. & PLANK, R. 2009d. Tying capacity of web cleat connections in fire, Part 2: Development of component-based model. *Engineering structures,* 31(3), pp.697-708.

YU, H., BURGESS, I., DAVISON, J. & PLANK, R. 2010. Experimental and numerical investigations of the behavior of flush end plate connections at elevated temperatures. *Journal of Structural Engineering,* 137(1), pp.80-87.

ZOETEMEIJER, P. 1990. *Summary of the research on bolted beam-to-column connections*, TU Delft, Faculteit der Civiele Techniek.